THÈSE

Pour obtenir le grade de

DOCTEUR DE L'UNIVERSITÉ GRENOBLE ALPES

École doctorale : STEP - Sciences de la Terre de l'Environnement et des Planètes
Spécialité : Sciences de la Terre et de l'Environnement
Unité de recherche : Institut des Géosciences de l'Environnement (IGE)

Dynamique de la zone d'échouage du glacier de l'Astrolabe (Antarctique de l'Est): apport de la sismologie et de la géodésie

Grounding zone dynamics of the Astrolabe Glacier (East Antarctica): insights from seismology and geodesy

Présentée par :

Tifenn LE BRIS

Direction de thèse :

Guilhem BARRUOL DIRECTEUR DE RECHERCHE, CNRS	Directeur de thèse
Florent GIMBERT CHARGE DE RECHERCHE, CNRS DELEGATION ALPES	Co-encadrant de thèse

Rapporteurs :

Alessia MAGGI
PROFESSEURE DES UNIVERSITES, Université de Strasbourg
Adam BOOTH
ASSOCIATE PROFESSOR, University of Leeds

Thèse soutenue publiquement le **26 février 2026**, devant le jury composé de :

Florent BRENGUIER, PHYSICIEN, Université Grenoble Alpes	Président
Guilhem BARRUOL, DIRECTEUR DE RECHERCHE, CNRS délégation Alpes	Directeur de thèse
Alessia MAGGI, PROFESSEURE DES UNIVERSITES, Université de Strasbourg	Rapporteure
Adam BOOTH, ASSOCIATE PROFESSOR, University of Leeds	Rapporteur
Romain MILLAN, CHARGE DE RECHERCHE, CNRS délégation Alpes	Examinateur
Malgorzata CHMIEL, CHARGEE DE RECHERCHE, CNRS délégation Côte d'Azur	Examinatrice

Invités :

Florent GIMBERT
CHARGE DE RECHERCHE, Université Grenoble Alpes

Remerciements

Je tiens tout d'abord à remercier Guilhem et Florent, pour leur accompagnement constant tout au long de ces trois années. Je suis très reconnaissante pour votre disponibilité, vos conseils avisés et vos relectures attentives qui m'ont permis d'arriver au bout de cette thèse. Merci Guilhem de m'avoir donné l'opportunité de découvrir l'Antarctique et Florent de m'avoir permis de découvrir le Groenland. Grâce à vous, j'ai eu le rare privilège d'avoir mis les pieds aux deux pôles.

Je voudrais adresser ma reconnaissance à mes collègues et collaborateurs pour nos échanges, leurs conseils et leurs regards critiques qui ont enrichi mes travaux. Je remercie également les membres de l'équipe Cryodyn pour toutes ces parenthèses agréables et ces repas sur la terrasse de la MCP, même lorsque la météo s'y prêtait peu. Je n'oublie pas les services administratifs pour leur aide indispensable et je tiens particulièrement à remercier Bertille pour la gestion de mes nombreuses missions et sa patience face à des outils informatiques parfois capricieux. Je garde en mémoire le soutien de mes collègues du bureau 122, Samidha pour ces pauses bienvenues, Hugo pour la relecture de mon manuscrit et Justine, désormais de l'autre côté de l'Atlantique, mais jamais très loin pour me venir en aide.

Un immense merci aux personnes croisées au fil de ces trois années : aux discussions improvisées dans les couloirs, aux échanges lors des conférences, et à celles et ceux qui m'ont entraînée hors de mon bureau, que ce soit autour d'un verre ou en montagne. J'ai une pensée particulière pour l'équipe avec qui j'ai passé un mois au Groenland : beaucoup de rires, quelques nœuds aux cerveaux, et bien plus de football que prévu.

Que soient ici remerciés ; Rachel, Daphné et les autres compagnons de Dumont d'Urville, pour cette expérience polaire hors norme ; Maryline, pour m'avoir souvent aidée à retrouver l'équilibre durant cette thèse ; Mes amis de longue date, parfois éloignés du monde de la recherche, mais toujours présents ; Et Jonas, pour nos aventures rares mais précieuses.

À mes chères Pauline(s), piliers depuis tant d'années : merci pour nos soirées, nos discussions, vos mots rassurants et merci d'être celles avec qui je peux rêver tout haut de projets toujours plus fous.

Et enfin, à ma famille, mes parents et mes sœurs, un merci du fond du cœur. C'est grâce à votre soutien inconditionnel que cette thèse a pu voir le jour. Je suis reconnaissante pour vos appels qui me montrent que vous n'êtes jamais très loin malgré les kilomètres, pour vos encouragements continus, pour croire en moi quand je commence à douter, et pour me suivre depuis toutes ces années dans mes aventures aux quatre coins du monde.

Je voudrais conclure ces remerciements avec une photographie rapportée d'Antarctique que j'aime particulièrement : une procession de manchots empereurs avançant sur la banquise, avec le glacier de l'Astrolabe en arrière-plan. J'ai moi aussi avancé ainsi: entourée et soutenue. Derrière moi, une famille et des amis toujours présents, qui m'ont accompagnée pas à pas tout au long de ce parcours de thèse.



Crédit photo: Daphné Laure

Résumé

Les glaciers côtiers assurent l'écoulement gravitaire de la glace depuis la calotte vers l'océan. Leur dynamique est principalement contrôlée par les processus se produisant au niveau de la zone d'échouage, qui constitue la transition entre la glace reposant sur le substratum rocheux et la glace flottante qui se jette dans l'océan. Cette zone subit à la fois l'influence de l'océan (marées, houle, courants) et celle de la résistance mécanique exercée par la glace de mer, ainsi que par la topographie latérale et sous-glaciaire du substratum, pouvant s'opposer à l'écoulement glaciaire. La zone d'échouage représente ainsi un élément clé du contrôle du bilan de masse de la calotte antarctique.

De nombreuses études ont examiné les évolutions à long terme (pluriannuelles à décennales) des glaciers côtiers, montrant comment les forçages externes influencent le recul de la zone d'échouage et l'accélération de l'écoulement glaciaire, contribuant ainsi à l'élévation du niveau marin. Cependant, bien que les méthodes actuelles, telles que la télédétection, offrent une couverture spatiale à grande échelle, elles ne disposent pas de la résolution spatiale et temporelle fine nécessaire pour comprendre en détail les processus de déformation et de dynamique de la glace, en particulier au niveau des zones d'échouage.

La sismologie passive constitue une approche efficace pour s'affranchir de ces limites, en enregistrant en continu les signaux sismiques générés par la déformation glaciaire et en offrant une fenêtre d'observation sur les processus se produisant dans l'ensemble de la colonne de glace, depuis la surface jusqu'à la base du glacier.

Dans cette thèse, nous caractérisons la dynamique à court terme du glacier de l'Astrolabe, un glacier côtier de l'Antarctique de l'Est, à partir de déploiements sismiques multi-échelles, allant de réseaux régionaux à des réseaux locaux denses. Notre analyse repose sur les données sismiques acquises dans le cadre du projet SEIS-ADELICE (2020–2025), durant lequel nous avons déployé des capteurs large bande, des sismomètres de fond de mer, des réseaux denses de nodes sismiques et des fibres optiques. À partir de ces enregistrements continus, nous détectons et localisons des événements sismiques de surface et basaux, révélant des modes de déformation distincts. Ces analyses sont complétées par des mesures GNSS qui permettent de mieux contraindre les déplacements et la déformation de la glace.

Nous montrons que l'occurrence et la distribution spatiale des événements sismiques à l'échelle journalière fournissent des informations précieuses sur les processus contrôlant la dynamique glaciaire au niveau de la zone d'échouage. À cette période de temps, les variations tidales du niveau marin induisent une flexure de la glace, générant des contraintes et une fracturation fragile en surface. La signature sismique de cette déformation est cohérente avec la flexure observée par géodésie (réseau GNSS) et permet de déduire la position et la migration à court terme de cette zone d'échouage géodésique. À la base du glacier, nous détectons et localisons des événements sismiques associés au glissement par à-coups de la glace (stick-slip) sur le substratum, dont l'occurrence est également modulée par les marées. Ces signaux semblent traduire

des intrusions périodiques d'eau océanique sous le glacier, modifiant les conditions de frottement à l'interface glace–substratum. Ce processus met en évidence la position des aspérités basales qui définissent la zone d'échouage mécanique.

Ce travail améliore notre compréhension de la dynamique de la zone d'échouage à de courtes échelles spatiales et temporelles ainsi que de sa sensibilité au forçage des marées océaniques. Il démontre comment les réseaux sismiques denses permettent un suivi robuste et à haute résolution des interfaces glaciaires, difficilement observables par ailleurs. Enfin, il ouvre des perspectives scientifiques à plus grande échelle, telles que le suivi à long terme du glissement basal en tant que proxy du recul de la zone d'échouage, et l'imagerie sismique et le couplage des observations avec la modélisation, afin de mieux contraindre les propriétés de propagation des ondes, les processus physiques et les mécanismes de déformation de la glace au sein des glaciers côtiers.

Abstract

Marine-terminating outlet glaciers accommodate gravitational ice flow from the continental ice sheet to the ocean. Their dynamics is primarily controlled by processes occurring at the grounding zone, the transition between grounded ice over the bedrock and floating ice extending over the ocean. This area suffers the effect of the ocean (tides, swells, currents), but also of the mechanical buttressing provided by sea ice, and lateral and subglacial bedrock topography that may oppose glacier motion. This makes the grounding zone a key control area on the ice mass balance of the Antarctic continent.

Numerous studies have investigated long-term (multi-year to decadal) changes in outlet glaciers, showing how external forcings influence grounding zone retreat and ice-flow acceleration, thereby contributing to sea-level rise. However, although current methods, such as remote sensing, provide large-scale resolution, they lack the fine spatial and temporal resolution needed to better understand the ice deformation and dynamical processes occurring at outlet glaciers, particularly at their grounding zones.

Passive seismology stands as an effective approach to fill this gap, recording continuous seismic signals generated by glacier deformation and providing a window into processes occurring throughout the ice column, from its surface to its base.

In this thesis, we characterize the short-term dynamics of the Astrolabe Glacier, an outlet glacier in East Antarctica, using multi-scale seismic deployments ranging from regional networks to dense local arrays. Our analysis relies on seismic data acquired in the frame of the SEIS-ADELICE project (2020–2025), during which we deployed broadband sensors, ocean-bottom seismometers, optical fibers, and dense arrays of seismic nodes. From these continuous records, we detect and locate surface and basal seismic events, revealing distinct modes of deformation. These analyses are complemented by GNSS measurements that further constrain ice motion and deformation.

We show that seismic events occurrence and spatial distribution at a daily timescale provide insights into the processes controlling glacier dynamics at the grounding zone. At daily timescales, variations in sea level induce tidal flexure over the grounding zone of the glacier, generating stress and brittle fracturing at its surface. The seismic signature of this deformation is compatible with the tidal flexure observed by geodesy (GNSS network) and is consequently used for inferring the position and short-term migration of this geodetic grounding zone. At the glacier base, we detect and locate seismic events associated with frictional sliding over bedrock, whose activity is similarly modulated by the tides. We interpret these signals as evidence of periodic seawater intrusion beneath the glacier, altering the frictional conditions at the ice–bed interface. This process reveals the position of basal asperities that underline the position of the mechanical grounding zone.

This work improves our understanding of grounding zone dynamics over short spatial and time scales and its control by tidal forcing. It demonstrates how dense seismic arrays can provide robust, high-resolution monitoring of glacier interfaces that are oth-

erwise difficult to observe. It encourages towards larger-scale scientific perspectives, such as long-term monitoring of basal slip as a proxy for grounding zone retreat and seismic imaging and coupling of observations with modeling to refine our understanding of wave propagation properties, physical processes and ice deformation mechanisms in outlet glaciers.

Contents

Remerciements iii

Résumé v

Abstract vii

1 Introduction 1
- 1.1 Antarctica: A threatened region under scientific scrutiny 2
  - 1.1.1 A continent of superlatives 2
  - 1.1.2 Climate crisis in Antarctica 5
  - 1.1.3 A scientific community at work 7
- 1.2 Marine-terminating glaciers: An interface between ice, ocean and bedrock 8
  - 1.2.1 Morphology and characteristics of marine-terminating glaciers . 9
  - 1.2.2 The grounding zone 10
  - 1.2.3 Ice-ocean and ice-bedrock interactions at the grounding zone of marine-terminating outlet glaciers 13
  - 1.2.4 Observation and modeling approaches to study marine-terminating glaciers dynamics 17
- 1.3 Cryoseismology: A window for studying marine-terminating glaciers dynamics 21
  - 1.3.1 Investigating cryospheric processes using seismology 21
  - 1.3.2 Cryoseismic signals associated with crevassing and ice brittle deformation 25
  - 1.3.3 Cryoseismic signals associated with basal and lateral shear friction 27
  - 1.3.4 Other cryoseismic signals 29
- 1.4 Research aims and focus 32

2 SEIS-ADELICE: seismic acquisition on the Astrolabe Glacier 35
- 2.1 The Astrolabe Glacier 36
  - 2.1.1 Description of the study site 36
  - 2.1.2 Previous and ongoing studies 40
- 2.2 Project SEIS-ADELICE (2020-2025) 41
  - 2.2.1 Objectives 41
  - 2.2.2 Seismic deployments and field campaigns 41

3 Methods for detection and location of cryoseismic events 45
- 3.1 Detection of seismic events 46
  - 3.1.1 Short term average (STA)/ Long term average (LTA) algorithm 46
  - 3.1.2 Template matching 50

3.2 Location of seismic events . . . 53
3.2.1 Grid search . . . 53
3.2.2 QuakeMigrate . . . 57
3.2.3 Polarization analysis . . . 59
3.3 Match Field Processing . . . 61

4 Seismic monitoring of tide-induced deformation at the Astrolabe Glacier surface 65
4.1 Context and strategy of the study . . . 66
4.2 Spatial and temporal variability in tide-induced icequake activity at the Astrolabe coastal glacier, East Antarctica (Le Bris et al., 2025) . . . 66
4.3 Comparison with 2024 and 2025 dense arrays . . . 89
4.4 Outcomes and outlook . . . 94

5 Daily migration of grounding lines: insights from tide-modulated icequake and stick-slip events 95
5.1 Introduction . . . 96
5.2 Surface icequakes and basal stick-slip events reveal daily grounding line migration and seawater intrusion at a marine-terminating glacier in East Antarctica (Le Bris et al., submitted) . . . 97
5.2.1 Abstract . . . 97
5.2.2 Introduction . . . 97
5.2.3 Data . . . 99
5.2.3.1 Study site . . . 99
5.2.3.2 Observations : dense array of seismic nodes, GNSS and tide data . . . 100
5.2.4 Methods . . . 101
5.2.4.1 Icequakes detection, occurrence and location . . . 101
5.2.4.2 Stick-slip events detection and location . . . 102
5.2.5 Results . . . 105
5.2.5.1 Migration of the grounding zone over tidal cycle: surface icequakes signature . . . 105
5.2.5.2 Stick-slip dynamics at the grounding zone during tidal cycles . . . 105
5.2.6 Discussion . . . 110
5.2.7 Conclusion . . . 113
5.2.8 Acknowledgements and Data Availability . . . 113
5.3 Outcomes and outlook . . . 114

6 Investigation on the seismic signature of Astrolabe Glacier shear margin 117
6.1 Ice dynamics at shear margins of outlet glaciers . . . 118
6.2 Data acquisition . . . 119
6.2.1 2025 dense array configuration and deployment . . . 119

6.2.2 Quality of the data and first observations . . . 119
6.3 Dynamic framework of the shear margin . . . 123
6.4 Stick-slip clusters identification . . . 126
6.4.1 Detection and location of stick-slip clusters . . . 126
6.4.2 Focal mechanisms . . . 127
6.5 Spatial and temporal analysis of stick-slip clusters activity . . . 130
6.5.1 Tidal influence on stick-slip clusters . . . 130
6.5.2 Lateral and depth distribution and comparison with radar data 132
6.6 Outcomes and outlook . . . 136

7 Thoughts on the deployment and performance of geophysical instrumentation in polar regions 137
7.1 Context and scope of the discussion . . . 138
7.2 Contrasted field conditions and logistical challenges across polar regions 139
7.2.1 Climatic constraints on missions . . . 139
7.2.1.1 Antarctica missions . . . 139
7.2.1.2 Greenland missions . . . 140
7.2.2 Logistical architectures: access and operational frameworks . . . 141
7.2.3 Risk management on the field . . . 144
7.3 Dense seismic arrays: instrumentation strategies and data quality analysis 146
7.3.1 Deployment . . . 147
7.3.2 Recovery . . . 150
7.3.3 Tilting . . . 152
7.3.4 Intercomparison of seismic sources: Astrolabe vs. Isunnguata Sermia . . . 156
7.4 Distributed Acoustic Sensing (DAS): instrumentation strategies and data quality analysis . . . 160
7.4.1 Deployment of optic fiber in Antarctica and Greenland . . . 161
7.4.2 Quality of the data acquired on the Astrolabe Glacier . . . 164
7.4.3 Preliminary analysis and comparison with data acquired on Isunnguata Sermia . . . 166
7.4.4 Can we substitute dense networks with DAS ? . . . 169
7.5 Data acquisition and scientific responsibility . . . 170
7.5.1 From acquisition to valorization . . . 170
7.5.2 Environmental cost and scientific sobriety . . . 171

Conclusion & Perspectives 173

Bibliography 203

List of figures 219

List of tables 221

A Appendix chapter 2 **223**

B Appendix chapter 4 **227**

C Appendix chapter 5 **233**

D Appendix chapter 6 **237**

CHAPTER 1

Introduction

Contents

1.1 Antarctica: A threatened region under scientific scrutiny 2

1.1.1 A continent of superlatives 2

1.1.2 Climate crisis in Antarctica 5

1.1.3 A scientific community at work 7

1.2 Marine-terminating glaciers: An interface between ice, ocean and bedrock 8

1.2.1 Morphology and characteristics of marine-terminating glaciers 9

1.2.2 The grounding zone 10

1.2.3 Ice-ocean and ice-bedrock interactions at the grounding zone of marine-terminating outlet glaciers 13

1.2.4 Observation and modeling approaches to study marine-terminating glaciers dynamics 17

1.3 Cryoseismology: A window for studying marine-terminating glaciers dynamics 21

1.3.1 Investigating cryospheric processes using seismology 21

1.3.2 Cryoseismic signals associated with crevassing and ice brittle deformation 25

1.3.3 Cryoseismic signals associated with basal and lateral shear friction 27

1.3.4 Other cryoseismic signals 29

1.4 Research aims and focus 32

1.1 Antarctica: A threatened region under scientific scrutiny

1.1.1 A continent of superlatives

"Lands doomed by nature to perpetual frigidness: never to feel the warmth of the sun's rays; whose horrible and savage aspect I have no words to describe"
— Captain James Cook

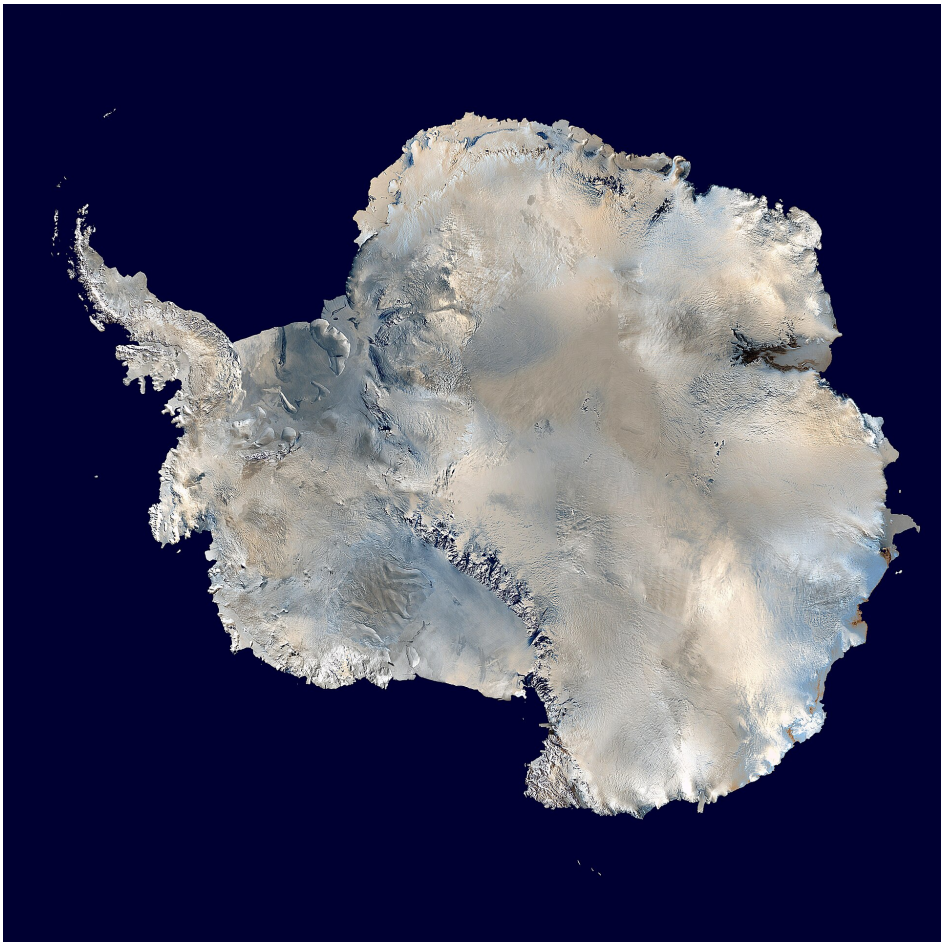

Figure 1.1: An orthographic projection of NASA's Blue Marble data set (1 km resolution global satellite composite). MODIS observations of polar sea ice were combined with observations of Antarctica made by the National Oceanic and Atmospheric Administration's AVHRR sensor-the Advanced Very High Resolution Radiometer.

Antarctica is a vast, icy landmass that proudly holds the title of the highest, driest, windiest and coldest continent on Earth (Fig. 1.1). Its average elevation is approximately 2 500 meters (Bedmap3; Pritchard et al., 2025), significantly higher than any other continent (all of which have average elevations below 1 000 meters). The South

Pole lies at an elevation of 2 835 meters, while the highest point on the Antarctic ice sheet reaches 4 093 meters (80°22′S, 77°21′E).

The climate is extremely harsh. Precipitation is averaging only about 175 mm per year, mainly along the coastal regions, where lower atmospheric pressure allows for higher moisture content (Hersbach et al., 2020). What makes the weather conditions very difficult is the presence of katabatic winds: cold, dense air masses that flow down slope on the ice sheet under the influence of gravity. These winds often reach speeds over 100 km per hour and can exceed 300 km per hour. Additionally, while temperatures vary between the coastal areas and the interior plateau, they remain extremely cold across the continent. Annual average temperatures range from approximately -10°C along the coast to -60°C in the interior (Turner et al., 2009b). The lowest temperature ever recorded on Earth, -89.2°C, was measured at Vostok Station in 1983 (Turner et al., 2009a).

Antarctica, including its islands and ice shelves, represents an area of 13 661 000 km^2, most of which is covered by the ice sheet (Fretwell et al., 2013; Pritchard et al., 2025). The ice sheet has been formed by snow accumulated over hundreds to millions of years and compressed into ice. Under the effect of the gravity field, the ice then flows in its solid state (or more so, creeps) from the center of the continent towards the surrounding ocean. The thickness of the ice sheet, averaging around 1 km, can reach up to 4 km at the thickest places (Pritchard et al., 2025). In total, the Antarctic ice sheet contains around 27.17 million km^3 of ice (Pritchard et al., 2025). Beneath, is hidden a landscape of mountains, valleys and plains. Figure 1.2 presents the bed topography, surface elevation and ice thickness across Antarctica. About 45% of the Antarctic landmass lies below sea level (Pritchard et al., 2025), a feature with important implications that will be addressed in subsequent sections. At the surface, only 1% of the bedrock is visible and includes coastal outcrops, mountain ranges and nunataks (isolated peaks emerging from the ice). The main feature is the Transantarctic Mountains extending from the north western corner of the Ross Sea to the south western corner of the Weddell Sea. They divide the continent into two parts: East Antarctica and West Antarctica.

Although gravity drives the ice flow from the Antarctic interior toward the ocean, its velocity is primarily controlled by the geometry and dynamics of ice streams, outlet glaciers, and ice shelves, which act as the main pathways for ice discharge. Figure 1.3 illustrates the spatial distribution of ice surface velocities along with flow directions across the Antarctic continent. Regions of fastest flow are concentrated along major ice streams. They are defined as fast-flowing corridors of ice bounded by slower-moving ice, channeling ice from vast interior basins toward the ocean and often draining into large floating ice shelves. Among the most prominent ice drainage systems are: the Filchner-Ronne Ice Shelf (FRIS) in the Weddell Sea, the Ross Ice Shelf (RIS) in West Antarctica, the Brunt Ice Shelf along the Weddell Sea coast, and the Amery Ice Shelf

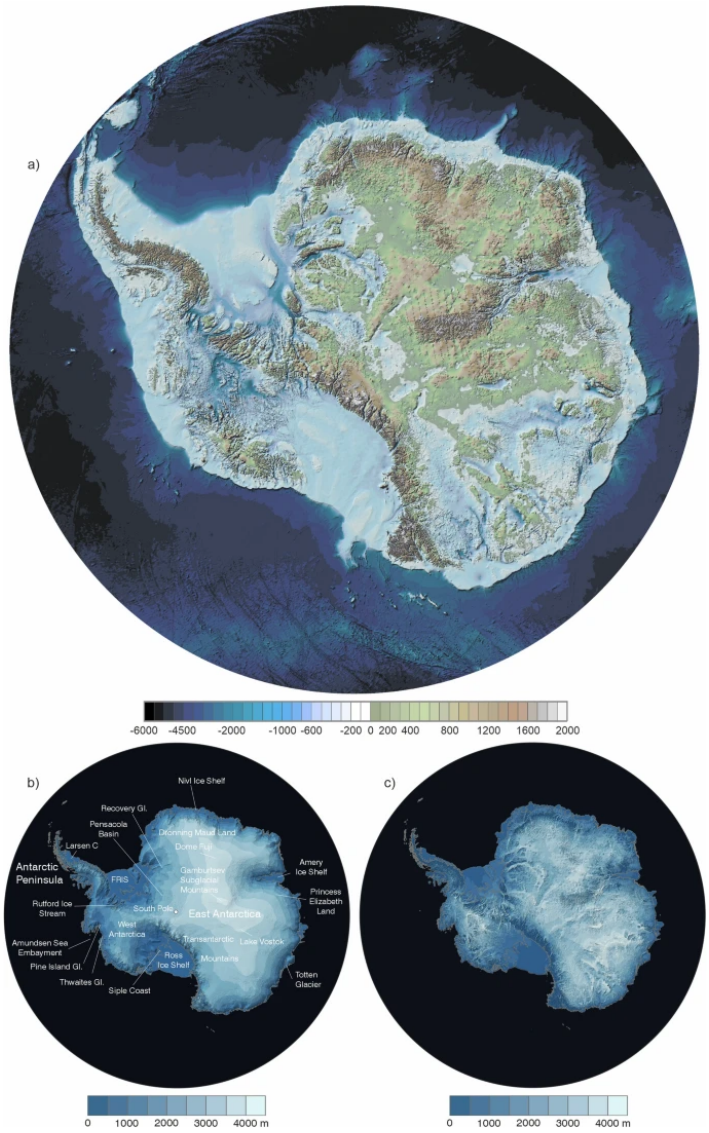

Figure 1.2: (a) Bed topography and (b) Surface elevation, in metres above sea level, and (c) Ice thickness in metres of Antarctica from Bedmap3 (Pritchard et al., 2025).

in East Antarctica. The flow speed within these ice streams ranges from hundreds to over a thousand meters per year. In contrast, glaciers are more localized, made of narrower ice flows constrained by fjord valleys. In Antarctica, most are outlet glaciers that channel ice from catchment basins or valleys to the coast. Flow speeds are usually slower, though some Antarctic glaciers (e.g. Pine Island, Thwaites) can match ice streams in velocity. Finally, ice shelves -large floating platforms fed by ice streams, act as buttresses to the continental ice, slowing the flow of ice toward the ocean. By regulating this discharge, they play a key role in controlling ice loss.

Understanding ice flow dynamics is a priority for scientists seeking to assess the

stability of the Antarctic Ice Sheet, its ice mass loss and ultimately its role in global sea level rise. These dynamics are tightly linked to external forcing, including both atmospheric and oceanic changes. The next section explores how Antarctica ice sheet dynamics fit into a context of warming climate, melting ice, and rising seas.

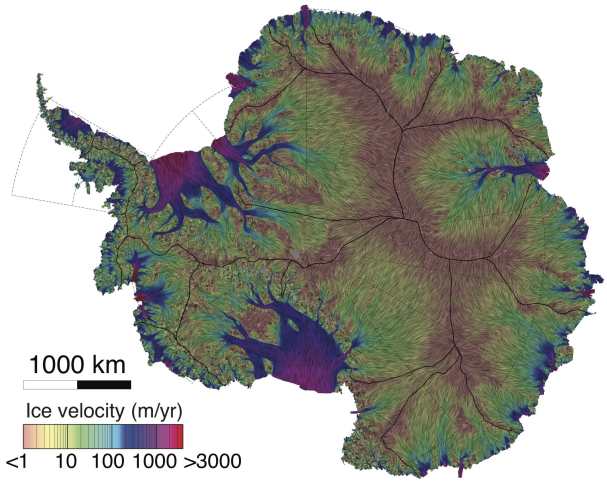

Figure 1.3: Complete map of ice motion in Antarctica, with speed colored on a logarithmic scale from brown (less than 1 m/year) to red (more than 3 km/year) and flow direction indicated by colored lines and showing the flow pattern of ice across the continent (Mouginot et al., 2019).

1.1.2 Climate crisis in Antarctica

"It is too late to expect to preserve the Antarctic in a pristine condition, but not too late to take steps to ensure that harmful interference is kept to a minimum and that undesirable trends are checked or reversed."
— Bonner, 1987

The Antarctic Ice Sheet (AIS) is the largest potential contributor to global sea level rise (Oppenheimer et al., 2019). If it was to melt completely, it would contribute to 58 m elevation of the sea level (Fretwell et al., 2013; Morlighem et al., 2020). While this scenario is not to happen in the near future, changes are already taking place and with it a need to assess and understand the processes at play. For the past three decades (1990s to 2020s), ice losses from Antarctica increased 6-fold (IMBIE team, 2018; IMBIE Team, 2020) participating in raising the global sea level (WCRP Global Sea Level Budget Group, 2018). The assessment of the contribution of AIS to sea level rise is based on computation of ice mass balance (IMB). The IMB is the net difference between the surface mass balance (in blue, Fig. 1.4) and the dynamic mass loss (in orange and pink, 1.4). Surface mass balance (SMB) is defined as the difference between snow accumulation (snowfall, rainfall) and surface ablation (evaporation, sublimation,

melting and runoff). Dynamic mass loss primarily occurs through solid ice discharge at the grounding line and at the ice-ocean interface of ice shelves. Basal mass balance, including processes such as basal fusion, are also accounted for in the IMB even if it is often overlooked in computations (in green, Fig. 1.4). If the IMB is negative, the ice sheet is losing more ice than it is gaining resulting in contributing to sea level rise.

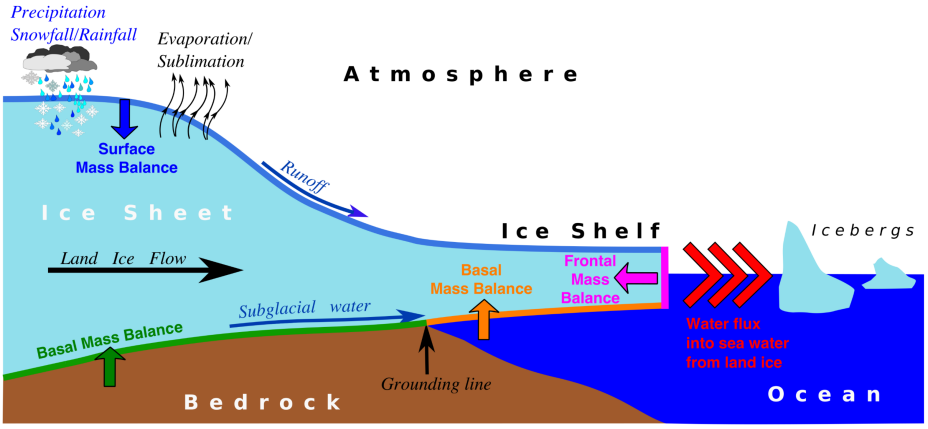

Figure 1.4: Illustration of the mass balance components and their key processes to assess the ice mass balance of ice sheets. Adapted from Nowicki et al. (2016).

Ice shelves play a primary role in regulating the IMB (Fürst et al., 2016). First, ice mass loss is governed by two main mechanisms occurring at ice shelves: basal melting and surface calving. Because these mechanisms happen at the interface with the ocean, they are particularly sensitive to variations in oceanic parameters (e.g., temperature, salinity, currents). These two processes will be explored in more detail in section 1.2.2 and 1.2.3. Ice shelves can also witness changes in their SMB due to the influence of atmospheric circulation patterns that affect near-surface air temperature and precipitation, which in turn control snowfall and surface melt (Noble et al., 2020; van Wessem et al., 2018). On one hand, increased snowfall as a result of the increased moisture-holding capacity of a warming atmosphere may lead to positive SMB in some regions (especially in East Antarctica) (Ligtenberg et al., 2013). On the other hand, atmospheric rivers, narrow corridors of warm, moisture-laden air, can bring intense precipitation and surface melt episodes, particularly in West Antarctica and coastal zones (Wille et al., 2021). These events contribute to surface melt and runoff, potentially offsetting gains from snowfall. Note that the net effect of atmospheric changes on SMB remains difficult to constrain due to interannual variability and the interplay of opposing processes. Recent estimates indicate that SMB anomalies contribute less to overall mass loss compared to dynamic ice loss processes (Rignot et al., 2019). Indeed, more than 80% of mass loss stems from ocean-driven basal melting and dynamic ice discharge, while SMB variability accounts for less than 20% (Davison et al., 2023). Independently from their respective contributions to ice mass loss, ongoing perturbations in climatic conditions (whether it is atmospheric or oceanic) due to global warming is

disrupting the overall IMB and as a consequence the equilibrium state of the AIS.

The resulting projections on sea-level rise from taking into account the climatic changes occurring, or set to occur, can seem worrying. I encourage anyone looking for clarity to turn to the Intergovernmental Panel on Climate Change (IPCC) reports. These reports do not just explain what is happening to our planet in terms of climate, they also show what can be done to change the current path. For example, the IPCC Sixth Assessment Report makes it clear that while some changes are already happening, we can still avoid the most severe impacts by limiting global warming below 2°C. This would reduce the risk of major ice sheet loss in Antarctica and the large sea level rise that could follow (IPCC, 2021). In that sense, the reports provide both a warning and a guide for what actions can be taken by governments to slow down the climate crisis.

1.1.3 A scientific community at work

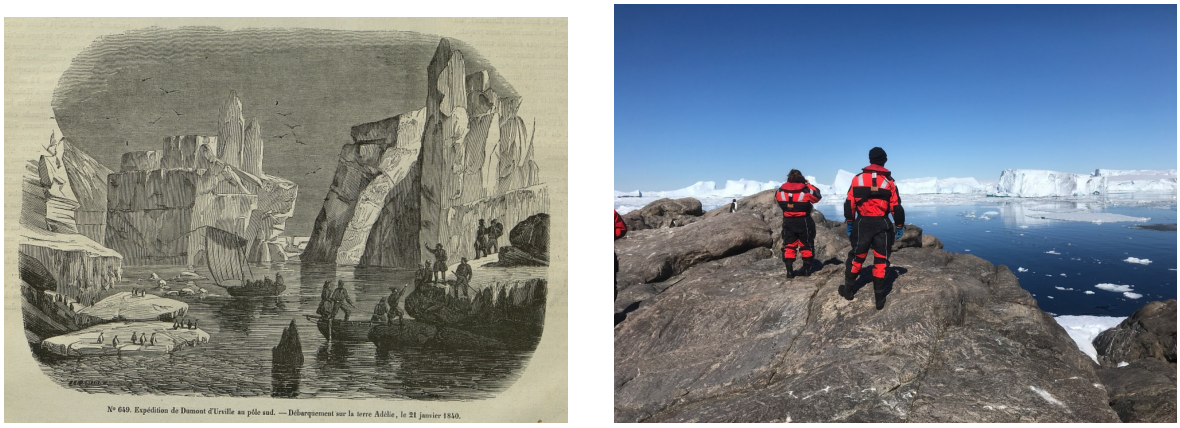

Figure 1.5: (left) Discovery of Adélie Land by Jules Dumont d'Urville. Picture from "Voyage illustré dans les cinq parties du monde" by Adolphe Joanne, published around 1850. (right) Picture of two scientists looking at the icebergs in front of the Astrolabe Glacier from Curie island, in Terre Adélie. Picture from the 2024 SEIS-ADELICE campaign in Dumont d'Urville.

Understanding the unfolding climate crisis in Antarctica demands sustained, long-term scientific observation and modeling. Making sense of the current and upcoming changes depends on decades of prior research. Continuing this effort is a race against time to improve our knowledge and our predictive capabilities.

Bonner (1987) traces the history of science in Antarctica from the early discovery of the continent in the late 1700s to the end of the 20th century. In the 19th century, exploration was closely tied to commercial seal hunting, for fur. While this industry

had devastating impacts on seal populations, it also led indirectly to the accumulation of geographical and biological knowledge. Numerous islands were mapped, and for the first time, expeditions circumnavigated the Antarctic continent. These early expeditions largely remained ship-based, and it was not until the quest to reach the South Pole emerged that true continental exploration began. This period, called the "Heroic Age" (1901-1922), saw landmark expeditions by, among others, Scott, Shackleton, and Amundsen, the latter of whom reached the South Pole in 1911. Although limited in terms of scientific focus, these expeditions laid the groundwork for future Antarctic research. Between the two World Wars, exploration shifted alongside the collapse of the seal industry, with whale hunting becoming the new economic driver. During this time, scientific observations, particularly in biology and oceanography, began to take place, still limited and often conducted from ships. A major turning point came with the International Geophysical Year of 1957-1958, during which 12 countries collaborated to establish more than 47 research stations across the continent. This unprecedented effort opened the door for collecting key data in various domains such as glaciology, meteorology, geology, and upper atmosphere physics. It redefined Antarctica as a space for peaceful, international scientific cooperation. Bonner's historical account ends in 1986, not yet fully grasping the scale of the climate change threats to the Antarctic ice sheet.

Since then, Antarctic research has developed into a highly international community, coordinated by bodies like the Scientific Committee on Antarctic Research (SCAR). It brings together many scientific disciplines, including climate science, glaciology, oceanography, geophysics, biology, and astrophysics. To study ice dynamics in Antarctica, researchers use a wide range of methods ranging from satellite observations and geophysical surveys to hands-on fieldwork, computer modeling, and laboratory experiments.

Today, Antarctic science is increasingly focused on major global concerns including climate change and sea level rise for which ice shelves and outlet glaciers, i.e. marine-terminating glaciers, are key components. These glaciers are at the interface with the ocean, which are at the frontline of ongoing perturbations in climatic conditions due to global warming and serve as objective indicators of the the current and forthcoming state of the AIS.

1.2 Marine-terminating glaciers: An interface between ice, ocean and bedrock

This chapter introduces marine-terminating outlet glaciers main physical and morphological characteristics, discusses the processes that control their dynamics and interactions with both the ocean and the bedrock, and reviews how these glaciers are currently studied through observations and modeling.

1.2.1 Morphology and characteristics of marine-terminating glaciers

Marine-terminating outlet glaciers are defined as glaciers whose ice flows directly into the ocean, primarily losing mass through calving (breaking of icebergs from the glacier front) and basal melting at the ice-ocean interface. These glaciers, sometimes also referred to as tidewater outlet glaciers, represent fast-flowing channels that drain ice from ice caps, ice fields, mountain glaciers or ice sheets. They typically flow through topographic depressions such as valleys or troughs and terminate in the ocean, either in a grounded or floating state (Benn & Evans, 2014). Their behavior is influenced by a combination of upstream ice supply and terminus boundary conditions, including oceanic and atmospheric forcing (Carr et al., 2013).

Within marine-terminating glaciers, a distinction is made based on whether the glacier terminus is floating or grounded. This distinction is particularly relevant since the physical processes driving mass loss and glacier dynamics differ between the two types. A floating terminus occurs when the end of the glacier is floating on seawater, or when it extends into an ice shelf (van der Veen, 2002; Vieli, 2011). The floating part, if it is confined by valley walls and has a narrow width relative to its length, is referred to as a floating tongue. If the platform extends in the ocean with important width relative to its length, then it is an ice shelf. In contrast, a grounded terminus refers to a glacier whose terminus is in direct contact with the bedrock or seafloor. Figure 1.6 presents schematic illustrations of these 2 typical morphologies of marine-terminating outlet glaciers. These diagrams are intended to represent idealized cases for explanatory purposes. However, it is important to note that the actual morphology of marine-terminating outlet glaciers varies significantly depending on factors such as bed topography, fjord geometry, and valley wall conditions.

The geographic distribution of these glacier types differs. Grounded marine-terminating glaciers are more commonly found in temperate regions, such as Alaska, Patagonia and parts of Canada. In contrast, floating marine-terminating glaciers are predominantly located in polar regions, including Greenland, Svalbard, and Antarctica, where colder conditions allow for the development of extensive floating termini and ice shelves. This tends to change with climate change though. For instance, in Greenland, most marine-terminating glaciers are now grounded (Catania et al., 2020). Sermeq Kujalleq is a good example of a glacier that transitioned from floating to grounded due to changing climatic conditions. In the 1990s, the floating tongue was extending far in the ocean, with a length of around 15 km. In the early 2000s, it disintegrated, likely triggered by warm subsurface ocean water (Holland et al., 2008) and increased meltwater draining to the glacier bed during preceding warmer summers, lubricating the ice-bedrock interface (Zwally et al., 2002). Such conditions accelerated the ice thinning, the ice flow velocity and the calving rate. The floating tongue broke into large icebergs up to the state of now being grounded.

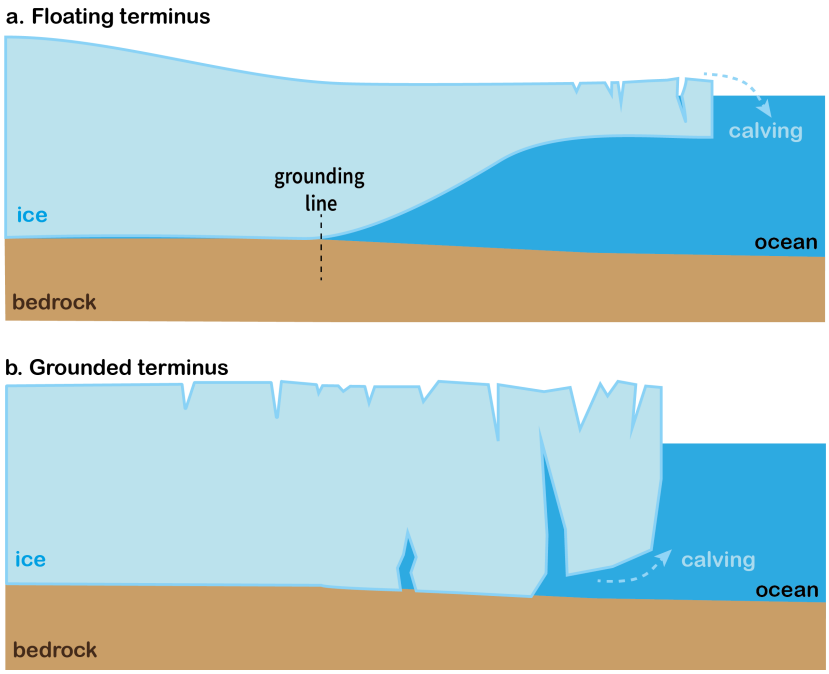

Figure 1.6: Schematic representation of 2 major marine-terminating glacier morphology: (a) Marine-terminating glacier with a floating terminus. (b) Marine-terminating glacier with a grounded terminus. The grounding line, indicated in panel (a), is the virtual limit from the glacier being grounded on the bedrock to floating on the ocean. The two sketches are not to scale. A similar thickness can be expected between the front of the floating glacier and the grounded glacier.

1.2.2 The grounding zone

A key feature of marine-terminating glaciers with a floating terminus or extending into an ice shelf is the grounding line. This line defines the transition from the glacier being grounded (in contact with the bedrock or seafloor) to floating on the ocean (see Fig. 1.6a). Such transition plays an important role in controlling glaciers and ice sheets dynamics. The location, displacement, stability of this boundary is thus at the center of much research surrounding marine-terminating glaciers. But this transition is more complex than the virtual line drawn in Fig. 1.6a. The grounding line is actually more a grounding zone that can cover several kilometres and that may vary with time, particularly with the tide influence. The grounding zone is defined as the region whose extent is determined by the landward limit where the ice is fully grounded to the seaward limit where the ice is in hydrostatic equilibrium with the underlying ocean and free-floating (Fricker & Padman, 2006; Fricker et al., 2009; Vaughan, 1994). Figure 1.7a summaries the structure of a grounding zone with the extent of the region (from F to H) and additional features.

The grounding zone dynamics is influenced by external atmospheric and oceanic forces and especially ocean tides. Over short periods of time, and due to the tide-

induced sea level variations, the floating tongue or the ice shelf can change its elevation. As a consequence, the section of ice at the grounding zone may suffer important strain from the tidal vertical movement of the ocean, leading to the flexuring (also referred as bending) of the ice. The grounding zone includes both the landward limit and the seaward limit of the tide-induced ice flexure (see Fig. 1.7a). Considering the variations in tides amplitudes during successive cycles, these landward and seaward limits are changing daily. There is therefore not an exact grounding line delineation, but instead a grounding zone whose extent varies on a daily scale, depending on tidal amplitudes. Accordingly, the grounding line (i.e. the most seaward contact point of the glacier ice with the underlying bedrock) is not static but moves back and forth across its grounding zone over the daily tidal cycles (Freer et al., 2023; Rignot et al., 2011a). This is called grounding line migration, and is represented in Figure 1.7b. Because it is controlled by the tides, the grounding line migrates on hourly timescales and can reach greatest migration rates during spring tides (i.e. highest tide amplitudes, happening twice a month).

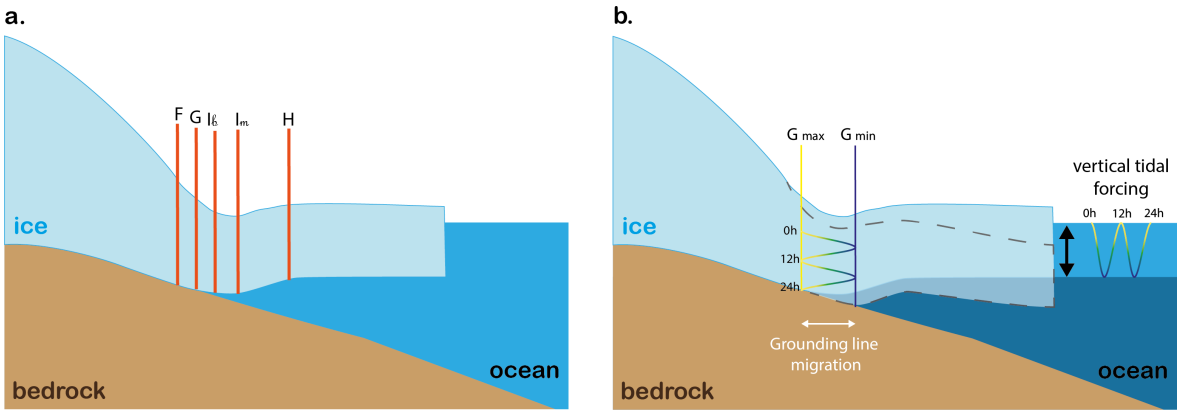

Figure 1.7: (a) Schematic representation of the key structural features of a grounding zone. F is the landward limit of ice flexure from tidal movement. G is the latest point of contact between the ice and the ground, i.e. the grounding line. I_b is the break-in-slope. I_m is the local elevation minimum and H is the landward limit of the hydrostatic zone of free-floating ice. It corresponds also to the seaward limit of ice flexure. Note that the distance between F, G, I_b, I_m and H depends on local ice thickness and properties, and local bedrock topography and properties. Adapted from Fricker et al. (2009). (b) Schematic representation of a grounding zone showing migration of the grounding line position (G) between high tide (Gmax) and low tide (Gmin) across a simplified semidiurnal tidal cycle over 24 hours. Adapted from Freer et al. (2023).

Grounding zone dynamics play a central role in regulating the stability and mass balance of marine-based ice sheets. The position of the grounding zone influences the rate of ice discharge into the ocean by modulating basal resistance and buttressing forces (Rignot et al., 2011a; Thomas et al., 2004; Vaughan, 1994). When the grounded ice is still in contact with bedrock, it is subject to basal drag. Once the ice is free-

floating, it experiences much less resistance and is primarily governed by lateral drag and gravitational spreading. The grounding zone thus represents a major shift in flow mechanics: from shear-dominated, friction-controlled ice streams to drag-free, buoyant ice shelf flow. And because the resistance to flow decreases once the ice is floating, it accelerates ice discharge into the ocean.

At large space and time scales, the position and stability of the grounding zone have direct implications for ice sheet stability. When the grounding zone retreats, it can trigger dynamic changes in glacier flow and mass loss as illustrated in Figure 1.8.

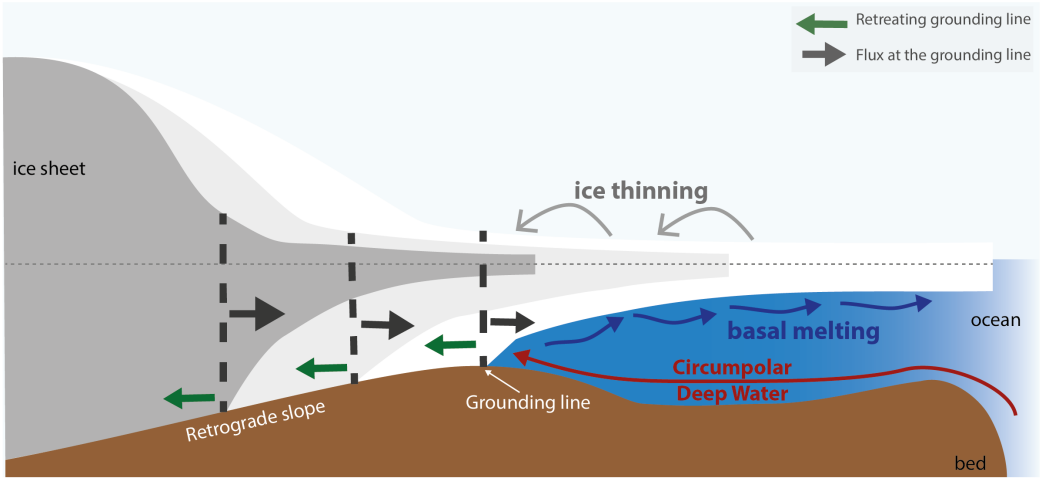

Figure 1.8: Schematic representation of key processes leading to rapid ice loss at marine-terminating glaciers. Modified from Pattyn et al. (2017).

A key driver of grounding zone retreat is basal melting, which thins the ice shelf (or the floating tongue) and weakens its structural integrity, reducing the buttressing force that resists the seaward flow of grounded ice (Jenkins et al., 2010; Reese et al., 2018). This process is intensified by the intrusion of warm ocean water masses, such as Circumpolar Deep Water (CDW), circulating beneath ice shelves and floating tongues (Pritchard et al., 2012). The loss of buttressing support leads to increased ice flow and eventual grounding zone retreat. In regions where the bed topography lies below sea level, as in much of West Antarctica and beneath large glacial basins from East Antarctica (see Fig. 1.2a), warm water can penetrate far inland once the grounding zone retreats, increasing basal melt over an even wider area that may destabilise the ice sheet far inland. In addition, as the glacier recedes onto reverse bed slopes (beds that deepen inland), it encounters thicker ice, which increases ice flux across the grounding zone (Schoof, 2007). This sets up a positive feedback loop: thinning initiates retreat, retreat exposes thicker ice, and thicker ice drives further acceleration and ice discharge. This dynamic process, known as Marine Ice Sheet Instability (MISI), implies that even small perturbations can lead to sustained and potentially irreversible grounding zone retreat. This phenomenon has already been observed in West Antarctica. In the Amundsen Sea, increased upwelling of the relatively warm CDW activated a positive

feedback loop resulting in rapid grounding zone recession at multiple glaciers including Pine Island Glacier with a retreat estimated up to 31 km from 1992 to 2011 and Thwaites Glacier with a retreat up to 14 km (Rignot et al., 2014). For all these reasons, locating and monitoring grounding zones over the years is essential for accurate mass budget calculations (Fricker et al., 2002; Rignot et al., 2011a).

1.2.3 Ice-ocean and ice-bedrock interactions at the grounding zone of marine-terminating outlet glaciers

Previous sections introduced key features of marine-terminating glaciers and processes occurring at the grounding zone, including basal melting and tide-induced grounding line migration. In this section, we take a broader look at the ice-ocean and ice-bedrock interfaces, exploring the range of processes involved and discussing the physical mechanisms that influence outlet glacier dynamics.

Tidal-induced ice flexuring and fracturing

Tides significantly affect the behavior and dynamics of ice shelves and floating glacier tongues, particularly near their grounding zones. Tidal fluctuations cause elevation changes of the floating tongue and bending (or flexure) of the ice at the grounding line, which induces both vertical and horizontal stress within the ice body (Brunt et al., 2010; Fricker & Padman, 2006; Vaughan, 1994). The flexure of the glacier, associated with changes in elevation, can be observed by both GNSS and satellite-based data and is extensively used to map the grounding line position. These tidal stress perturbations can also affect ice motion and modulate glacier flow velocity near marine margins (Padman et al., 2018). The tide is dominated by diurnal (daily) and semidiurnal (twice daily) tides, although the prevailing tidal regime can vary by location. For example, at the Ross Ice Shelf, flow speeds near the grounding zone exhibit a clear diurnal modulation that aligns with the dominant frequency of the Ross Sea tides (Anandakrishnan et al., 2003). In contrast, at the grounding zone of the Rutford Ice Stream on the Ronne Ice Shelf, where semidiurnal ocean tides dominate, the glacier's velocity exhibits its strongest response at fortnightly (14-day) periods (Gudmundsson, 2007).

Repeated tidal flexure not only influences ice dynamics but also contributes to surface brittle deformation of the ice and fracture development. This includes the formation of crevasses and strand cracks, which originate from the daily strain cycles imposed by tidal bending (Hulbe et al., 2016). Strand cracks, in particular, are surface fractures that form in response to tidal displacement at or near the grounding line (Vaughan, 1994). These features are frequently used as complementary markers to infer the location of grounding lines (Stephenson, 1984). More generally, fracturing related to the tidal flexuring can develop both at the surface and base of the glacier.

Despite their importance, tidal information in Antarctica remains limited due to the difficulty of obtaining continuous in-situ measurements such as those from tide gauges. As a result, satellite-based observations, which can track changes in Earth's gravitational field, are currently the most effective method for mapping tidal cycles around the continent.

Ocean-driven melting and thinning of ice

Basal melting is one of the primary mechanisms of mass loss for marine-terminating outlet glaciers (Davison et al., 2023; Rignot et al., 2019). When warm ocean water enters sub-ice-shelf cavities, it erodes the underside of the floating ice, progressively thinning the ice column and reducing structural integrity, as discussed in Section 1.2.2. (Jacobs et al., 2011; Jenkins & Jacobs, 2008; Pritchard et al., 2012; Shepherd et al., 2004). Intense basal melting can also result in undercutting of the ice front, further weakening mechanical support and potentially leading to collapse of the floating tongue (Benn et al., 2017; Vieli, 2011).

This process is particularly severe in regions where the ice shelf base is exposed to relatively warm ocean waters, such as in the Amundsen and Bellingshausen Seas (Khazendar et al., 2016; Paolo et al., 2015). In these areas, basal melt is often driven by incursions of Circumpolar Deep Water (CDW), a warm, saline, and dense water mass originating from the Antarctic Circumpolar Current. CDW may be driven onto the continental shelf through bathymetric troughs in the sea floor and can reach the base of ice shelves at temperatures up to 4°C above the in-situ freezing point, driving basal melting (Jacobs et al., 2011). In addition to direct oceanic heat delivery, tidal processes modulate basal melting in complex ways. Tidal flexure of ice shelves induces cyclic tidal currents and pressure variations periodically modulating subglacial drainage and promoting seawater intrusion into subglacial cavities. It increases the melt surface area, enhancing mixing between glacial meltwater and ocean water, and generating turbulence that increases heat exchange at the ice-ocean interface (MacAyeal, 1984; Pattyn, 2018). This process is referred to as tidal pumping or tidal breathing (Begeman et al., 2020; Christmann et al., 2021; Gadi et al., 2023; Walker et al., 2013). Recent findings show that tidal motion can transport ocean water several kilometers upstream of the grounding line, exposing deeper portions of the ice to warm water and promoting melting farther inland (Rignot et al., 2024).

Finally, seasonal and long-term variability in basal melting is strongly controlled by climate-driven oceanographic processes, including wind-driven upwelling, ocean stratification, and variations in sea ice and ice mélange conditions. For instance, reduced sea ice cover can enhance surface wind stress, increase upwelling of warm deep waters, and drive higher melt rates at glacier fronts. Together, coupled oceanic, atmospheric, and hydrological processes govern not only the intensity but also the variability of basal

melting and its influence on marine ice sheet stability.

On a sidenote, in Greenland, a predominant process in ice mass loss dynamics is surface melting and runoff (Enderlin et al., 2014). In Antarctica, the surface melting is mostly limited due to overall colder temperatures during summers. However, it is worth mentioning that in recent years the climatic conditions have changed leading to higher temperatures in summer, particularly in West Antarctica, with evidence of large-scale surface melting (Deb et al., 2025). Basal melting still remains the main driver in this region.

Calving

Calving is the second of the principal mechanisms of mass loss for marine-terminating outlet glaciers at their terminus. It is driven by fracturing and crevassing progressively weakening the structural integrity of the glacier front resulting in the break off of icebergs. If the glacier system is in dynamic equilibrium, ice flow from upstream compensates for this mass loss, maintaining a stable terminus position. However, when instability dominates (e.g. due to increased melting or structural weakening), calving can outpace ice flow, leading to glacier retreat. In extreme cases, retreat continues until the glacier becomes entirely grounded, losing its floating portion (e.g. Sermeq Kujalleq in Greenland).

Fracture propagation leading to calving are primarily controlled by internal glaciological stresses within the ice body, but are also strongly influenced by the geometry of the terminus and external forcing from the ocean and atmosphere (Bassis, 2011; Benn et al., 2007; Massom et al., 2018). While calving begins with the formation of large-scale rifts, i.e. fractures that extend through the full thickness of the ice, their propagation can be triggered by changes in stress regimes directly or indirectly modulated by these external forces (Rousseau et al., 2024). Among external triggers, tidal flexure is especially important. Vertical tidal oscillations can bend the floating ice, producing stress fields that, if large enough, may initiate or accelerate fracture growth. At the base of ice shelves, tidally driven sub-ice-shelf currents can exert drag forces that further promote rift propagation (Bassis et al., 2008). In Greenland, tidal fluctuations have been linked to calving by enhancing the vertical growth of crevasses, influenced by changing subglacial water pressure (Bartholomaus et al., 2015b; van Dongen et al., 2020). Additional external factors that can either trigger or modulate calving include oceanic waves and swell (Massom et al., 2018), atmospheric extremes such as cyclones and katabatic winds (Francis et al., 2022), sea ice conditions (Wadhams, 2014), and iceberg collisions (Massom et al., 2015). Each of these can act individually or in combination to influence stress regimes at the glacier front. In Antarctica, change of ocean tide height, wind speed, and an iceberg collision in August 2021, as well as the long-term ice dynamics triggered rift propagation on the Brunt ice shelf leading to major calving of a tabular iceberg (Marsh et al., 2025). Grounded tidewater glaciers also

calve, although the mechanisms differ from those in floating ice. Calving in grounded glaciers may be initiated by rapid thinning or localized sea level changes that disrupt hydrostatic equilibrium. This can cause parts of the glacier terminus to lift from the bed and begin to float, leading to crevasse formation and the eventual detachment of large ice blocks (Benn et al., 2017).

When sufficiently large, iceberg calving events involving capsizing processes can produce "glacial earthquakes", seismic signals with magnitudes exceeding Md 5, and that are detectable worldwide by global seismic networks.(Ekström et al., 2003; Nettles & Ekström, 2010; Pirot et al., 2024; Sergeant et al., 2016).

While calving is part of the natural glacier cycle, what poses a major threat to ice sheet stability are major calving events, in which large sections of ice collapse and break away rapidly, significantly accelerating ice loss and glacier retreat. Irregular or accelerated rates of calving can destabilise ice shelves and reduce their ability to buttress outlet glaciers upstream (Hogg & Gudmundsson, 2017).

Subglacial hydrology

In addition to ocean-driven heat flux, subglacial hydrology can modulate melt rates beneath floating termini. Pressurized meltwater exits beneath the glacier and enters the ocean at the grounding zone, forming buoyant freshwater plumes that rise along the ice base. These plumes mix with warmer ocean water, enhancing the heat exchange beneath the ice tongue and increasing basal melting (Enderlin et al., 2013; Motyka et al., 2011; Rignot et al., 2010). This mechanism is especially significant for Greenland's marine-terminating glaciers, where seasonal surface meltwater contributes to subglacial discharge. For Antarctic ice shelves, the surface meltwater is minimal and cavities are larger (Nakayama et al., 2021). Subglacial hydrology can still generate mixing and heat exchange in these cavities, but its long-term impact on basal melt rates is smaller than in Greenland, since there is little seasonal variation in surface melt. The contribution of subglacial hydrology to Antarctic basal melting remains challenging to assess and is still debated among scientists.

Ice-bedrock interactions

The flow of ice, controlling ice discharge from glaciers and ice sheets, is governed by an interplay of internal ice deformation and basal processes, which operate across a range of spatial and temporal scales. In regions where ice is frozen to the bedrock, viscous deformation (or creep) dominates ice flow. However, in fast-flowing areas such as ice streams and outlet glaciers, the dynamics are primarily controlled by basal sliding over wet beds and bed deformation (Noble et al., 2020). In other words, the ice-bed interface is governed by frictional shear stress and deformation processes at the contact between ice and the underlying soft sediments (till) or bedrock. Cuffey & Paterson

(2010) gathered both processes of sliding over hard beds and deformation within soft sediments into the term basal slip. To describe the processes at play, they use the relationship connecting basal shear stress to basal velocity, water pressure, and basal conditions as a friction law. Despite its central role in ice dynamics, basal slip and its interconnected processes remain poorly understood due to the difficulty of accessing and observing the base of the glacier. As a result, numerical models often rely on inversions of surface velocity and geometry to constrain basal boundary conditions, particularly by estimating frictional stress and slip. The nature of the bed (whether it is hard bedrock or soft, deformable till) along with bed temperature, till properties, and subglacial hydrology, all influence how ice slips over the substrate (Cuffey & Paterson, 2010). For instance, impermeable, low-porosity beds encourage basal sliding via thin water films or channels, while permeable, porous tills allow water to infiltrate and deform, promoting more complex and often faster ice flow behavior (Kufner et al., 2021 and references therein). Subglacial fluids further modulates basal ice stream flow: Fluctuations in subglacial water pressure influence the basal friction and slip, often triggering episodic or persistent fast flow. While distributed and pressurized water systems reduce basal drag and enhance sliding, channelized drainage can locally increase resistance, slowing ice motion (Bindschadler, 1983; Hudson et al., 2023a; Parizek, 2024; Tulaczyk et al., 2000). In addition, localized "sticky spots" can develop at the bed where microseismic stick-slip behavior creates intermittent resistance to flow (Kufner et al., 2021). Finally, bed topography and elevation exert a strong control on ice dynamics (Enderlin et al., 2013). Ice flow tends to slow over major subglacial mountain ranges or emergent topographic highs, which either deflect ice flow or confine it within narrow corridors, increasing basal friction and creating zones of restricted slowed ice flow (Rignot et al., 2011b).

1.2.4 Observation and modeling approaches to study marine-terminating glaciers dynamics

In the previous section, I discussed the processes acting at the ice–ocean and ice–bedrock interfaces and their influence on outlet glacier dynamics. In this section, I present the observational and modeling approaches employed to identify and characterize these mechanisms.

Observations

The study of marine-terminating outlet glaciers relies on observations that combines remote sensing techniques (e.g., satellite altimetry, synthetic aperture radar (SAR), and interferometry) with in situ measurements (e.g., ground-penetrating radar (GPR), global navigation satellite systems (GNSS), and seismology). These methods, individually or combined, give information on outlet glacier geometry, grounding line position, ice velocity, and dynamic interactions at the ice-ocean and ice-bedrock interfaces across

a range of spatial and temporal scales.

Satellite imagery and SAR provide high-resolution, two-dimensional radar images of the glacier surface, enabling the measurement of displacement through interferometric techniques (InSAR, DInSAR). These methods provide high spatial resolution (meters to hundred meters) and cover large areas, making it possible to map glacier flow velocities at the scale of the Antarctic Ice Sheet (Goldstein et al., 1993; Lucchitta & Ferguson, 1986; Millan et al., 2022; Mouginot et al., 2019; Rignot et al., 2011b). They are particularly useful for detecting surface features such as crevasse fields and rifts propagation (e.g., Marsh et al., 2021), calving fronts (Baumhoer et al., 2018 and references therein), sea ice extent and thickness (Kwok, 2010), as well as monitoring grounding line retreat (e.g., Li et al., 2023). By analysing radar interferometry, DInSAR has made a major contribution to grounding line mapping in Antarctica by measuring the vertical motion of floating ice shelves in response to tidal forcing with millimeter precision and a spatial resolution of $\sim$50 m (Mohajerani et al., 2021). Indeed, grounding lines can be inferred from observations of surface elevation changes along the transition zone from grounded to floating. Additionally, repeated mappings over time allow evaluation of both short- and long-term grounding line migration (Freer et al., 2023; Rignot et al., 2024). However, temporal resolution remains limited: satellite imagery is typically acquired at most once per day making it challenging to resolve tidal flexure and daily grounding line migration (Mohajerani et al., 2021).

Airborne gravity surveys offer an efficient remote sensing approach for reconstructing bathymetry over large areas (An et al., 2019; Charrassin et al., 2025; Constantino & Tinto, 2023; Hodgson et al., 2019; Millan et al., 2017; Tinto & Bell, 2011; Tinto et al., 2019). By measuring subtle variations in Earth's gravitational field from aircraft-mounted gravimeters, these surveys detect density contrasts within the bedrock but also between bedrock and seawater, allowing the inference of seafloor depth and geometry beneath ice shelves and outlet glaciers. Modeling and inverting gravity anomalies reveals the structure and connectivity of ice-shelf cavities, helping understanding grounding zone geometry, ocean circulation pathways, and the potential for warm-water intrusion that can accelerate glacier retreat.

GNSS measurements provide high-precision horizontal and vertical positioning, enabling the evaluation of ice velocity and strain rates (Hulbe & Whillans, 1994) as well as their tidal modulation related to grounding zone flexure (Minowa et al., 2019). They can delineate grounding zones by directly detecting extent of tidal-induced flexuring of the ice (Drews et al., 2021) and have been linked to estimates of basal melt rates (Klein et al., 2020). They also help validating satellite and radar altimetry (e.g., Schröder et al., 2017; Brunt et al., 2019), calibrating elevation models, and mapping ice surface topography and elevation change. While GNSS along-track measurements provide high vertical precision, their spatial coverage is limited.

GPR is a high-resolution, non-invasive geophysical method that transmits short electromagnetic pulses into the ice. Reflections occur at boundaries between materials with different dielectric permittivity, such as ice-air, ice-water, or ice-bedrock interfaces. This allows mapping of ice thickness, internal layering, and subglacial water bodies. GPR is widely used in glaciology for internal ice imaging (Lamsters et al., 2022), estimating glacier mass balance over time (Barzycka et al., 2020; Prakash et al., 2022; Santin et al., 2019), reconstructing glacier volumes (Farinotti et al., 2019), and modeling glacier hydrology and dynamics (Fukui et al., 2008). Inversion methods have also been developed to image interfaces between freshwater ice and frozen sea ice (Li & Deng, 2024). However, standard GPR data are collected along survey lines, providing travel times and reflection strengths along linear profiles that require additional calibration (e.g., drilling, sampling) and complex inversion to yield quantitative physical properties.

Drilling through ice shelves is logistically challenging, requiring specialized equipment, complex field operations, and significant logistical support in extreme environments. However, it provides one of the few means to directly access subglacial cavities beneath ice shelves or floating tongues. Once boreholes are established, oceanographic sensors can be deployed to measure temperature, salinity, pressure, depth and current velocities. These direct observations have significantly advanced understanding of sub-ice-shelf circulation and tidal mixing processes, as well as the role of warm water intrusions in driving basal melt and crevassing (e.g., Begeman et al., 2020; Stanton et al., 2013). More recently, autonomous ocean moorings and borehole-deployed instruments (e.g.,Wild et al., 2025) have enabled multi-year time series that capture the response of these environments to seasonal and interannual oceanic forcing. In parallel, newly autonomous underwater vehicles (AUVs), capable of mapping subglacial cavities, grounding zones, and monitoring basal melting, provide complementary and less logistically demanding, in-situ measurements of cavities (Graham et al., 2022; Jenkins et al., 2010; Rignot et al., 2025; Wåhlin et al., 2024).

Finally, seismology, traditionally focused on the study of seismic waves generated by earthquakes, is increasingly used to investigate ice dynamics and properties in marine-terminating glaciers. As it forms the central focus of this thesis, its principles and applications will be described in details in section 1.3.

Physical and numerical modeling

Physical and numerical modeling has long been used to describe and reconstruct glacier flow, deformation processes and evolution. In glaciology, models serve multiple purposes. They can be employed to understand fundamental physical mechanisms or for projecting future glacier evolution under different climatic and oceanic conditions. These models use computational methods to simulate the physical processes that govern ice flow, thermodynamics, and the mass and energy balance within the cryosphere.

When constrained by observational datasets such as surface velocities, ice thickness, or basal topography, they provide a framework to test hypotheses on physical mechanisms, quantify glacier sensitivity to oceanic or atmospheric forcing, and project the future stability of glaciers and ice sheets.(Pattyn et al., 2017).

In modeling marine-terminating glaciers, both elastic and viscoelastic rheologies have been applied to simulate ice deformation, with the choice depending partly on how well modeled deformation fit observations (Reeh et al., 2003; Vaughan, 1995). The realism of such models strongly depends on the accuracy of the geometric and physical boundary conditions, particularly bedrock topography, ice thickness, and basal friction. However, these parameters remain difficult to constrain, as bed topography beneath ice shelves is often poorly resolved, limiting model accuracy and increasing uncertainty in simulated ocean circulation and basal stress fields (Millan et al., 2020).

Models may differ in dimensionality and in the interfaces they represent. Some focus solely on ice deformation (capturing viscous behavior or brittle rate-independent mechanisms) while others couple ice flow with bedrock friction, ocean circulation, or atmospheric forcing. In the context of marine-terminating glaciers, models are particularly effective for studying processes such as ice-shelf buttressing, basal melting and ice-ocean coupling. For instance, coupled ice-ocean models have been used to simulate grounding line migration, sub shelf melting, and calving processes (Dinniman et al., 2016; Pattyn et al., 2017). These models account for exchanges of heat, freshwater, and momentum between the ice and ocean, as well as the dynamic response of floating ice to tidal and hydrostatic loading. Recent advances have focused on two-way coupled frameworks in which both ice and ocean models evolve synchronously, allowing the simulation of transient phenomena such as tidal flexure and grounding line movement (Albrecht et al., 2011; Christmann et al., 2016; Robel et al., 2017).

Ultimately, the most robust reconstructions of ice dynamics at marine-terminating glaciers emerge from combined approaches that integrate modeling with multi-sensor observations (e.g., InSAR, altimetry, gravity, bathymetry, GNSS data) to jointly constrain ice geometry, deformation, and basal conditions. Persistent uncertainties in parameters like sub-ice bathymetry and basal friction currently limit the predictive capability of models, but continued integration of observations and physics-based simulations remains key to improving projections of Antarctica's future contribution to sea-level rise.

1.3 Cryoseismology: A window for studying marine-terminating glaciers dynamics

"I can hear reports from the glacier. It lies up there on the crest of the mountain like a mighty ice-giant peering down at us through the clefts. It spreads its giant body all over the land, and stretches out its limbs on all sides into the sea. But whenever it turns cold–colder than it has hitherto been–it writhes horribly, and crevice after crevice appears in the huge body; there is a noise like the discharge of guns, and the sky and the earth tremble so that I can feel the ground that I am lying on quake."
— Nansen, 1897

1.3.1 Investigating cryospheric processes using seismology

What is cryoseismology ?

Seismology has been historically devoted to investigating processes associated with tectonic earthquakes and elastic waves propagation in the solid Earth. However, in recent decades there has been growing interest in applying seismological techniques to investigate dynamic processes occurring near or at the Earth's surface. More precisely, processes occurring at the interface between solid Earth and surficial unconsolidated solids, fluid and gas envelopes of the Earth (Montagner et al., 2020). This emerging branch of geophysics is broadly referred to as Environmental Seismology (Larose et al., 2015). Environmental seismology encompasses a wide range of surface-related phenomena, including volcanic activity, rivers dynamics, floods and landslides, ocean waves interactions, ice sheet and glacier dynamics, snow avalanches, sediment transport, erosion, hurricanes, anthropogenic and biogenic activity, etc. The analysis of the signals generated by these events, their characteristics, occurrence rates, or spatial distribution participate to significantly improve our understanding of the underlying mechanisms. This is particularly important, as environmental seismology now sits at the forefront of some of the most challenging global climate change crises. By unveiling temporal and spatial patterns of the precursors and triggering processes of events such as landslides (Hibert et al., 2017), glacier calving (e.g., Sergeant et al., 2016), or flash floods, we are aiming to develop early warning systems and improve our capacity for rapid disaster response, ultimately helping to mitigate the risks to vulnerable populations. The development of environmental seismology has been driven by significant technological and methodological advances. These include the widespread deployment of seismic stations worldwide, on land and at sea, the development of dense nodal networks, the improvements in the robustness and portability of seismic sensors, coupled with high sensitivity to ground motion and the growing amount of continuous seismic recordings. More recently, Distributed Acoustic Sensing (DAS) has emerged as an innovative technique, using optical fibers to measure strain along their length, making it comparable to dense, large-scale seismic arrays. Together, these technologies provide efficient ways to respond to a wide range of observational goals. Researchers can adapt

seismic deployments (whether short-term or long-term, sparse or dense) depending on the specific processes or regions of interest. This makes seismology particularly powerful in remote or logistically challenging environments. In addition, through continuous recording of ground motion and deployment of networks of stations recording at high sampling rates, we obtain a high spatial and high temporal resolution monitoring of seismic activity. Together with greater data accessibility, refined signal processing techniques, and increased computational power, researchers are able to delve deeper into the source mechanisms of the environmental phenomena.

Cryoseismology is the study of seismic waves propagating within cryospheric environments, i.e. where water exists in solid form. This includes, though not an exhaustive list, snow cover, glaciers, ice sheets, ice shelves, icebergs, sea ice, lake ice, river ice, permafrost, seasonally frozen ground, and solid precipitation. By analyzing seismic waves generated by ice deformation, cryoseismology offers a powerful means to investigate and monitor ice properties, structure and dynamics, stress accommodation over time, and glacier response to external forces at critical boundaries or within ice bodies (e.g. tides, temperature, water pressure). In this way, it provides indirect observations in inaccessible areas, such as the base of glaciers or beneath floating ice shelves, with high resolution otherwise difficult to look at with other geophysical or remote sensing methods.

Two perspectives: Imaging the structure and characterizing the sources

We can distinguish two approaches in cryoseismology: structural imaging and seismic source characterization.

On one hand, structural imaging uses seismic waves to image and characterize the medium through which they travel. In cryoseismology, this approach is applied to determine the physical properties and internal structures of the subsurface of ice sheets and glaciers by analyzing how seismic waves propagate through ice bodies. A first possibility is to use natural cryoseismic events and study their propagation characteristics. For instance, Harland et al. (2013) and Smith et al. (2017) measured elastic anisotropy in Antarctic ice streams using records of basal seismicity. Meanwhile, Lindner et al. (2019) used icequake signals to identify crevasse-induced anisotropy in an Alpine glacier from velocity anomalies. Walter et al. (2015a) used transient seismic signals generated in moulins to estimate the depth of the ice-to-bedrock transition beneath a seismic network deployed on the Greenland Ice Sheet (GIS). Preiswerk & Walter (2018)demonstrated that glacier thickness and bed properties could be estimated with seismic noise records of flowing water, icequakes and anthropogenic sources. An alternative approach is to use ambient seismic noise originating from climatic and oceanic activity (Sergeant et al., 2020, and references therein). The use of ambient noise for imaging the subsurface was first demonstrated by Shapiro & Campillo (2004) and Shapiro et al. (2005), who showed that surface waves could be reconstructed from continuous seismic noise

to perform crustal tomography in California. Since then, the technique has evolved into a powerful tool for constraining elastic properties of the Earth's crust and imaging subsurface structures at multiple scales. Ambient noise methods have also been successfully applied to monitor tectonic fault zones (Brenguier et al., 2008; Olivier et al., 2015) and volcanic systems (Brenguier et al., 2008; Sens-Schönfelder & Wegler, 2006). In the cryospheric context, studies have used ocean-generated ambient noise recorded at permanent broadband seismic stations located on rocky glacier margins or on polar ice sheets to investigate subsurface processes. For instance, Mordret et al. (2016) used ambient noise correlations to track seasonal strain variations within the crust beneath the Greenland Ice Sheet (GIS), driven by cyclic loading and unloading associated with melting and refreezing. More recently, Zhan (2019b) detected a decrease in surface-wave velocities within the basal till layer of Alaska's Bering during a surge, which was interpreted as a transition from channelized to distributed subglacial drainage.

On the other hand, seismic source characterization focuses on understanding the origin, mechanism and dynamics of seismic events themselves. In the cryospheric environment, seismic sources arise from a range of processes, including crevasse opening, basal stick-slip motion, lateral friction, calving events or hydrofracturing. By analyzing waveforms, frequency content, and spatiotemporal patterns of these events, it provides insight into the stress regimes, fracture mechanics, and internal or external forces acting on the ice and generating seismic energy. Early on, several studies have shown that glaciers can generate seismic signals called icequakes (e.g. Anandakrishnan & Bentley, 1993; Neave & Savage, 1970; Qamar, 1988; VanWormer & Berg, 1973; Weaver & Malone, 1979; Wolf & Davies, 1986). As with tectonic earthquakes, these cryoseismic events can theoretically be analyzed in terms of duration, magnitude, location, source mechanisms, waveform characteristics, and frequency content. However, doing such presents challenges. The waveforms often originate from multiple sources, simultaneously activating at varying depths and locations, generating a potentially high number of events. This abundance of signals makes cryoseismic records rich in information to study underlying source processes, but it also complicates efforts to identify, differentiate and classify individual events. Further complexity arises from the nature and rheology of the ice itself that may affect seismic wave propagation through anisotropy, internal layering, and crevassing, introducing uncertainty in travel paths and complicating the accurate localization and characterization of events. Despite these complexities, the past decades have seen a notable increase in cryoseismological studies, leading to improved understanding of cryoseismic sources and their link to ice dynamics (e.g., Podolskiy & Walter, 2016).

In marine-terminating glacier environments, seismic instruments are sensitive to any process that generates elastic waves within glacier ice or the underlying bed. Figure 1.9 schematically presents a marine-terminating outlet glacier with a floating terminus, with a highlight on the range of cryoseismic sources observable. These sources include ice brittle deformation, crevassing, basal sliding, lateral friction, subglacial hydrology,

calving, ocean waves-ice interactions, iceberg-iceberg, iceberg-sea ice and iceberg-rock collisions. The associated seismic signals span a variety of event types (e.g. high-frequency icequakes, basal stick-slip events, tremors, long-period glacial earthquakes), each with distinct waveform characteristics and source mechanisms. Seismic signals can also generate hydroacoustic waves that can be recorded in the ocean (i.e., by ocean bottom seismometers). This is for instance the case for calving events, where chunks of ice fall directly into the water and create these hydroacoustic signals. More often than not, cryoseismic events produce relatively weak, highly attenuated signals (compared to tectonic earthquakes) and may only be detectable at distances of less than ten to hundreds of kilometers using local or regional networks. In the present study, we even show that some small magnitude icequakes may be recorded only at the scale of few hundreds of meters around the source. Their associated magnitude (on the Richter scale) can easily span in the negative values. Glacial earthquakes, associated with calving events, are the only exception known in terms of cryoseismic signals. They can reach magnitudes superior to 5 and therefore can be observed on global seismic networks, similarly to teleseisms (Ekström et al., 2003; Nettles & Ekström, 2010; Sergeant et al., 2016). This shows how cryoseismology covers a large range of magnitudes, with energy releases of several orders of magnitude of difference from one type of signal to another.

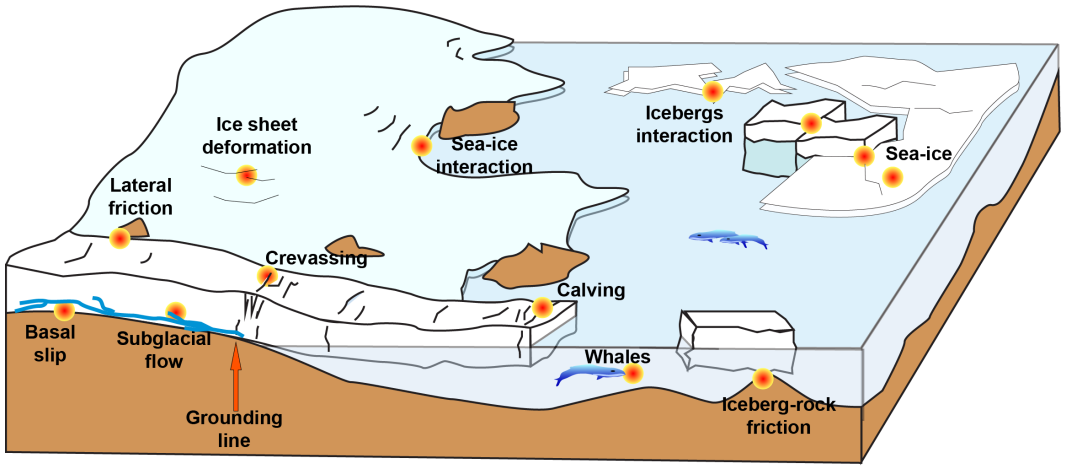

Figure 1.9: Overview of cryoseismic sources in a marine-terminating glacier environment. These sources come from processes at the glacier ice-bedrock, glacier ice - slow moving ice, glacier ice - ocean, and iceberg-ocean interfaces.

A source-focused approach in this thesis

In the following chapters, we focus on two primary types of cryoseismic signals that dominate observations of ice dynamics at marine-terminating glaciers: (1) surface brittle failure (crevassing) and (2) basal stick-slip motion associated with glacier

sliding. This focus results from the first years of seismic data acquisition within the project SEIS-ADELICE (see chapter 2), during which these two processes emerged as the most prominent and recurrent signals recorded across the grounding zone. Given the exploratory nature of my research and the richness of the dataset, priority was given to characterizing these dominant signal types. Consequently, the following sections will describe in detail the source mechanisms, seismic signatures, and implications of both icequakes and stick-slip events for understanding glacier dynamics at the grounding zone. Other cryoseismic processes, although important within their respective contexts, lie beyond the scope of this work. Therefore, they will simply be briefly reviewed to outline their occurrence, source mechanisms, and expected seismic signatures. Calving, although not the focus of analyses presented in future chapters, will be discussed in greater detail owing to its role as a major contributor to ice mass loss and its distinctive seismic characteristics, which allow for relatively easy identification in seismic records.

1.3.2 Cryoseismic signals associated with crevassing and ice brittle deformation

The most common cryoseismic signals recorded on glaciers originate from brittle ice deformation, primarily associated with the initiation and propagation of crevasses. In high-melt and steep-slope regions, such events account for 95–99% of all short-duration seismic signals (Métaxian et al., 2003; Röösli et al., 2014; Walter et al., 2009). Foundational studies (Lewandowska & Teisseyre, 1964; Neave & Savage, 1970; Osten-Woldenburg, 1990; Röthlisberg, 1955; Röthlisberger, 1972) established the characteristic seismic signatures of ice fracturing under tensile stress. These events typically occur in near-surface layers, where overburden pressure is lower and accumulated strain reaches the ice rupture threshold, leading to cracks and crevasse formation and the release of short, discrete seismic bursts.

Icequakes from crevassing are typically short in duration, often with negative or very low magnitudes. They display high-frequency content, generally concentrated between 10 and 50 Hz, sometimes extending up to 100 Hz. Their waveforms are impulsive, with sharp onsets but without distinct seismic phases, and are dominated by surface waves, particularly low-frequency Rayleigh waves. The rupture source itself is relatively simple, limited to the fracturing ice surface (Röösli et al., 2014). However, propagation effects introduce significant complexity in the resulting waveform. The presence of near-surface heterogeneities, crevasses and anisotropy strongly affect wave propagation, producing attenuation and distortion in waveforms (Stuart et al., 2005; Walter et al., 2009). This introduces challenges in signal interpretation and event localization, which will be discussed further in chapter 3 and chapter 4. An example of an icequake event is shown in Figure 1.10 recorded by a broadband seismic station deployed above the grounding zone of the Astrolabe Glacier (Terre Adélie, East

Antarctica). The waveform is characterized by a typical impulsive onset dominated by surface waves, particularly visible on the vertical component (Fig. 1.10a). A three-hour record reveals numerous discrete bursts, varying in amplitude but dominating the overall signal (Fig. 1.10b). The frequency content is broad, with energy ranging from 5 Hz to 60-80 Hz 1.10c).

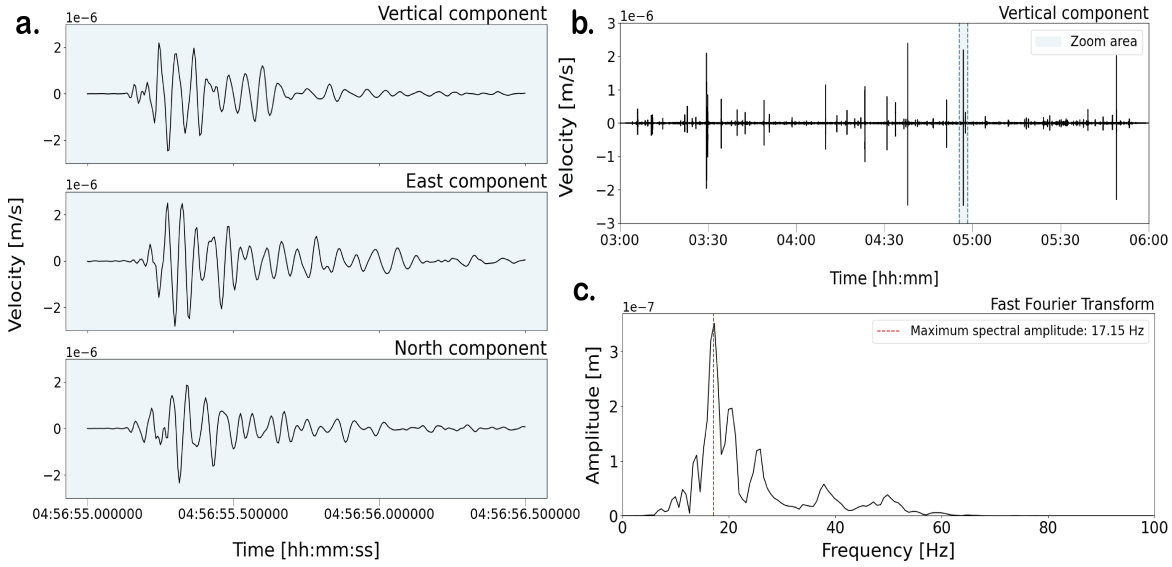

Figure 1.10: Example of icequake cryoseismicity recorded by a broadband seismic station deployed on the surface of the Astrolabe Glacier, a marine-terminating outlet glacier with a floating terminus in Terre Adélie, East Antarctica. The icequake was recorded on Jan. 18, 2022 by station AST08, positioned near the grounding zone. (a) Three-component seismogram (Vertical, East, North) of an icequake event, lasting approximately 1 second. (b) Three-hour segment of continuous seismic data highlighting the numerous high-amplitude icequakes. For both panels, the instrumental response is removed and a bandpass filtered between 10 Hz and 50 Hz is applied. (c) Frequency analysis of the vertical component of the event shown in (a) using Fast Fourier Transform (FFT), revealing dominant spectral energy between 10 Hz and 30 Hz, with energy extending up to 60 Hz.

Seismic records often contain hundreds of icequakes per hour, saturating datasets and masking weaker signals. However, this high rate of seismic activity provides a high-resolution tool for understanding and monitoring ice dynamics. Temporal and spatial variations in icequake occurrence reveal evolving strain-rate regimes and glacier responses to external forcings such as tidal forcing, meltwater input, or seasonal stress changes. While satellite imagery provides spatial coverage of fracture patterns, it lacks the sub-daily temporal resolution necessary to track fracture evolution, a gap that cryoseismology can fill. Across the years, numerous studies have shown that cyclical bending of outlet glacier at their grounding zones produces intense icequake activity (Barruol et al., 2013; Cooley et al., 2019; Fromm et al., 2023; Hammer et al., 2015; Lombardi et al., 2016; Lucas et al., 2023; Minowa et al., 2019). These studies consis-

tently show that such icequake activity is modulated by dominant tidal cycles (diurnal, semidiurnal, and terdiurnal) reflecting surface crevassing driven by tide–induced flexure and extension of ice shelves and ice tongues. As such, icequake activity serves as a sensitive proxy for quantifying mechanical stress, strain evolution, and tidal coupling in marine-terminating outlet glaciers (Hudson et al., 2020; Hulbe et al., 2016).

1.3.3 Cryoseismic signals associated with basal and lateral shear friction

The second dominant type of cryoseismicity observed in marine-terminating outlet glacier seismic records is associated with shear friction at the interface between the ice and its underlying substrate. This process can also occur along lateral shear margins, such as in glaciers confined within valley fjords. The ice-bed interface of glaciers can be lubricated, allowing sliding over a substrate with relatively low friction coefficient and minimal resistance to the forward motion. But the basal area can be punctuated by sudden and localized areas of increased friction opposite to the glacier motion (Alley, 1993). These zones, so-called asperities or "sticky spots", can produce abrupt slip episodes of short duration accommodated through sudden releases of accumulated shear stress energy as seismic waves. Events generated by the slipping over asperities behaviors are often referred to as "stick-slip" events.

The spatial scale, time occurrence and detectability of stick-slip events vary with glacier type. Large-scale, slow stick-slip episodes have been documented beneath major ice shelves, where signals may be recorded more than 1 000 km from the source (Bindschadler et al., 2003). In some cases, these events are the primary drivers of ice motion, with absence of motion between slips. In other cases, stick-slip events can appear as small-amplitude, highly repetitive signals, only visible locally with seismic stations in close vicinity. These stick-slip events are characterized by short durations (< 1 s) and clear P- and S-wave arrivals. They are generally of smaller amplitude compared to surface brittle icequakes, making them harder to detect. However, they frequently occur in prolonged bursts, often hundreds of events spanning several hours, with highly regular interevent times. With such characteristics, it becomes easier to find them in the seismic records. Within a 'stick-slip' seismic burst, events typically arise from a unique family/ cluster associated with a single seismic source, thus exhibiting nearly identical waveforms; only amplitudes vary slightly over time. Their frequency content is broad, with substantial high-frequency energy (10 Hz to > 100 Hz). Documentation of these stick-slip events remains limited. It is therefore difficult to assess their relationship with aseismic sliding. Studies focusing on stick-slip events at marine-terminating glaciers are scarce and often focused on the grounding zone. It is thus unclear whether such events occur or can be detected far inland. Moreover, observations at marine-terminating glaciers are strongly influenced by local geometry, environmental conditions, and deployment configuration, resulting in only a partial

view of the underlying dynamics.

Figure 1.11 presents an example of a stick-slip seismic signal recorded on January, 16th, 2023 by a seismic node (07x04, A1) deployed above the grounding zone of the Astrolabe Glacier (Terre Adélie, East Antarctica). A representative 'stick-slip' event shows an impulsive onset, with P- and S-waves clearly visible on the vertical component, and S-waves dominating the horizontal components. (Fig. 1.11a). Over a six-hour period, hundreds of stick-slip events occur at consistent interevent intervals (Fig. 1.11b). Amplitudes are approximately 2.5 times smaller than those of the surface brittle icequakes shown in Figure 1.10. The frequency content is very broad, with energy ranging from 5 Hz to 200 Hz (Fig. 1.11c).

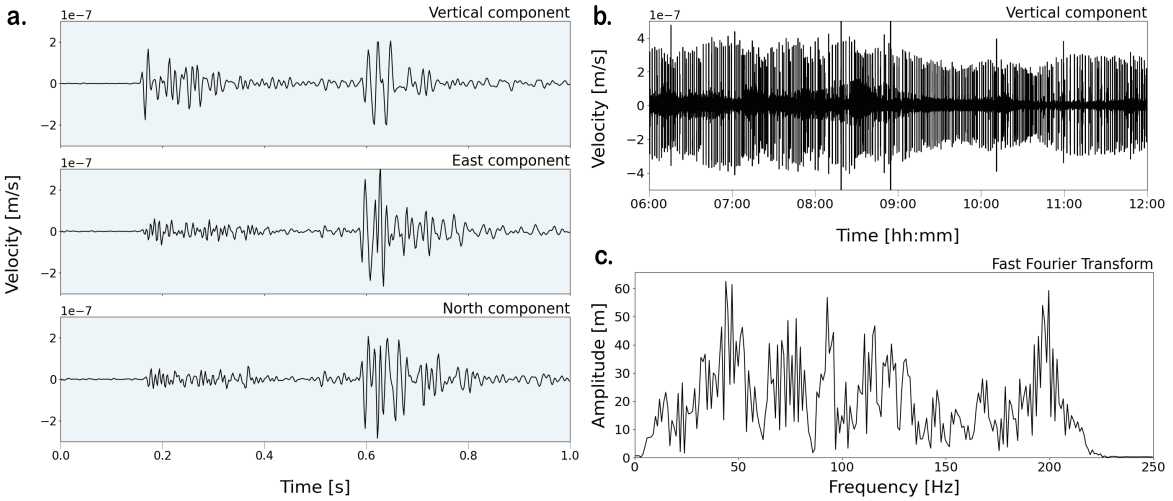

Figure 1.11: Example of a "stick-slip" event recorded on Jan. 16, 2023 by a seismic node (07x04, dense array A1) deployed on the surface of the Astrolabe Glacier, a marine-terminating outlet glacier with a floating terminus in Terre Adélie, East Antarctica. (a) Three-component seismogram (Vertical, East, North) of a "stick-slip" event, lasting 0.6 seconds. (b) Six-hour segment of continuous seismic data highlighting the high number of "stick-slip" events. For both panels, the instrumental response is removed and a bandpass filtered between 10 Hz and 200 Hz is applied. (c) Frequency analysis of the vertical component of the event shown in (a) using Fast Fourier Transform (FFT), revealing dominant spectral energy between 10 Hz and 225 Hz.

As for icequakes from surface brittle deformation or crevasses, analysing the temporal and spatial distribution of "stick-slip" events informs on ice dynamics and mechanisms related to basal shear friction at the ice-bed interface of glaciers. "Stick-slip" events have been employed to map bed asperities, often over relatively small regions, yielding information on the topography of the bedrock and its properties (e.g. hard versus. soft till) (Bannister & Kennett, 2002; Danesi et al., 2007; Kufner et al., 2021; Zoet et al., 2012). Beyond bed morphology, the monitoring of "stick-slip" seismicity can also be used to infer spatial variability in hydrologic conditions and stress distri-

bution at the ice–bed interface (Smith, 2006; Smith et al., 2015). Studies suggest that these events are controlled by spatial variations in shear stress loading, rather than by basal properties alone (Walter et al., 2015b). Even minor changes in basal stress can reorganize the subglacial hydrological system, modifying the spatial distribution of basal shear stresses and triggering activation of "stick-slip" sources (Kavanaugh & Clarke, 2001). Tracking the activation and migration of such seismic sources can thus be used to reconstruct underlying shifts in basal conditions, estimate the shear modulus, and quantify the contribution of "stick-slip" events to overall basal motion, as well as to estimate bed frictional shear strength (Hudson et al., 2020, 2023b).

The timing of "stick-slip" activation and deactivation relative to tidal cycles provides further constraints on conditions at the ice-bed interface. In certain regions where surface velocity is tidally modulated, basal asperities may remain unaffected, implying that these "sticky spots" possess strengths exceeding the perturbations imposed by tidal forcing (Aðalgeirsdóttir et al., 2008; Smith et al., 2015). In contrast, several studies have reported tidal modulation of basal seismicity in large outlet glaciers, where periodic stress changes from tidal forcing can trigger slow, large-magnitude "stick-slip" events (Pratt et al., 2014; Walter et al., 2015b; Winberry et al., 2009; Zoet et al., 2012). Analyses of local small-amplitude "stick-slip" events, particularly in grounding zones, remain sparse, and clear tidal modulation in such cases has yet to be demonstrated. This gap in observation persists despite the theoretical expectation that tidal-induced stress changes should influence basal seismicity. As processes such as tidal loading-unloading may modulate basal lubrication, sediment deformation, and till strength, they should exert significant control on ice-stream dynamics and grounding line stability(Walker et al., 2013) visible through "stick-slip" behaviors. Consequently, high-resolution monitoring of basal "stick-slip" activity, in combination with tidal cycle analysis, holds considerable potential for better understanding the mechanical coupling between tidal forcing, basal shear stress, and glacier flow.

All in all, despite multiple seismological and geodetic observations documenting the 'stick-slip' behavior as part of glacier basal motion, there are still gray areas that remain to be understood. As a result, stick-slip phenomena are often neglected in numerical models, which tend to represent basal motion solely as viscous deformation and regelation processes (i.e. partial melting of ice under pressure, followed by refreezing once the pressure is released) (Weertman, 1957).

1.3.4 Other cryoseismic signals

Among the cryoseismic sources that could be explored, calving events stand out as particularly important to mention due to their direct association with ice mass loss, as discussed in the previous sections.While it has not been a focus in my work, I will touch on them here, discussing their seismic signatures and how cryoseismic analyses

can help us understand the ice dynamics involved in calving. Calving events generate distinctive seismic signals that are fundamentally different from earthquakes and other cryoseismic sources such as crevassing and basal stick-slip (Qamar, 1988). They are typically of long duration, ranging from a few seconds up to over 1000 seconds, and display concentrated energy in the frequency band 1-5 Hz (Bartholomaus et al., 2015b; O'Neel & Pfeffer, 2007; Qamar, 1988; Wolf & Davies, 1986). They are powerful and can be detected tens of kilometers from the glacier terminus (Bartholomaus et al., 2015b). Magnitudes of calving events, although variable, have been mainly found to be around 2 although some events could reach magnitudes of 5 (Ekström et al., 2003; Nettles & Ekström, 2010). In Greenland, iceberg capsizing at marine-terminating glaciers have been demonstrated to apply large scale forces on the glacier, transformed in large magnitude seismic events (Sergeant et al., 2018). Signals rarely show clear seismic phase arrivals, which is attributed to the complex rupture mechanisms involved. Rather than a single-point rupture, calving events are thought to result from a cascade of multiple small-scale dynamic processes (e.g. fracturing, avalanching of ice debris, and interaction with water or sea ice) ultimately destabilizing and detaching large ice blocks (Amundson et al., 2008; O'Neel & Pfeffer, 2007). These processes often generate high-frequency seismic energy and result in complex and variable waveforms. Recently, submarine DAS acquisition was used to precisely trace an iceberg calving process chain, from calving initiation with persistent ice fracturing, to iceberg detachment, exciting local tsunamis, internal gravity waves and transient currents at the ice front before decaying into fragments (Gräff et al., 2025). This demonstrates how all these processes can be monitored by DAS in addition/ instead of seismometers.

An illustrative example of a calving-generated seismic signal is presented in Figure 1.12, which shows the recording of an event at the Astrolabe Glacier (Terre Adélie, East Antarctica). The seismic waveform, recorded at a broadband station (AST14) on Curie island close to the glacier front, displays a 10-second duration event with no discernible phase arrivals (Fig. 1.12a). The energy is concentrated in the 1-5 Hz frequency band with additional but lower levels of high-frequency energy up to 30Hz (Fig. 1.12b). A Fast Fourier Transform (FFT) highlights a dominant spectral peak near 3.5 Hz, consistent with calving seismic characteristics reported in the literature (Fig. 1.12c).

While few studies have linked calving icequake properties directly to iceberg size and calving flux, ice shelf collapse is known to result from structural weakening via crevasses and rifts, sometimes triggered by ocean swell-induced flexural waves and associated strain inputs (Sergienko et al., 2009). Rupture of calving can be induced by tides, and monitoring these signals can help predict the rupture and calving of icebergs (Marsh et al., 2025).

There are other numerous seismic sources that can be activated in marine-terminating outlet glacier environments (see Fig. 1.9). The term tremor is a broad category en-

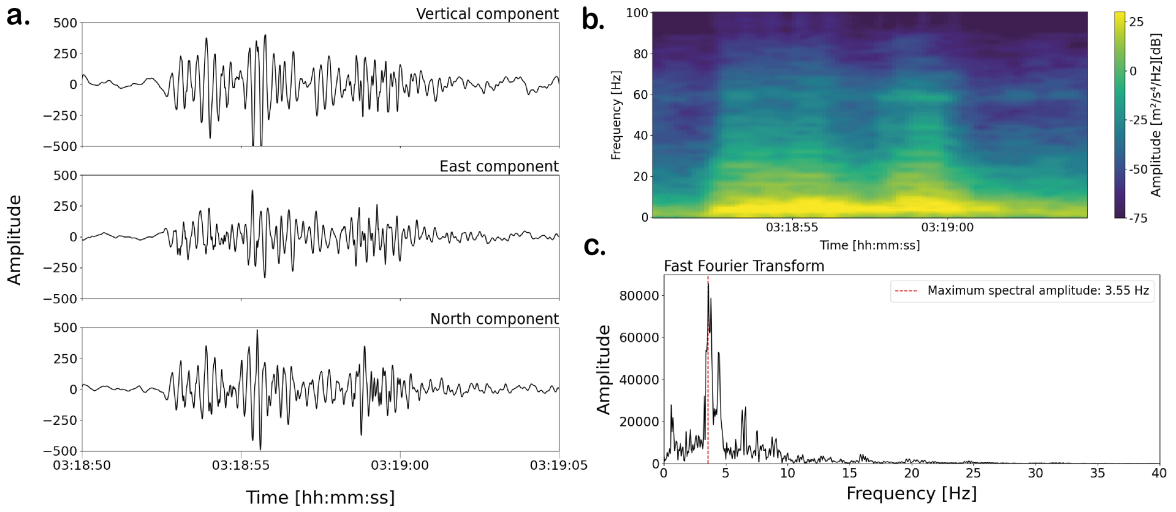

Figure 1.12: Example of a calving event recorded by a seismic station near the front of the Astrolabe Glacier, a marine-terminating outlet glacier with a floating terminus in Terre Adélie, East Antarctica. The broadband seismic station AST14 was installed on Curie Island, located in the Pointe Géologique Archipelago near the French research station Dumont d'Urville. (a) Seismic waveform of the calving event recorded on the three components (Vertical, East, North). The event occurred on Jan. 18 2024 at 03:18:52 UTC. (b) Spectrogram for the corresponding time window, showing the signal energy distribution. (c) Frequency content spectrum using a Fast Fourier Transform (FFT), showing the spectral characteristics of the event. The calving signal lasts approximately 10 seconds, with dominant energy between 3 Hz and 5 Hz and broader energy extending from approximately 1 Hz to 20 Hz. Note that the instrument response has been removed on all plots.

compassing low-frequency, long-duration seismic signals that can arise from a variety of processes but share similar spectral characteristics. Tremors are often linked to subglacial hydrology, including channelized water flow or drainage of isolated water pockets. In such cases, the tremor amplitude has been shown to serve as a useful proxy for subglacial water discharge (Bartholomaus et al., 2015a). Tremors can also originate from interactions involving sea ice and icebergs. In the case of sea ice, coupling between ocean waves and the solid Earth produces surface-wave signals within the 1–20 s period band, referred to as microseisms. Variations in sea ice cover can be inferred from the power spectral density (PSD) of these microseisms recorded by broadband seismic stations (Grob et al., 2011). Iceberg-related tremors occur when icebergs interact with shallow seafloors or collide with other icebergs. Friction between grounded icebergs and the seabed can produce high-magnitude, long-lasting signals, sometimes termed "singing icebergs" (Müller et al., 2005). It usually generates powerful harmonic and chaotic signals. Additionally, collisions between icebergs or with the ocean floor may generate repetitive "stick-slip" events that merge into prolonged harmonic tremor sequences (MacAyeal et al., 2008). Sea ice and icebergs may also generate harmonic tremors of long duration (Kanao, 2017) and experience tide-induced cracking, providing insights into strain accumulation and mechanical strength. Finally, basal non-shear

seismicity, distinct from the shear-friction-induced stick-slip events described earlier, is associated with basal tensile faulting, subglacial water movement, and cavity collapse. This type of seismicity likely requires the presence of pressurized water near the glacier bed, allowing tensile fracturing to occur under high ice-overburden pressures (van der Veen, 1998).

For a detailed overview of cryoseismology, including existing literature and analyses, I recommend the comprehensive reviews by Podolskiy & Walter (2016) and Aster & Winberry (2017).

1.4 Research aims and focus

Understanding the dynamics and stability of Antarctic outlet glaciers requires investigating the processes that operate at their grounding zones, the transitional regions between grounded and floating ice. As presented in Section 1.2, the position and migration of the grounding line exert a first order control on ice flow and therefore on ice mass balance. Internal ice deformation and the mechanical role of shear margins are also key processes of glacier behaviour. These processes are further influenced by local geometry and external forcings such as ocean tides, which periodically modulate stress and deformation from the glacier base to its surface.

Glacier ice produces distinct and repeatable seismic signals from internal deformation or from interactions with the ocean and bedrock. The aim of this PhD is to make use of these seismic signals through the following research questions:

1. How can seismology and dense seismic networks overcome the limitations of existing approaches in resolving spatial and temporal changes in seismic sources at glaciers grounding zones and shear margins ?

2. How do glaciers respond to deformation from tidal flexure and daily grounding line migration ?

3. How does the mechanical state of the ice-bedrock interface changes during successive tidal cycles ?

To answer these questions, my research focuses on the Astrolabe Glacier, an outlet glacier in East Antarctica instrumented through successive seismic deployments as part of the SEIS-ADELICE project (2020-2025).

The thesis is structured as follows. Chapter 2 introduces the Astrolabe Glacier and the SEIS-ADELICE project. Chapter 3 details the methodologies used to detect and locate cryoseismic signals. Chapter 4 analyses the spatial and temporal variability of

seismic activity at the grounding zone inferred from surface icequakes. Chapter 5 combines surface and basal seismicity to constrain grounding line position and dynamics, proposing new approaches for monitoring grounding zone migration. Chapter 6 focuses on the seismicity of the shear margin using dense-array observations. Finally, Chapter 7 synthesizes the insights gained from the multiple field campaigns and discusses the deployment and performance of geophysical instrumentation in polar environments.

CHAPTER 2

SEIS-ADELICE: seismic acquisition on the Astrolabe Glacier

Contents

2.1 The Astrolabe Glacier 36

2.1.1 Description of the study site 36

2.1.2 Previous and ongoing studies 40

2.2 Project SEIS-ADELICE (2020-2025) 41

2.2.1 Objectives 41

2.2.2 Seismic deployments and field campaigns 41

Cryoseismology has established itself as an effective tool for improving our understanding of ice dynamics by providing high-resolution information on glacial processes. Building on this potential, the SEIS-ADELICE project aims at applying cryoseismology to the study of a marine-terminating outlet glacier in East Antarctica: the Astrolabe Glacier. By deploying seismometers both on and around the glacier, on land and at sea over multiple years, SEIS-ADELICE seeks to record cryoseismic activity and develop methodological expertise in running high-resolution seismic surveys in polar regions. In this chapter, I introduce the Astrolabe Glacier, outline its key characteristics, and review previous and ongoing studies that provide a relevant context for the project. I then describe the objectives of SEIS-ADELICE and detail the seismic deployments that were conducted.

2.1 The Astrolabe Glacier

2.1.1 Description of the study site

The Astrolabe Glacier is a small marine-terminating outlet glacier located near the French research station Dumont d'Urville (DDU), located in the Terre Adélie region (Fig. 2.1a). Terre Adélie is a narrow strip of the Antarctic continent that spans approximately 432,000 km^2 and lies between the 66° S parallel and the South Pole, and between 136° E and 142° E. Claimed by France following the 1959 Antarctic Treaty, it is administered by the Terres Australes et Antarctiques Françaises (TAAF). The Dumont d'Urville base (66°40′S, 140°01′E) was established in 1956 on the Île des Pétrels, a rocky island in the Pointe Géologie archipelago, just a few kilometers off the Antarctic mainland (Fig. 2.1b).

Despite its close proximity, only about 1 km from DDU, direct access to the glacier by foot is rather difficult. The area between the base station and the glacier is covered by sea ice or open ocean depending on the time of year and is characterized by rugged, unstable terrain. Lateral sections of the glacier collapse onto the rocky outcrops and sea ice, creating a chaotic landscape rightfully called "the chaos". As a result, reaching the glacier typically requires a short helicopter ride from DDU. Cap Prud'Homme (CPH), a logistical base located 5 km south of DDU on the continental mainland (Fig. 2.1b), has an alternative on-foot access. It requires hiking a 3 to 5 km path that crosses the lateral shear margin of the glacier, marked by chaotic crevasses. In any case, given its proximity to the base station and logistical support, the Astrolabe Glacier presents a natural laboratory for studying marine-terminating glacier dynamics. From the glacier front to its lateral shear margins and grounding zone, we are able to closely observe and evaluate the main structural and dynamic characteristics.

The Astrolabe Glacier is fed by a drainage basin extending over 200 km inland into Wilkes Land (Mouginot et al., 2014). Its floating tongue is relatively small in size:

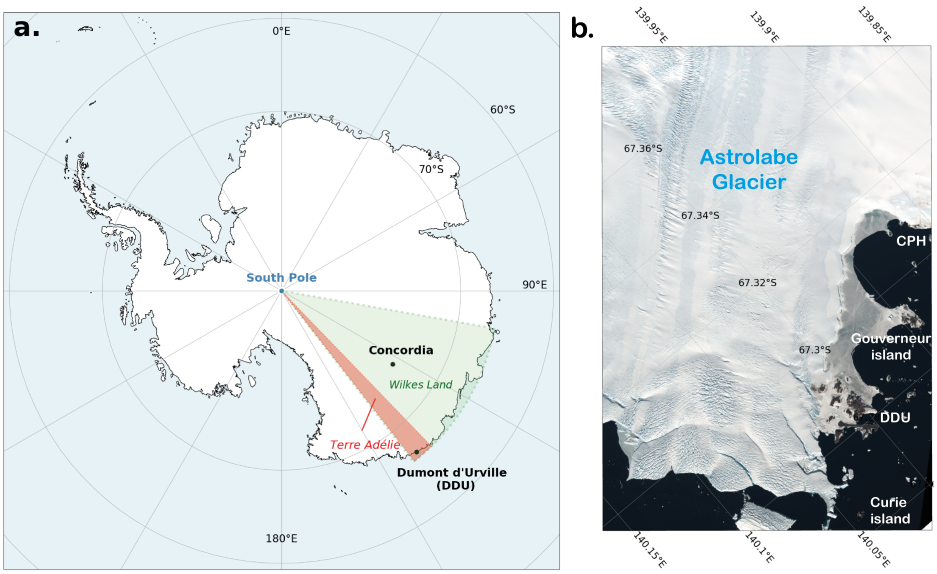

Figure 2.1: (a) Map of Antarctica highlighting the location of Wilkes Land (light green) and Terre Adélie (red). The positions of the French research stations Dumont d'Urville (DDU) and Concordia (a joint French–Italian station) are also indicated. (b) Detailed map of the Pointe Géologie Archipelago, showing the scientific and logistical bases Cap Prud'Homme (CPH) and DDU, and Curie and Gouverneur islands.

approximately 6 to 8 km wide and 15 km long. It does not compare in scale to its neighbours glaciers and their associated ice shelves. Its catchment area is around 1,500 km^2, which is significantly smaller than that of Cook Glacier ($\sim 307,741\ km^2$), Mertz Glacier ($\sim 84,543\ km^2$), and Ninnis Glacier ($\sim 70,000\ km^2$) (Rignot et al., 2011b, 2013).

The glacier advances at an average rate of 1 to 1.5 meters per day. Surface velocity maps reveal increased velocity rates near the terminus, along with well-defined lateral shear margins associated with sharp velocity gradients (Fig. 2.2). Complementary GNSS observations indicate spatial variations in horizontal velocity, modulated by proximity to the front and to the margins. These observations will be further discussed throughout the manuscript.

The glacier is situated within a deep fjord, flanked by steep valley walls. The fjord depth in front of the glacier reaches 1,000 meters (Beaman et al., 2011). Imaging has revealed valley walls extending as deep as 600 meters below the surface (Le Meur et al., 2014). Figure 2.3 presents some distinct surface features, visible from satellite imagery, that provide further insight into the glacier structure. These include a crevassed floating tongue approximately $4 \times 10\ km^2$, two clearly defined shear margins and a heavily crevassed glacier front prone to frequent calving of icebergs into the ocean (Fig. 2.3).

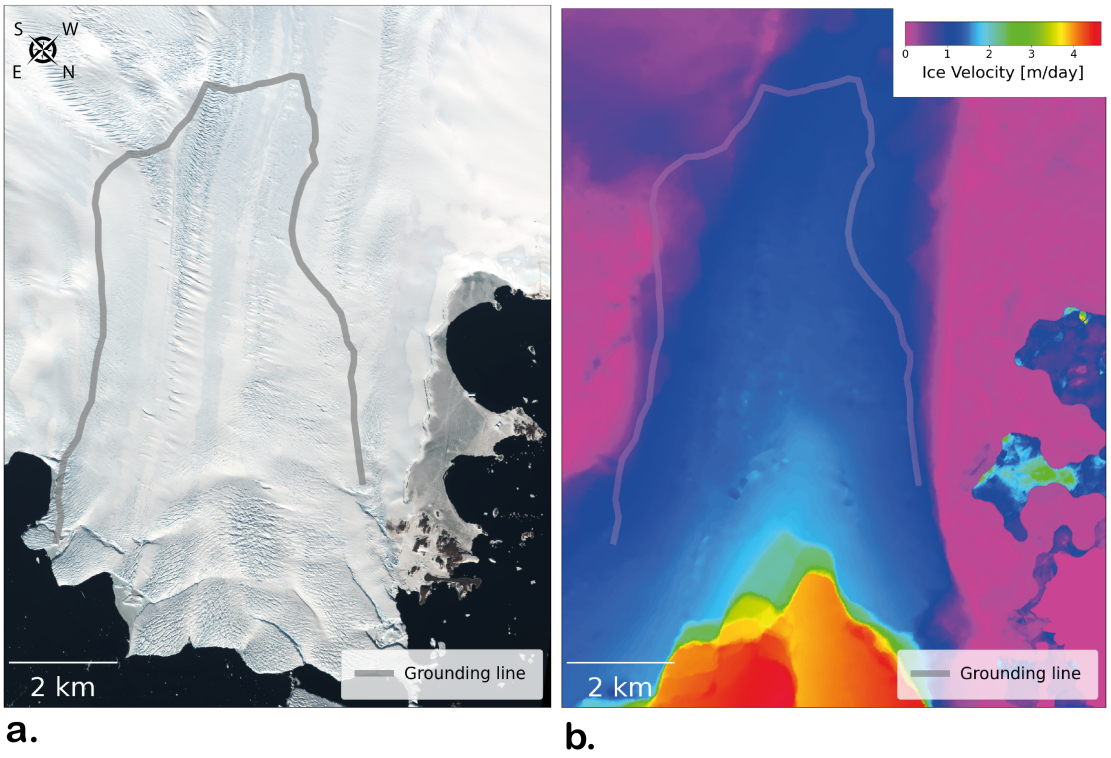

Figure 2.2: (a) High-resolution satellite image of the Astrolabe Glacier, acquired by Pleiades on 10th January, 2025. The position of the grounding line from (Le Meur et al., 2014) is displayed in light grey. (b) Surface ice velocity map of the Astrolabe Glacier (Provost et al., 2024). The map highlights a sharp lateral velocity gradient between the slow-moving ice (in purple) and the fast-flowing glacier (in blue), indicating the location of shear margins, and a distinct acceleration near the glacier front, associated with active calving processes.

On certain glaciers, topographic clues at the surface can indicate the position of the grounding line. However, the Astrolabe Glacier has no clear features to hint at its location. It was long thought that the slope rupture was linked to the grounding line, before concluding that it was most likely the result of a slope failure in the bedrock instead. The grounding line position has been thus estimated based on GNSS observations. It exhibits a U-shaped geometry that closely follows the left shear margin, while the right-hand section extends in a more irregular crooked pattern (Fig. 2.3).

The Astrolabe Glacier is influenced by tidal forcing which, as discussed in chapter 1, influence ice dynamics patterns particularly at the grounding zone. In the region, sea level height is measured every 2 minutes by an automatic tide gauge, DUMON, installed at DDU since 1997. The dataset is managed by the NIVMER/ROSAME project (Calzas et al., 1992).

Most coastal regions experience two high tides and two low tides each day of roughly equal height, a pattern known as a semidiurnal tide. In some locations however, the

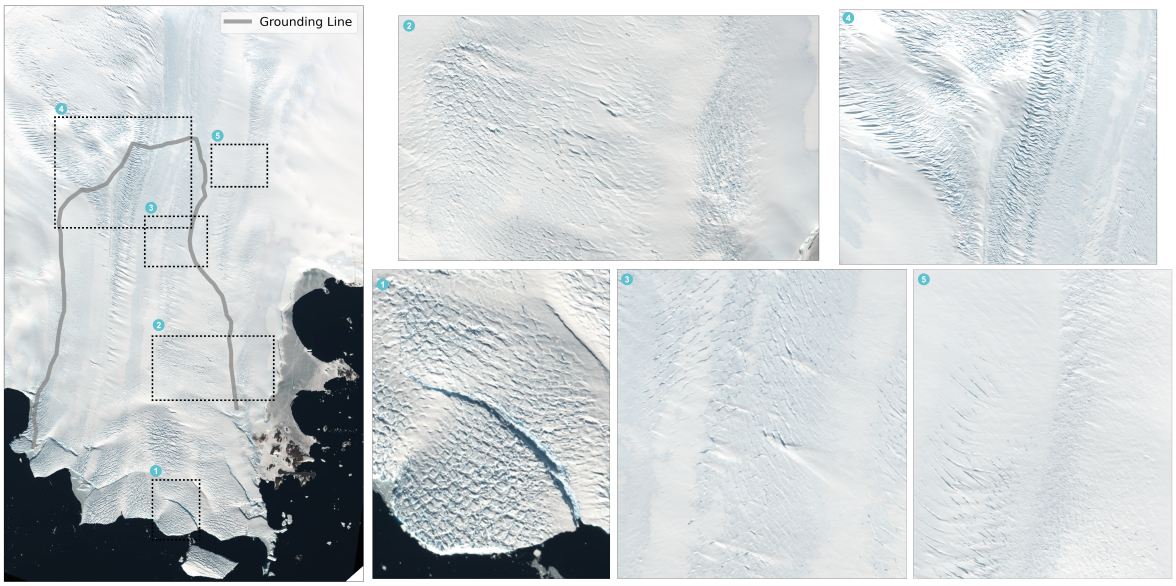

Figure 2.3: Surface imagery of the Astrolabe Glacier with zoom-ins on visible features hinting at distinct glacier structural elements. (1) Heavily crevassed calving front. (2) Right lateral shear margin showing important surface deformation. (3) Central glacier zone exhibiting complex surface crevassing. (4) Left lateral shear margin characterized by two intersecting crevasse fields, where a secondary ice flow is merging with the shear margin. (5) Upper right lateral shear margin, featuring narrow, linear crevasses adjacent to a more chaotic, heavily deformed surface. The background image is a Pleiades satellite acquisition from January 10, 2025.

successive high and low tides differ in height, producing a mixed (semi)diurnal tide. Other regions may experience only one high and one low tide per day, referred to as a diurnal tide. Beyond these daily cycles, tides also vary over a monthly cycle. Twice each month, spring tides occur around the new and full moon (when the Sun, Earth, and Moon align), producing the largest tidal ranges with highest high tides and lowest low tides. Conversely, neap tides occur during the first and third quarters of the moon, when the Sun and Moon are at right angles, resulting in the smallest tidal ranges. In Antarctica, there are only sparse data available and they show mainly diurnal to mixed diurnal tidal cycles.

In the area surrounding the Astrolabe Glacier, the tidal cycle has a complex regime that varies from one day to another across the monthly tidal cycle. Figure 2.4 illustrates tide amplitudes recorded at DDU over a full month, capturing two spring and two neap tides. The daily tidal pattern alternates between diurnal cycles (more frequent during spring tides) and mixed diurnal cycles. In mixed diurnal cycles, the dominant sea level height peak reaches 1.5–2 m (low to high), while the secondary peak is much smaller, on the order of only a few tens of centimeters. At neap tides, the amplitudes of the two peaks become more similar, whereas during spring tides the difference between them increases, often approaching a purely diurnal cycle. This tidal complexity translates

into highly variable oceanic forcing on glacier dynamics, with significant implications for the stress regime within the ice.

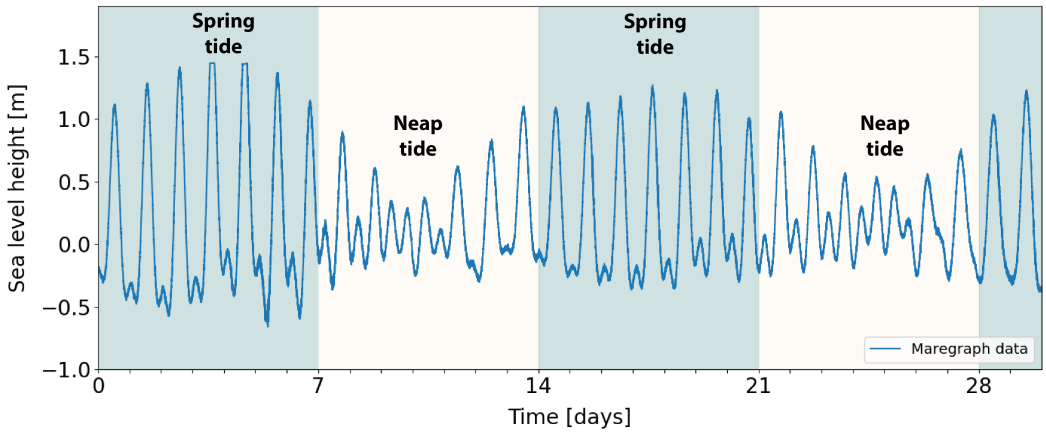

Figure 2.4: Thirty days of sea-level records from the DUMON tide gauge at DDU. The data capture two spring tides and two neap tides within a monthly tidal cycle (from 2022, December 21th to 2023, January 20th). The daily tidal cycle predominantly follows a mixed diurnal pattern, characterized by a dominant tidal amplitude of $\sim 1.5-2m$ (low to high) and a secondary amplitude peak of $\sim 20cm$. Occasional diurnal cycles are also observed (e.g., on days 27–29).

2.1.2 Previous and ongoing studies

The Astrolabe Glacier has been the focus of several scientific studies, both past and ongoing. One of the most significant long-term initiatives is the project originally named DACOTA, which has since been incorporated into the broader GLACIOCLIM - SAMBA observatory program led by the Observatoire des Sciences de l'Univers de Grenoble (OSUG).The GLACIOCLIM observatory program aims at establishing a long-term glacial-meteorological database to understand the relationships between climatic variations and glacial mass balances in the Alps, Andes and Antarctica. The objectives of this project are to improve understanding of glaciers physical characteristics and dynamic behavior and to provide empirical data for numerical modeling aimed at forecasting the glacier's evolution under future environmental changes. On the Astrolabe Glacier, the GLACIOCLIM - SAMBA is mainly based on data collected from a network of eight permanent GNSS stations, producing a continuous time series of surface motion since 2011. These observations enable high-resolution tracking of ice flow velocities and seasonal and interannual variations in glacier dynamics. In the early phase of the DACOTA project, additional field campaigns including airborne radar and ground-penetrating radar surveys were conducted to estimate the glacier ice thickness and derive mass balance estimates (Le Meur et al., 2014; Mouginot et al., 2014). These data have supported three-dimensional ice flow modeling using the Elmer/Ice finite

element code as part of a doctoral research project (Drouet, 2012).

In parallel to the geodetic monitoring, the DRV Geoscope seismic station at Dumont d'Urville Station (DDU) has operated since 1986. The primary aim of this station, embedded in a global seismological network, is the continuous broadband high-resolution observation of ground motion in Antarctica. Seismic data from the DRV station are openly shared with the international scientific community, contributing to studies of regional and global seismicity, tomography, and microseismic noise analyses. Recent work has also focused on the calving behavior of the glacier. Provost et al. (2024) conducted a study using multi-temporal satellite imagery to analyze the evolution of the floating ice tongue, strain rate patterns, and the cyclicity of calving events.

2.2 Project SEIS-ADELICE (2020-2025)

2.2.1 Objectives

The work conducted during my PhD is directly integrated into the SEIS-ADELICE project. The SEIS-ADELICE project (2020-2025), supported by the French Polar Institut (Institut Paul Emile Victor, IPEV) is dedicated to recording and analysing the cryoseismic activity of the Astrolabe Glacier (Terre Adélie, East Antarctica) through a combination of land-based and ocean-bottom seismological deployments. This project brings a complementary instrumental approach to previous and current projects that have been/ are running in parallel on the Astrolabe Glacier. Its aim is to study the glacier dynamics and its interaction at the different interfaces: the ocean, the bedrock and the surrounding slow-moving ice. To capture the most exhaustive picture possible, a variety of seismic arrays have been deployed. The instruments were installed on rocky islands, on the glacier surface, particularly over the grounding zone, on slow-moving ice and on the seafloor in front of the glacier. The specific objectives of SEIS-ADELICE include: (1) Analyzing cryoseismicity associated with ice flow and ice brittle deformation. (2) Imaging the internal structure of the glacier and the three-dimensional geometry of the underlying bedrock. (3) Investigating processes at the grounding zone where glacier dynamics are most sensitive yet remain poorly observed (Rignot, 2023). (4) Studying the lateral shear margins of the glacier, where it accommodates deformation relative to adjacent slow-moving or stationary ice and bedrock. (5) Examining the glacier terminus at sea, particularly the processes governing calving and iceberg formation. Note that the point (2) dedicated to structure imaging is the subject of a PhD thesis (Lisa Operto) starting in autumn 2025 at ITES Strasbourg.

2.2.2 Seismic deployments and field campaigns

To achieve the scientific objectives of the SEIS-ADELICE project, a multi-scale deployment strategy was designed and implemented, combining short- and long-term seismic instrumentation, and adapted specifically to the harsh environmental condi-

tions and logistical challenges of coastal East Antarctica. Between 2020 and 2025, five austral summer field campaigns were conducted, with the main activities taking place from 2022 to 2025, following pandemic-related delays. The deployments include broadband seismic stations, dense nodal arrays, ocean-bottom seismometers (OBSs), and distributed acoustic sensing (DAS). A summary of the instruments deployed during each field season is provided below and is further presented in greater details in a dedicated paper (Barruol et al., 2025). The location of seismic stations and dense arrays is shown in Figure 2.5.

2020
Installation of 1 broadband station (AST01) on slow-moving ice near CPH.

2022
Installation of 3 broadband stations (AST02, AST09, AST10) on slow-moving ice close to the glacier for 3 years. Installation of 6 broadband stations (AST03 to AST08) on the glacier, over the grounding zone, for a 3-week deployment. Deployment of 4 OBSs in front of the glacier terminus for 2-3 weeks. After successful recovery, 2 OBSs were redeployed in early February 2022 for a full-year wintering.

2023
Deployment of a dense array (A1) of 50 seismic nodes over the grounding zone, operated for 3 weeks. Installation of 1 broadband station (AST13) on Gouverneur Island (see Fig. 2.1b). Maintenance and servicing of previously deployed broadband stations. Deployment of 4 OBSs for a second wintering until early 2024.

2024
Deployment of a second dense array (A2) of 35 seismic nodes over the grounding zone. Deployment of 2x2 km of optical fiber for DAS acquisition within the array extent. Installation of 1 broadband station (AST14) on Curie Island (Fig. 2.1b). Maintenance and servicing of previously deployed broadband stations. Installation of a long-term station (AST15) on the glacier for a full-year wintering. Recovery of the 4 OBSs.

2025
Deployment of a third dense array (A3) comprising 44 nodes, focused on the right lateral shear margin of the glacier. Recovery of broadband stations previously deployed on rocky outcrops and slow-moving ice.

An exhaustive summary of the seismic datasets, including location coordinates, sampling rate, recording durations, and sensor types, is presented in Tables 2.1, 2.2, and 2.3.

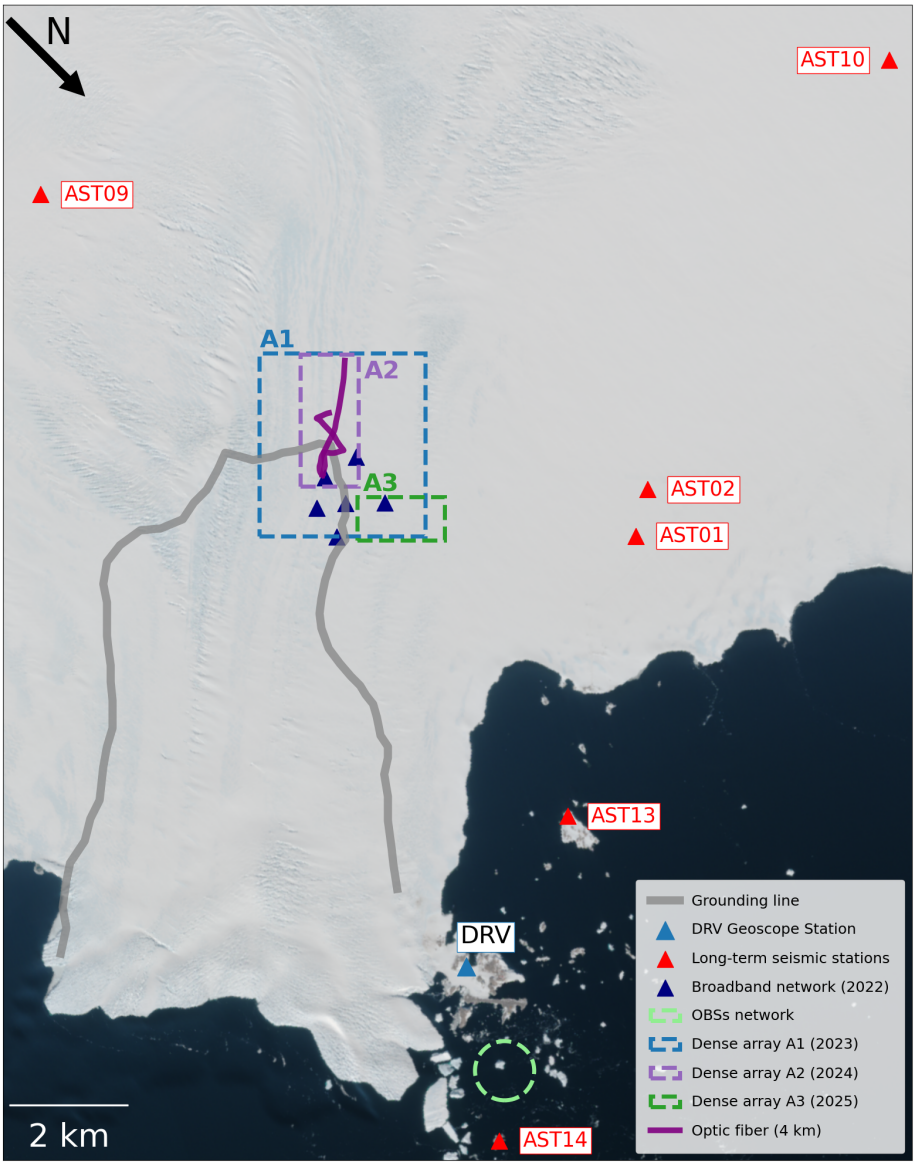

Figure 2.5: Map of seismic deployments conducted during the SEIS-ADELICE project (2020-2025).

Dense array	Year	Number of seismic nodes	Surface area	Average recording duration	Average station spacing	Sampling rate
A1	2023	50	2x2 km^2	20 days	400-500 m	500 Hz
A2	2024	35	2,000x700 m^2	19 days	150-200 m	500 Hz
A3	2025	45	1,500x700 km^2	15 days	100-150 m	500 Hz

Table 2.1: Summary of dense arrays of seismic nodes deployed from 2023 to 2025, including surface area, number of nodes, total recording days and sampling rates. Tables with precise localizations of each node of the arrays are given in Tables A2.1, A2.2, A2.3.

Station	Long (°E)	Lat (°N)	Altitude	Starting date	Ending date	instrument	Sampling rate
DRV	140.00207	-66.66491	40 m	1986	ongoing	STS-1	20 Hz
AST01	139.8570	-66.7004	160 m	2020-01-18	2025-01-15	NT 120PA	100 HZ
AST02	139.8420	-66.7047	228 m	2022-01-07	2025-01-18	NT Horizon 120	100 Hz
AST03	139.9420	-66.7343	74 m	2022-01-12	2022-02-01	NT compact	200 Hz
AST04	139.9330	-66.7370	80 m	2022-01-13	2022-02-01	NT 120QA	200 Hz
AST05	139.9200	-66.7364	95 m	2022-01-11	2022-01-31	NT 120QA	200 Hz
AST06	139.9210	-66.7284	76 m	2022-01-13	2022-02-01	NT 120QA	200 Hz
AST07	139.9440	-66.7291	81 m	2022-01-12	2022-02-01	NT 120QA	200 Hz
AST08	139.9330	-66.7321	81 m	2022-01-11	2022-02-01	NT 120QA	200 Hz
AST09	139.9460	-66.7967	370 m	2022-01-15	2024-01-24	NT 120PA	100 Hz
AST10	139.6680	-66.7302	450 m	2022-01-15	2025-01-14	NT 120PA	100 Hz
AST11	139.9480	-66.7406	72 m	2023-01-10	2023-02-02	NT 120QA	200 Hz
AST12	139.9070	-66.7476	111 m	2023-01-10	2023-02-02	NT 120QA	200 Hz
AST13	139.9450	-66.6740	15 m	2023-02-02	2025-01-20	NT 120QA	100 Hz
AST14	140.0440	-66.6448	12 m	2024-01-17	2025-01-20	NT 120QA	100 Hz
AST15	139.9369	-66.7312	86 m	2024-01-30	2024-11-06	3D Geoph.HL-6B	200Hz
AST16	139.9359	-66.7309	86 m	2025-01-12	2025-01-23	3D Geoph.HL-6B	200Hz

Table 2.2: Summary of broad band seismic stations (except AST15 and AST16 that are short-period) deployed during the SEIS-ADELICE project, including installation and removal dates, total recording days, instrument types and sampling rates. NT: Nanometrics Trillium

Station	Long (°E)	Lat (°N)	Starting date	Ending date	Duration	Instrument	Sampling rate
OBS01	140.0296	-66.6484	2022-01-10	2022-01-29	20 days	OBS INSU	250 Hz
OBS02	140.0355	-66.6515	2022-01-18	2022-01-30	13 days	OBS GURALP	100 Hz
OBS03	140.0247	-66.6543	2022-01-18	2022-01-29	12 days	OBS INSU	250 Hz
OBS04	140.0245	-66.6519	2022-01-10	2022-01-29	20 days	OBS INSU	250 Hz
OBS05	140.0345	-66.6502	2022-02-01	2023-01-05	339 days	OBS INSU	62.5Hz
OBS06	140.0295	-66.6501	2022-02-01	2022-10-07	249 days	OBS GURALP	100 Hz
OBS07	140.0357	-66.6522	2023-01-11	2023-12-19	342 days	OBS INSU	62.5Hz
OBS08	140.0348	-66.6554	2023-01-10	2023-09-13	246 days	OBS GURALP	125 Hz
OBS09	140.0396	-66.6523	2023-01-10	2023-08-17	219 days	OBS GURALP	125 Hz
OBS10	140.0291	-66.6498	2023-01-10	2023-08-09	223 days	OBS GURALP	125 Hz

Table 2.3: Summary of OBS deployed during the SEIS-ADELICE project, including installation and removal dates, total recording days, instrument types and sampling rates.

CHAPTER 3

Methods for detection and location of cryoseismic events

Contents

3.1 Detection of seismic events 46

3.1.1 Short term average (STA)/ Long term average (LTA) algorithm 46

3.1.2 Template matching 50

3.2 Location of seismic events 53

3.2.1 Grid search 53

3.2.2 QuakeMigrate 57

3.2.3 Polarization analysis 59

3.3 Match Field Processing 61

The analysis of seismic sources from recordings is based on the identification, detection, and localization of signals. Given the large number and diversity of seismic signals that coexist, it is necessary to develop strategies to isolate events of interest and develop approaches adapted to events waveform characteristics. In this chapter, I present the different methods applied and discuss the parametrization choices made based on the type of seismic waves, as well as the challenges and limitations encountered.

3.1 Detection of seismic events

3.1.1 Short term average (STA)/ Long term average (LTA) algorithm

The short-term average/long-term average (STA/LTA) algorithm is a common detection method that uses automatic triggers to identify impulsive signals within continuous seismic records (Allen, 1978; Lesage, 2009). It is particularly efficient when scanning through long-term records. The method is conceptually similar to a signal-to-noise ratio. It is based on the calculation of the average absolute amplitude of the seismic signal within two moving time windows: a short-term window (STA), sensitive to sudden changes caused by events, and a long-term window (LTA), sensitive to the background seismic noise level. The ratio of STA to LTA is then continuously evaluated against a predefined trigger threshold. When the ratio exceeds this threshold, an event is declared, and once the signal decays, the STA/LTA ratio drops below a separate, lower detrigger threshold and terminates the detection of the event.

There are four parameters to set and optimize for the automatic detection algorithm. The STA and LTA window lengths, the STA/LTA ratio trigger on threshold (thrOn) and the STA/LTA ratio trigger off threshold (thrOff). These parameters must be chosen to balance highest sensitivity to impulsive events and lowest possible false detections. These parameters are highly dependent on the seismic noise conditions at the study site, on the properties of the seismic signals and the type of sensor. In that regard, there is no given optimal setting parameters. Instead, parameters must be adapted according to the specificities of the seismic data. To choose the parameters values, one must be aware of their influence on the detection performance. The short term average window measures the 'instant' value of a seismic signal. Therefore, the duration set must be longer than a few periods of expected seismic signals but shorter than its total duration. If the window is too short, the averaging of the signal amplitude will not work properly and will be biased by individual periods of the seismic content. The other risk of setting the window too short is the false trigger of spike-like events not associated with cryoseismic signals. The choice of long-term average (LTA) window length depends both on the signal characteristics and the typical period of seismic noise fluctuation. A long LTA window increases sensitivity to low amplitude

emergent events, because the background average is less rapidly influenced by gradual signal onsets. A short LTA duration allows the LTA value to adjust to the slowly increasing amplitude of emergent seismic waves, the STA/LTA ratio remains low (both STA and LTA values increase) and stays below the set threshold. In the case of an impulsive P wave arrival, longer LTA window duration are also preferred, to keep seismic noise amplitude estimates from being contaminated by the start of the signal. Finally, in case of long continuous or smaller changes (like long tremors), shorter LTA window adapts more quickly to gradual noise fluctuations, allowing improved sensitivity. An optimal LTA duration should therefore be long enough to smooth background noise variations while remaining responsive to the event of interest. STA/LTA ratio trigger on threshold depends on background seismic noise amplitude, targeted seismic signals and the tolerance to false detections. The higher the value is set to, the less cryoseismic signals will be detected, but the fewer the false detections will result. Knowing so, one should fit the threshold to its dataset for the best compromise between correct detections, false detections and missed events. The STA/LTA ratio trigger off threshold value determines how much of the seismic event coda is included in the event detection time window. To include as much of the coda waves as possible, a low value is required. It also should take into account the seismic noise amplitude as a thrOff too low can prevent the STA/LTA ratio to fall below it and cause a very long detection window. This is particularly important in the case the duration of the event is used to estimate its magnitude. Finally, before applying the STA/LTA algorithm, filtering the data can improve detection performance and help decide parameter settings. A bandpass filter can help remove high frequency background noise and reduce the overall seismic noise amplitude. The STA/LTA amplitude ratio can be sharpened by filtering the data around the dominant frequency of the target seismic signal, as long as this frequency does not overlap with the dominant frequency of the background noise, which would be counterproductive.

Figure 3.1 illustrates how the choice of STA and LTA window lengths affects the ability of the STA/LTA algorithm to correctly identify an icequake and determine its duration. This is adapted for the case of the SEIS-ADELICE dataset, and particularly here on the data from the dense array A1. Parameter settings of STA=0.5 s and LTA=5 s provide a good balance. The ratio rises well above the trigger-on threshold during the event and drops back below the trigger-off threshold once the signal ends, thus capturing the event's duration accurately. By contrast, parameter settings of STA=0.9 s and LTA=5 s illustrate the effect of a STA window that is too long. The ratio barely exceeds the trigger-on threshold and decays too slowly, so the end of the event is not well resolved. In this case, the STA window length exceeds the actual event duration, reducing sensitivity. The parameter settings of STA=0.5 s and LTA=1 s highlights the limitations of a LTA window that is too short. Because the long-term average is strongly influenced by the seismic signal itself, the ratio remains below the trigger-on threshold and the event is missed. Overall, this example shows that tuning of STA and LTA parameters is imperative: the STA must be short enough to capture the impulsive

onset of an event, while the LTA must be long enough to represent background noise without being contaminated by the event signal itself.

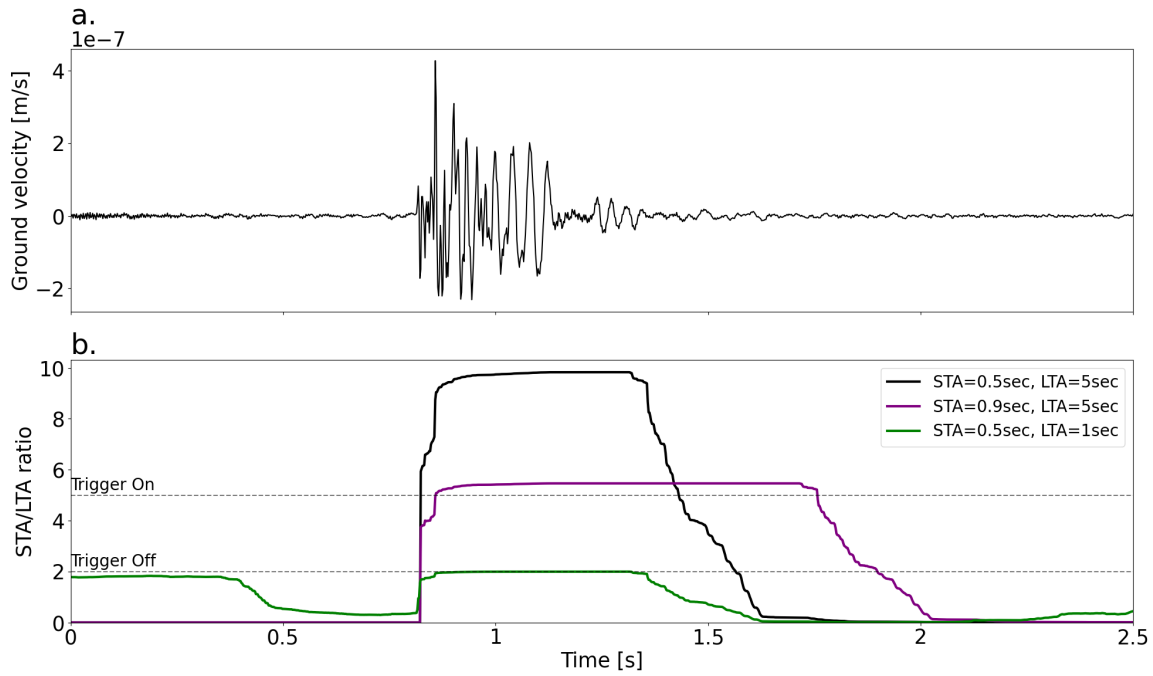

Figure 3.1: Influence of STA/LTA parameters on the detection of an icequake. (a) Waveform of an icequake recorded on the vertical component.(b) Comparison between different STA/LTA parameters. The trigger-on and trigger-off thresholds are set to 5 and 2, respectively. Black curve: STA=0.5 s, LTA=5 s. The ratio rises well above the trigger-on threshold and drops below the trigger-off threshold at the end of the event, correctly capturing its duration. Purple curve: STA=0.9 s, LTA=5 s. The ratio barely exceeds the trigger-on threshold and decays too slowly, failing to match the actual event duration. This occurs because the STA window is longer than the event itself, reducing sensitivity. Green curve: STA=0.5 s, LTA=1 s. The ratio never reaches the trigger-on threshold. Here, the LTA window is too short, so background noise is strongly influenced by the signal itself. Both the STA and LTA amplitudes are increasing, keeping the ratio curve below the threshold and preventing proper detection. Parameters of the black curve are those kept for the detections of icequakes in future analyses. The icequake waveform shown for example is from station 01x07 of dense array A1.

The STA/LTA algorithm is particularly efficient for detecting icequakes in seismic records. These icequakes, originating from brittle deformation, have impulsive onsets and amplitudes that clearly stand out from background seismic noise. They can be detected and differentiated from other types of cryoseismic signals like tremors (longer durations, emergent and gradual increase of amplitudes) or stick-slip events (low amplitude signals close to the seismic noise amplitude, very short duration). By setting STA/LTA parameters adjusted to only detect high amplitude, impulsive onset events

of average duration around 1 sec, we ensure to not detect other cryoseismic signals. Figure 3.2 illustrates the application of the STA/LTA detection algorithm on a typical record of seismicity at the grounding zone of the Astrolabe Glacier. Icequakes are identifiable in the timeseries as they have large amplitudes and dominate the records (Fig. 3.2a). Zooming in on 10 minutes of records, hundreds of icequakes are detected (see dotted red lines on Fig. 3.2b). We can validate the parameter settings by checking if the thrOn and thrOff are triggered at the right time to contain the full event duration (Fig. 3.2c). From the detections, we can then access, for instance, information on icequake occurrences to highlight patterns in temporal distribution (Fig. 3.2d).

A manual check of a subset of detections still seems necessary to assess the quality of the STA/LTA results, i.e. the proportion of false detections and missed events. This step ensures that the parameter settings are well adapted to the characteristics of the data. For example, in Figure 3.2b, the algorithm successfully detects all visible events in the time series. However, some detections do not align with high-amplitude signals and may represent false positives. This illustrates the trade-off between being the most exhaustive and capture all events of interest and having a high number of false detections.

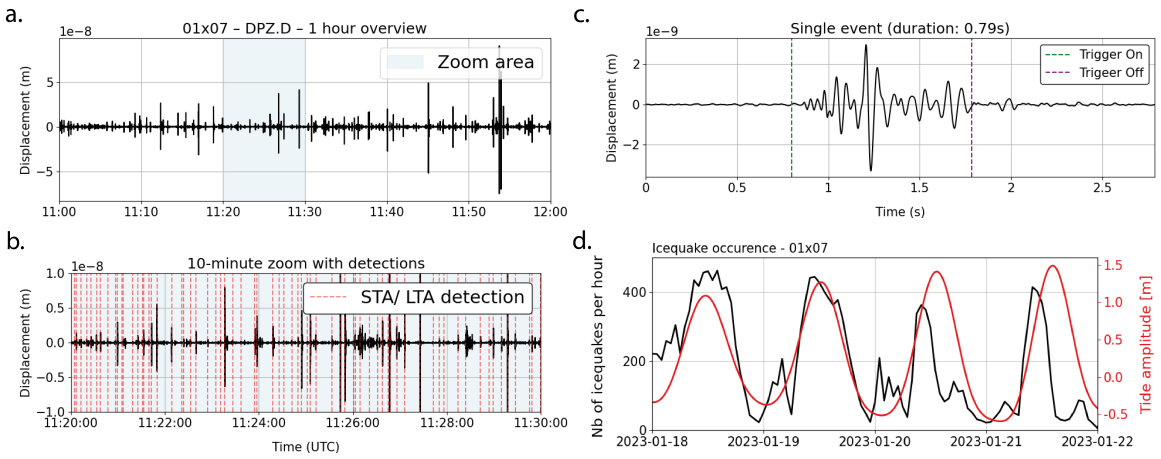

Figure 3.2: Icequake detection at station 01x07, on 18th January, 2023. (a) Vertical seismogram, filtered between 10 and 100 Hz, showing the numerous icequakes appearing as impulsive events. (b) Zoom on 10 minutes-long seismogram of the vertical component, displaying the detected icequakes marked by the red dotted lines. (c) Example of a 1 s-long detected icequake with indication of the STA/LTA ratio threshold triggers for the start (green) and the end (purple) of the event. (d) Comparison between the occurrence of icequakes detected at station 01x07 (black curve, in count per hour) and the tide amplitude (red curve, in meters) during the period Jan, 18 to 22.

3.1.2 Template matching

Template matching (or cross correlation) is a powerful method to detect and/or classify events based on their similarity. It relies on comparing a reference waveform (the template) and a seismic record and finding stream sections whose waveform fits the template. It is particularly effective for detecting low-amplitude signals that may be hidden within seismic noise and thus missed by amplitude- or energy-based detectors. Groups of events with high waveform similarity often reflect spatial or process-related proximity of seismic sources. For example, stick-slip events resulting from basal friction over asperities are highly repetitive, producing nearly identical waveforms. It makes them easily detected through template matching.

The method operates by sliding a fixed template across the continuous data stream and computing a normalized correlation coefficient at each step. This coefficient, which ranges between 0 and 1, reaches its maximum when the incoming signal most closely matches the template. A detection catalog is built by applying a similarity threshold: only windows with correlation coefficients above this threshold are retained as events, while the rest are discarded. The efficiency of the method depends on the quality of the template itself. In practice, the ObsPy function correlation_detector( ) implements this approach, returning timestamps of detected events together with their correlation coefficients. Afterwards, manual checking is often necessary to fix the optimized correlation coefficient threshold and exclude false detections.

Similarly to the STA/LTA detection method, one can systematically apply the template matching method to long-term continuous seismic records to detect all the events associated with a same seismic source. Figure 3.3 illustrates the application of template matching on a two hours long stream with numerous “stick-slip” events.

Figure 3.4 shows the stacking of 150 events detected using the template presented in Figure 3.3, together with the associated correlation coefficient distribution. The quality of the detection, considering that the template is chosen wisely to resemble other events, is overall pretty satisfying. Stacking of the waveforms from the detection catalog reveals overall a good match between all events. We observe high coefficient and well superposing waveforms. However, it happens that several events do not fit with the mean stacked waveform. One way to remove all these outliers is by manually scanning the events and comparing them with the mean waveform from the stacking. Figure 3.5 presents four examples of detected events, each superimposed on the mean trace of all detections with correlation coefficient superior to 0.90. The first example (Fig. 3.5a) illustrates an event that closely matches the mean trace, with a correlation coefficient of 0.96, indicating a clear and accurate detection. In contrast, the second example (Fig. 3.5b) shows a case where the correlation coefficient is similarly high (0.97), yet the signal does not visually align with the mean trace. This apparent inconsistency may arise from the short time window. When applying template matching, the time window should ideally be slightly longer than the target signal to minimize

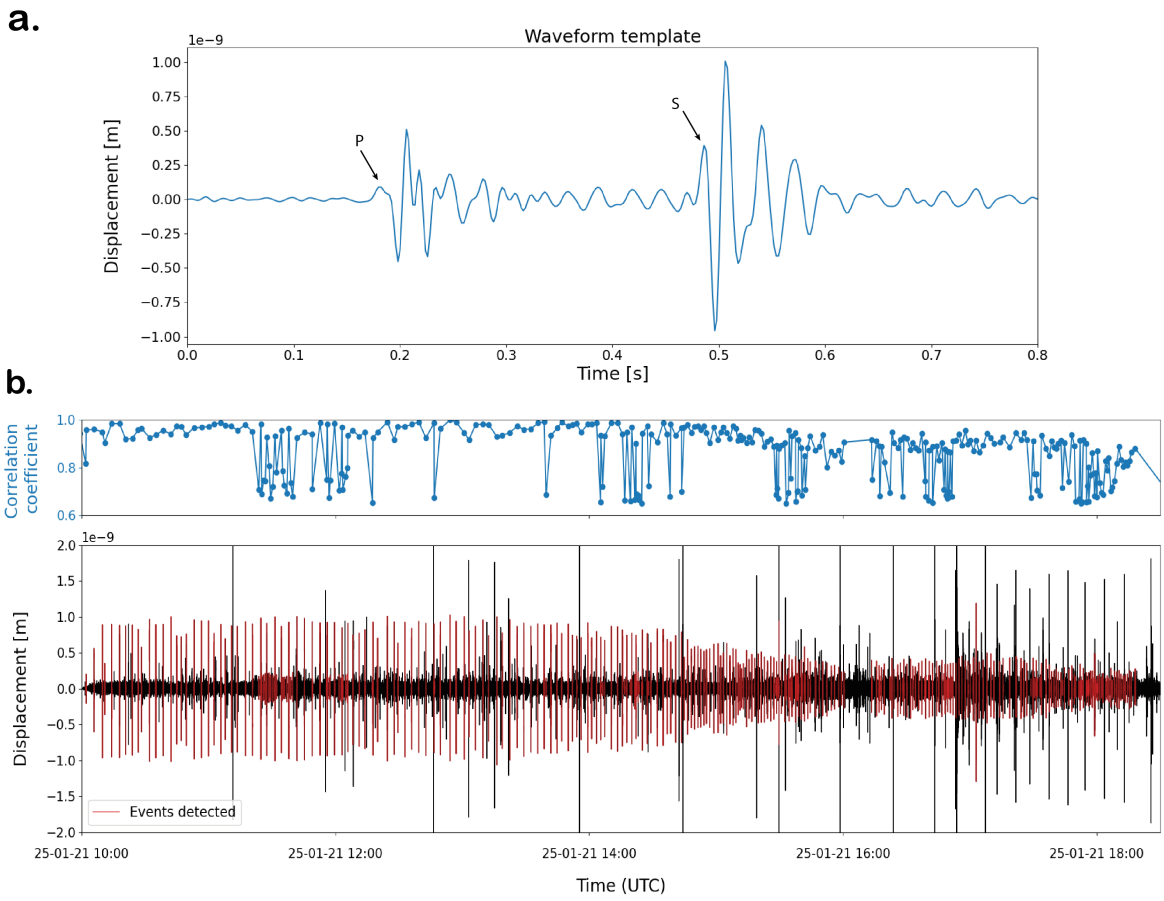

Figure 3.3: Template matching applied on seismic data from the node 34x08 of the dense array A3 on Jan. 21, 2025. (a) Template of a "stick-slip" event used for the template matching detector. (b) (bottom) Two hours of seismic records with repetitive "stick-slip" events detected by template matching colored in red. (top) Correlation coefficient for each detection over the seismic record. Only events with a correlation coefficient superior to 0.65 are displayed.

background noise, but if the signal in itself is too short, there are insufficient sampling points to effectively discriminate between signals, particularly in the frequency domain. Consequently, background noise that happens to share the same frequency content as the template may produce incorrect high correlation values, leading to false detections. Although such cases are rare, they highlight an intrinsic limitation of the method. The last two examples demonstrate how elevated background noise affects detection performance. In Fig. 3.5c, the event emerges distinctly enough from the noise to confirm it manually, although the correlation coefficient is reduced by the higher background noise. In Fig. 3.5d, however, the background noise amplitude is comparable to that of the signal, making it difficult to visually assess whether the detection is valid or false.

These examples underscore two key points. First, the similarity threshold should

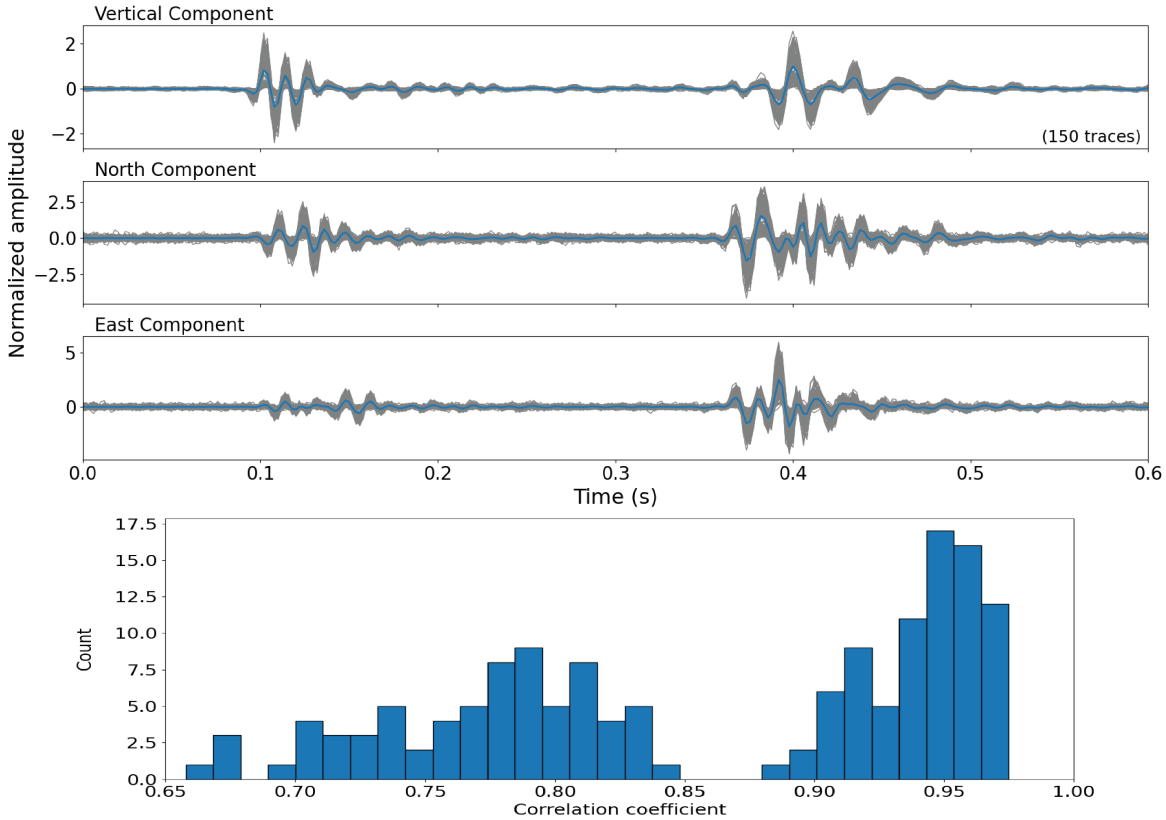

Figure 3.4: Results of the template-matching detection algorithm applied to station 34X08 (A3) using the template presented in Fig. 3.3a (a) Stack of 150 detected event waveforms (grey curves) for the three seismic components, with the mean seismic trace superimposed (blue curve). (b) Distribution of the correlation coefficients associated with the 150 waveforms shown in (a). Coefficients are distributed into two groups, with events with correlation coefficient above 0.90, translating strong matching with the template and events with correlation coefficient between 0.65 and 0.85 where matching is probably weaker.

be carefully adjusted: low enough to avoid missing weak events, yet high enough to minimize false detections. Second, ambiguous detections are inevitable, and visual verification alone cannot always provide reliability. Overall, these four examples illustrate that, much like the STA/LTA approach, the main challenge of the template matching method lies in finding an optimal balance between missed events and false detections. Manual inspection helps refine results, as will be shown in chapter 5, but it remains subjective in some cases.

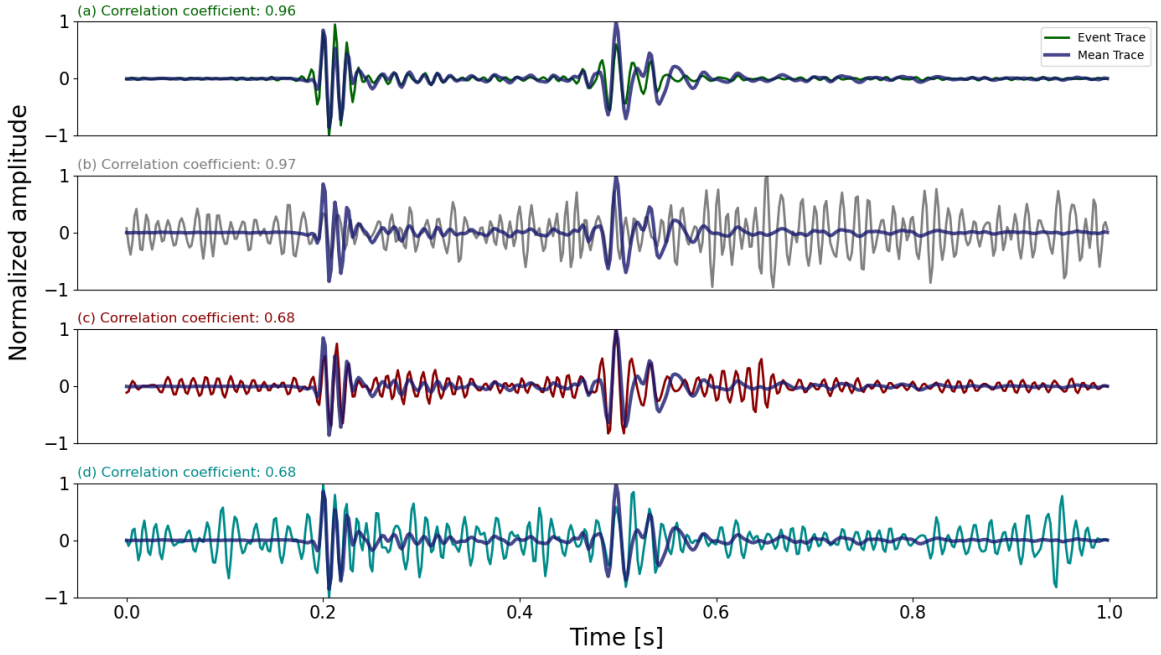

Figure 3.5: Examples of template-matching detections illustrating the limitations of the method and the importance of manual verification and careful selection of the correlation coefficient threshold. (a) Example of a correctly identified stick-slip event (green curve) that closely matches the mean trace, with a correlation coefficient of 0.96. (b) Example of a false detection (grey curve) with a waveform diverging from the mean trace despite a high correlation coefficient of 0.97. (c) Correctly identified low-amplitude event (red curve) with a correlation coefficient of 0.68; such events would be missed if the threshold was set too high. (d) Seismic trace of a detection (cyan curve) with a low correlation coefficient of 0.68. The background seismic noise is elevated, although some peaks in the signal match well with the mean trace. It shows the difficulty to distinguish between a correct and a false detection, especially when the event amplitude is small. These examples demonstrate the trade-off between minimizing false detections and avoiding missed events, and emphasize the need for a robust approach when aiming to build the most exhaustive event catalogue possible.

3.2 Location of seismic events

3.2.1 Grid search

A common approach to locate seismic sources recorded at multiple stations is the grid search method. This method consists in defining a three-dimensional grid of possible source positions and finding the grid cell that minimizes the misfit between observed and predicted variables related to seismic phases arrival times. The grid cell associated with the lowest misfit is considered as the most likely source location. Different variables can be used to quantify the misfit in a grid search. Since the absolute origin time of the source is unknown, it is generally constrained using relative timing, either inter-station time delays of one seismic phase or time delay between seismic phases

at each station, depending on whether P-wave arrivals, S-wave arrivals, or both can be reliably picked. When only P-wave arrivals are available, the comparison is made between observed and predicted P-wave time delays across station pairs. The misfit between predicted and observed delays is typically quantified using the root mean square error (RMSE; Eq. 3.1), defined as follow:

$$RMSE = \sqrt{\frac{\sum_{i=1}^{N}(\Delta t_{\mathrm{pred}_i} - \Delta t_{\mathrm{obs}_i})^2}{N}} \tag{3.1}$$

where N is the number of pairs of stations, Δt_{pred} and Δt_{obs} are respectively the predicted and observed time delay between the arrival of the P-wave at the first station and its arrival at the second station of the pair.

Predicted time delay (Eq. 3.2) depends on both the source-station distances of the station couple and the assumed P-wave velocity (V_P) and is defined as follow:

$$\Delta t_{\mathrm{pred}_i} = \frac{dist_{\text{source-sta}_2}}{V_P} - \frac{dist_{\text{source-sta}_1}}{V_P} \tag{3.2}$$

where $dist_{\text{source-sta}_2}$ and $dist_{\text{source-sta}_1}$ are the distance between a seismic source from the 3D grid and $station_2$ and $station_1$ respectively.

Observed time delay (Eq. 3.3) is defined as the difference between the P-wave arrival at the first station ($T_P^{sta_1}$) and the P-wave arrival at the second station ($T_P^{sta_2}$):

$$\Delta t_{\mathrm{obs}_i} = (T_P^{sta_1} - T_P^{sta_2})_i \tag{3.3}$$

In cases where both P and S wave phases can be picked on stations records, we can compute source-stations distance using time delay between S-wave time arrival T_S and P-wave time arrival T_P.

The RMSE to compute the misfit between predicted and observed distance of stations to the source is then defined as follow (Eq. 3.4):

$$RMSE = \sqrt{\frac{\sum_{i=1}^{M}(\Delta d_{\mathrm{pred}_i} - \Delta d_{\mathrm{obs}_i})^2}{M}} \tag{3.4}$$

where M is the number of stations used to compute the RMSE, Δd_{pred} and Δd_{obs} are respectively the predicted and observed distances from the source to the station.

The predicted source-station distance is expressed as follow (Eq. 3.5):

$$\Delta d_{\text{pred}_i} = \sqrt{(x_{source} - x_{station_i})^2 + (y_{source} - y_{station_i})^2 + (z_{source} - z_{station_i})^2} \quad (3.5)$$

where (x_{source}, y_{source}, z_{source}) are the cartesian coordinates of the trial seismic source from the 3D grid, and ($x_{station}$, $y_{station}$, $z_{station}$) are the cartesian coordinates of the station.

Observed source-station distance is expressed as follow (Eq. 3.6):

$$\Delta d_{\text{obs}_i} = (T_S - T_P)_i . \frac{V_P . V_S}{V_S - V_P} \quad (3.6)$$

Note that this approach is particularly advantageous in field conditions where clock synchronization may be imperfect (e.g., ocean-bottom seismometers).

During a grid search, the root mean square error (RMSE) is computed for each trial source location (x_{source}, y_{source}, z_{source}) within a 3D volume defined by the grid extent and resolution. The location associated with the lowest RMSE is selected as the best-fitting solution. In practice, the seismic velocities V_P and V_S can either be fixed to standard values for ice or allowed to vary to account for uncertainties. In the latter case, the RMSE is computed across a range of velocities, introducing additional loops in the search. While this improves precision by jointly constraining location and velocity, it also increases computational cost. Indeed, with such settings, the search becomes five-dimensional (x,y,z,V_P,V_S).

Figure 3.6 presents an example of the grid-search location output for a seismic event detected near the dense array A1. The RMSE map shows a well-defined minimum value, indicating good convergence toward the source location (Fig. 3.6a). Seismic traces from the stations included in the grid search (i.e., station with both P- and S-wave arrivals sufficiently clear for manual picking), are plotted as a function of their distance from the inferred source (Fig. 3.6b). The consistent alignment of P- and S-wave arrivals across stations supports the reliability of the located source. Figures 3.6c and 3.6d display the fitted linear regressions for the P- and S-wave arrivals, respectively, with slopes corresponding to the estimated seismic velocities.

The grid search method has several limitations and requires careful tuning depending on the type of seismic events being located. A key challenge lies in the requirement to pick seismic phases. In glacial ice, waveforms are often distorted by heterogeneities such as crevasses or anisotropy, which complicates phase identification and increases picking uncertainties. The grid search is highly sensitive to picking errors, and the RMSE may fail to converge to a unique minimum, instead displaying several low RMSE regions across the grid. As a result, the method often performs poorly for small or emergent icequakes with unclear P-wave onsets. Several options can mitigate

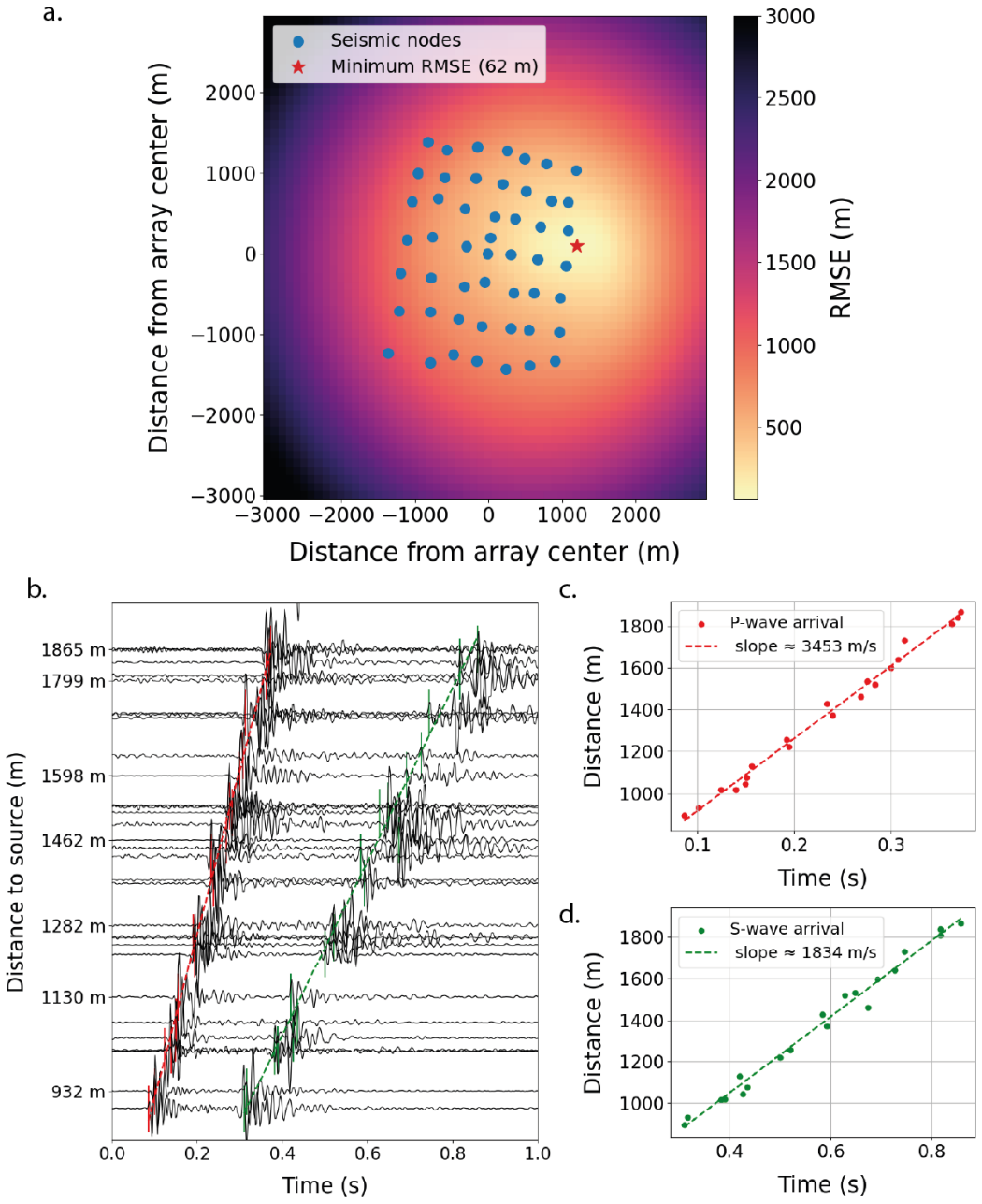

Figure 3.6: Example of a grid-search location using the differential arrival time ($T_S - T_P$) for a stick-slip event recorded by dense array A1. (a) Root Mean Square Error (RMSE) heatmap showing the convergence to a minimum RMSE value and the best-fitting source location (red star). (b) Distance-to-source versus time plot displaying the manually picked P-wave (red) and S-wave (green) arrivals. (c) Scatter plot of P-wave arrival times used for manual picking, with a fitted linear regression providing the slope and corresponding P-wave velocity. (d) Same as (c) for the S-wave arrivals.

these limitations. One approach is to explicitly account for phase-picking uncertainty. For example, if the P- or S-wave arrival is uncertain within more or less 3 ms, the grid search can be repeated across this range of possible arrival times. The resulting source locations can then be combined, either by averaging or by defining error bounds around the source location. Another strategy is waveform stacking, which improves the visibility of both P- and S-wave arrivals, allowing more reliable phase picking.

The number of station pairs used in the misfit calculation also influences performance. With N stations, up to $N(N1)/2$ P-wave time-delay pairs are possible (e.g., 1,225 pairs for 50 stations). While using a large number of pairs should in principle improve stability, in practice even a few poorly constrained picks can propagate errors and prevent RMSE convergence to its lowest value. For this reason, it is often better to restrict the number of pairs to only the most reliable picks. A complementary solution is to enforce the correct ordering of P-wave arrivals across stations, ensuring coherence even if this solution does not correspond to the absolute minimum RMSE.

Depth resolution poses another challenge: when only P arrivals are used, depth is poorly constrained, as multiple combinations of vertical and lateral positions can reproduce similar arrival times. In contrast, S-P delays provide stronger depth sensitivity, since at a given epicentral distance, deeper sources produce shorter S-P delays due to more vertical ray paths. Incorporating S-P delays therefore improves depth estimates. The existing trade-off between depth and velocity also impacts the depth estimation. At a minimum, during the grid search, we constrain the velocity to not have any extreme or unexpected values which limits the trade off but does not fully remove it. It will be more discussed in chapter 5 and chapter 6.

Finally, the computational cost of the method is a significant limitation. The spatial extent of the grid and the grid cell size must be selected to balance resolution against computation time. While this trade-off is manageable for a small number of events, it becomes limiting when attempting to locate thousands of events.

3.2.2 QuakeMigrate

QuakeMigrate is an open-source Python package developed for the automatic detection and location of earthquakes using seismic arrays (Hudson et al., 2019; Winder et al., 2025). It is particularly well suited for locating microseismicity and for environments where traditional phase picking or grid-search methods are difficult to apply. A key advantage of QuakeMigrate is that it integrates both detection and location routines within a single workflow, enabling the processing of large, continuous seismic datasets with minimal manual intervention.

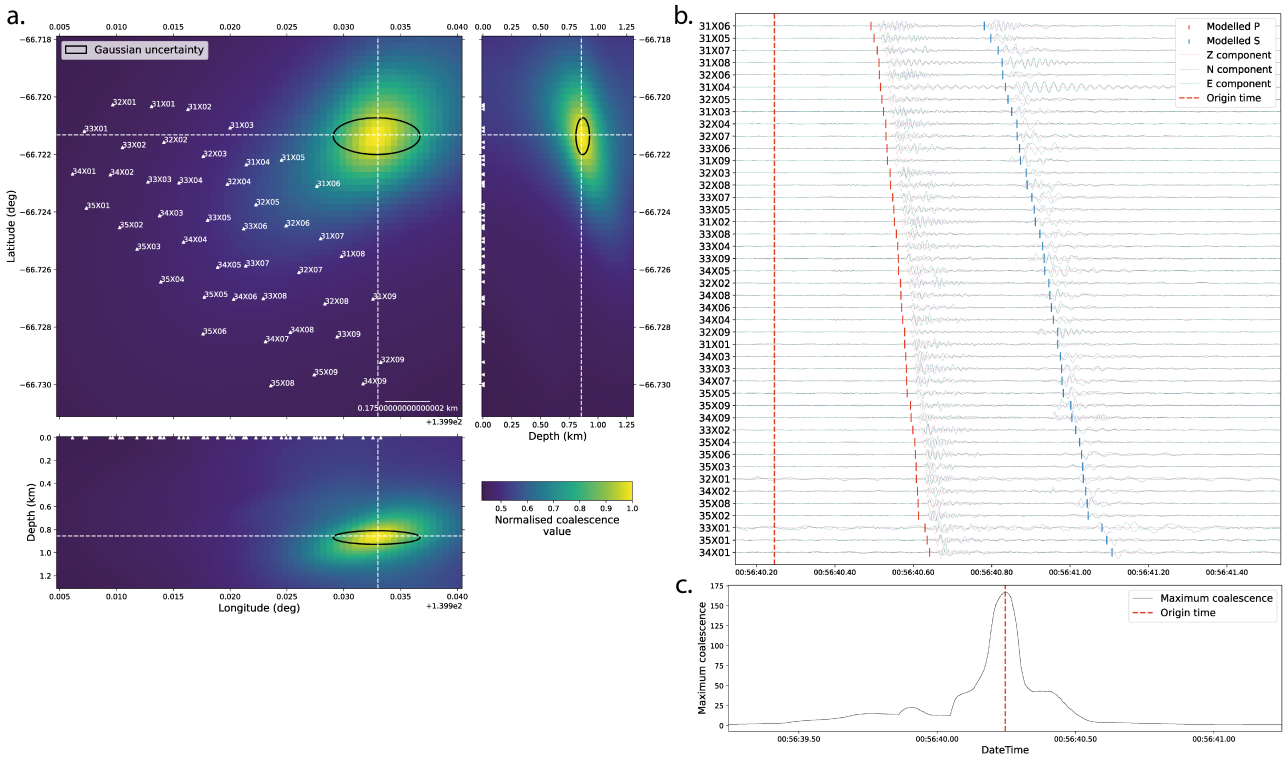

Figure 3.7: Example of QuakeMigrate event location output on dense array A3. (a) Slices through a 3D coalescence map. We see convergence of the coalescence to a local maximum (yellow shades). (b) Seismogram of event waveform ordered by time of arrival, with predicted P-phases indicated in red and S-phases in blue. (c) Maximum coalescence function with a peak corresponding to possible seismic arrivals.

Detection in QuakeMigrate is based on a migration-stacking approach, which evaluates the coherence of seismic energy across a 3D grid of potential source locations. The workflow begins with preprocessing of continuous seismic waveforms, including filtering to enhance signal-to-noise ratios. The algorithm then applies a STA/LTA-based function at each station, which serves as a proxy for seismic energy by highlighting energy increases above background noise. Peaks in these onset functions correspond to possible seismic arrivals. For each trial source location and origin time, predicted travel times are computed using a specified 1D velocity model. The onset functions from all stations are time-shifted according to these predicted arrivals and then stacked. This process back-propagates seismic energy through space and time, so that if the waveforms across the network are consistent with a common source, their energy coherently aligns. The resulting coalescence function quantifies this alignment: strong peaks indicate the most likely seismic source. Candidate events are then selected based on whether their coalescence peak exceeds a user-defined threshold. Once an event is detected, QuakeMigrate performs a more refined hypocentre location by maximizing coalescence and by quantifying location uncertainty. This provides a robust measure of confidence in the final source location. The most recent versions of QuakeMigrate

further improve location accuracy by incorporating explicit phase association, where detected arrivals are matched to predicted P- and S-wave times. This hybrid strategy improves depth resolution and increases robustness, particularly in heterogeneous or sparse networks.

Figure 3.7 shows an example of QuakeMigrate location output with the 3D coalescence map (Fig. 3.7a) pointing to the source location associated with the highest coalescence value. Seismic traces are matched to predicted P- and S-wave time arrivals in Fig. 3.7b. Finally, Fig. 3.7c displays the coalescence function with a dominant pick corresponding to the most likely seismic source arrival. For the SEIS-ADELICE dataset, QuakeMigrate requires careful tuning of parameters depending on the type of event. It performs particularly well for stick-slip events which have clear P- and S-wave arrivals, and therefore easier to parameterize consistently (see Chapter 5). Once the optimal parameter set is established, the method can be applied reliably. However, for surface icequakes with indistinct P and S phases, parameterization becomes more challenging. The onset functions can be difficult to identify across all stations due to variable signal characteristics, leading to higher uncertainties. Moreover, because the optimal settings differ across event types, achieving precise locations with low uncertainties generally requires tailoring the parameters specifically to each event class. As a result, application of QuakeMigrate to heterogeneous signals is less straightforward.

3.2.3 Polarization analysis

To further constrain the source location, and in particular the depth, one can use polarization analysis of the P-wave first arrivals (Flinn, 1965; Jurkevics, 1988; Montalbetti & Kanasewich, 1970). The method is based on analyzing the particle motion recorded on three-component seismograms within a short time window around the P-wave onset. It relies on the fact that the first-arriving P-wave is characterized by rectilinear particle motion in the direction of wave propagation. The analysis provides constraints on both the azimuthal direction and the take-off angle of the incoming wave.

By isolating the P-wave onset on each of the three components, the particle motion can be represented through ellipsoids derived from the ratios between the North-Vertical, East-Vertical, and North-East components. Figure 3.8 shows an example of polarization analysis for a well-defined event showing both P- and S-wave arrivals. The ellipsoid shapes give information about the direction of motion: (i) In the Vertical-North plane, the particle motion appears as a skewed linear ellipsoid, indicating predominantly vertical displacement with a significant contribution from the North-South component. (ii) In the Vertical-East plane, the ellipsoid is linear and vertical with no visible tilt, showing purely vertical motion and the absence of any East-West contribution. From these two planes, we can already infer that the wave approaches with a steep incidence angle, nearly vertical, and close to the North-South direction. (iii) In

the East-North plane, the ellipsoid is comparatively small and elongated close to the North-South axis, indicating that the horizontal motion is indeed dominated by the North-South component, with negligible East-West contribution.

From these windows on the P-wave onset, we can compute the azimuth and incidence angle, using the eigenstructure decomposition method of Flinn (1965) method. The ground motion at each time step can be expressed as a three-component vector $x(t) = [E(t), N(t), Z(t)]^T$ with $E(t)$, $N(t)$ and $Z(t)$ respectively corresponding to the East, North, and Vertical components. From this vector, we construct the covariance matrix

$$C = \frac{1}{N}.\sum_{t=1}^{N} x(t).x(t)^T \tag{3.7}$$

which quantifies the variance and covariance of motion along each axis. The eigendecomposition of C yields three eigenvalues λ_1, λ_2, λ_3 and corresponding eigenvectors v_1, v_2, v_3. The eigenvector associated with the largest eigenvalue, v_1, represents the dominant direction of particle motion. From the dominant polarization vector $v_1 = (v_E, v_N, v_Z)$, we derive the back-azimuth and incidence angle of the incoming wave. The azimuth θ is obtained from the horizontal projection:

$$\theta = arctan(v_E, v_N) \tag{3.8}$$

measured clockwise from north. The incidence angle ϕ, measured from the vertical axis, is given by

$$\theta = arctan(\sqrt{v_E^2 + v_N^2}, v_Z) \tag{3.9}$$

In the case of Fig. 3.8, the computation of both the azimuth and the incidence angle confirms an event arriving from the North (37°N) with an incidence angle of 27° from the vertical.

Several sources of uncertainties can arise when applying this method. First, incorrect sensor orientation to the geographic north during deployment may bias azimuth estimates, unless corrected through re-orientation processing. Second, the choice of the analysis window strongly affects incidence angle estimates, requiring careful selection around the P-wave onset to capture rectilinear motion only. If the window is too wide, contamination from scattered energy, noise, or S-wave energy can influence the estimate. Third, the seismic anisotropy may slightly influence the P-polarization by inducing a slight rotation of the P into a quasi-P wave. Such rotation is dependent on the azimuth but also the frequency content (Fontaine et al., 2009; Schulte-Pelkum &

Blackman, 2003). Despite these limitations, polarization analysis brings an independent constraint on hypocentral location, particularly the source depth.

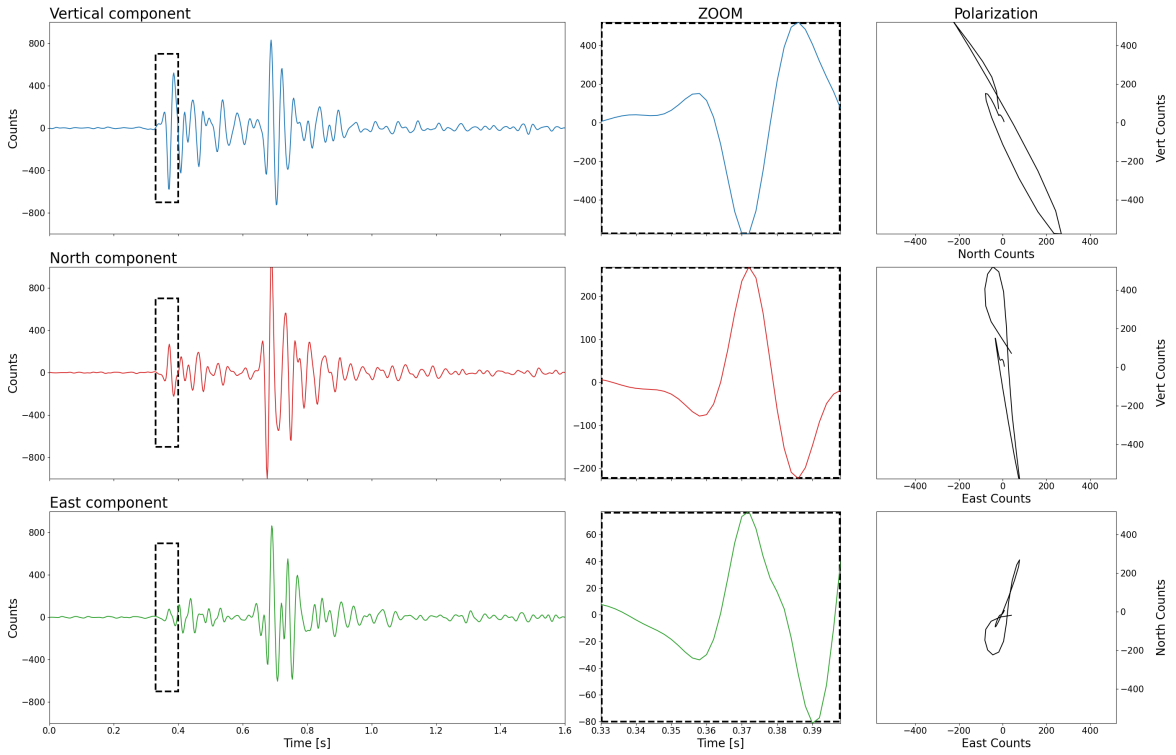

Figure 3.8: Example of particle motion analysis applied to a three-component seismic record of a stick-slip event (station 01x02, A1). (From top to bottom) First column: full waveform of the event on the three components - vertical (blue), north (red), and east (green). Second column: zoom on the P-wave onset for each component. Third column: amplitude ratios between the North-Vertical, East-Vertical, and East-North components. The resulting ellipses provide information on the azimuth and incidence angle of the incoming wave, offering an estimate of the source position relative to the station.

Polarization analysis was only employed in this study as a verification tool to confirm the azimuthal direction of seismic sources and to validate event locations obtained by other methods. Consequently, no section is devoted to this approach, which was instead applied punctually in the background in order to cross-check and reinforce the reliability of our results.

3.3 Match Field Processing

Matched Field Processing (MFP) is a beamforming method that uses the seismic wavefield recorded by a dense array to automatically locate seismic sources. Unlike localiza-

tion methods that rely on the prior detection of individual events, MFP systematically scans the entire continuous seismic records to locate sources making it particularly suited for large datasets. The method relies on evaluating the phase coherence of a seismic signal across an array. To do so, it compares the observed wavefield phase delays between stations with the phase delays of a model-based synthetic field. The observed wavefield is represented in the frequency domain: for a given frequency ω, we compute the discrete Fourier transform of the recorded data vector $d(t)$ to obtain the complex data vector $d(\omega)$. From this, we compute the cross-spectral density matrix (CSDM) as

$$K(\omega) = d(\omega).d^H(\omega) \tag{3.10}$$

where H is the Hermitian transpose. This CSDM encodes the relative phase delays between sensors. The observed wavefield is compared with a synthetic one derived from a trial source model. For a trial source defined by the coordinates (x, y, z) and a homogeneous phase velocity c (i.e. assumed constant within the array), the frequency-domain Green's function defines a synthetic replica vector as

$$d(\omega, a) = e^{i\omega r_a/c} \tag{3.11}$$

where r_a is the distance between the trial source and each receiver. This formulation accounts for spherical wave propagation and allows the location of sources both within and close to the array (Gimbert et al., 2021). The similarity between the observed and synthetic wavefields is evaluated using the Bartlett processor, which measures phase coherence, and serves as the MFP output:

$$Bartlett(\omega, a) = \sum_{\omega} |d(\omega, a)^H K(\omega) d(\omega, a)| \tag{3.12}$$

This normalized coefficient ranges between 0 and 1, where higher values indicate stronger coherence and a better match between modeled and observed fields. For example, a MFP output value of 0.2 implies that approximately 20% of the array records coherent phase information. In practice, MFP is applied systematically to short time windows of continuous seismic data (e.g., 2-s windows with 0.5-s overlap), typically on the vertical component, which is most sensitive to body-wave sources. Usually, MFP is applied to a range of frequency bands in order to explore sources detectable at different frequencies. It is also important to test different frequencies since a source located with a similar MFP output is not expected to bear the same accuracy, since the phase coherence increases with increasing seismic wavelength (Rost & Thomas, 2002).

Because exhaustive multi-dimensional grid search is computationally heavy for large datasets, we use a gradient-based minimization algorithm based on the downhill simplex search method (Nelder-Mead optimization) from Nelder & Mead (1965) and La-

garias et al. (1998). This allows the algorithm to converge toward the best-fitting source without evaluating every grid point. Convergence is controlled by two criteria: (1) the optimization stops once the variance of a set number of successive solutions falls below a predefined threshold, and (2) a maximum number of iterations is imposed to avoid endless searches when convergence is not reached.

By default, we aim for highest MFP output values to trust the localization of events. However, simultaneous events within the same time window can reduce overall phase coherence, lowering the MFP output value. To address this, the optimization is initialized from multiple starting points distributed within the dense array extent, with varying depth and in all azimuthal directions. Two cases can typically occur. First, there is a dominant source in the time window investigated. All initializations converge to the same solution with a MFP output close to 1, indicating a single event dominates the wavefield. Second, there are multiple sources occurring simultaneously within the time window investigated. Solutions converge to different local minima, each with lower MFP output values, highlighting distinct overlapping sources that make up for the wavefield. As for the precision of the localization, we expect a resolution of around $\lambda/4$ (around 150m for 2.5 Hz) (Rost & Thomas, 2002).

Application of the method on dense arrays is further discussed in (Le Bris et al., 2025) and in chapter 7 where we compare the performance of the MFP for dense arrays deployed on the Astrolabe Glacier in Antarctica and on Isunnguata Sermia in Greenland. We particularly discuss how the environment context and the type of seismic sources can impact the MFP performance and output interpretation.

CHAPTER 4

Seismic monitoring of tide-induced deformation at the Astrolabe Glacier surface

Contents

4.1 Context and strategy of the study 66

4.2 Spatial and temporal variability in tide-induced icequake activity at the Astrolabe coastal glacier, East Antarctica (Le Bris et al., 2025) 66

4.3 Comparison with 2024 and 2025 dense arrays 89

4.4 Outcomes and outlook 94

4.1 Context and strategy of the study

As discussed in Chapter 1, marine-terminating outlet glaciers are subject to external forcing at their ocean-ice interface, where tides induce cyclic up and down motion of the floating tongue and induce flexure and deformation close to their grounding zone. While these processes are expected to generate strong internal stresses, direct observations of the resulting deformation remain limited. Icequakes, defined here as seismic signals generated by brittle deformation of ice, offer an indirect yet powerful means to investigate these dynamics.

Previous studies have shown that icequake activity at outlet glaciers is often modulated by tides, but no clear consensus has emerged on the mechanisms controlling these occurrence patterns. Partly because glacier-specific factors such as geometry, size, and dynamic regime may influence the icequake occurrence patterns and make it difficult to generalize observations to all outlet glaciers. Additionally, because seismic deployments vary widely between studies in terms of number, spacing, and placement of stations, raising the question of how much observational setup conditions impact the apparent characteristics of icequake activity.

In this chapter, we use the SEIS-ADELICE dataset, complemented by GNSS measurements of ice motion, to evaluate spatial and temporal changes in tide-induced icequake activity at the Astrolabe Glacier, first at a broad space scale and then specifically at its grounding zone. Our objectives are threefold: to document the temporal and spatial patterns of icequake activity; to compare these patterns with those reported for other outlet glaciers; and to integrate our results into a conceptual mechanical framework that accounts for the three-dimensional geometry of the glacier and the surface brittle deformation patterns at its grounding zone, in response to tides.

In the following section, I present the paper detailing the results of this analysis, published in *Journal of Geophysical Research*.

4.2 Spatial and temporal variability in tide-induced icequake activity at the Astrolabe coastal glacier, East Antarctica (Le Bris et al., 2025)

Check for updates

JGR Earth Surface

RESEARCH ARTICLE
10.1029/2024JF008054

Spatial and Temporal Variability in Tide-Induced Icequake Activity at the Astrolabe Coastal Glacier, East Antarctica

Tifenn Le Bris[1], Guilhem Barruol[1], Florent Gimbert[1], Emmanuel Le Meur[1], Dimitri Zigone[2,3], Anuar Togaibekov[1], Denis Lombardi[4], Maxime Bès de Berc[2], and Armelle Bernard[3]

[1]CNRS, University Grenoble Alpes, INRAE, IRD, Grenoble INP, IGE, Grenoble, France, [2]Université de Strasbourg/CNRS, Institut Terre et Environnement de Strasbourg, UMR7063, Strasbourg Cedex, France, [3]Université de Strasbourg/CNRS, Ecole et Observatoire des Sciences de La Terre, UAR830, Strasbourg Cedex, France, [4]SEISTREAM, Versailles, France

Key Points:

- Icequake activity over the grounding zone (GZ) is modulated by tides, with peaks either at high tides or during both rising and falling tides
- Most large-magnitude events are associated with shear margins, whereas small-magnitude events are mostly associated with the GZ
- Cryoseismicity provides insights into the 3D dynamics of the GZ system as it undergoes tide-induced flexuring

Supporting Information:

Supporting Information may be found in the online version of this article.

Correspondence to:

T. Le Bris,
tifenn.le-bris@univ-grenoble-alpes.fr

Citation:

Le Bris, T., Barruol, G., Gimbert, F., Le Meur, E., Zigone, D., Togaibekov, A., et al. (2025). Spatial and temporal variability in tide-induced icequake activity at the Astrolabe coastal Glacier, East Antarctica. *Journal of Geophysical Research: Earth Surface*, *130*, e2024JF008054. https://doi.org/10.1029/2024JF008054

Received 7 OCT 2024
Accepted 28 JUL 2025

© 2025. The Author(s).
This is an open access article under the terms of the Creative Commons Attribution-NonCommercial-NoDerivs License, which permits use and distribution in any medium, provided the original work is properly cited, the use is non-commercial and no modifications or adaptations are made.

Abstract The grounding zones (GZ) of marine-terminating glaciers, where ice transitions from grounded to floating, experience strong mechanical changes in response to ocean tides. The spatial and temporal dynamics of these changes remain poorly documented, as they require multi-scale observations capable of resolving internal ice deformation. Here, we use seismic observations, collected across different years and various scales, coupled with GNSS observations, to evaluate the brittle deformation at the GZ and shear margins of the Astrolabe Glacier (East Antarctica, Terre Adélie). Automatic detection of icequakes reveals that seismic occurrence patterns vary with tides and sensor locations. At a multi-kilometer scale, we observe and locate numbers of large-duration magnitude events (average Md around 0.0) associated with shear margins. At a smaller scale (a few hundreds of meters), using a dense array of seismic nodes deployed across the GZ and GNSS observations of vertical ice motion, we capture numerous small-magnitude events (Md as low as −4.0) with spatial and time occurrences set by tide-modulated GZ dynamics. At rising tides, seismicity is dominant on the floating part of the glacier, while at falling tides, it is dominant over its grounded part. Based on these observations, we propose a conceptual framework for the dynamics of icequake activity at the glacier GZ, accounting for its three-dimensional tidal-induced bending, generating strain rates large enough to induce brittle deformation. Our findings highlight the value of multiscale seismic observations of outlet glaciers for capturing GZ space and time high-resolution seismic and displacement responses to tidal forcing.

Plain Language Summary The Antarctic ice sheet naturally flows from its interior toward the oceans through ice shelves and/or outlet glaciers, which develop floating ice tongues at the ocean surface. As glaciers transition from grounded over the continent to floating over the ocean at their grounding zone (GZ), they are impacted by the ocean effects, such as mechanical deformation caused by tides. Here, we present the analysis of ice deformation at the GZ of the Astrolabe Glacier, in Terre Adélie, East Antarctica. This analysis is based on data recorded by seismic instruments deployed on and around the glacier, on land and at sea, from a few weeks to several years, with a particular focus on its GZ. It is complemented by GNSS-based ice motion observations. We quantify the time and space occurrence of cryoseismic activity relative to the GZ geometry and its tide-induced dynamics. We show that the ice flow is accommodated laterally by large-magnitude events along the lateral shear zones and that the tides are accommodated at the GZ by numerous small-magnitude icequakes occurring sometimes at high tides but dominantly during mid-rising and mid-falling tides, suggesting a three-dimensional bending and bulging of the floating tongue.

1. Introduction

Outlet glaciers in Antarctica and Greenland are at the forefront of global climate change (Jordan et al., 2023). Monitoring their dynamics is key for evaluating their vulnerability and stability as well as improving the accuracy of model predictions of future sea level rise. Following the IPCC reports (IPCC Report, 2022), international initiatives such as RINGS Action Group (2022) or INSTANT (https://scar.org/science/research-programmes/instant) point to the importance of better constraining the past and present geometries of ice sheets and glaciers, particularly at their continent-ocean transition (e.g., ice thickness, bedrock depth, grounding line (GL) and subglacial cavity geometry). The GL is classically defined from large-scale satellite imagery as the linear boundary between grounded and floating ice. However, at smaller scales, three-dimensional complexities in basal

21699011, 2025, 8, Downloaded from https://agupubs.onlinelibrary.wiley.com/doi/10.1029/2024JF008054 by Tifenn Le Bris - Cochrane France , Wiley Online Library on [02/09/2025]. See the Terms and Conditions (https://onlinelibrary.wiley.com/terms-and-conditions) on Wiley Online Library for rules of use; OA articles are governed by the applicable Creative Commons License

topography as well as tidal influence on ice flexure can transform this boundary into a broader area, referred to as the grounding zone (GZ) (Brunt et al., 2010; Fricker & Padman, 2006; Le Meur et al., 2014). Depending on the bedrock topography, this frontier region may be affected by the effects of sea level variations, particularly those at the diurnal scale induced by tides, generating potential landward retreats and oceanward advances. As the tide rises, water may indeed intrude beneath the floating ice and at the ice-bedrock interface, increasing buoyancy and causing the GZ to retreat landward. Conversely, as the tide falls, reduced buoyancy may lead to ice regrounding and an oceanward displacement of the GZ. This motion could affect the ice flux entering the ocean and the stability of the entire upstream basin (e.g., Pattyn, 2018; Rignot et al., 2011; Schoof, 2007). Further difficulty in apprehending the behavior of outlet glaciers resides in the multiple thermal and mechanical interactions at the different interfaces: at its basal and lateral boundaries where ice slides over the bedrock (Weertman, 1957), at its front where it faces the ocean and sea-ice (Amundson et al., 2010; Bartholomaus et al., 2015), and at the base of its floating tongue up to its GZ where it faces potential warm ocean water intrusion that triggers basal melting. The dynamics of Antarctic outlet glaciers GZ have been widely studied through remote sensing, providing a large-scale picture of ice mass displacements (Friedl et al., 2020; Rignot et al., 2011), sometimes complemented by ground GNSS measurements (King et al., 2010; Winberry et al., 2013). However, these measurements solely provide a surface-level perspective, with limited abilities to constrain processes occurring at depth, and over extended time spans (hours to days, even years), often lacking temporal continuity down to a few seconds at which processes may occur.

As a complementary approach, cryoseismology offers a valuable tool to gain insights into glacier flow and deformation within the ice column and over short spatial and temporal scales. Continuous recordings of ice-related seismic activity enable the detection and location of seismic events with spatial resolution down to a few meters and temporal variability ranging from seconds to seasons. This approach can provide a comprehensive view of the main underlying processes and external forces at play, such as tides for coastal glaciers (e.g., Aster & Winberry, 2017; Podolskiy & Walter, 2016).

Descriptions of seismic records from grounded glaciers show two dominant signals. The first group consists of icequakes generated by ice brittle deformation, which is the focus of the present study. A second group of episodic events, known to be induced by the stick-slip motion at the ice-bedrock interface (e.g., Helmstetter et al., 2015; Lucas et al., 2023; Pirli et al., 2018; Winberry et al., 2013; Zoet et al., 2012), is also present in our data set. It is characterized by much smaller amplitudes than the icequakes and will be the subject of an independent study. In comprehensive overviews, Podolskiy and Walter (2016) followed by Aster and Winberry (2017) synthesized the literature related to ice-induced seismicity and particularly the early works on the so-called "icequakes" relevant to surface brittle deformation and crevasse activity (Lewandowska & Teisseyre, 1964; Neave & Savage, 1970; Osten-Woldenburg, 1990; Röthlisberg, 1955, 1972). In recent years, subsequent research has continued to build upon these studies and gained spatial resolution by densifying seismic networks (e.g., Hammer et al., 2015; Hudson et al., 2019; Kufner et al., 2023). For instance, using a 100 seismic nodes network with a hundred-meter interstation distance, icequakes generated by the opening of crevasses have been successfully located to precisely map the crevasse field of an Alpine glacier and its dynamics (Gimbert et al., 2021; Nanni et al., 2022). Although cryoseismicity has been, in a few cases, attributed to temperature variations (e.g., Lombardi et al., 2019), most events originate from complex temporal and spatial variations in stress. These variations arise from the brittle behavior of ice in response to flexure (e.g., Hulbe et al., 2016) as well as extension and shearing regimes (e.g., Hudson et al., 2020). For coastal glaciers, the cyclic bending of the glacier floating tongue under the ocean tidal modulation has been shown to generate such intense seismic activity (Barruol et al., 2013; Cooley et al., 2019; Fromm et al., 2023; Lombardi et al., 2016).

Seismic records in GZ areas depict recurring patterns in response to tides. At the Ekström Ice Shelf, dominant local and regional icequakes were found to mainly occur during rising tides and were proposed to be associated with the opening of crevasses at the bottom of the glacier, driven by the upward bending of the floating tongue (Fromm et al., 2023; Hammer et al., 2015). Near the Roi Baudouin Ice Shelf, Lombardi et al. (2016) identified periodic seismic activity correlated with tide-induced bending, particularly during rising and high tides, that they also linked to potential basal crevassing. By contrast, a study focused on Ice Stream C from Anandakrishnan and Alley (1997), with a 6-week deployment of 3 short-period seismometers at a distance of 85 km from the GZ, revealed basal seismicity mostly activated just before the minimum tide. In the vicinity of the Mertz Glacier GZ in East Antarctica and the Bowdoin Glacier in West Greenland, Barruol et al. (2013) and Podolskiy et al. (2016) highlighted icequake seismicity to have a clear tidal modulation with a dominant peak of seismic activity at falling

21699011, 2025, 8, Downloaded from https://agupubs.onlinelibrary.wiley.com/doi/10.1029/2024JF008054 by Tifenn Le Bris - Cochrane France , Wiley Online Library on [02/09/2025]. See the Terms and Conditions (https://onlinelibrary.wiley.com/terms-and-conditions) on Wiley Online Library for rules of use; OA articles are governed by the applicable Creative Commons License

tide, that is, during the downward bending of the glacier floating tongue and a weaker activity during tide rising phases. In addition to the double-peak diurnal oscillation, Podolskiy et al. (2016) also found an increase in seismicity associated with the horizontal acceleration of the glacier at falling tide, interpreted as its longitudinal stretching. Minowa et al. (2019) suggested that the extension movement associated with the bending during falling tide could generate crevasse opening at the surface, leading to higher icequake activity. There is no consensus on whether this bending generates seismic energy mainly during rising and/or falling tides, and whether it results from basal or surface crevassing or both. This raises the question of the seismic regime in response to the glacier tide-induced bending, and the role of the glacier geometry in determining the seismic activity pattern. Additionally, the relative importance of the various mechanisms occurring at different places of the glacier remains uncertain, including lateral shear zone events or surface extensional or compressional events caused by the glacier horizontal motion.

In order to address these questions, the present study analyzes the cryoseismic activity of the Astrolabe Glacier in Terre Adélie, East Antarctica, with a focus on icequake events, by combining large and small spatial scales, as well as long and short-term temporal seismic network deployments. This strategy allows us to investigate the distribution of events by magnitude and location, and to understand how these are influenced by the instrumental setup, the 3D geometry of the glacier GZ and of its lateral shear zones.

2. Data and Methods

2.1. Study Site

The Astrolabe Glacier (66°41′S, 140°05′E) is located in Terre Adélie, East Antarctica, near the Dumont d'Urville (DDU) French polar base (Figure 1). The floating tongue of this outlet glacier is approximately 4 km wide and 10 km long and is fed by a basin extending more than 200 km into the continent (Mouginot et al., 2014). In the studied area, the ice flows at a rate of up to 500 m/year (Le Meur et al., 2014; Provost et al., 2024). Compared to its eastward neighbors Cook and Mertz glaciers, the catchment area of the Astrolabe Glacier is relatively small (~1,500 km^2 against 307,741 km^2 for the Cook basin and 84,543 km^2 for the Mertz basin, see Rignot et al. (2013)). Its small size and easy access from the nearby DDU station provide a unique opportunity to cover the entire system from its grounded zone to its ocean terminus with a limited number of instruments that can be deployed with reasonable logistical support.

The floating part of the Astrolabe glacier is laterally constrained within a fjord with valley walls 500–600 m deep and covered by slow-moving grounded ice, as imaged by radar surveys on the glacier (Le Meur et al., 2014). These features create strong shear zones on both sides of the glacier, accommodating the relative displacement between the glacier, the bedrock, and the surrounding slow-moving ice, as evidenced by satellite imagery (e.g., Provost et al., 2024) and illustrated on the ice velocity map presented in Figure 1c. The floating tongue thickness is estimated to be around 600 m at the GZ, progressively thinning to about 300 m at its terminus on the ocean (Le Meur et al., 2014). In front of the terminus, sparse bathymetric surveys offshore (Beaman et al., 2011) show that the fjord bathymetry extends deeper than 1,000 m, suggesting a large subglacial cavity beneath the floating ice tongue prone to ocean intrusion and ice basal melting. The glacier front is directly exposed to ocean swells (when there is no sea ice in summer), storms and tides.

2.2. Seismological Deployments

With support from the French Polar Institute, we deployed from 2020 to 2025 several networks of seismometers on and around the glacier, on land and at sea, including ocean-bottom seismometers (OBS) (Figure 1 and Table S1 in Supporting Information S1 for details). Starting in 2020, broadband stations were deployed during several years around the glacier on slow-moving grounded ice and on rocky outcrops. For these stations, the sampling rate was set to 100 Hz.

We also use the broadband permanent Geoscope station DRV at the DDU base, operational since 1986 (Institut de physique du globe de Paris & Ecole et Observatoire des Sciences de la Terre de Strasbourg, 1982; Leroy et al., 2023) and sampling data at 20 Hz frequency since 1999, allowing long-term seismological investigation over several decades (Grob et al., 2011; Stutzmann et al., 2009).

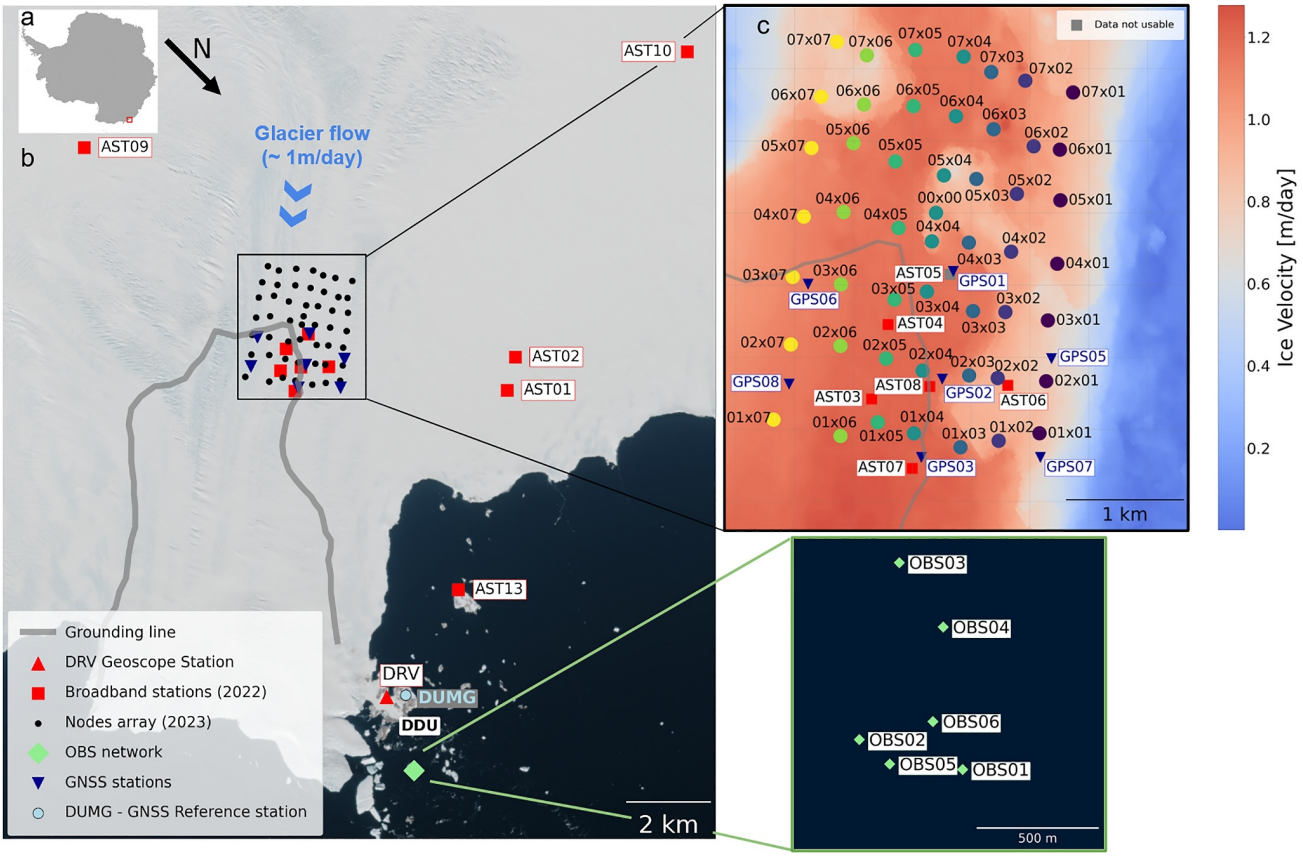

Figure 1. Map of the deployments on and around the Astrolabe glacier. (a) Study site location in East Antarctica. (b) Astrolabe glacier with locations of the seismic and GNSS permanent stations (symbols explained in the insert) in the neighborhood of the Dumont d'Urville (DDU) French Polar base. Satellite background image is from Sentinel 2. Gray line represents the grounding line inferred from geodetic GNSS analyzes from Le Meur et al. (2014). (c) Zoom on the instrumented grounding zone area of the glacier with location of the GNSS permanent stations (blue triangles), the broadband seismic network deployed for 3 weeks in January 2022 (red squares) and the seismic nodes deployed for 2 weeks in January 2023 (colored dots). Each NE–SW line is color-coded for reference in Figure 7. Background satellite-derived ice velocity map is extracted from Provost et al. (2024). (d) Zoom on the coastal area where ocean-bottom seismometers (OBSs) have been deployed in 2022–2023. See technical details on instrument deployment in Table S1 in Supporting Information S1.

In January 2022, a temporary network of 6 broadband seismometers was deployed for 3 weeks in the GZ area of the glacier (Figure 1), all recording at 200 Hz. Due to melt-induced sensor tilting, data from AST05 were unusable.

Simultaneously, four short period (4.5 Hz geophone) and two intermediate-band [0.1–100] Hz Ocean Bottom Seismometers (OBSs) were deployed in front of the glacier terminus for 2–3 weeks in January 2022. Two of these were redeployed in early February 2022 for a full year, including a wintering under the sea ice.

In January 2023, in order to enhance event detection and structural imaging, we deployed a network of 50 three-component seismic node sensors over the GZ (Figure 1). Spaced 300–400 m apart, the seismic nodes covered ~2 × 2 km^2 and recorded continuously at 500 Hz for about two weeks. Seismic nodes were placed in an approximately ~50 cm deep hole in the ice, oriented to geographic north using solar shadow casting from a vertical rod (i.e., the gnomon method), and then covered with snow debris that tended to freeze again. In the present paper, data analysis focuses on the period January 17–24, 2023, after which stormy weather considerably decreased the data quality.

2.3. GNSS Deployments

Ground-based GNSS measurements completed the observation system. We used multifrequency Trimble NetR9 receivers and Trimble Zephyr Geodetic antennas to collect ice motion at 7 sites (Figure 1). Each GNSS antenna

21699011, 2025, 8, Downloaded from https://agupubs.onlinelibrary.wiley.com/doi/10.1029/2024JF008054 by Tifenn Le Bris - Cochrane France , Wiley Online Library on [02/09/2025]. See the Terms and Conditions (https://onlinelibrary.wiley.com/terms-and-conditions) on Wiley Online Library for rules of use; OA articles are governed by the applicable Creative Commons License

21699011, 2025, 8, Downloaded from https://agupubs.onlinelibrary.wiley.com/doi/10.1029/2024JF008054 by Tifenn Le Bris - Cochrane France , Wiley Online Library on [02/09/2025]. See the Terms and Conditions (https://onlinelibrary.wiley.com/terms-and-conditions) on Wiley Online Library for rules of use; OA articles are governed by the applicable Creative Commons License

was mounted on a beacon drilled several meters into the ice. We processed GNSS phase observables, sampled at 30 s intervals, in kinematic mode using the TRACK software (Chen, 1999; Herring et al., 2018). The position of the survey sites on the glacier was determined with respect to the reference station DUMG, located at the Dumont d'Urville (DDU) base (Figure 1). We used the ionosphere-free linear combination of GPS phase observables and applied a double-difference technique, which effectively eliminates phase biases caused by ionospheric delay and drifts in satellite and receiver clock oscillators (Bock et al., 1986). We used multiple GNSS constellations (GPS, GLONASS, and Galileo) with lower tolerance to discard noisy observables, which better resolves ambiguities to integer values, crucial for accurate phase estimations. The most conservative uncertainties associated with position estimates at each epoch are approximately ±10 mm in the horizontal direction and ±20 mm in the vertical direction. We applied a Gaussian low-pass filter with a 6-hr moving kernel to attenuate high-frequency noise in kinematic position estimates while preserving short-term physical signals (Andrews et al., 2014; Bartholomew et al., 2012). Horizontal velocities (u_H) are calculated by differencing positions at each 30-s epoch, applied across the entire time series of filtered positions. Vertical velocities (u_Z) are also calculated from the filtered position time series, with the linear trend removed to focus on short-term variability rather than long-term seasonal trends. In addition to characterize individual GNSS station displacement, we also evaluate glacier deformation between two neighboring stations by computing the vertical shear strain rate (ϵ_Z) and the horizontal longitudinal strain rate (ϵ_H) as:

$$\epsilon_Z = \left(u_{z,s1} - u_{z,s2}\right)/d_{s1,s2} \quad (1)$$

$$\epsilon_H = \left(u_{H,s1} - u_{H,s2}\right)/d_{s1,s2} \quad (2)$$

with $d_{s1,s2}$ the distance between the two stations s1 and s2.

2.4. Tide Data

Sea-level height used in the present work is measured using the PM36S MarArgos automatic tide gauge called DUMON installed at the DDU base (NIVMER/ROSAME project, Calzas et al., 1992). The sampling interval is 2 min. Data are transmitted in real time via Argos. To extract phases and amplitudes of the tidal components, and to compare seismic activity with tidal dynamics, we performed frequency spectral harmonic analysis of the signal using the T-Tide software package (Pawlowicz et al., 2002).

2.5. Icequake Detection

We identify icequakes within continuous seismic records and analyze their occurrence using a systematic event triggering algorithm based on the STA/LTA (short-term average/long-term average) method (Allen, 1978; Lesage, 2009), which is well adapted for detecting impulsive events. Figure 2a presents a representative 8-min seismic recording from the AST08 broadband station located over the Astrolabe GZ, highlighting the detected icequakes. Among the diverse signals, icequakes are easily identifiable by their impulsive arrivals and the lack of a clear distinction between seismic phases. We use the following parameters: STA is set to 0.5 s, LTA to 5 s, and trigger threshold on and off to 5 and 2, respectively. These values were determined by minimizing missed events and false detections based on visual comparisons between detections and phase arrivals observed in the waveforms (1 hr of record screened per day). Due to their much lower amplitudes, stick-slip events (not visible at this scale) are not detected by this algorithm using the selected parameters. To determine the frequency band where most icequake energy is concentrated, we compute spectrograms using the Logarithmic Power Spectral Density method on the vertical (Z) component. All spectrograms are generated using Welch's method applied on 10-s segments and averaged over 10-min windows spanning 1–100 Hz. The mean power is converted to decibels. Spectrograms such as the one presented in Figure 2b show that icequakes have a broad energy content over the whole spectrum, starting at 5 Hz for the low frequencies and up to at least 50–100 Hz, this upper corner being limited by the instruments sampling rates. We therefore apply a bandpass filter between 5 and 40 Hz before performing the icequake detections, adapted to all our instruments. Figures 2c and 2d respectively present an example of the trigger on and trigger off thresholds over a single event and its corresponding STA/LTA ratio curves, respectively. In our analysis, events with durations smaller than 0.4 s are set aside as they are underrepresented and might originate from false detections.

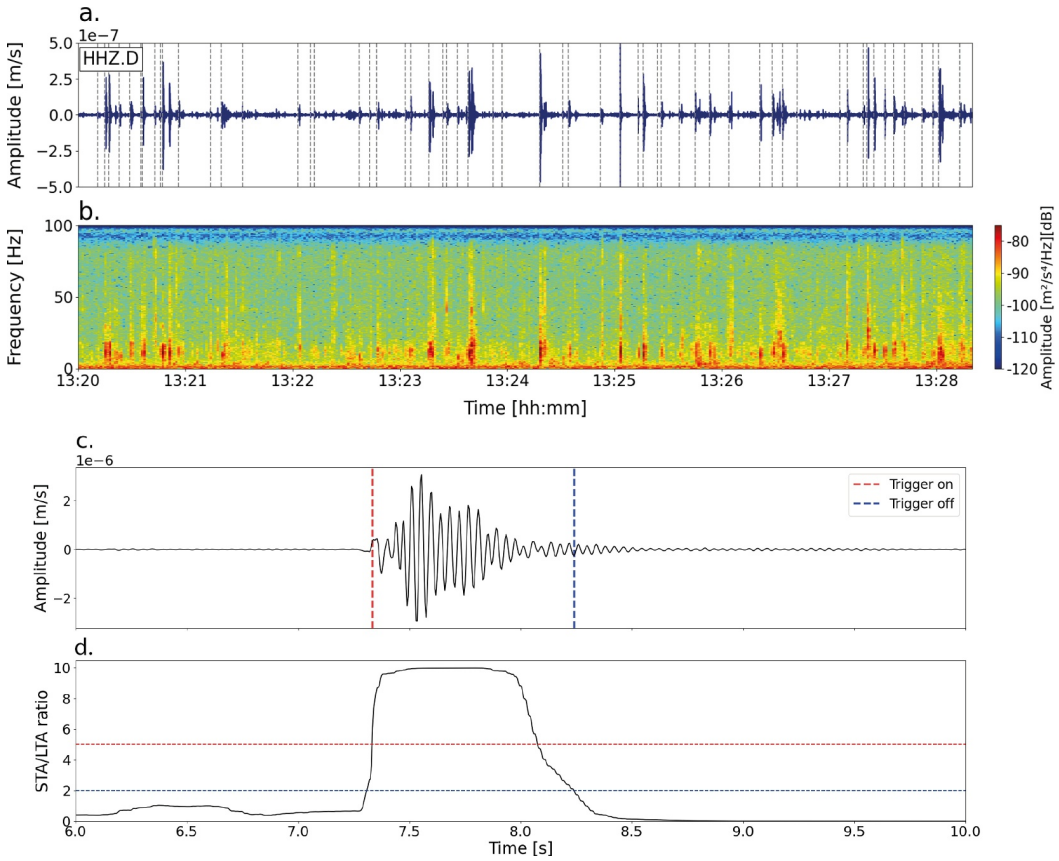

Figure 2. Seismic waveforms and icequake detection. (a) Seismic waveform and (b) spectrogram of an eight-minutes recording on the Z component of station AST08, located on the grounding zone of the Astrolabe glacier (Figure 1), on 20 Jan. 2022. The data, sampled at 200 Hz, are bandpass filtered between 5 and 100 Hz. Seismic event detections using the STA/LTA algorithm are marked in (a) by timestamps (gray dotted lines). (c) Zoom over 8 s of records (vertical, HHZ component) showing a single detection with the trigger on (red) and off (blue) timestamps. (d) Corresponding STA/LTA amplitude ratio curve with the amplitude ratio trigger on (red) and trigger off (blue) thresholds.

Despite the limitations inherent to the method (i.e., false detections, missing events), we expect some consistency in the error rates for each station, ensuring a rather robust relative comparison between them. Systematic detections performed at each station display a significant number of events with considerable hourly variability (typically ranging between few tenths and 500 events/hour). From the catalogs of detections obtained for each station, we compute a time series of icequake occurrences on an hourly basis, which is long enough to gather sufficient statistics, while short enough to investigate diurnal modulation.

The systematic use of the STA/LTA detection algorithm also provides an event duration for each detected icequake (Figure 2c). From this measured duration, we attribute an event magnitude of duration (Md) using the empirical relationship expressed as $\mathrm{Md} = -0.9 + 2\log(d)$ with d the event duration (Lee et al., 1972). While this empirical relationship is commonly used in earthquake studies, we acknowledge limitations in our present situation, mainly due to difficulties in precisely identifying event start and end times (due to the unclear phase arrivals in the waveform of icequakes) but also due to icequakes not necessarily obeying laws similar to that of earthquakes. The duration magnitudes thus should not be interpreted in an absolute sense but rather as a proxy for relative comparison between events.

2.6. Icequakes Locations Using the Seismic Node Array

To evaluate icequake locations, we use a dense seismic array and adopt two distinct strategies. For the large-magnitude events which generate a coherent wave field across the whole seismic node array, we apply Match Field Processing (MFP) as described and detailed in other studies (Chmiel et al., 2019; Gimbert et al., 2021; Nanni

21699011, 2025, 8, Downloaded from https://agupubs.onlinelibrary.wiley.com/doi/10.1029/2024JF008054 by Tifenn Le Bris - Cochrane France , Wiley Online Library on [02/09/2025]. See the Terms and Conditions (https://onlinelibrary.wiley.com/terms-and-conditions) on Wiley Online Library for rules of use; OA articles are governed by the applicable Creative Commons License

21699011, 2025, 8, Downloaded from https://agupubs.onlinelibrary.wiley.com/doi/10.1029/2024JF008054 by Tifenn Le Bris - Cochrane France , Wiley Online Library on [02/09/2025]. See the Terms and Conditions (https://onlinelibrary.wiley.com/terms-and-conditions) on Wiley Online Library for rules of use; OA articles are governed by the applicable Creative Commons License

et al., 2022). This method recursively matches the observed seismic wavefield phase delays with a modeled one using a point-like source and a frequency domain Green's function, which depends on four parameters: the source spatial coordinates (x, *y*, z) and the medium homogeneous phase velocity (c). The frequency range where MFP can be applied is conditioned by subwavelength spatial sampling, which, for an average sensor spacing of around 350 m and surface wave velocities on the order of 1,600 m/s (Gimbert et al., 2021), corresponds to an upper limit frequency of about 3 Hz. Since signals below 1 Hz may be contaminated by the ocean-induced secondary microseisms, which are not of our interest here, we apply the MFP in the [1–3] Hz frequency band. In this frequency band, only the largest icequakes are observed, where seismic waves are not significantly attenuated across the 3-km scale of the seismic array, such that spatial seismic waveform coherency is preserved. For each time window fixed to 2 s to approximate the seismic wave travel time across the whole array, the best source likelihood is determined by minimizing the relative difference between observed and modeled phase delays. Instead of using a computationally expensive multi-dimensional grid search, we employ a minimization algorithm based on the downhill simplex method (Nelder-Mead optimization) as described by Nelder and Mead (1965) and Lagarias et al. (1998). To maximize the likelihood of identifying dominant sources within the 2-s time windows, we initiate the algorithm from 13 different starting points distributed over a $1{,}500 \times 1{,}500\ m^2$ area centered on the node array, reducing the azimuthal bias. All localizations from these 13 minimizations are evaluated based on their associated MFP output values. Values range from 0 to 1, with values closer to one indicating a better match and greater confidence in the source location. For instance, a value of 0.7 means that 70% of the observed phase field is explained by the prediction given by the inferred source location and wave speed. The algorithm is allowed to detect multiple sources within the same time window; selecting those with MFP outputs above 0.2 ensures meaningful source localization. The horizontal precision of source localization is typically on the order of $\lambda/6$ to $\lambda/18$, where λ is the wavelength of the dominant seismic signal (Nanni et al., 2022). This means that for the typical frequency of 3 Hz and velocity 1,600 m/s considered here, MFP localization uncertainties are on the order of a few tens of meters. Regarding the depth, it is not as precisely constrained due to (a) depth-vs-velocity ambiguity and (b) the large spreading of the surface wave sensitivity kernel with depth (Gimbert et al., 2021).

For the numerous small-magnitude events, which have a frequency content above 5 Hz and do not generate coherent waves across the entire array, MFP cannot be applied. Instead of locating individual seismic events, we use a statistical approach to geographically investigate source activity. We first compare the average icequake occurrence, in event count per hour, across seismic nodes to analyze the spatial distribution of icequake activity. Second, we assess the number of seismic nodes detecting each event to infer event size and its spatial distribution. Third, we investigate the event time occurrence relative to tides to precisely determine the temporal distribution of events.

3. Results

3.1. Long-Term Tide-Modulated Seismicity at Sites Remote From the Grounding Zone

We first characterize the relationship between icequake activity and ocean tides using the example of data from two stations located at a large distance from the GZ (>10 km), on a rocky outcrop (DRV) and on the ocean bottom (OBS06) and running over the course of the year 2022. The 3 months event detection on the DRV 20 Hz vertical data channel (Figure 3a) shows a clear modulation in icequake hourly occurrence across successive spring and neap tide cycles, exhibiting event counts ranging from 10 to over 200 events per hour. Zooming in on a shorter time scale, we observe double peaks for diurnal cycles aligned with rising and falling tides (Figure 3a). During periods with high tide amplitude, we often observe a stronger activity during the falling tide phase (from June 26 to July 2 and from 10 July 2022 to 14 July 2022 on zoom Figure 3a). Although this pattern is recurring across consecutive tide cycles, it does not consistently appear throughout the entire analyzed time series. At station OBS06, deployed at sea close to the glacier front, we also observe a clear correlation of the icequake occurrence with the tidal amplitudes across spring tide cycles (Figure 3b). It showcases an increase in icequake activity during high tide. On average, the rate of icequake occurrence surpasses that observed at the DRV station, varying between 100 and 400 events per hour. Additionally, we identify distinct double peaks of seismicity during diurnal cycles, also aligning with rising and falling tides (zoom Figure 3b). The two peaks of seismicity mainly exhibit similar amplitudes, but punctually, we find a slightly higher activity during the falling tide, with around 50 to 100 more events per hour. While the OBS06 station displays overall similar seismic patterns as DRV during spring tide cycles, we observe some peaks of seismicity during neap tides that are unlikely related to tide amplitudes. This could be explained either by different local ground coupling or by the local sea-ice or iceberg activities.

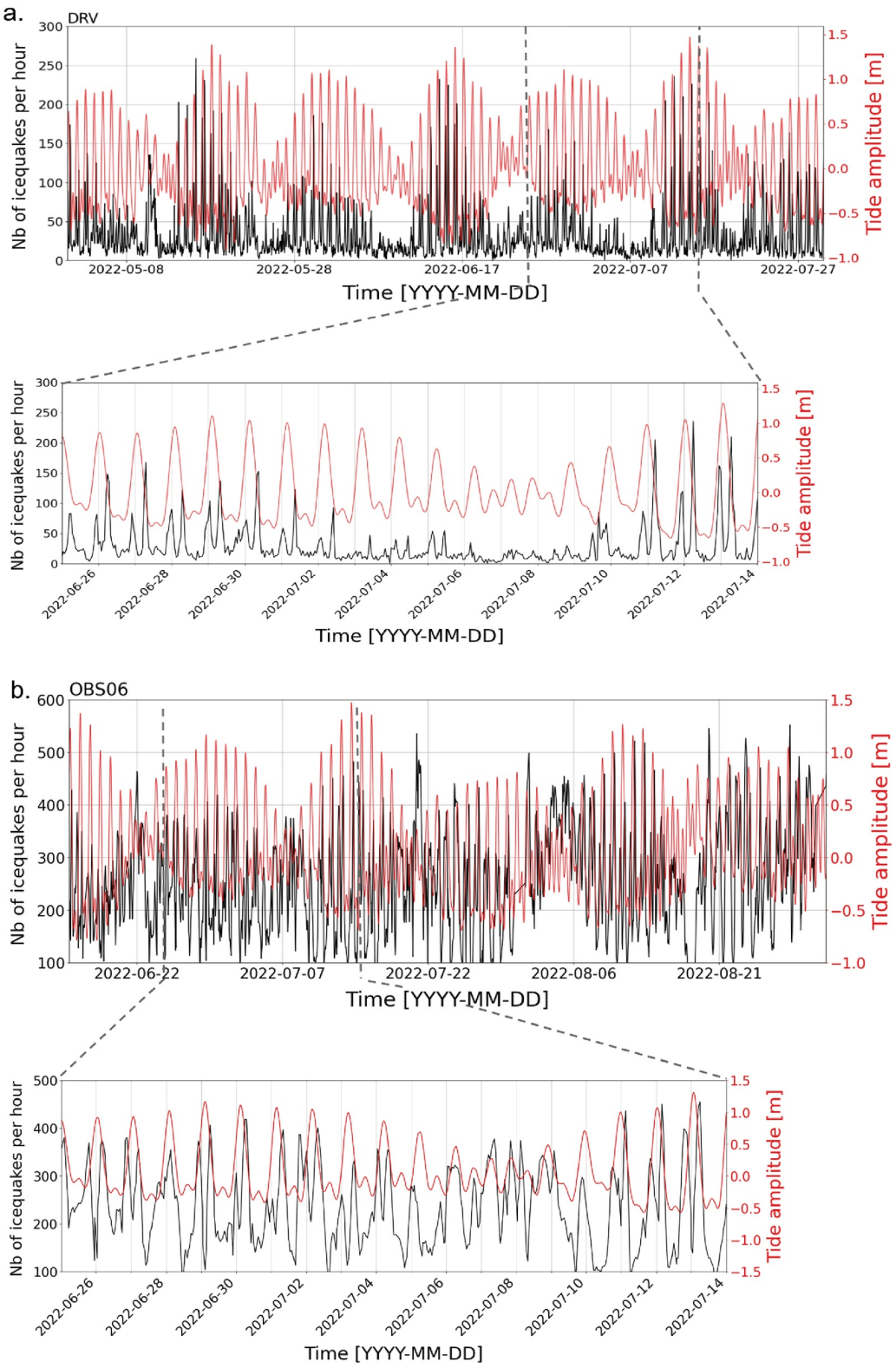

Figure 3. Examples of icequake occurrence (black curves, number of icequakes per hour) compared to the local tide amplitudes measured at the DUMON tide gauge at the Dumont d'Urville (DDU) base station (red curves, tide amplitude in meters). (a) Top: icequake seismic detection at station DRV over 3 months (May-July 2022). Bottom: same time series zoomed in on the period from June 25 to 14 July 2022. (b) Top: Icequakes detection at ocean bottom seismometer OBS06 deployed on the seafloor near the glacier terminus over the period June–August 2022. Bottom: Zoomed-in view of OBS06 for the same period as DRV from June 25 to 14 July 2022.

21699011, 2025, 8, Downloaded from https://agupubs.onlinelibrary.wiley.com/doi/10.1029/2024JF008054 by Tifenn Le Bris - Cochrane France , Wiley Online Library on [02/09/2025]. See the Terms and Conditions (https://onlinelibrary.wiley.com/terms-and-conditions) on Wiley Online Library for rules of use; OA articles are governed by the applicable Creative Commons License

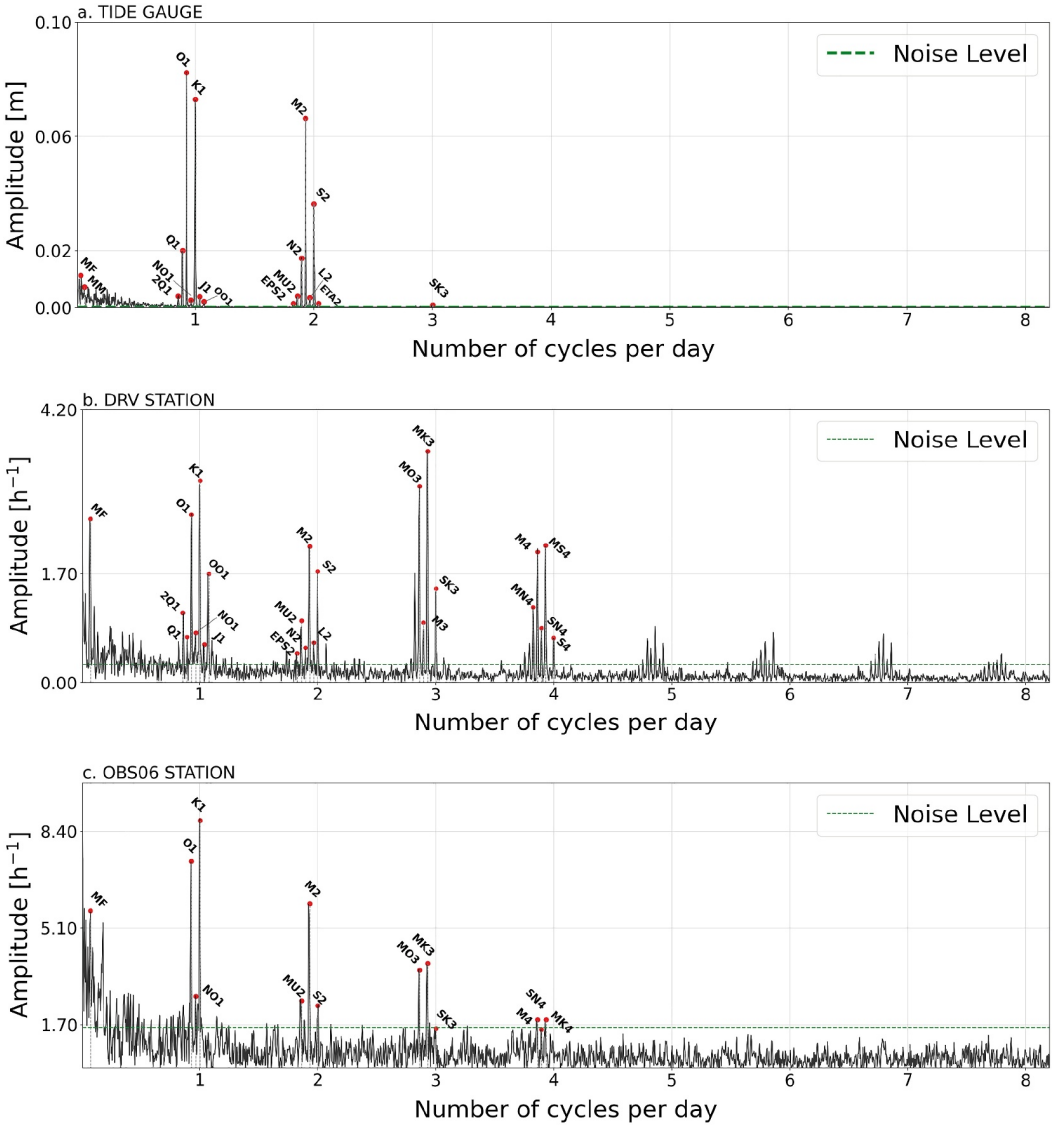

Figure 4. Tides and cryoseismic spectra. (a) Fast Fourier Transform (FFT) of the tide amplitude measured at the DUMON tide gauge installed at the Dumont d'Urville base station. (b) FFT of the icequake hourly occurrence at the Geoscope DRV seismological station (over 9 months). (c) FFT of the icequake hourly occurrence at the ocean bottom station OBS06 (over 9 months). Seismic frequency peaks are well correlated with tide harmonics as calculated from the T-Tide software package (Pawlowicz et al., 2002) (see Table S2 in Supporting Information S1 for tidal components output). The identified tidal components indicated by red dots include: Fortnightly (MSF), diurnal (2Q1, Q1, O1, NO1, K1, J1, OO1), semidiurnal (EPS2, MU2, N2, M2, L2, S2, ETA2), terdiurnal (MO3, M3, MK3, SK3) and quarterdiurnal (MN4, M4, SN4, MS4, MK4, S4, SK4) cycles. The horizontal green dotted line represents the noise level, defined as 3 times the median FFT amplitude. Only peaks exceeding this threshold are considered significant.

We perform a Fast Fourier Transform (FFT) spectral analysis on the hourly icequake occurrence time series and compare it with tidal harmonics issued from tide gauge data (Figure 4). The time series, of same duration (i.e., 9 months), allow to compare spectral amplitudes and are long enough to properly resolve periods of up to 1 month. Tide gauge measurements mostly show diurnal and semidiurnal tidal cycles, with smaller amplitude peaks for monthly, fortnightly (every 2 weeks) and terdiurnal (3 times per day) cycles (Figure 4a). These cycles stand out very clearly for the FFT spectra of DRV and OBS06 icequake activities (Figures 4b and 4c). OBS06 frequency peak amplitudes are twice as strong as those at DRV, and the noise level is also higher. This difference with DRV may be due to either OBS06 proximity to the glacier terminus and the local submarine conditions, respectively, increasing both seismic activity and noise or to the lower sampling rate at DRV that may reduce its capacity in

21699011, 2025, 8, Downloaded from https://agupubs.onlinelibrary.wiley.com/doi/10.1029/2024JF008054 by Tifenn Le Bris - Cochrane France , Wiley Online Library on [02/09/2025]. See the Terms and Conditions (https://onlinelibrary.wiley.com/terms-and-conditions) on Wiley Online Library for rules of use; OA articles are governed by the applicable Creative Commons License

21699011, 2025, 8, Downloaded from https://agupubs.onlinelibrary.wiley.com/doi/10.1029/2024JF008054 by Tifenn Le Bris - Cochrane France , Wiley Online Library on [02/09/2025]. See the Terms and Conditions (https://onlinelibrary.wiley.com/terms-and-conditions) on Wiley Online Library for rules of use; OA articles are governed by the applicable Creative Commons License

detecting high frequency events. The monthly and fortnightly, as well as diurnal and semidiurnal, tidal modulations of the cryoseismicity are well-documented in several studies focused on ice displacement and icequake activity (Aðalgeirsdóttir et al., 2008; Barruol et al., 2013; Bindschadler et al., 2003; Fromm et al., 2023; Gudmundsson, 2007; Minowa et al., 2019; Murray et al., 2007), reflecting that ice deformation at the GZ is controlled by glacier displacement and tidal amplitudes. Sensitivity to higher tidal cycle frequencies (3 and 4 cycles per day–cpd for both seismic stations and up to 8 cpd for DRV) have also been observed in other seismic or GNSS data sets (Barruol et al., 2013; Fromm et al., 2023; Minowa et al., 2019). While the 4 cpd peak can be explained by the double seismicity peak at mid-rising and mid-falling tides, the terdiurnal peak at 3 cpd and higher frequency peaks remain open to interpretation. They could reflect tidal overharmonics (generated by non-linear interactions of the main tidal harmonics as a result of ice/ocean interactions) as proposed by Fromm et al. (2023) or alternatively result from anelastic processes at the GZ as suggested by Pedley et al. (1986).

3.2. Tide-Modulated Seismicity on and Around the Glacier

3.2.1. Tidal Modulation of Icequake Occurrence

While long-term seismic records (Figure 3) from sites at a large distance from the GZ exhibit icequake occurrences generally correlated with tides (Figure 4), we observe variability in the phasing between tides and icequake peak occurrence (Figure 5) between stations located on and around the glacier. For instance, at station AST03 (Figure 5a) located over the GZ, we detect a large number of events (up to 450 events per hour) clearly modulated by the tides with peak seismicity mostly occurring at highest tide amplitude, such as before 21 Jan. 2022. We can occasionally observe double peaks of seismicity (well visible after 27 Jan. 2022 for AST03 in Figure 5a) that match double peaks in absolute tide vertical velocity (calculated as the norm of the time derivative of sea surface height). For the OBSs at sea such as OBS01 presented in Figure 5c, at larger distances from the GZ, we mainly observe double peaks of seismicity, well visible on the three first days of the example. It is also happening when the tide vertical velocity is the highest (mid-rising and mid-falling tide), and is visible as well in Figure 3b for OBS06. Icequake activity follows a different pattern for stations AST02 (Figure 5b), AST09 (Figure S5 in Supporting Information S1) and AST01 (Figure S1 in Supporting Information S1), all located on the slow-moving grounded ice (see Figure 1). At these locations, we detect only a small number of events (generally less than 100 events per hour) with no correlation with the ocean tides. This suggests that dominant tide-modulated seismicity occurs locally near the GZ and along the lateral boundary of the glacier (well visible for instance at DRV and at the OBSs) but is of sufficiently low magnitude to not be detected at larger distances.

Seismic power on spectrograms from stations located over the GZ (e.g., AST03, Figure 5a) exhibits similar variations with tides, with peaks during both rising and falling tides. The tidally modulated increase of energy is particularly strong between 10 and 20 Hz, matching with the frequency band where icequake energy is most prominent (Figure 2b). At station AST02 installed on the slow-moving grounded ice, the spectrogram also shows daily seismic power modulation (Figure 5b), which is likely dominated by the wind daily variation and not by the icequake activity, which is found to be very low in this area (Figure 5b, top panel). The spectrogram from the OBS01 (Figure 5c) shows strong seismic power levels above 20 Hz during high tide, especially between the 16th and 22nd of January.

Distinct temporality in seismicity across seismic stations also reflect distinct event magnitude distributions (see few selected stations in Figure 6), among which two distinct regimes emerge. Stations on the glacier (e.g., AST03, AST08) and near the glacier terminus (e.g., OBS01) exhibit similar icequake duration and magnitude distributions. Duration completeness typically ranges between 0.5 and 0.7 s (corresponding magnitude completeness between -1.5 and -1.2) consistent with observations of Barruol et al. (2013) and Podolskiy et al. (2016). Stations located outside the glacier catchment area or at a larger distance from its GZ (e.g., AST02, DRV) display a notably different distribution, characterized by a completeness shifted toward longer durations, around 1.0 s (magnitude of completeness around -0.9). The strong deficit in short-duration/small-magnitude events indicates that these sites do not record the icequake activity coming from the GZ, which is dominated by much smaller magnitude events ($Md < -1.0$).

3.2.2. MFP-Based Seismic Source Locations for Large-Magnitude Events

We locate large-magnitude, lower-frequency icequakes by applying the MFP method described in Section 2.6 on the 2023 dense array of 50 seismic nodes (Figure 1c). We locate 2534 events, in the 16 km^2 area around the dense

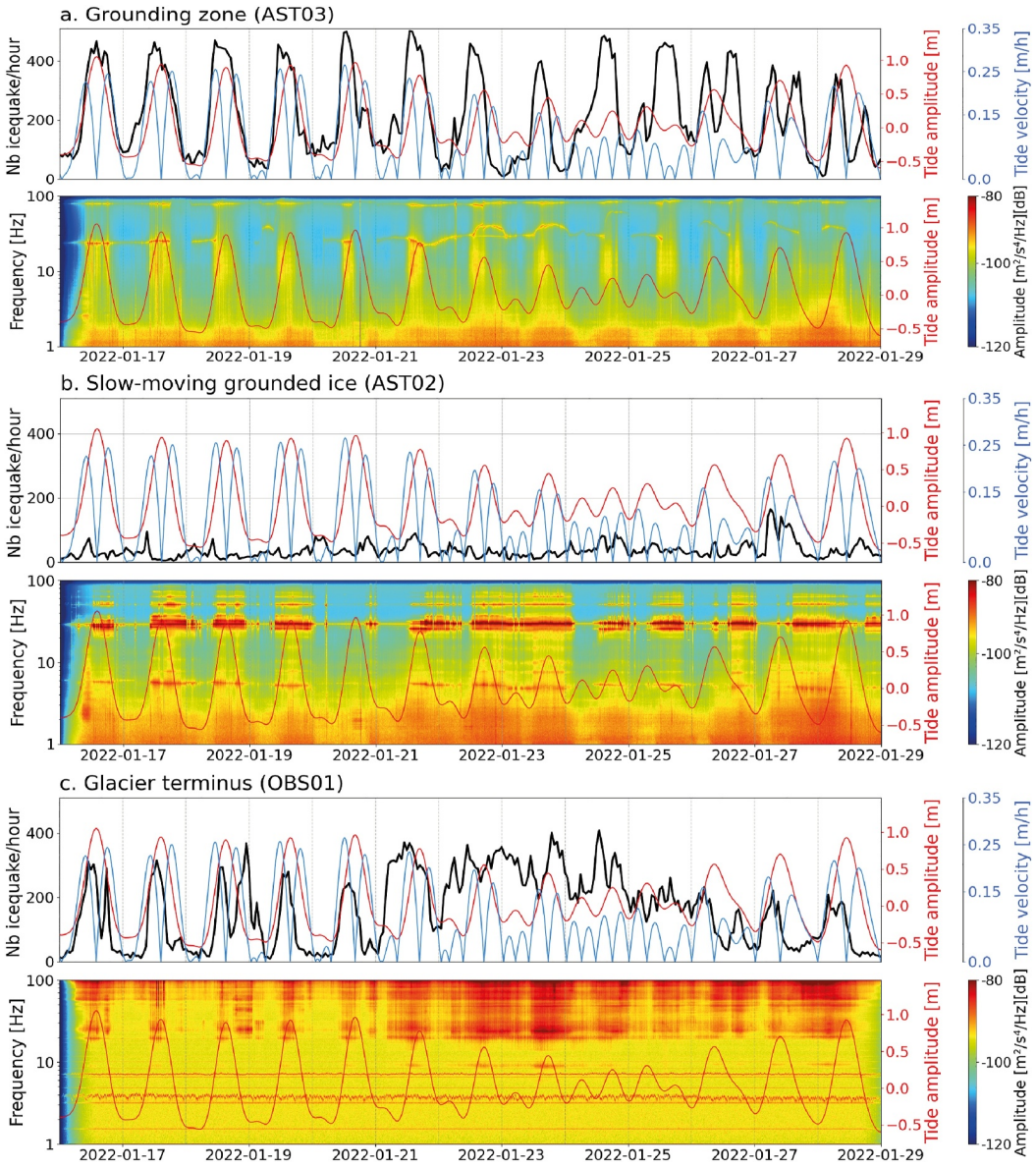

Figure 5. Tide amplitudes, tide vertical velocity, icequake hourly occurrence and spectral energy at few examples of terrestrial and ocean bottom seismic stations for the period January 16 to 29, 2022. Top three plots: Number of detected seismic events (black curve) per hour compared with tide amplitude measured at sea by the DUMON local tide gauge (red curve) and tide vertical velocity (blue curve) computed as the derivative of the tide amplitude for (a) broadband seismic stations AST03 on floating ice, (b) AST02 on slow-moving grounded ice and (c) OBS01 on the seafloor near the glacier terminus. Bottom plots: Spectrograms of seismic energy alongside tide amplitude (red curves) for the same seismic stations. For broadband stations, the instrumental response is removed. This correction is not yet available for the ocean-bottom seismometers station and affects only the absolute value of the recorded energy amplitude but not its relative variations. The distinct monochromatic spectral lines at ~30 Hz and higher frequencies at AST02 are likely caused by wind-induced vibrations affecting the cables holding the station solar panels.

array, over the selected period 17 Jan 2023 to 24 Jan 2023 (Figure 7). We find that events have Md averaging 0.3, well above the Md of completeness of small seismicity over the GZ (i.e., stations AST03 and AST08, Figure 6). They are dominantly clustered along the two lateral shear margins. These shear margins are visible in the ice velocity map in Figure 1c and their existence is hinted at by surface crevasses in these areas of the glacier (well visible from satellite imagery and during fieldwork deployments). Some of these large-magnitude events are also located in the floating part of the node array. We find in particular evidence of a population of deeper events

21699011, 2025, 8, Downloaded from https://agupubs.onlinelibrary.wiley.com/doi/10.1029/2024JF008054 by Tifenn Le Bris - Cochrane France , Wiley Online Library on [02/09/2025]. See the Terms and Conditions (https://onlinelibrary.wiley.com/terms-and-conditions) on Wiley Online Library for rules of use; OA articles are governed by the applicable Creative Commons License

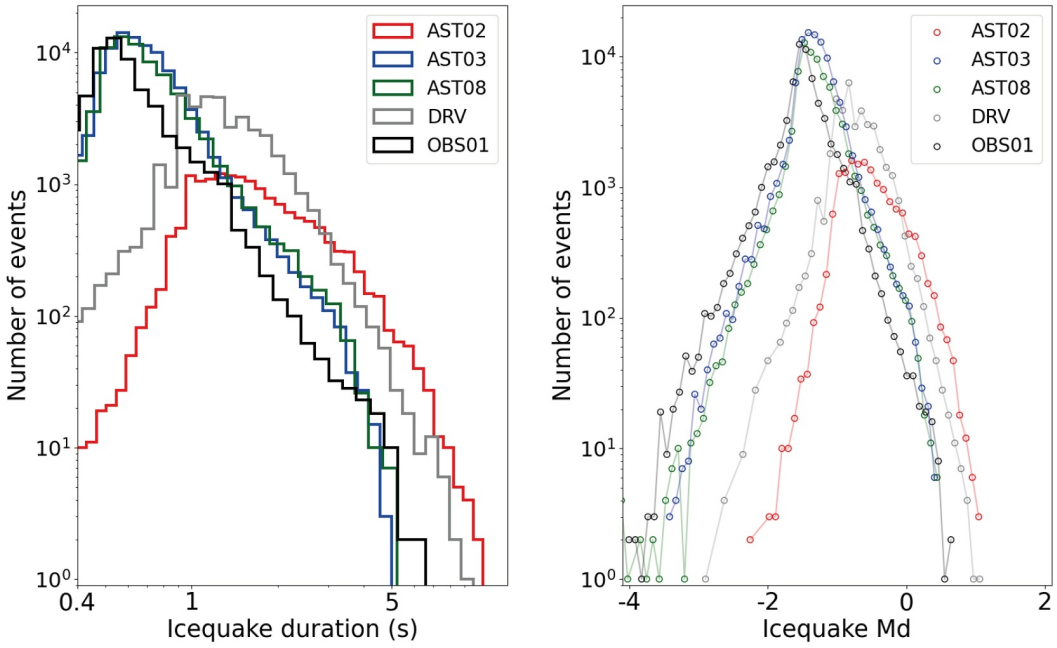

Figure 6. Icequake duration (left) and magnitude distribution (right) for stations AST02 (red), AST03 (blue), AST08 (green), DRV (gray) and OBS01 (black). *X*-axis and *y*-axis are in logarithmic scale.

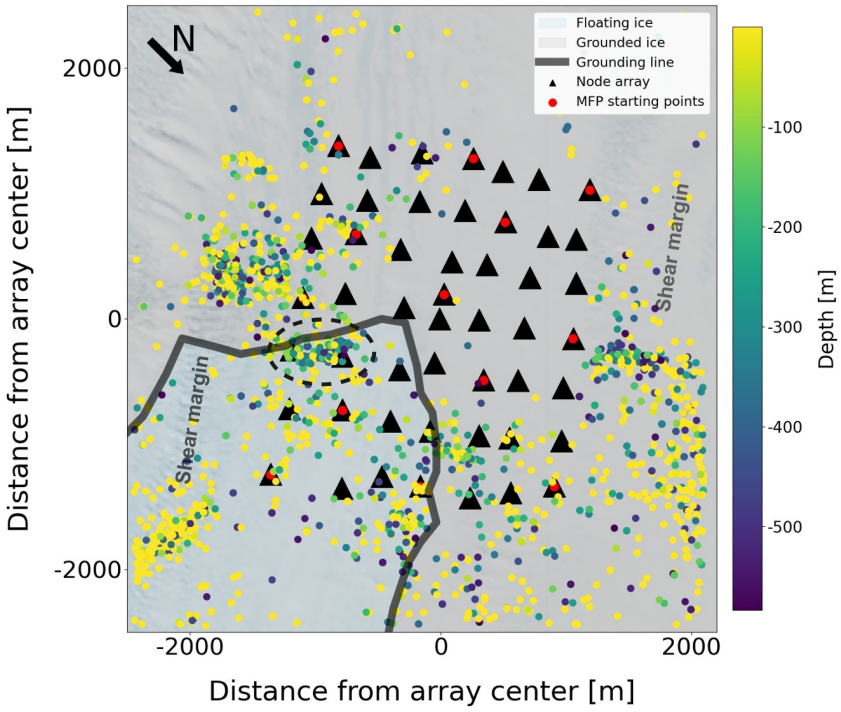

Figure 7. Map of the large-magnitude seismic sources located using Match Field Processing (MFP) analysis applied to the seismic node array. Black triangles mark the positions of the seismic nodes, while red dots represent the starting points for the MFP computations (see method). The continuous gray line represents the grounding line (GL) inferred from GNSS observations (Le Meur et al., 2014). Seismic sources are shown as colored dots, with colors representing their depth as defined by the color bar. The dotted black circle shows a cluster of deep events located on the GL.

21699011, 2025, 8, Downloaded from https://agupubs.onlinelibrary.wiley.com/doi/10.1029/2024JF008054 by Tifenn Le Bris - Cochrane France , Wiley Online Library on [02/09/2025]. See the Terms and Conditions (https://onlinelibrary.wiley.com/terms-and-conditions) on Wiley Online Library for rules of use; OA articles are governed by the applicable Creative Commons License

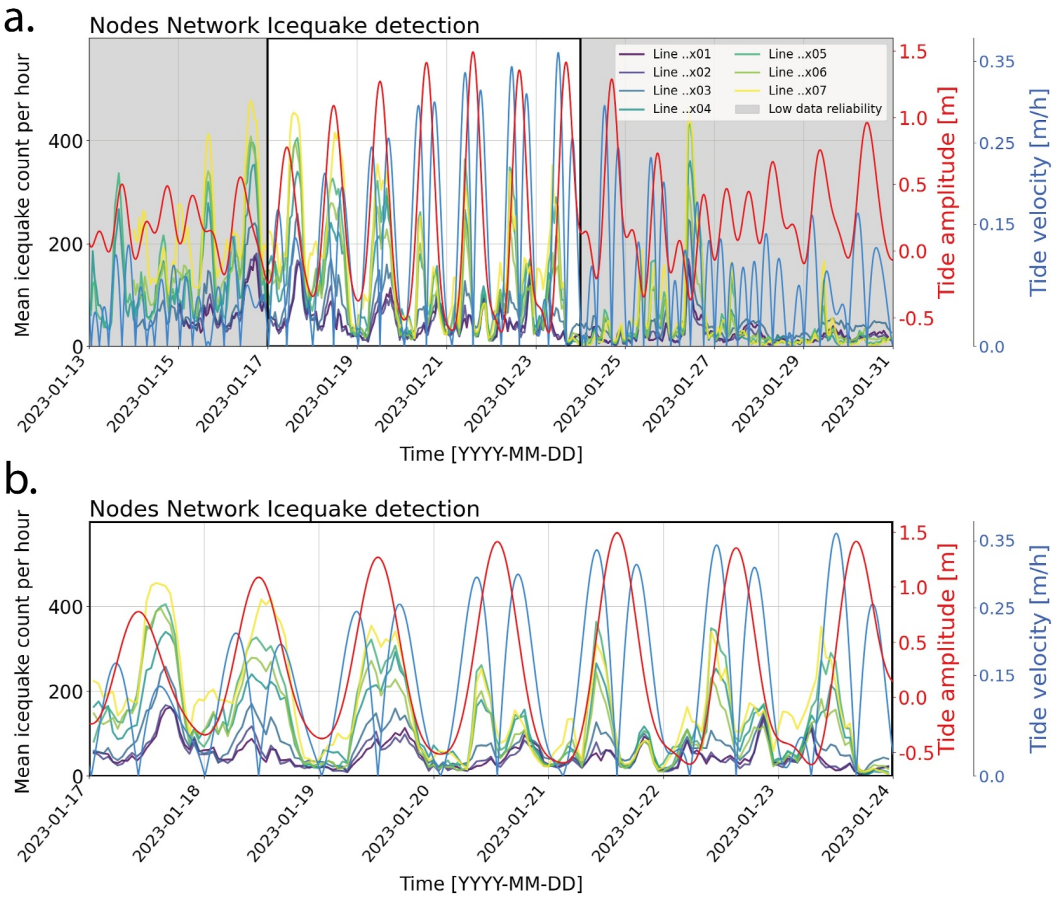

Figure 8. Icequake occurrences at the seismic nodes. (a) Time series of average icequake hourly occurrence along the 7 along-flow lines of the node array (color-coded as stations on Figure 1c) along with the tide amplitude (red curve) and the derived tide vertical velocity (blue curve) during the period January 13–31, 2023. Gray areas represent the periods of either weak tide amplitude variations or wind-induced high noise levels, perturbing the detection and interpretation process. (b) Zoom on the period January 17–24, 2023. The network deployment was completed on 16 January 2023. STA/LTA parameters: sta = 0.5s, lta = 5s, ThrOn = 5, ThrOff = 2.

distributed over the area, including a small linear cluster of events located over a section of the GZ border. These deeper events could correspond to brittle deformation at the base of the glacier related to the opening of basal crevasses during the tide-induced upward bending of the glacier. This large-magnitude seismicity shows little activity in the southwestern part of the array. For all of these large-magnitude events, we do not identify any clear occurrence correlated with the tides (Figure S6 in Supporting Information S1).

3.3. Small-Scale Spatial and Temporal Icequake Activity in the Grounding Zone Area

3.3.1. Tidal Modulation of Small-Magnitude Icequake Occurrence

In order to explore the temporal and spatial variability of small-magnitude icequake activity over the GZ at high-resolution, we apply STA/LTA detection on the data acquired with the dense seismic array. In Figure 8a, we present an overlay of the mean icequake hourly occurrence calculated along the 7 along-flow lines of seismic nodes (indicated by different colors, as specified in Figure 1c) superimposed with the measured tide amplitude and the derived tide vertical velocity. We also present a zoom in Figure 8b on the 7 days where data are most reliable due to strong tide amplitudes and quiet weather conditions providing good detection capabilities. Consistent with our observations from the 2022 seismic broadband network (Section 3.2, Figure 5), we observe periods of seismic quiescence at low tides, followed by peak(s) of seismic activity either at high tides or at both rising and falling tides. Second, we evidence a clear gradient in icequake occurrence from the northwestern lines of the node array (dark purple in Figures 1c and 8) to the southeastern lines (light green and yellow in Figures 1c

21699011, 2025, 8, Downloaded from https://agupubs.onlinelibrary.wiley.com/doi/10.1029/2024JF008054 by Tifenn Le Bris - Cochrane France , Wiley Online Library on [02/09/2025]. See the Terms and Conditions (https://onlinelibrary.wiley.com/terms-and-conditions) on Wiley Online Library for rules of use; OA articles are governed by the applicable Creative Commons License

21699011, 2025, 8, Downloaded from https://agupubs.onlinelibrary.wiley.com/doi/10.1029/2024JF008054 by Tifenn Le Bris - Cochrane France , Wiley Online Library on [02/09/2025]. See the Terms and Conditions (https://onlinelibrary.wiley.com/terms-and-conditions) on Wiley Online Library for rules of use; OA articles are governed by the applicable Creative Commons License

and 8). On the northwestern lines, we detect less than 100 events per hour, while on the southeastern lines, we detect up to 300–400 events per hour. Third, we observe double peaks in icequake occurrence during tidal cycles with larger amplitudes, which are well correlated with peaks in tidal velocities, clearly visible from January 21 to January 23.

3.3.2. Seismic Source Locations and Occurrences of Small-Magnitude Events

We did not succeed to locate small-magnitude events individually for two main reasons: (a) They have high frequency contents (5–40 Hz) and cannot be located using MFP due to aliasing effects (see Section 2.6); (b) Most of them are recorded by too few stations and exhibit strong waveform variations likely caused by surface crevassing impeding any phase pick or phase correlation (examples of waveforms available in Figure S7 in Supporting Information S1). However, as mentioned previously, we observe that the number of detected events strongly varies across the 7 along-flow lines of the array. Examining the average detected seismicity at each individual node (Figure 9a) reveals with more details this spatial pattern: nodes located on the floating ice, east of the GZ, exhibit much higher seismic activity (indicated by stronger reddish colors, Figure 9a) than nodes on the north and western parts of the network. The transition from high to low icequake activity, from southeast to northwest, matches well with the GL position suggested by Le Meur et al. (2014). The along-flow transition from floating to grounded ice is less distinct. This could be linked to the migration of the GZ landward, inducing seismic activity along the flow direction propagating through time and making the transition blurrier when averaging over the course of multiple days.

The spatial distribution of the icequake activity matches well with GNSS-derived ice vertical motion measurements (see gray squares, Figure 9a). They are computed by averaging the absolute values of the envelope over the selected time period (17 January 2023–24 January 2023). In the northeastern corner of the area, where the glacier is floating and seismicity is high, we observe large average vertical displacements of the ice of 135 mm (GPS08), 130 mm (GPS03) and 88 mm (GPS06). In contrast, in the northwestern regions, where the glacier is likely grounded and seismicity is low, average vertical displacement is significantly lower, such as 27 mm at GPS07 and 32 mm at GPS05.

To further investigate the fine-scale spatial pattern of icequakes, we count the number of stations detecting any given event within a 2-s time window. The example presented in Figure 9b is the number of events detected by less than 10 stations for one day (17 January 2023) representative of an "average" tide cycle (i.e., with a mean tide height of ±0.5 m). We observe that these stations are clearly concentrated in the eastern part of the network, corresponding to the floating ice sector. The statistics of events by bins of number of sensors, summarized in Table S3 in Supporting Information S1, are particularly informative: The large majority of events (63%) are detected by less than 10 stations or between 11 and 20 stations (25%), while only a very small percentage of events (2%) are detected by more than 40 stations. This detection pattern aligns well with the magnitude distribution presented in Figure 6, where small-magnitude events clearly dominate in numbers.

Finally, we evaluate temporal changes in the distribution of events between rising and falling tides by calculating the variance of icequake occurrences at each station, with the variance being defined as the difference between the average hourly icequake number during rising and falling tides divided by the average number during rising tides. Results for the period 17 January 2023 to 24 January 2023 are presented in Figure 10. During rising tides, icequake activity is dominant in the floating part of the network (reddish dots in Figure 10), while during falling tides, activity increases in the grounded part (blueish dots in Figure 10), particularly in the western and southern sectors. In both cases, the variance of icequake occurrence can reach up to 40%, indicating a significant shift of the seismic activity at a fine spatial and temporal scale, from the floating area at rising tides toward the grounded area at falling tides.

3.3.3. Link With Horizontal and Vertical Ice Motions

We evaluate the link between icequake activity and ice motion by analyzing the GNSS-derived vertical and horizontal velocity time series. We show the results for two stations aligned along the flow of the glacier: GPS08 and GPS06 (respectively Figures 11a and 11b). The vertical motion varies significantly between these stations: GPS08, closer to the ocean on the floating ice and thus more influenced by tide-driven sea height changes, experiences large vertical motion amplitudes with peaks of vertical velocity between 600 mm.day-1 and 800 mm.day-1. GPS06, located closer to the GZ, experiences maxima of vertical velocity well below 300 mm.day-1.

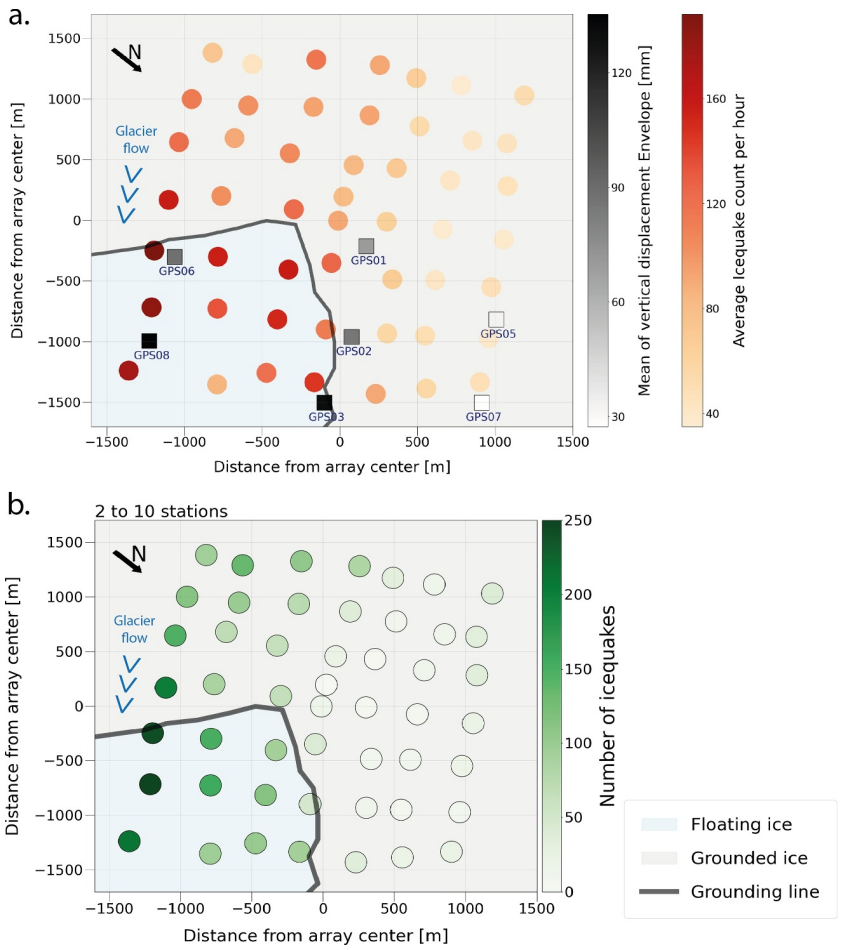

Figure 9. (a) Map of the hourly average icequake activity during the period January 17–24, 2023 (color-coded in red, indicating the average icequakes count per hour) recorded at each station of the seismic node network (circles), together with the average vertical ice displacements shown as squares filled with a level of gray indicating the mean value in mm measured by the GNSS stations. The continuous gray line represents the grounding line inferred from GPS observations (Le Meur et al., 2014). (b) Map of the number of icequakes detected by less than 10 stations (color-coded in green) for one day (17 January 2023) representative of an "average" tide cycle (i.e., with a mean tide height of ±0.5 m). Each station is color-coded based on the number of icequakes detected in the corresponding category.

Stations closer to the lateral shear zone (i.e., GPS07 and GPS05, not shown here) show almost non-existent vertical velocities. Horizontal velocities recorded at GPS08, on floating ice, are also higher than those recorded at GPS06. Additionally, while vertical motion shows one peak at mid-rising tide and one peak at mid-falling tide, horizontal motion shows one peak at mid-falling tide and a second one at low tide. FFT spectral analysis over 30 days confirms that both vertical and horizontal velocities vary with main tidal cycles (i.e., diurnal, semidiurnal and terdiurnal cycles). To assess the role of horizontal and vertical motion in the generation of seismicity through ice deformation, we compute strain rates (Equations 1 and 2 in method Section 2.3) between GPS08 and GPS06 (Figure 11c). The vertical shear strain rate averages around 1.5×10^{-9} s^{-1} reaching peaks of 1×10^{-8} s^{-1}, while the horizontal longitudinal strain rate is lower, averaging around 3.6×10^{-10} s^{-1} with peaks up to 4.7×10^{-9} s^{-1}. Similar to seismicity recorded in this area, the vertical shear strain rate shown in Figure 11c varies in response to tide velocity, peaking at mid-rising and mid-falling tides. In contrast, the horizontal longitudinal strain rate, which is approximately two times weaker, appears to only peak at low tide, a period where there is generally no or very low seismicity detected.

21699011, 2025, 8, Downloaded from https://agupubs.onlinelibrary.wiley.com/doi/10.1029/2024JF008054 by Tifenn Le Bris - Cochrane France , Wiley Online Library on [02/09/2025]. See the Terms and Conditions (https://onlinelibrary.wiley.com/terms-and-conditions) on Wiley Online Library for rules of use; OA articles are governed by the applicable Creative Commons License

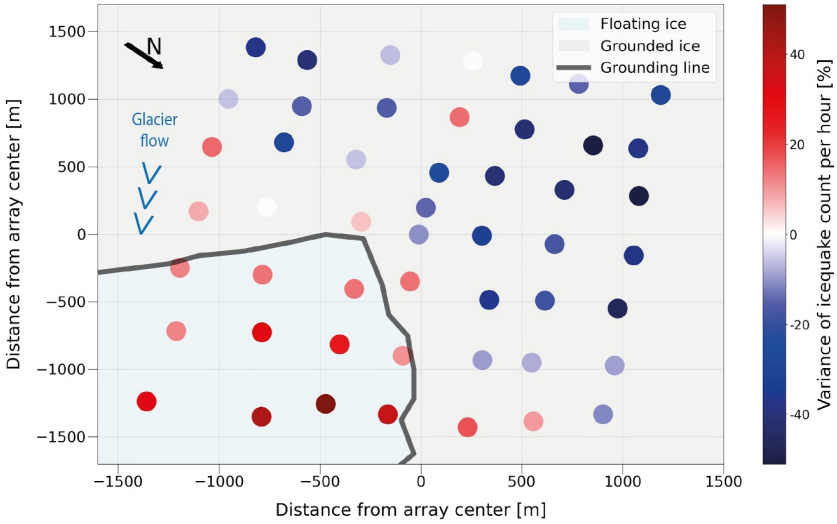

Figure 10. Map summarizing the icequake variance between the number of events occurring during rising and falling tides (in %) for the period January 17–24, 2023. Reddish colors indicate dominant icequake activity during rising tides, whereas blueish colors indicate dominant icequake activity during falling tides. The continuous gray line represents the grounding line inferred from GNSS observations (Le Meur et al., 2014).

4. Discussion

4.1. Tide-Induced Stress Accommodation at the Grounding Zone

The computation of both icequake occurrences and the vertical and horizontal ice velocities provides insights into how stress from the glacier floating tongue flexure is accommodated during tide cycles. We observe that seismicity often peaks during rising and/or falling tides, similar to the pattern observed in the vertical shear strain rates deduced from the GNSS data (Figure 11c), suggesting that the glacier bending could be the controlling factor for icequake generation. We further verify that the observed vertical shear strain rates are sufficient to generate brittle deformation by estimating the associated changes in stress. Considering vertical shear strain rates on the order of 6×10^{-9} s^{-1}, which is a typical threshold crossed at rising tide for several cycles (as seen in Figure 11c), we apply Glen's law using the recommended base value of ice creep for ice temperatures of −10°C to −5°C (reasonable estimates from drillings at site) and a Glen exponent of 3 (Cuffey & Paterson, 2010). Such simple calculation yields stress on the order of 250–450 kPa, which is well above the stress threshold of about 100 kPa for brittle deformation in ice (Vaughan, 1993). The horizontal longitudinal strain rate is also high enough to generate a stress level for brittle behavior. However, as shown in Figure 11c, contrary to the vertical shear strain rate, its variation in time does not match that observed in the seismicity. This leads us to conclude that the bending of the floating tongue is likely responsible for the majority of the observed seismicity, while the longitudinal extension likely plays a minor role. Generally, but not systematically, the intensity of the flexure-related icequake activity correlates well with the tide magnitude. However, we observe that some stations show persistent seismic activity despite small tide amplitudes, indicating possible nonlinear interactions between ocean tides and non-elastic processes at the GZ.

4.2. Spatial Distribution of Icequake Activity From 2D to 3D GZ Geometries

Our analysis demonstrates the benefit of high-resolution seismic observations for revealing the three-dimensional (3D) nature of the GZ. We propose, in Figure 12, a conceptual framework based on schematized longitudinal and transverse cross-sections of the Astrolabe Glacier as the dotted lines located in Figure 12a. For a hypothetical two-dimensional (2D) GZ, downward bending of the glacier should occur at falling tides, as schematized in Figure 12b. This bending would primarily result in an extensional regime, opening cracks and crevasses near the surface upstream from the GZ (blue star, Figure 12b), as described by Hulbe et al. (2016). In contrast, rising tides would cause the floating tongue to move upward, resulting in an extensional regime downstream from the GZ (red star, Figure 12b), as proposed by Rack et al. (2017). The spatial offset between icequake activity during falling and rising tides, related to the glacier curvature and ice thickness at the GZ, aligns well with our observations in

21699011, 2025, 8, Downloaded from https://agupubs.onlinelibrary.wiley.com/doi/10.1029/2024JF008054 by Tifenn Le Bris - Cochrane France , Wiley Online Library on [02/09/2025]. See the Terms and Conditions (https://onlinelibrary.wiley.com/terms-and-conditions) on Wiley Online Library for rules of use; OA articles are governed by the applicable Creative Commons License

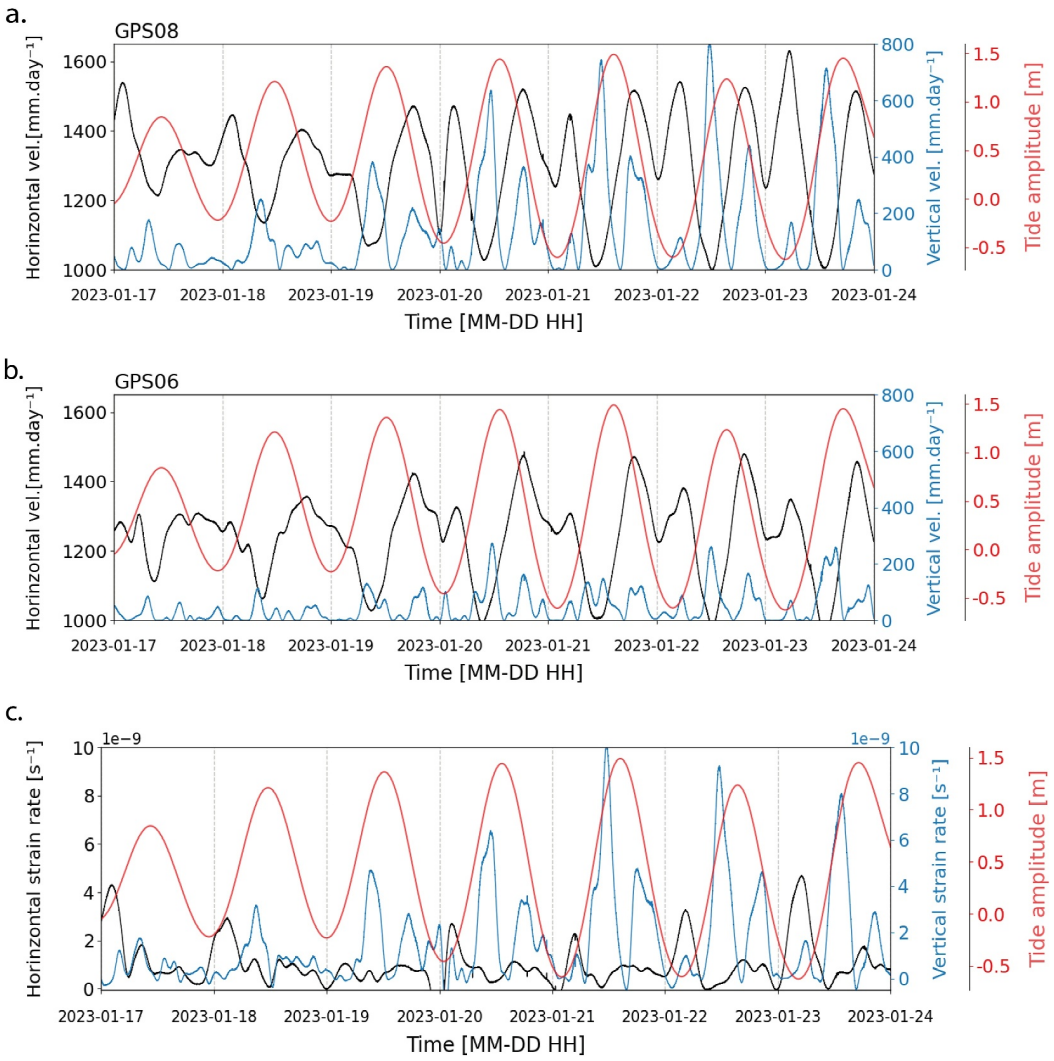

Figure 11. (a) Horizontal (black curve) and vertical (blue curve) velocities superposed with tide amplitude measured at the DUMON tide gauge (red curve) for GNSS stations GPS08 over the period January 17–24, 2023. (b) Same for GPS06. (c) Horizontal longitudinal strain rate (black curve) and vertical shear strain rate (blue curve) between stations GPS08 and GPS06, superposed with tide amplitude (red curve).

Figure 10 that more icequakes occur on the floating ice during rising tides, and more on the grounded ice during falling tides. In addition to this 2D picture, we expect that the 3D geometry of the Astrolabe Glacier also plays a role, given that the glacier is 3–4 km wide, about 0.6 km thick at its GZ, and laterally confined within a fjord with steep walls, schematized in Figure 12c. Our GNSS measurements, along with the seismic node network over the U-shaped GZ (Figure 1), indicate that the glacier is grounded beneath both its southern and western sections, as seen by the small vertical motions observed at the GPS05 and GPS07 (Figure 9a) located along the western lateral boundary of the glacier. During rising tides, the fixed glacier lateral boundaries restrict vertical displacement, causing transverse bulging of the floating part of the glacier and extension near the surface all along the lateral sides of the glacier (red stars, Figure 12c). We propose that this tide-modulated bulging effect could be responsible for the seismicity pattern evidenced at DRV and at the OBSs at sea. Considering the distance of these stations to the GZ (about 10 km) and the fact that the small seismicity at the GZ is recorded very locally (as shown Figure 9b), seismicity detected at DRV and OBSs most probably originates from the glacier lateral margins (at about 1 km from each site) and not from the GZ itself. This points that similar icequake patterns may originate from different locations, which is compatible with the proposed conceptual cartoon in Figure 12. For a more

21699011, 2025, 8, Downloaded from https://agupubs.onlinelibrary.wiley.com/doi/10.1029/2024JF008054 by Tifenn Le Bris - Cochrane France , Wiley Online Library on [02/09/2025]. See the Terms and Conditions (https://onlinelibrary.wiley.com/terms-and-conditions) on Wiley Online Library for rules of use; OA articles are governed by the applicable Creative Commons License

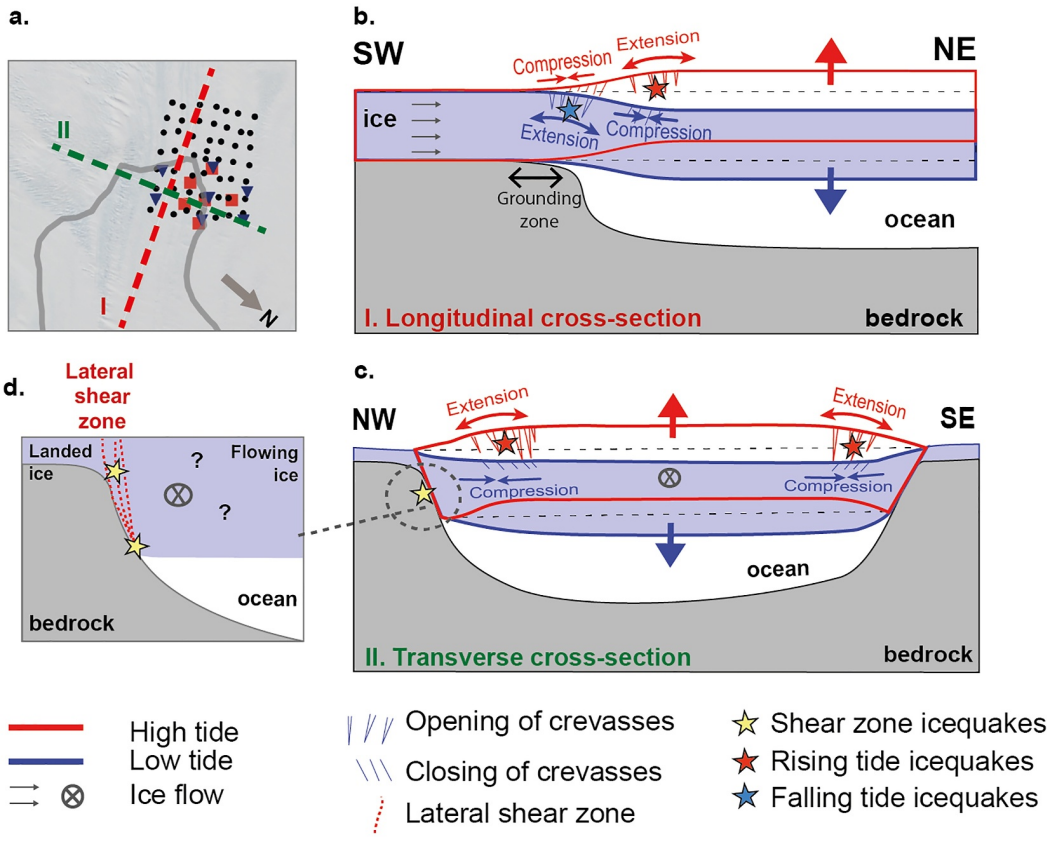

Figure 12. Schematic cartoons illustrating the possible origins of the surface icequakes observed on the Astrolabe Glacier: (a) Position of the longitudinal (red) and transverse (green) schematic cross sections. (b) Cartoon of the longitudinal cross-section (I, in red) illustrating icequakes generated by the longitudinal bending of the glacier in response to tidal vertical variations. The blue star indicates the surface crevasse opening during falling tides and the red star indicates the surface crevasse opening during rising tides. (c) Cartoon of the transverse cross-section (II, in green) illustrating the bulging of the glacier during rising tides. (d) Location of large-magnitude icequakes (yellow stars), primarily associated with the lateral shear zones, accommodating the displacement of the glacier horizontal flow relative to the stationary ice at the surface or close to the bedrock at greater depths.

detailed understanding of the flexure and associated seismicity, further modeling of stress distribution across GZ systems under tidal oscillations would be required, including bedrock topography and realistic tide activity.

4.3. Small Versus Large-Magnitude Seismicity-Designing Seismic Arrays for Glaciers and GZ Monitoring

Our seismic measurements reveal a wide range of icequake activities. Small-magnitude events (minimum Md down to −4.0, magnitude of completeness around −1.5, see Figure 6) have frequency contents dominating in the range of 5–40 Hz and can occur up to 5,000 times per day at some stations. They exhibit hardly discernible seismic phases and their waveforms and arrival times are strongly affected along their traveling paths–likely by surface heterogeneities induced by open crevasses and attenuation. These small events are most prominent on the glacier floating tongue. They exhibit clear tidal modulation, peaking at mid-rising tides predominantly on the floating ice and at mid-falling tides in the (partly) grounded area upstream of the GZ (Figure 12b). Larger-magnitude events (magnitude of completeness around 0.3 for located events) occur at lower-frequencies (down to 1 Hz) up to 400 times per day on average, and are well detected using MFP analysis. These large events are primarily located outside the seismic node network (Figure 7), often at shallow depths (<100 m), particularly in the lateral shear zones where the glacier accommodates its flow relative to the slow-moving ice or bedrock (yellow stars in Figures 12c and 12d). Few tenths of them are also observed on the floating part of the network (such as the cluster close to the GZ underlined in Figure 7), suggesting significant deformation possibly linked to longitudinal glacier acceleration during low tides or to basal crevassing. These large-magnitude events

21699011, 2025, 8, Downloaded from https://agupubs.onlinelibrary.wiley.com/doi/10.1029/2024JF008054 by Tifenn Le Bris - Cochrane France , Wiley Online Library on [02/09/2025]. See the Terms and Conditions (https://onlinelibrary.wiley.com/terms-and-conditions) on Wiley Online Library for rules of use; OA articles are governed by the applicable Creative Commons License

21699011, 2025, 8, Downloaded from https://agupubs.onlinelibrary.wiley.com/doi/10.1029/2024JF008054 by Tifenn Le Bris - Cochrane France , Wiley Online Library on [02/09/2025]. See the Terms and Conditions (https://onlinelibrary.wiley.com/terms-and-conditions) on Wiley Online Library for rules of use; OA articles are governed by the applicable Creative Commons License

are clearly absent from the grounded part of the node network, where deformation is dominated by small-magnitude events accommodating the glacier flexure.

Therefore, our observations indicate that the type of seismicity recorded at a given site is dependent on the sensor location relative to the GZ. Seismicity over the GZ is dominated by a large number of small-magnitude events that are not regionally detectable, while the more sporadic higher-magnitude seismicity issued from the shear margin activity dominates records at stations farther away from the GZ. Similarly, outside the glacier area, sensors are primarily sensitive to the local seismicity, and are missing small events generated at the GZ, likely too far away (i.e., AST02, see Figure 5b). At a smaller scale within the GZ area, our findings (see Figure 10) also show that the sensor location may also control whether the maximum icequake detection occurs either at mid-rising (on the floating ice) or mid-falling tide (on the grounded ice). Depending on the sensor location, one can therefore expect to record different numbers of small versus. large events, but also of rising-versus. falling-tide events. This suggests that similar tidally modulated processes can produce different seismic signatures depending on location and sensitivity to the source area. This study highlights the importance of combining simultaneous large- and small-scale seismic deployments in the design of seismic networks to catch the glacier dynamics at various scales.

Despite limitations in instrument number and fieldwork logistics, our setup on the Astrolabe Glacier effectively captures and discriminates the diverse signals generated by the glacier. Initial observations with a limited number of broadband stations deployed around the glacier and on its GZ already provided a great overview of key patterns: (a) absence of tide-induced recordable seismicity at stations at large distance to the glacier (e.g., Figure 5b, Figure S5 in Supporting Information S1); and (b) extremely contrasted seismicity in the GZ area, with very low seismic activity at low tides and increased seismicity during rising and/or falling tides (e.g., Figure 5a). The kilometer-scale dense network of seismic nodes on the GZ proved, however, much higher resolution in both time and space, allowing detailed monitoring of the glacier response to tidal movements within its bedrock geometry and, in our case, even partially outlining the GZ position. This refined understanding of the GZ location and dynamics is achievable only with such a dense network of seismic stations, as sparse or remote setups would not capture the fine-scale and fine-temporal variations of seismicity associated with tidal cycles such as the one presented Figures 9 and 10.

In addition to networks deployed over the GZ, future deployments on outlet glaciers should include dense arrays covering the shear margins, with the aim of better identifying and locating their large and small seismicity. Additionally, in order to properly locate the small seismicity within the GZ, one should reduce the inter-station distance to increase the aliasing threshold to higher frequencies. In a case such as the Astrolabe Glacier, this would require having a dense array with average inter-station distance around or even below 100 m over the GZ. Fiber-optic sensing could offer such an alternative for detecting and precisely locating small-magnitude events in the GZ. Finally, while our kilometer-scale experiment was sufficient for a moderate-sized glacier, deploying similar setups on larger outlet glaciers would require careful a priori estimation of the GZ position to ensure the full transition zone is spanned by the dense seismic array, which can extend tens of kilometers.

5. Conclusions

By deploying broadband and short-period seismometers and a dense seismic node array over periods ranging from weeks to several years on and around an Antarctic outlet glacier and particularly at its GZ, we quantified icequake activity at this critical frontier where continental ice reaches the ocean. While diurnal and semidiurnal tidal periods dominate in the seismic patterns, we also observe significant effects at fortnightly, monthly, terdiurnal, and quarterdiurnal cycles, indicating intricate interactions between tides, the floating ice tongue, and the underlying ocean. We observe very low seismicity at low tide and peaks of seismicity often occurring during rising and falling phases, which are well correlated with GNSS-derived vertical motion and consequent shear strain at the surface. From the dense seismic array, we detect and locate large-magnitude cryoseismic events, primarily induced by deformation along the glacier lateral shear margins. Our detections also reveal numerous small-magnitude events in the vicinity of the GZ, strongly influenced by tidal amplitudes and GZ geometry. This latter seismicity is found to be more intense on the floating part of the glacier near the GZ, where vertical velocities are strongest, suggesting that small but numerous icequakes accommodate its tide-induced bending. We propose that the icequake activity could be explained by the successive flexure and bulging of the glacier confined within a fjord in response to falling and rising tides, respectively. Finally, the dense seismic array covering a large part of the GZ enables us to capture short-scale spatial and temporal variations in icequake activity reflecting its

Acknowledgments
The SEIS-ADELICE project benefited from the support of the French Polar Institute Paul-Émile Victor (IPEV) for the program #1214, from the French CNRS-INSU SYSTER and LEFE-IMAGO programs, from the Grenoble University UGA-IRGA funding, for the project NODES-ADELICE supported by the French National Research Agency (ANR) in the framework of the "Investissements d'avenir" program (ANR-15-IDEX-02), from the LabEx OSUG@2020 (Investissements d'avenir–ANR10 LABX56) for the project DAS-ADELICE, from the ANR Bruit-FM (project ANR-21-CE01-0031) for the OBS deployments, and from IGE Grenoble. We are grateful to EPOS-France (European Plate Observing System https://www.epos-france.fr/) and SISMOB (http://sismob.epos-france.fr) for the station and the data management and to the IPGP INSU-OBS pool and the SMM (Sismologie Mobile Marine) (http://smm.epos-france.fr) for providing and deploying the OBS instruments. Thanks to IPGP for the funding the mechanical adaptation of the shallow water Guralp "BREVE" OBS (BQR IPGP 2020), and for hiring Denis Lombardi for preparing the first 2022 broadband seismic experiment. Thanks to the French global broadband seismic network Geoscope for the quality and availability of the data. The Geoscope DRV station in the Dumont d'Urville base is managed with support from IPEV program #133 "Global Seismological Observatory (SISMOLOGIE/OBS)." Part of the seismic nodes used in this study have been provided by the "Plateforme instrumentale sismologique" of EOST. The permanent GNSS network is funded and maintained in the framework of the GLACIOCLIM Observatory (https://www.osug.fr/missions/observation/ocean-atmosphere-surfaces-continentales/glacioclim/), whose field support is provided by the IPEV Program #411. Thanks to the Astrolabe vessel crew from the French Navy for helping in the deployment and recovery of OBSs. Thanks to Romuald Daniel, Tom Dumouch, Simon Besançon, Paul Michaud, Iban Fernandez, Lucien Goulet, Louis Grauwin, Enzo Tahon, Léonard Barthélémy, Arnaud Reboud, Killian Pareilleux, Aubin Ignazi, and Paul Tudes for their efficient help in the field work. Thanks to François Pallandre, Pierre Rizzardo, Fred Valet and Charles Noirot from ENSA Chamonix for their help and for securing the field work on the glacier. Thanks to Jean-Yves Thoré for his technical and logistical contribution. Thanks to Erwann Rouzaud, P. Peltier, Piel Pawlowski, Arthur Nennig, Tillian Galego, and Josselin Champigny for their help in processing and analyzing the data. Thanks to A. Lecointre for her help in using the MFP codes. Thanks to P. Techine, M. Calzas and L. Testut for providing access to the tide gauge data managed by the NIVMER/ROSAME

outline. Such precise monitoring of the GZ will be of great importance in characterizing its potential retreat induced by the changing climate, threatening the future stability of the upstream ice sheet basin.

Data Availability Statement

The SEIS-ADELICE seismic data are available at the RESIF data center under the FDSN network code ZR (Barruol et al., 2023). Seismological data from the Geoscope DRV station can be accessed through the IPGP web services or the Epos-France Seismological Data Center under the FDSN network code *G* (Institut de physique du globe de Paris & Ecole et Observatoire des Sciences de la Terre de Strasbourg, 1982). Raw and processed GNSS data acquired on the Astrolabe Glacier GZ are available under a Creative Commons Attribution 4.0 International license in Togaibekov et al. (2024). Tide gauge data, managed by the NIVMER/ROSAME project (Calzas et al., 1992) are available at https://doi.org/10.17183/REFMAR#108. Seismic data were processed using ObsPy version 1.4.0 (Beyreuther et al., 2010; The ObsPy Development Team, 2022), available under the ObsPy license at https://docs.obspy.org/. The MFP codes used in this study to localize seismic sources are available via the GRICAD GitLab repository under a Creative Commons Attribution 4.0 International license at https://gricad-gitlab.univ-grenoble-alpes.fr/lecoinal/resolve. Figures were made with Matplotlib version 3.5.3 (Caswell et al., 2022; Hunter, 2007), available under the Matplotlib license at https://matplotlib.org/. All data and scripts used to generate the figures and results in this study are openly available under a Creative Commons Attribution 4.0 International license. The full data set, including icequake detection and location data, station metadata, and scripts, is archived in Le Bris (2025).

References

Allen, R. V. (1978). Automatic earthquake recognition and timing from single traces. *Bulletin of the Seismological Society of America*, *68*(5), 1521–1532. https://doi.org/10.1785/BSSA0680051521

Amundson, J. M., Fahnestock, M., Truffer, M., Brown, J., Lüthi, M. P., & Motyka, R. J. (2010). Ice mélange dynamics and implications for terminus stability, Jakobshavn Isbræ, Greenland. *Journal of Geophysical Research*, *115*(F1), F01005. https://doi.org/10.1029/2009JF001405

Anandakrishnan, S., & Alley, R. B. (1997). Tidal forcing of basal seismicity of ice stream C, West Antarctica, observed far inland. *Journal of Geophysical Research*, *102*(B7), 15183–15196. https://doi.org/10.1029/97JB01073

Andrews, L. C., Catania, G. A., Hoffman, M. J., Gulley, J. D., Lüthi, M. P., Ryser, C., et al. (2014). Direct observations of evolving subglacial drainage beneath the Greenland Ice Sheet. *Nature*, *514*(7520), 80–83. https://doi.org/10.1038/nature13796

Aster, R. C., & Winberry, J. P. (2017). Glacial seismology. *Reports on Progress in Physics. Physical Society (Great Britain)*, *80*(12), 126801. https://doi.org/10.1088/1361-6633/aa8473

Aðalgeirsdóttir, G., Smith, A. M., Murray, T., King, M. A., Makinson, K., Nicholls, K. W., & Behar, A. E. (2008). Tidal influence on Rutford Ice Stream, West Antarctica: Observations of surface flow and basal processes from closely spaced GPS and passive seismic stations. *Journal of Glaciology*, *54*(187), 715–724. https://doi.org/10.3189/002214308786570872

Barruol, G., Cordier, E., Bascou, J., Fontaine, F. R., Legrésy, B., & Lescarmontier, L. (2013). Tide-induced microseismicity in the Mertz glacier grounding area, East Antarctica. *Geophysical Research Letters*, *40*(20), 5412–5416. https://doi.org/10.1002/2013GL057814

Barruol, G., & Zigone, D., & RESIF. (2023). SEIS-ADELICE temporary experiment measuring the cryoseismicity of the Astrolabe glacier in Terre Adelie, Antarctica (RESIF-SISMOB) [Dataset]. *RESIF - Réseau Sismologique et géodésique Français*. https://doi.org/10.15778/RESIF.ZR2020

Bartholomaus, T. C., Larsen, C. F., West, M. E., O'Neel, S., Pettit, E. C., & Truffer, M. (2015). Tidal and seasonal variations in calving flux observed with passive seismology. *Journal of Geophysical Research: Earth Surface*, *120*(11), 2318–2337. https://doi.org/10.1002/2015JF003641

Bartholomew, I., Nienow, P., Sole, A., Mair, D., Cowton, T., & King, M. A. (2012). Short-term variability in Greenland Ice Sheet motion forced by time-varying meltwater drainage: Implications for the relationship between subglacial drainage system behavior and ice velocity. *Journal of Geophysical Research*, *117*(F3), F03002. https://doi.org/10.1029/2011JF002220

Beaman, R. J., O'Brien, P. E., Post, A. L., & Santis, L. D. (2011). A new high-resolution bathymetry model for the Terre Adélie and George V continental margin, East Antarctica. *Antarctic Science*, *23*(1), 95–103. https://doi.org/10.1017/S095410201000074X

Beyreuther, M., Barsch, R., Krischer, L., Megies, T., Behr, Y., & Wassermann, J. (2010). ObsPy: A python toolbox for seismology. *Seismological Research Letters*, *81*(3), 530–533. https://doi.org/10.1785/gssrl.81.3.530

Bindschadler, R. A., King, M. A., Alley, R. B., Anandakrishnan, S., & Padman, L. (2003). Tidally controlled stick-slip discharge of a West antarctic ice stream. *Science*, *301*(5636), 1087–1089. https://doi.org/10.1126/science.1087231

Bock, Y., Gourevitch, S. A., Counselman, C. C., King, R. W., & Abbot, R. I. (1986). Interferometric analysis of GPS phase observations. *Manuscripta Geodaetica*, *11*(4), 282–288. https://doi.org/10.1007/BF03655099

Brunt, K. M., Fricker, H. A., Padman, L., Scambos, T. A., & O'Neel, S. (2010). Mapping the grounding zone of the Ross Ice Shelf, Antarctica, using ICESat laser altimetry. *Annals of Glaciology*, *51*(55), 71–79. https://doi.org/10.3189/172756410791392790

Calzas, M., Techine, P., & Testut, L. (1992). Nivmer. https://doi.org/10.18142/135

Caswell, T., Lee, A., Droettboom, M., Sales de Andrade, E., Hoffmann, T., Klymak, J., et al. (2022). Matplotlib V3.5.3 [Software]. *Zenodo*. https://doi.org/10.5281/zenodo.6982547

Chen, G. (1999). GPS kinematic positioning for the airborne laser altimetry at Long Valley, California *(Thesis)*. Massachusetts Institute of Technology. Retrieved from https://dspace.mit.edu/handle/1721.1/9680

Chmiel, M., Roux, P., & Bardainne, T. (2019). High-sensitivity microseismic monitoring: Automatic detection and localization of subsurface noise sources using matched-field processing and dense patch arrays. *Geophysics*, *84*(6), KS211–KS223. https://doi.org/10.1190/geo2018-0537.1

Cooley, J., Winberry, P., Koutnik, M., & Conway, H. (2019). Tidal and spatial variability of flow speed and seismicity near the grounding zone of Beardmore Glacier, Antarctica. *Annals of Glaciology*, *60*(79), 37–44. https://doi.org/10.1017/aog.2019.14

21699011, 2025, 8, Downloaded from https://agupubs.onlinelibrary.wiley.com/doi/10.1029/2024JF008054 by Tifenn Le Bris - Cochrane France , Wiley Online Library on [02/09/2025]. See the Terms and Conditions (https://onlinelibrary.wiley.com/terms-and-conditions) on Wiley Online Library for rules of use; OA articles are governed by the applicable Creative Commons License

project (Calzas et al., 1992). Finally, we thank three anonymous reviewers and the associate editor for their constructive comments which helped improve this paper.

Cuffey, K. M., & Paterson, W. S. B. (2010). *The physics of glaciers*. Academic Press.
Fricker, H. A., & Padman, L. (2006). Ice shelf grounding zone structure from ICESat laser altimetry. *Geophysical Research Letters*, *33*(15), L15502. https://doi.org/10.1029/2006GL026907
Friedl, P., Weiser, F., Fluhrer, A., & Braun, M. H. (2020). Remote sensing of glacier and ice sheet grounding lines: A review. *Earth-Science Reviews*, *201*, 102948. https://doi.org/10.1016/j.earscirev.2019.102948
Fromm, T., Schlindwein, V., Helm, V., & Fofonova, V. (2023). Observing tidal effects on the dynamics of the Ekström Ice Shelf with focus on quarterdiurnal and terdiurnal periods. *Journal of Glaciology*, 1–11. https://doi.org/10.1017/jog.2023.4
Gimbert, F., Nanni, U., Roux, P., Helmstetter, A., Garambois, S., Lecointre, A., et al. (2021). A multi-physics experiment with a temporary dense seismic array on the Argentière Glacier, French alps: The RESOLVE Project. *Seismological Research Letters*, *92*(2A), 1185–1201. https://doi.org/10.1785/0220200280
Grob, M., Maggi, A., & Stutzmann, E. (2011). Observations of the seasonality of the Antarctic microseismic signal, and its association to sea ice variability. *Geophysical Research Letters*, *38*(11), L11302. https://doi.org/10.1029/2011GL047525
Gudmundsson, G. H. (2007). Tides and the flow of rutford ice stream, West Antarctica. *Journal of Geophysical Research*, *112*(F4), F04007. https://doi.org/10.1029/2006JF000731
Hammer, C., Ohrnberger, M., & Schlindwein, V. (2015). Pattern of cryospheric seismic events observed at Ekström Ice Shelf, Antarctica. *Geophysical Research Letters*, *42*(10), 3936–3943. https://doi.org/10.1002/2015GL064029
Helmstetter, A., Nicolas, B., Comon, P., & Gay, M. (2015). Basal icequakes recorded beneath an Alpine glacier (Glacier d'Argentière, Mont Blanc, France): Evidence for stick-slip motion? *Journal of Geophysical Research: Earth Surface*, *120*(3), 379–401. https://doi.org/10.1002/2014JF003288
Herring, T. A., King, R. W., Floyd, M. A., & McClusky, S. C. (2018). *Introduction to GAMIT/GLOBK*. Massachusetts Institute of Technology.
Hudson, T. S., Brisbourne, A. M., Walter, F., Gräff, D., White, R. S., & Smith, A. M. (2020). Icequake source mechanisms for studying glacial sliding. *Journal of Geophysical Research: Earth Surface*, *125*(11), e2020JF005627. https://doi.org/10.1029/2020JF005627
Hudson, T. S., Smith, J., Brisbourne, A. M., & White, R. S. (2019). Automated detection of basal icequakes and discrimination from surface crevassing. *Annals of Glaciology*, *60*(79), 167–181. https://doi.org/10.1017/aog.2019.18
Hulbe, C. L., Klinger, M., Masterson, M., Catania, G., Cruikshank, K., & Bugni, A. (2016). Tidal bending and strand cracks at the Kamb Ice Stream grounding line, West Antarctica. *Journal of Glaciology*, *62*(235), 816–824. https://doi.org/10.1017/jog.2016.74
Hunter, J. D. (2007). Matplotlib: A 2d graphics environment. *Computing in Science and Engineering*, *9*(3), 90–95. https://doi.org/10.1109/MCSE.2007.55
Institut de physique du globe de Paris (IPGP) and Ecole et Observatoire des Sciences de la Terre de Strasbourg (EOST). (1982). GEOSCOPE, French global network of broad band seismic stations [Dataset]. Institut de physique du globe de Paris (IPGP). https://doi.org/10.18715/GEOSCOPE.G
IPCC Report. (2022). *The Ocean and Cryosphere in a changing climate: Special report of the intergovernmental Panel on climate change*. Cambridge University Press. https://doi.org/10.1017/9781009157964
Jordan, J. R., Miles, B. W. J., Gudmundsson, G. H., Jamieson, S. S. R., Jenkins, A., & Stokes, C. R. (2023). Increased warm water intrusions could cause mass loss in East Antarctica during the next 200 years. *Nature Communications*, *14*(1), 1825. https://doi.org/10.1038/s41467-023-37553-2
King, M. A., Altamimi, Z., Boehm, J., Bos, M., Dach, R., Elosegui, P., et al. (2010). Improved constraints on models of glacial isostatic adjustment: A review of the contribution of ground-based geodetic observations. *Surveys in Geophysics*, *31*(5), 465–507. https://doi.org/10.1007/s10712-010-9100-4
Kufner, S.-K., Wookey, J., Brisbourne, A. M., Martín, C., Hudson, T. S., Kendall, J.-M., & Smith, A. M. (2023). Strongly depth-dependent ice fabric in a fast-flowing Antarctic ice stream revealed with icequake observations. *Journal of Geophysical Research: Earth Surface*, *128*(3), e2022JF006853. https://doi.org/10.1029/2022JF006853
Lagarias, J. C., Reeds, J. A., Wright, M. H., & Wright, P. E. (1998). Convergence properties of the Nelder--Mead simplex method in low dimensions. *SIAM Journal on Optimization*, *9*(1), 112–147. https://doi.org/10.1137/S1052623496303470
Le Bris, T. (2025). Dataset repository [Dataset]. *Zenodo*. https://doi.org/10.5281/zenodo.15747923
Lee, W. H. K., Bennett, R. E., & Meagher, K. L. (1972). *A method of estimating magnitude of local earthquakes from signal duration (Open-File Report)*. U.S. Geol. Surv.
Le Meur, E., Sacchettini, M., Garambois, S., Berthier, E., Drouet, A. S., Durand, G., et al. (2014). Two independent methods for mapping the grounding line of an outlet glacier – An example from the Astrolabe Glacier, Terre Adélie, Antarctica. *The Cryosphere*, *8*(4), 1331–1346. https://doi.org/10.5194/tc-8-1331-2014
Leroy, N., Vallée, M., Zigone, D., Romanowicz, B., Stutzmann, E., Maggi, A., et al. (2023). GEOSCOPE network: 40 Yr of global broadband seismic data. *Seismological Research Letters*, *95*(3), 1495–1517. https://doi.org/10.1785/0220230176
Lesage, P. (2009). Interactive Matlab software for the analysis of seismic volcanic signals. *Computers and Geosciences*, *35*(10), 2137–2144. https://doi.org/10.1016/j.cageo.2009.01.010
Lewandowska, H., & Teisseyre, R. (1964). Investigations of the ice microtremors on Spitsbergen in 1962. *Biul Inf Komisji Wypraw Geof PAN*, *37*, 1–5.
Lombardi, D., Benoit, L., Camelbeeck, T., Martin, O., Meynard, C., & Thom, C. (2016). Bimodal pattern of seismicity detected at the ocean margin of an Antarctic ice shelf. *Geophysical Journal International*, *206*(2), 1375–1381. https://doi.org/10.1093/gji/ggw214
Lombardi, D., Gorodetskaya, I., Barruol, G., & Camelbeeck, T. (2019). Thermally induced icequakes detected on blue ice areas of the East Antarctic ice sheet. *Annals of Glaciology*, *60*(79), 45–56. https://doi.org/10.1017/aog.2019.26
Lucas, E. M., Nyblade, A. A., Aster, R. C., Wiens, D. A., Wilson, T. J., Winberry, J. P., & Huerta, A. D. (2023). Tidally modulated glacial seismicity at the foundation ice stream, West Antarctica. *Journal of Geophysical Research: Earth Surface*, *128*(7), e2023JF007172. https://doi.org/10.1029/2023JF007172
Minowa, M., Podolskiy, E. A., & Sugiyama, S. (2019). Tide-modulated ice motion and seismicity of a floating glacier tongue in East Antarctica. *Annals of Glaciology*, *60*(79), 57–67. https://doi.org/10.1017/aog.2019.25
Mouginot, J., Rignot, E., Gim, Y., Kirchner, D., & Le Meur, E. (2014). Low-frequency radar sounding of ice in East Antarctica and southern Greenland. *Annals of Glaciology*, *55*(67), 138–146. https://doi.org/10.3189/2014AoG67A089
Murray, T., Smith, A. M., King, M. A., & Weedon, G. P. (2007). Ice flow modulated by tides at up to annual periods at Rutford Ice Stream, West Antarctica. *Geophysical Research Letters*, *34*(18), L18503. https://doi.org/10.1029/2007GL031207
Nanni, U., Roux, P., Gimbert, F., & Lecointre, A. (2022). Dynamic imaging of Glacier structures at high-resolution using source localization with a dense seismic array. *Geophysical Research Letters*, *49*(6), e2021GL095996. https://doi.org/10.1029/2021GL095996

21699011, 2025, 8, Downloaded from https://agupubs.onlinelibrary.wiley.com/doi/10.1029/2024JF008054 by Tifenn Le Bris - Cochrane France , Wiley Online Library on [02/09/2025]. See the Terms and Conditions (https://onlinelibrary.wiley.com/terms-and-conditions) on Wiley Online Library for rules of use; OA articles are governed by the applicable Creative Commons License

Neave, K. G., & Savage, J. C. (1970). Icequakes on the athabasca Glacier. *Journal of Geophysical Research (1896-1977)*, *75*(8), 1351–1362. https://doi.org/10.1029/JB075i008p01351

Nelder, J. A., & Mead, R. (1965). A Simplex method for function minimization. *The Computer Journal*, *7*(4), 308–313. https://doi.org/10.1093/comjnl/7.4.308

Osten-Woldenburg, H. V. D. (1990). Icequakes on ekström ice Shelf near Atka Bay, Antarctica. *Journal of Glaciology*, *36*(122), 31–36. https://doi.org/10.3189/S0022143000005517

Pattyn, F. (2018). The paradigm shift in Antarctic ice sheet modelling. *Nature Communications*, *9*(1), 2728. https://doi.org/10.1038/s41467-018-05003-z

Pawlowicz, R., Beardsley, B., & Lentz, S. (2002). Classical tidal harmonic analysis including error estimates in MATLAB using T_TIDE. *Computers and Geosciences*, *28*(8), 929–937. https://doi.org/10.1016/S0098-3004(02)00013-4

Pedley, M., Paren, J. G., & Potter, J. R. (1986). The tidal spectrum underneath Antarctic ice shelves. *Journal of Geophysical Research*, *91*(C11), 13001–13009. https://doi.org/10.1029/JC091iC11p13001

Pirli, M., Hainzl, S., Schweitzer, J., Köhler, A., & Dahm, T. (2018). Localised thickening and grounding of an Antarctic ice shelf from tidal triggering and sizing of cryoseismicity. *Earth and Planetary Science Letters*, *503*, 78–87. https://doi.org/10.1016/j.epsl.2018.09.024

Podolskiy, E. A., Sugiyama, S., Funk, M., Walter, F., Genco, R., Tsutaki, S., et al. (2016). Tide-modulated ice flow variations drive seismicity near the calving front of Bowdoin Glacier, Greenland. *Geophysical Research Letters*, *43*(5), 2036–2044. https://doi.org/10.1002/2016GL067743

Podolskiy, E. A., & Walter, F. (2016). Cryoseismology. *Reviews of Geophysics*, *54*(4), 708–758. https://doi.org/10.1002/2016RG000526

Provost, F., Zigone, D., Le Meur, E., Malet, J.-P., & Hibert, C. (2024). Surface dynamics and history of the calving cycle of Astrolabe Glacier (Adélie Coast, Antarctica) derived from satellite imagery. *The Cryosphere*, *18*(7), 3067–3079. https://doi.org/10.5194/tc-18-3067-2024

Rack, W., King, M. A., Marsh, O. J., Wild, C. T., & Floricioiu, D. (2017). Analysis of ice shelf flexure and its InSAR representation in the grounding zone of the southern McMurdo Ice Shelf. *The Cryosphere*, *11*(6), 2481–2490. https://doi.org/10.5194/tc-11-2481-2017

Rignot, E., Jacobs, S., Mouginot, J., & Scheuchl, B. (2013). Ice-Shelf melting around Antarctica. *Science*, *341*(6143), 266–270. https://doi.org/10.1126/science.1235798

Rignot, E., Mouginot, J., & Scheuchl, B. (2011). Ice flow of the antarctic ice sheet. *Science*, *333*(6048), 1427–1430. https://doi.org/10.1126/science.1208336

RINGS Action Group. (2022). RINGS: Collaborative international effort to map all Antarctic ice-sheet margin. *Zenodo*. (Scientific Committee on Antarctic Research). https://doi.org/10.5281/zenodo.6638327

Röthlisberg, H. (1955). Studies in Glacier physics on the Penny Ice Cap, Baffin Island, 1953: Part III: Seismic sounding. *Journal of Glaciology*, *2*(18), 539–552. https://doi.org/10.3189/002214355793702064

Röthlisberger, H. (1972). Water pressure in Intra- and subglacial channels. *Journal of Glaciology*, *11*(62), 177–203. https://doi.org/10.3189/S0022143000022188

Schoof, C. (2007). Ice sheet grounding line dynamics: Steady states, stability, and hysteresis. *Journal of Geophysical Research*, *112*(F3), F03S28. https://doi.org/10.1029/2006JF000664

Stutzmann, E., Schimmel, M., Patau, G., & Maggi, A. (2009). Global climate imprint on seismic noise. *Geochemistry, Geophysics, Geosystems*, *10*(11), Q11004. https://doi.org/10.1029/2009GC002619

The ObsPy Development Team. (2022). ObsPy 1.4.0 [Software]. *Zenodo*. https://doi.org/10.5281/zenodo.6645832

Togaibekov, A., Le Bris, T., Le Meur, E., Barruol, G., Gimbert, F., Zigone, D., & Lombardi, D. (2024). GNSS data at the Astrolabe Glacier [Dataset]. *Zenodo*. https://doi.org/10.5281/zenodo.14003385

Vaughan, D. G. (1993). Relating the occurrence of crevasses to surface strain rates. *Journal of Glaciology*, *39*(132), 255–266. https://doi.org/10.3189/S0022143000015926

Weertman, J. (1957). On the sliding of glaciers. *Journal of Glaciology*, *3*(21), 33–38. https://doi.org/10.3189/S0022143000024709

Winberry, J., Anandakrishnan, S., Wiens, D. A., & Alley, R. B. (2013). Nucleation and seismic tremor associated with the glacial earthquakes of Whillans Ice Stream, Antarctica. *Geophysical Research Letters*, *40*(2), 312–315. https://doi.org/10.1002/grl.50130

Zoet, L. K., Anandakrishnan, S., Alley, R. B., Nyblade, A. A., & Wiens, D. A. (2012). Motion of an Antarctic glacier by repeated tidally modulated earthquakes. *Nature Geoscience*, *5*(9), 623–626. https://doi.org/10.1038/ngeo1555

21699011, 2025, 8, Downloaded from https://agupubs.onlinelibrary.wiley.com/doi/10.1029/2024JF008054 by Tifenn Le Bris - Cochrane France , Wiley Online Library on [02/09/2025]. See the Terms and Conditions (https://onlinelibrary.wiley.com/terms-and-conditions) on Wiley Online Library for rules of use; OA articles are governed by the applicable Creative Commons License

4.3 Comparison with 2024 and 2025 dense arrays

We compare some of the results obtained for the dense 2023 array A1, presented and analyzed in detail in the paper, with those from the two other dense arrays A2 and A3 deployed on the glacier. Figure 4.1 shows the locations of the seismic nodes of the dense arrays A2 and A3 respectively deployed during the 2024 and 2025 field campaigns. In particular, we compare the icequake activity rates to assess the degree of repeatability between A1, A2, and A3 across the overlapping sections of the arrays deployed over successive years. We also discuss the differences in activity rates that may arise from their respective locations: A1 and A2 near the grounding zone, and A3 along the lateral shear margin.

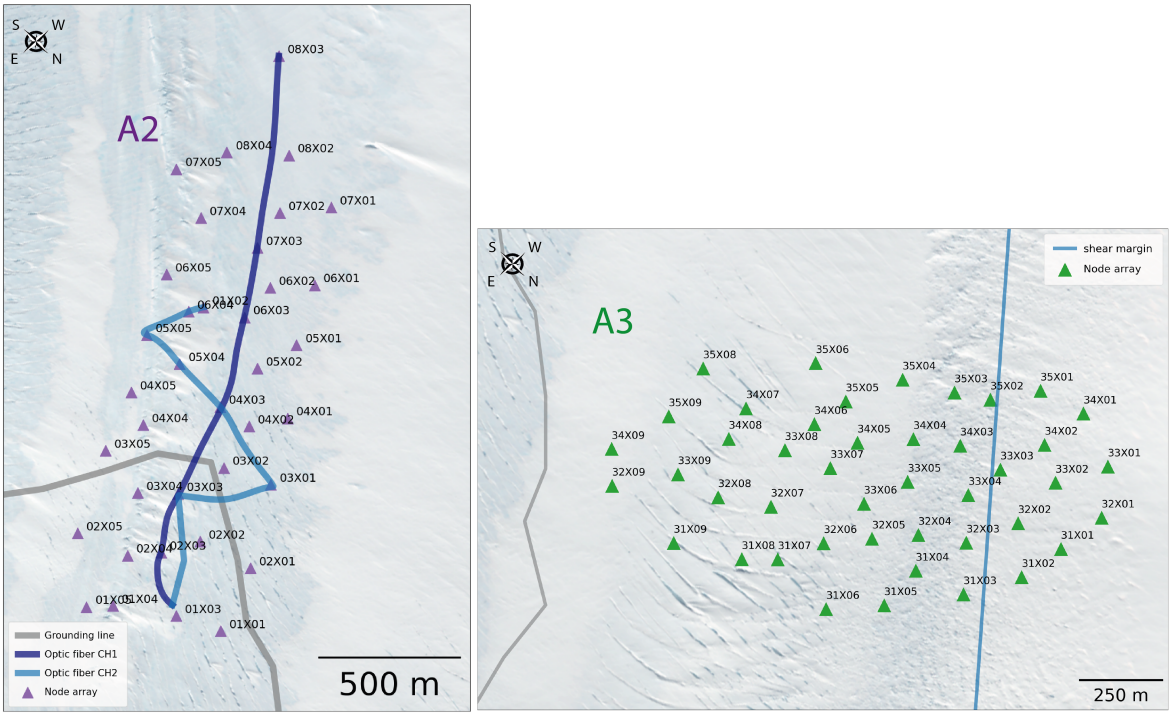

Figure 4.1: Map of the seismic nodes positions for the dense arrays A2 (left) and A3 (right). For position of the arrays on the glacier, see Fig. 2.5, Chapter 2.

As in previous analyses, temporal variations in icequake activity recorded by the dense arrays are characterized by computing the number of detected events per hour, providing an effective proxy for spatiotemporal variability in seismicity. As for the dense array A1, icequake detections are performed using the STA/LTA algorithm introduced in Chapter 3. For A3, the detection parameters are slightly adjusted to account for local variations in the signal-to-noise ratio: the short-term average (STA) was set to 0.5 s, the long-term average (LTA) to 6 s, with triggering thresholds thrOn = 4 and thrOff = 2.

Figure 4.2 presents the average hourly icequake activity (in count per hour) over the deployment period, and its standard deviation for the three arrays (A1, Fig. 4.2a; A2, Fig. 4.2b; A3, Fig. 4.2c) superimposed on the tidal amplitude. For A1, the icequake activity typically exhibits one or two peaks per tidal cycle. During the initial cycles, a single peak is observed either at high tide (11–13 January 2023) or immediately after (16–17 January 2023). As the tidal regime evolves and tide amplitudes increase, the pattern transitions to two peaks per cycle, occurring at mid-rising and mid-falling tide. For A2, the maximum activity occurs near high tide, occasionally displaying two peaks at mid-rising and mid-falling tide. Between 19 and 23 January 2024, activity is dominated by a single peak coinciding with the falling tide. The transition from spring to neap tides, associated with reduced tidal amplitudes, does not significantly modify either the overall activity rate or its temporal distribution.

For A3, between 9 and 15 January 2025, two peaks are generally observed per tidal cycle, with the mid-falling tide peak consistently exceeding that at mid-rising tide. During neap tides (from 17 January onward), the pattern simplifies to a single peak per cycle, centered around high tide. During the period of adverse weather (16–17 January 2025), the correlation with the tide becomes less distinct, likely due to elevated noise levels making events detections less reliable. Over the period of instrumental deployment, the activity rate is lower than for A1 and A2 with peaks respectively rarely exceeding 100 events per hour against above 200 and 150 events per hour. This decrease coincides with both a transition towards neap tide (lower tidal amplitudes) and a shift from a diurnal to a semi-diurnal tidal regime. During the shift from spring to neap tides and from diurnal to semi-diurnal cycles, the icequake activity pattern evolves from two daily peaks to a single peak occurring near high tide, despite the lower overall tidal amplitude. Notably, icequake activity tends to be stronger during the falling tide. This observation is consistent with previous results (see Fig. 10 in (Le Bris et al., 2025)), which demonstrate that seismic activity along the glacier's lateral margins peaks during the falling tide. This behaviour likely reflects enhanced stress accumulation during the flexural response of the floating tongue at falling tide, which may induce brittle fracturing (icequakes).

Despite complexities in the patterns, the observations collectively confirm that icequake activity is modulated by tidal forcing, whether considering the grounding zone or the lateral shear margin. The variability in the number of peaks per tidal cycle remains difficult to interpret. However, some consistent features emerge. When two peaks occur, they systematically coincide with mid-rising and mid-falling tides, corresponding to the periods of highest tidal velocity. When only one peak is observed, it typically occurs near high tide (maximum tidal amplitude) or mid-falling tide. The amplitude of the icequake rate peaks does not appear to depend strongly on the overall tidal amplitude (i.e., between spring and neap tides). But the shifting from spring to neap tide seems to impact whether it is single or double peak, or even just affect the pattern without clear peak during the daily tidal cycle (for instance, on 14 January 2023).

Overall, the icequake activity appears to be tidally driven yet capable of maintaining its own quasi-periodic rhythm, oscillating in sync with but not strictly controlled by the tidal cycle.

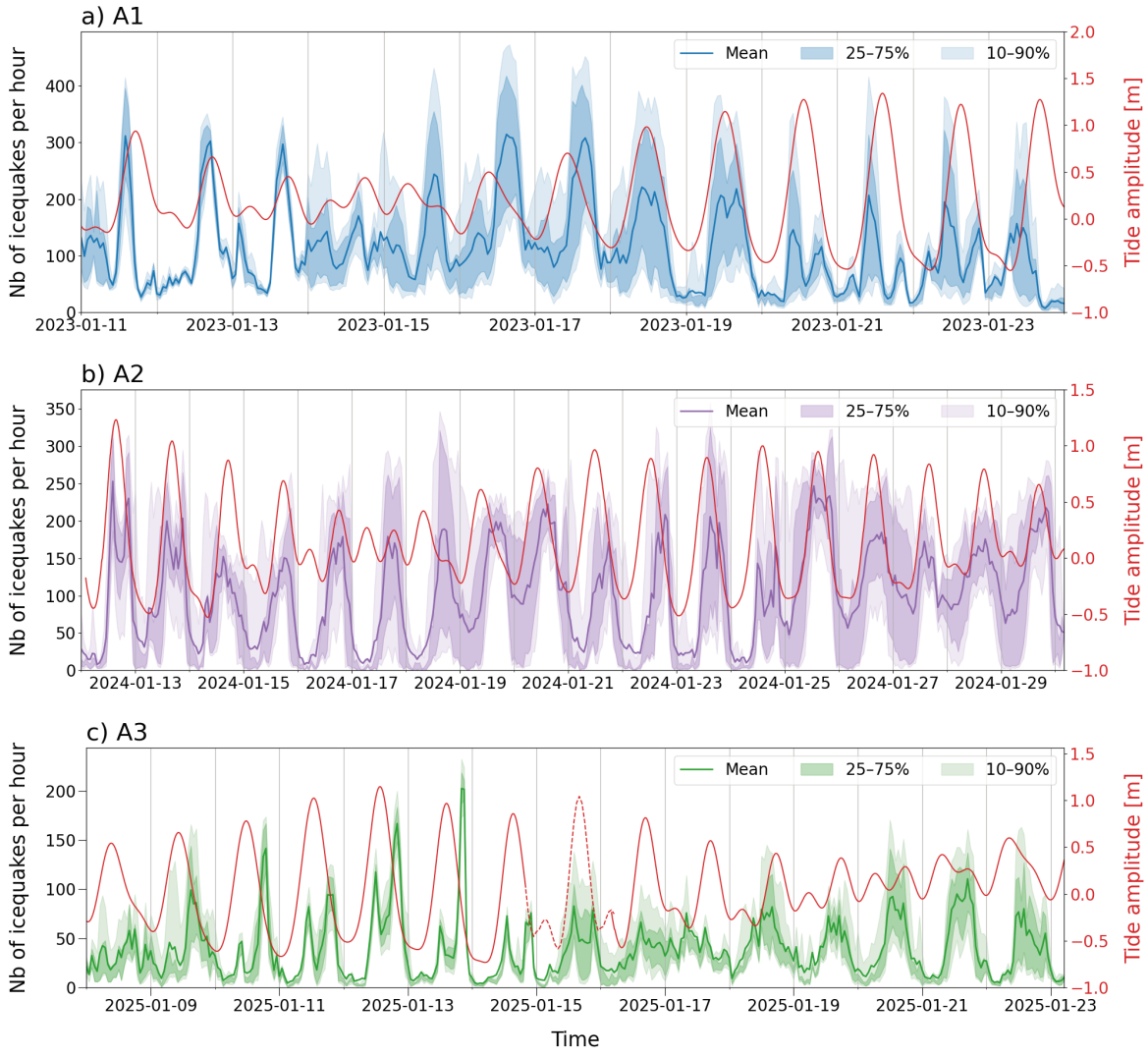

Figure 4.2: Comparison of the correlation between the mean icequake activity rate (in count per hour) and tide amplitude (red) for the dense arrays A1 ((a), in blue), A2 ((b), in purple) and A3 ((c), in green). The 25-75% and 10-90% percentiles are presented in light colors. Note the y-axis are different for each panel.

Note that correlation between icequake activity rate and weather parameters (wind, temperatures) has been explored but does not show any clear link, except that strong wind may increase the overall seismic noise level and decrease the detection reliability (see Figure B.8).

Figure 4.3a now compares the icequakes rate (in count per hour) distribution for the three dense arrays. Because A1 covers different areas (e.g., floating ice, grounded ice, shear margin) with varying icequake rates (see Fig. 9, Le Bris et al., 2025), the distribution is more spread. It ranges from few tens of events per hour to more than 400 events per hour. For the dense array A2 of 2024, it is located within the array A1 delineation, in the active part. Icequake rate is between tens of events per hour to 350 events per hour. It is slightly lower than for the array A1 because it is not covering the floating part of the grounding zone which A1 lays over (as defined by Le Meur et al., 2014) and where events are the most frequent. As for dense array A3, icequake rate is mainly below 100 events per hour and does not exceed 200 events per hour. It is in accordance with the icequake rates of the northwest most lines of array A1, which corresponds to the grounded part of the array, in the shear margin area.

We can further confront the icequake activity rates of the three dense arrays by looking at the spatial distribution of the activity rates. Figure 4.3b shows a map of the average icequake rate at each station of each dense array A1, A2 and A3. We observe a good coherence, despite each array being deployed in different years. The A3 stations icequake rates match with the A1 stations that were in the same area the year before. We will further investigate this dense array located over the shear margin in chapter 6. Between A1 and A2, it is also mostly the same order of magnitude between stations in the same area. This intercomparison suggests an overall good consistency and reliability of the measures over the three years of field experiments.

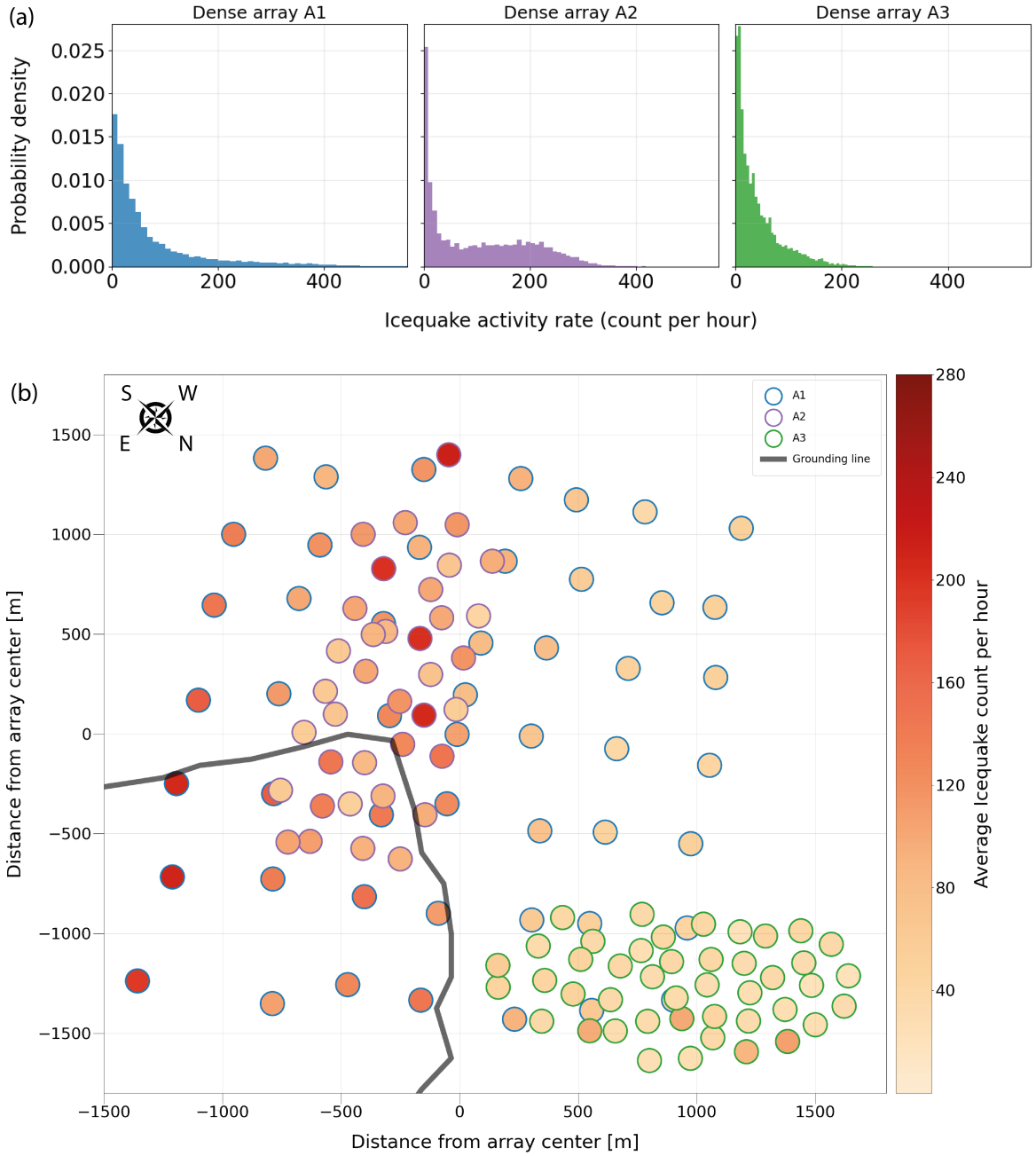

Figure 4.3: (a) From left to right. Histogram of icequake activity rates (in count per hour) for all stations of dense array A1 (blue), dense array A2 (purple), both deployed over the grounding zone and dense array A3 (green) deployed over the shear margin. (b) Map of the hourly average icequake activity (color-coded in red, indicating the average icequake count per hour) recorded at each station of the seismic dense arrays A1 (blue circle), A2 (purple circle) and A3 (green circle) during their respective periods of deployment.

4.4 Outcomes and outlook

By combining long-term broadband recordings with dense-array observations, this study provides a multi-scale characterization of icequake activity at the Astrolabe Glacier. Using the STA/LTA automatic detection method, thousands of events were identified across multiple years and deployment configurations. We quantify seismic activity through event rates, providing a robust metric for analyzing temporal and spatial variations in glacier response to tidal forcing.

At the glacier-wide scale, long-term broadband stations capture the temporal variability of icequake activity across several years, revealing a clear modulation by tides. At finer spatial and temporal scales, dense arrays deployed across the grounding zone provide higher-resolution observations, resolving localized changes in seismicity over individual tidal cycles. Within the grounding zone, seismicity exhibits a distinct spatial partitioning: during rising tides, activity is concentrated over the floating tongue, while during falling tides, it shifts upstream to the grounded ice. Independent GNSS measurements confirm strain rates consistent with brittle failure, supporting the interpretation that icequakes result from tidal flexure of the glacier. Moreover, this spatial pattern aligns with the geometry of the grounding line, suggesting that icequake activity can serve as a reliable proxy for its position.

Intercomparison of datasets acquired in 2023, 2024, and 2025 reveals consistent spatial patterns of icequake activity, indicating stable deformation regimes at the surface of the grounding zone. It reinforces the robustness of the observed tidal modulation and point to persistent mechanical processes operating over multiple years.

Some aspects of the tidal modulation still remain difficult to understand. The occurrence of either one or two seismicity peaks within a diurnal cycle, and the persistence of activity even during neap tides suggest that additional processes may influence glacier deformation. Indeed, surface brittle deformation appears largely tidally driven, yet it maintains a quasi-periodic rhythm at times where the tide amplitude is minimal. Understanding this behavior will require integrating seismic observations with models of ice deformation that take into account both surface brittle fracture of the ice and cyclic strain in response to tides.

Building on the main results presented in this chapter, we further investigate the grounding zone dynamics of the Astrolabe Glacier. In particular, we look into how seismic observations can be used to track grounding line migration at sub-daily timescales, providing new high-resolution constraints on a process that remains poorly resolved in glacier dynamics.

CHAPTER 5

Daily migration of grounding lines: insights from tide-modulated icequake and stick-slip events

Contents

5.1 Introduction 96

5.2 Surface icequakes and basal stick-slip events reveal daily grounding line migration and seawater intrusion at a marine-terminating glacier in East Antarctica (Le Bris et al., submitted) 97

5.2.1 Abstract 97

5.2.2 Introduction 97

5.2.3 Data 99

5.2.3.1 Study site 99

5.2.3.2 Observations : dense array of seismic nodes, GNSS and tide data 100

5.2.4 Methods 101

5.2.4.1 Icequakes detection, occurrence and location 101

5.2.4.2 Stick-slip events detection and location 102

5.2.5 Results 105

5.2.5.1 Migration of the grounding zone over tidal cycle: surface icequakes signature 105

5.2.5.2 Stick-slip dynamics at the grounding zone during tidal cycles 105

5.2.6 Discussion 110

5.2.7 Conclusion 113

5.2.8 Acknowledgements and Data Availability 113

5.3 Outcomes and outlook 114

5.1 Introduction

In Chapter 4, we demonstrated that the seismic signature of surface brittle deformation induced by tidal flexure provides a reliable proxy for delineating the grounding line position and, more broadly, for characterizing grounding zone dynamics under tidal forcing. The high temporal and spatial resolution of our dense seismic array enabled us to capture sub-daily variations in icequake occurrence linked to the tidal cycle. These findings raise a key question: can we constrain short-term changes in grounding line position and map its daily migration as tidal forcing drives seawater intrusion beneath the glacier?

Current observational techniques, such as satellite altimetry, radar interferometry, and ground-based radar, can track grounding line position with meter-scale spatial precision. However, they cannot continuously monitor its migration over consecutive tidal cycles, as their uneven and sparse temporal coverage limits high-frequency observations (Mohajerani et al., 2021). No continuous time series currently captures grounding line motion at sub-daily resolution. Our analysis of surface icequakes has shown that seismic monitoring can overcome this limitation, by providing a means to track grounding line position continuously over short time periods. However, as with most surface-based observations, these icequakes which are induced by tidal flexure, provide only indirect information on the mechanical grounding line, which is located at the glacier bed. To better constrain our interpretation, we also look into seismic signals originating from the glacier base, so-called stick-slip events. These basal events are generated by frictional sliding of the ice over bedrock asperities, periodically reactivated by glacier flow. Because they occur directly at the ice–bed interface, they reflect processes governing the critical transition zone between ice, ocean, and bedrock, including grounding line migration, seawater intrusion, and hydrostatic pressure variations driven by tides.

Using the dense seismic array A1 deployed over the grounding zone, we analyze the occurrence patterns and spatial distribution of both surface icequakes and basal stick-slip events over consecutive tidal cycles. This combined approach provides an integrated, high-resolution view of grounding zone dynamics and help constrain the daily migration of the grounding line under tidal forcing.

In the following section, I present the paper detailing this analysis, submitted in *The Cryosphere*.

5.2 Surface icequakes and basal stick-slip events reveal daily grounding line migration and seawater intrusion at a marine-terminating glacier in East Antarctica (Le Bris et al., submitted)

Tifenn Le Bris[1], Guilhem Barruol[1], Florent Gimbert[1], Emmanuel Le Meur[1], Dimitri Zigone[2,3], Maxime Bès de Berc[2], Armelle Bernard[3]

[1]. Univ. Grenoble Alpes, CNRS, INRAE, IRD, Grenoble INP, IGE, 38000 Grenoble, France
[2]. Université de Strasbourg/CNRS, Institut Terre et Environnement de Strasbourg, UMR7063, 67084 Strasbourg Cedex, France
[3]. Université de Strasbourg/CNRS, Ecole et Observatoire des Sciences de la Terre, UAR830, 67084 Strasbourg Cedex, France

Key words: Grounding zone, Cryoseismology, Antarctica, Marine-terminating glacier

5.2.1 Abstract

As they reach the ocean, Antarctic outlet glaciers transition from grounded to floating at their so-called grounding lines (GL). This transition is known to be mechanically controlled by tides, which induce ice flexure visible at the surface from satellite and ground geodesy and often used as a proxy for grounding line position. Here, we use a dense seismic nodes array to study the spatial and temporal dynamics of surface, crevasse-induced icequake activity and basal, sliding-induced seismicity at the grounding zone of the Astrolabe Glacier, a fast-moving outlet glacier in East Antarctica. We observe that surface icequakes mimic the expected ice, tide-induced, flexure pattern, as they delineate the grounding line position inferred from previous geodetic studies, and migrate landward as tides rise. We show, however, that the actual grounded to floating transition is better evidenced by the spatial distribution of basal sliding-induced stick-slip events, occurring on a limited number of clusters and which depict a grounding line position that is offset inland compared to that identified from the surface. These basal events undergo tidally-driven cycles of activation and de-activation, consistent with sea water intrusion inland over at least 3 kilometers at high tides. Following these results, we propose that the monitoring of stick-slip events could be used as the most accurate means of tracking grounding line retreat over long timescales.

5.2.2 Introduction

The Antarctic ice sheet naturally flows towards the ocean through outlet glaciers that meet the ocean at their grounding lines (GL), which represent the boundary between

grounded ice sheet and floating ice shelves. Foundational studies have shown that variations in grounding line position strongly influence ice mass loss (Rignot et al., 2011a; Schoof, 2007; Vaughan, 1994). As the grounding line retreats toward the continent, for instance by the effect of basal melting and ice thinning, the reduction in buttressing effect allows faster ice flow, increasing ice mass loss and ultimately contributing to sea level rise. Improving projections of future sea-level rise therefore requires a more detailed understanding of the processes and boundary conditions that govern grounding lines positions and dynamics.

While we tend to focus on the long-term changes for sea-level projections, a major control on grounding line dynamics may occur at a short time scale under the response of the glacier to the daily and sub-daily tidal forcing. Tide-induced variations in sea level height cause indeed a vertical up-and-down displacement of the floating ice and therefore a horizontal back-and-forth migration of the grounding line, forming a dynamic area at the ice-bedrock interface called grounding zone (GZ) (Freer et al., 2023; Rignot et al., 2024). This daily migration changes the coupling state at the ice-bedrock interface, modulating the glacier basal sliding behavior (Christmann et al., 2021; Yan et al., 2024). Rising water pressure during high tides is expected to lubricate the bed and to enhance sliding (Gagliardini et al., 2007; Lliboutry, 1968; Schoof, 2005), while falling tides increase basal friction at the ice-bedrock interface (Robel et al., 2017). This tidal "breathing" is also expected to generate strong subglacial ocean water advection that may enhance ocean-ice interaction and basal melt processes.

A range of observational techniques, including satellite altimetry, radar interferometry (InSAR), optical imagery, airborne and terrestrial radar systems, have expanded our capabilities to track grounding line positions, down to meter-scale spatial resolution (e.g., Bindschadler et al., 2011). However, their uneven and sparse temporal data coverages limit the high temporal resolution analysis needed for studying daily GL migration and associated changes in basal conditions (Mohajerani et al., 2021). Altimetry data from ICESat observations revealed tide-induced flexure of the southern Ronne Ice Shelf and, by combining multiple tracks spread over several years, enabled regional-scale estimates of tidally driven GL migration at different tide heights (Freer et al., 2023). Similarly, daily DInSAR observations from the ICEYE constellation captured short-term GL migration at the main trunk of Thwaites Glacier (Rignot et al., 2024). Yet, neither approaches provide continuous grounding line position time series or constraints on basal friction states. Both are however essential to fully capture GL behavior over tidal cycles (Friedl et al., 2020; Rignot et al., 2011a) and to provide constraints on the tidal pumping effect that could enhance ice-ocean thermal exchanges and basal melting at GL (Begeman et al., 2020; Gadi et al., 2023; Walker et al., 2013).

By its ability in detecting and locating events generated by ice friction and brittle deformation, cryoseismology is a good candidate for such continuous and high resolution monitoring of grounding line dynamics. Among cryoseismic signals recorded

at outlet glaciers, tide-modulated icequakes occurring close to the surface have been linked to temporal and spatial variations in stress from the glacier cyclic bending in response to tidal forcing on sea-level height (e.g. Barruol et al., 2013; Cooley et al., 2019; Fromm et al., 2023; Hulbe et al., 2016; Le Bris et al., 2025; Lombardi et al., 2016). When recorded by a dense seismic array, icequakes also demonstrated their ability to provide a means of delineating the grounding line (Le Bris et al., 2025).

Seismic events at the ice-bed interface reveal the complementary mechanisms of glaciers sliding over the bedrock. The so-called stick-slip events have been observed across a variety of glacial environments, including Antarctic ice streams (Anandakrishnan & Alley, 1997; Barcheck et al., 2018; Danesi et al., 2007; Hudson et al., 2023a; Kufner et al., 2021; Winberry et al., 2013; Zoet et al., 2012), Greenland Ice Sheet (McBrearty et al., 2020; Roeoesli et al., 2016) and Alpine glaciers (Gräff et al., 2021; Helmstetter et al., 2015; Hudson et al., 2020). In some cases of coastal ice streams and outlet glaciers, tidal cycles have been demonstrated to modulate basal seismicity, with periodic basal stress changes triggering stick-slip behavior (Pratt et al., 2014; Walter et al., 2015b; Winberry et al., 2009; Zoet et al., 2012). However, no direct means of monitoring grounding line migration from these events has yet been established.

Through the combined analysis of surface icequakes and basal stick-slip seismicity, this study aims at providing direct insights into the grounding line position and migration at daily timescales. By using a dense array of seismic nodes deployed over the grounding zone of an outlet glacier from East Antarctica, we detect and determine the temporal and spatial distribution of both types of events recorded during consecutive daily tidal cycles and investigate how tide-induced surface brittle deformation and changes in frictional conditions at the ice-bedrock interface are connected to the grounding line dynamics.

5.2.3 Data

5.2.3.1 Study site

The Astrolabe Glacier (Terre Adélie, East Antarctica) is an outlet glacier located next to the Dumont d'Urville (DDU) research station. It has been the site of several studies including GNSS, radar and seismology surveys, all focused on constraining the glacier dynamics (Barruol et al., 2025; Le Bris et al., 2025; Le Meur et al., 2014; Provost et al., 2024). Figure 5.1 presents the site location. The floating part of the Astrolabe Glacier is laterally constrained within a fjord with valley walls estimated to be at least 500 to 600 m deep, covered by grounded stable ice. In some areas of the GZ, the thickness of the floating tongue has been estimated at approximately 700 m, gradually thinning to around 300 m at its terminus (Le Meur et al., 2014). With only limited direct observations, these values likely vary along the glacier. In front of the terminus, sparse bathymetric surveys offshore (Beaman et al., 2011) show that the fjord bathymetry

extends deeper than 1,000 m, suggesting a large subglacial cavity beneath the floating ice tongue, prone to ocean intrusion and ice basal melting. The current grounding line position is determined by integrating ice thickness data defining the line of buoyant flotation with kinematic GPS measurements of vertical motion due to tidal flexure (Le Meur et al., 2014).

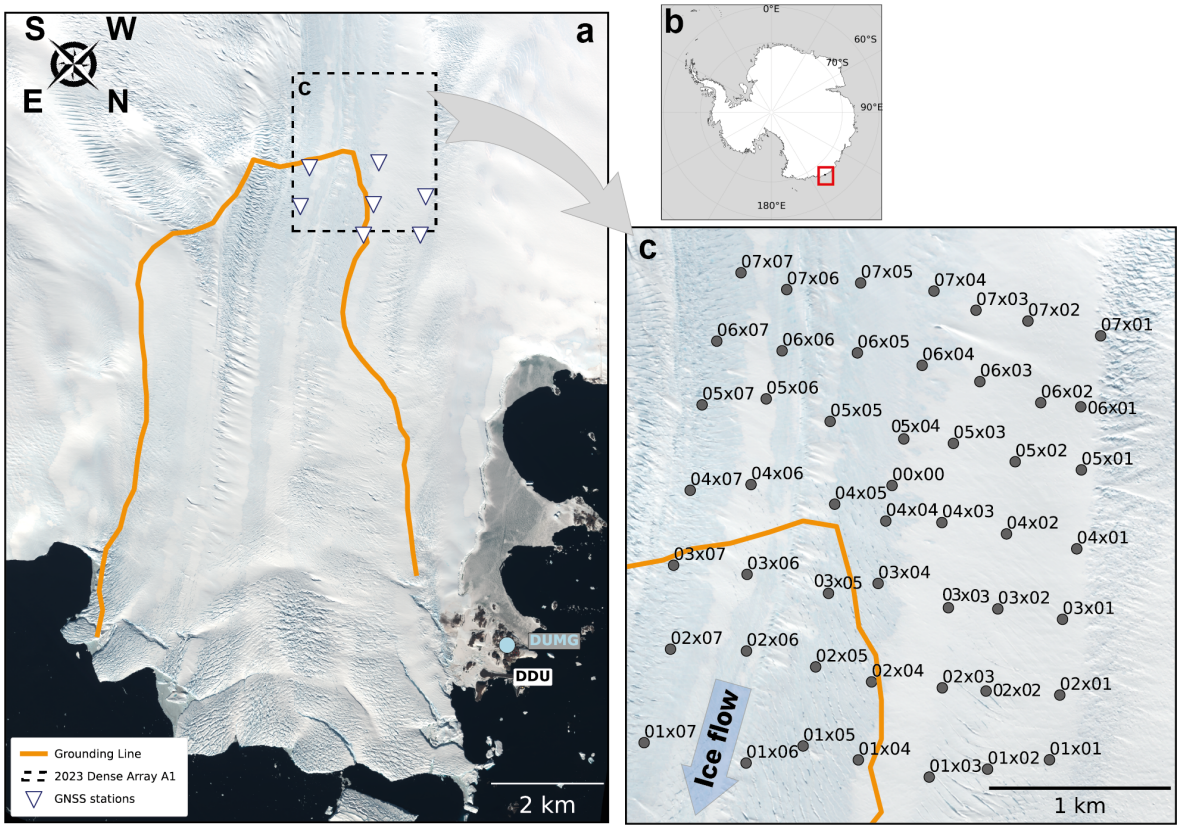

Figure 5.1: 2023 seismic deployment on the Astrolabe Glacier, East Antarctica. (a) Map of the Astrolabe Glacier region, near the French base station Dumont d'Urville (DDU). The background image is a Pleiades satellite acquisition from January 10, 2025. The dotted black rectangle indicates the locations of the 2023 dense seismic array and includes the GNSS permanent stations (white triangles) and the DUMG reference station. The orange line represents the "geodetic" grounding line as estimated by Le Meur et al. (2014). (b) Location of the study area along the East Antarctica coast. (c) Close-up view of the 2023 deployment: 50 seismic nodes (black dots) installed across the grounding zone.

5.2.3.2 Observations : dense array of seismic nodes, GNSS and tide data

During the Austral summer 2023, a dense seismic node array was deployed on the Astrolabe Glacier using *SmartSolo* IGU-16HR 3C instruments (Barruol et al., 2025). The deployment consisted of 50 three-component stations installed across the grounding zone, as delineated by Le Meur et al. (2014) from surface geodetic measurements.

The array operated continuously from 10, Jan. 2023 to 02, Feb. 2023, with a sampling rate of 500 Hz. The inter-station spacing averages 400 m, covering an area of approximately 7 km^2. This configuration was designed to resolve fine-scale seismic sources along the transition from grounded to floating ice. Seismic nodes were inserted into drilled snow pits approximately 50 cm deep and covered with compacted snow to favor re-freezing around them. We observed an expected horizontal station displacement up to ∼20 m, over the deployment period.

We collected ground-based GNSS measurements at 7 sites on the glacier, using multifrequency Trimble NetR9 receivers and Trimble Zephyr Geodetic antennas (Figure 5.1). We processed GNSS phase observables, sampled at 30 s intervals, in kinematic mode using the TRACK software (Chen, 1999; Herring et al., 2018) and using multiple GNSS constellations (GPS, GLONASS, and Galileo). The position of the survey sites on the glacier was determined with respect to the reference station DUMG installed at the close-by Dumont d'Urville site (Figure 5.1).

Sea level height is obtained using the PM36S MarArgos automatic tide gauge DUMON, installed at the DDU base (NIVMER/ROSAME project, Calzas et al., 1992). The sampling interval is 2 minutes. The daily tidal pattern alternates between diurnal cycles (one high tide per 24 hours) and mixed diurnal cycles. In mixed diurnal cycles, the dominant high tide reaches 1.5-2 m amplitude, while the secondary high tide amplitude is much smaller, on the order of only a few tens of centimeters.

5.2.4 Methods

5.2.4.1 Icequakes detection, occurrence and location

Icequakes are impulsive seismic events broadly accepted to be generated by brittle fracturing within the ice (Lewandowska & Teisseyre, 1964; Neave & Savage, 1970; Osten-Woldenburg, 1990; Röthlisberg, 1955; Röthlisberger, 1972).These events generally dominate the seismic records by their amplitudes. Their waveforms are characterized by a lack of clear P- or S-wave onsets or distinguishable seismic phases. They often exhibit a dominant frequency content between 5 and 40 Hz. Here, we apply the same method as Le Bris et al. (2025) to detect icequakes in the continuous time series using a standard Short-Term Average over Long-Term Average (STA/LTA) algorithm (Allen, 1978; Lesage, 2009). We perform the detection on the vertical component of the seismic signal band-pass filtered between 5 Hz and 40 Hz with the following detection parameters: STA = 0.5 seconds; LTA = 5 seconds; trigger-on and off thresholds set to 5 and 2, respectively.

We detect thousands of low-magnitude icequakes across the dense array area. To assess their activity spatial variations, we adopt a statistical approach. This is particularly relevant here, as we overcome the challenge of locating icequakes using standard

methods which fail to accurately pick phases, likely due to surface crevassing affecting the waveforms (Le Bris et al., 2025). For each station, we compute the icequake occurrence rates, defined as the number of events detected in a two-hour window. Occurrence rates observed at each node are then spatially interpolated over the array surface using a kriging method (Cressie, 1993; Kitanidis, 1997) (Text C, 7.5.2). Here, we compute occurrence rates over seven consecutive 24-hour tidal cycles, from January 17 to 24, 2023 and then average and interpolate the occurrence rates to build a time series extending over a single representative 24-hour tidal cycle.

5.2.4.2 Stick-slip events detection and location

Stick-slip events are pervasively present in the seismic data but have amplitudes overall three times smaller than the icequakes. They are characterized by their short duration (typically < 1 second), high frequency content (25–100 Hz), and highly repetitive waveforms with distinct P- and S-wave arrivals (Fig. 5.2a) suggesting an extremely constant source and focal mechanism. In the raw waveform data, they appear as bursts of repeating signals occurring at very constant time intervals and clustered over several hours (Fig. 5.2b).

Our stick-slip detection methodology operates in three main steps. First, through visual inspection of the continuous seismic data, we select a template characterized by clear P- and S-phases (Gräff et al., 2021; Helmstetter et al., 2015; Hudson et al., 2023a; Roeoesli et al., 2016). The window is typically 0.5 s long. Second, using a Template Matching Detection approach, we look for events matching the selected template over the full time series of one station showing the best signal quality. We consider a detection as a potential stick-slip event if the correlation is above 0.65. This threshold is chosen based on the correlation coefficient gaussian distribution of manually checked events, which decays exponentially below 0.65. Finally, we limit false positive detections by performing visual comparison of all events detected with the mean waveform computed from averaging events with highest correlation coefficient (usually above 0.95 to ensure very little variations in waveform amplitude between events) (Fig. 5.2a). If some of the false positives have similar characteristics to the template but show different waveforms, they are classified as new clusters, and are then used as templates to detect associated events. Similar methods have frequently been used to detect basal events, with correlation coefficient thresholds depending on whether a more cautious (higher threshold) or more exhaustive (lower threshold) approach is chosen (Allstadt & Malone, 2014; Carmichael et al., 2012; Helmstetter et al., 2015; Mikesell et al., 2012; Thelen et al., 2013).

We then locate clusters of stick-slips using the Python package QuakeMigrate (Hudson et al., 2020; Winder et al., 2025). Due to the wide spacing between seismic stations ($\sim$400 m), S-wave arrivals are often difficult to observe (Fig. 5.2c), such that we only rely on P-wave arrivals for initial location. As a consequence, the initial depth esti-

mates carry high uncertainty (Fig. 5.2d). To refine it, we perform a grid search around the initial QuakeMigrate location on stacked waveforms which better resolve S-wave arrivals (Fig. 5.2e). We test different source positions to minimize the misfit between observed and predicted source-receiver distances. To evaluate the misfit, we compute the Root Mean Square Error (RMSE) using the following equation:

$$RMSE = \sqrt{\frac{\sum_{i=1}^{M}(\Delta d_{\mathrm{pred}_i} - \Delta d_{\mathrm{obs}_i})^2}{M}} \tag{5.1}$$

where M is the number of stations used to constrain the RMSE and Δd_{pred} and Δd_{obs} are respectively the predicted and observed source-station distance with

$$\Delta d_{\mathrm{obs}_i} = (T_S - T_P)_i . \frac{V_P . V_S}{V_S - V_P} \tag{5.2}$$

where T_P and T_S are the P-wave and S-wave arrival times, and V_P and V_S the P-wave and S-wave velocities. We manually pick P- and S- wave arrival times from stacked waveforms, where the S-wave is made more visible as shown Fig. 5.2e.

We perform the grid search in the 6 dimensions X, Y, Z, V_P, V_S and $(T_S - T_P)$, where (X, Y, Z) vary within a 2 km x 2 km x 1 km cube around the initial source location, V_P in the range 3,800 - 4,000 m/s and VS in the range 1,700 –1,900 m/s (Llorens et al., 2020; Wittlinger and Farra, 2012). This refinement reduces the uncertainty for the depth estimate, giving a more confident location (Fig. 5.2f). We account for picking error by performing the grid search with $(T_S - T_P)$ varying within an uncertainty of ± 8 ms. P-wave incidence angles determined from polarization analysis confirms the depth of the clusters and reliability of the method. For clusters where S-wave arrivals are too difficult to pick precisely, even after stacking, no depth is assigned (around 24% of the clusters).

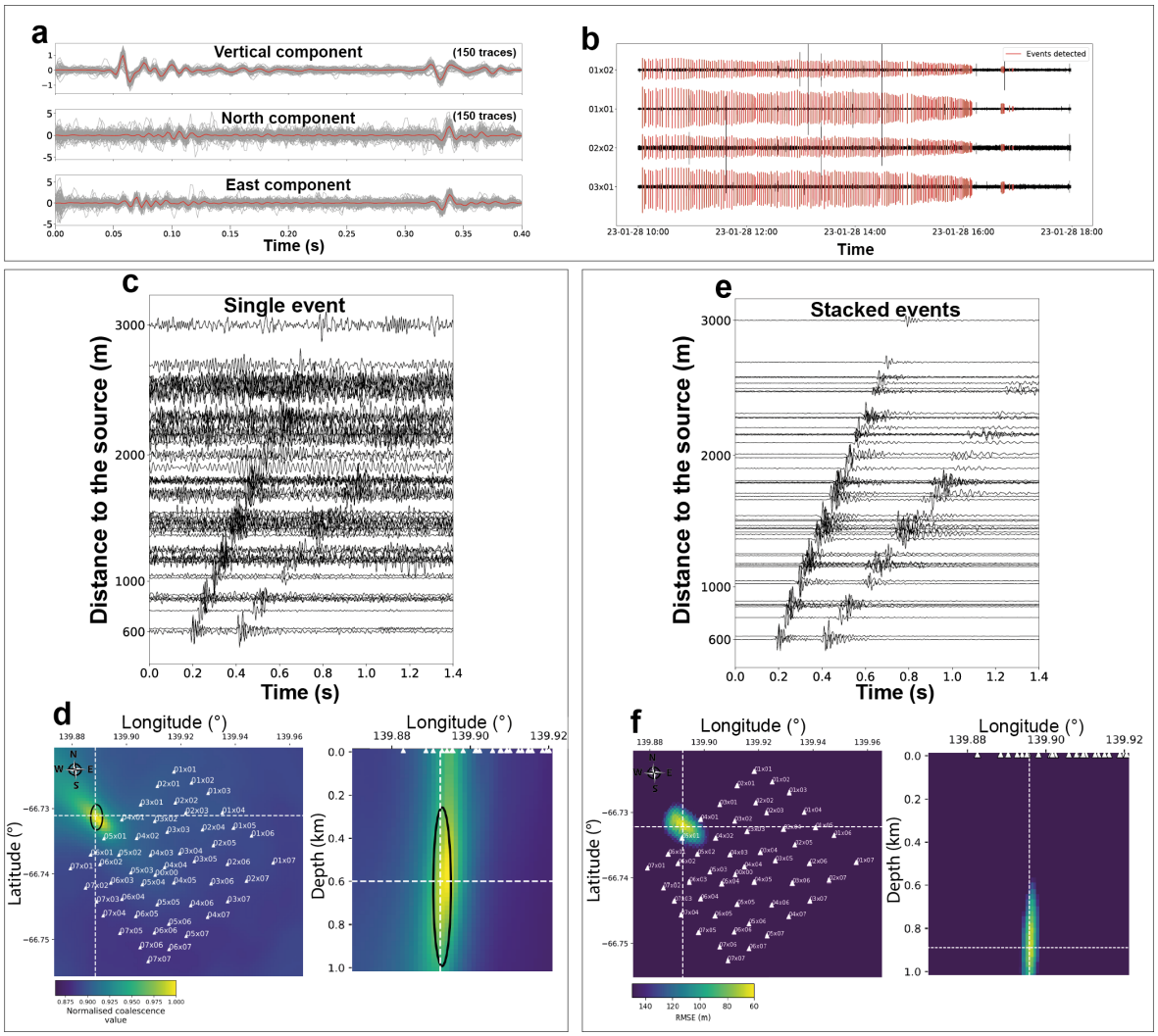

Figure 5.2: Stick-slip detection and location procedure. (a) Stacked waveform (red) from a cluster of stick- slip events (cluster 15), as observed at station 03x01 on the three components. Individual normalized waveforms from the cluster (150 traces) are shown in grey, highlighting the high waveform similarity within the cluster. (b) Eight-hour window of continuous seismic data on Jan. 28, 2023 from four stations (03x01, 02x02, 01x01, and 01x02), on the vertical component, during a period of activity for cluster 15. Red segments indicate individual detections identified via template matching with the selected cluster template. Amplitudes are independently normalized for each station. (c) Waveforms of a single event from cluster 15 (vertical component) recorded at the 50 stations plotted as a function of epicentral distance from the cluster source location. Seismograms are filtered between 25 and 100Hz. (d) Location of cluster 15 based on QuakeMigrate (Winder et al., 2025). Normalised coalescence value represents how well seismic arrivals from all stations "stack" coherently at a given point in the 3D grid. (e) Stacked waveforms of 767 events from cluster 15 (vertical component) at the 50 stations plotted as a function of epicentral distance from the cluster source location. Seismograms are filtered between 25 and 100Hz. (f) Refined location of cluster 15 from grid search. RMSE value is based on the difference between observed and modeled time arrival of P and S waves from manual picking.

5.2.5 Results

5.2.5.1 Migration of the grounding zone over tidal cycle: surface icequakes signature

Figure 5.3 presents a series of maps showing the interpolated icequake activity across the dense array during the different stages of a tidal cycle. The grounding line as identified geodetically by Le Meur et al. (2014) separates the grounded ice (top section and right corner of the array) and the floating ice (lower left corner of the array). At low tide (Fig. 5.3a), icequake activity is weak and concentrated on the east side of the array, showing no apparent link with the position of the grounding line. At mid-rising tide (Fig. 5.3b), the icequake activity migrates within the floating ice area, consistent with the grounding line position. At high tide (Fig. 5.3c), icequake activity intensifies over the floating area but also migrates upstream, in the opposite direction to the ice flow, well beyond the grounding line position. At falling tide (Fig. 5.3d and Fig. 5.3e), the icequake activity is still high but no longer matches the grounding line position, instead diffusing over the dense array without a clear pattern. At the end of the cycle (10h after the high tides) the icequake levels decrease and go back to the initial levels (Fig. 5.3a). Vertical displacement from GNSS stations (colored triangles in Fig. 5.3) confirm the uplift movement during rising to high tide and downlift movement during falling to low tide, coherent with tidal flexuring. Vertical displacement across GNSS stations shows higher displacement magnitude for northeastmost stations located on the floating tongue of the glacier (i.e. GPS08, GPS03 and GPS02). Figure 5.3f focuses on a single day, the 18th of January 2023, when icequake activity is highest, likely due to high tide (spring tides) and to low noise level that day. We draw the contour of the average icequake activity rate for each hour from mid-rising (-6h) to high tide (0h). During this small time window, this map reveals an extremely dynamic migration of the icequake activity from approximately the "geodetic" grounding line position extending landward to both the northwest (with a lateral migration of less than 1km) and southwest directions (with an upstream, along-flow migration of more than 2 km).

5.2.5.2 Stick-slip dynamics at the grounding zone during tidal cycles

Stick-slip locations

We present in Figure 5.4 a the map with the location of the 29 stick-slip clusters detected within the deployment duration, along with their estimated depths for 22 of them. Table C.1 (7.5.2) summarizes the number of events detected for each cluster and the source coordinates. The striking feature of this map is that all the detected clusters are located at the periphery or outside of the network with no event detected beneath it. This suggests the absence of seismically active gliding at the ice-bedrock interface in this area, consistent with a floating ice shelf. Several clusters located at the periphery of the network outline the east and west lateral shear margins of the glacier. Along the west lateral shear margin, depths vary from 225 m to 915 m. Beneath the east lateral

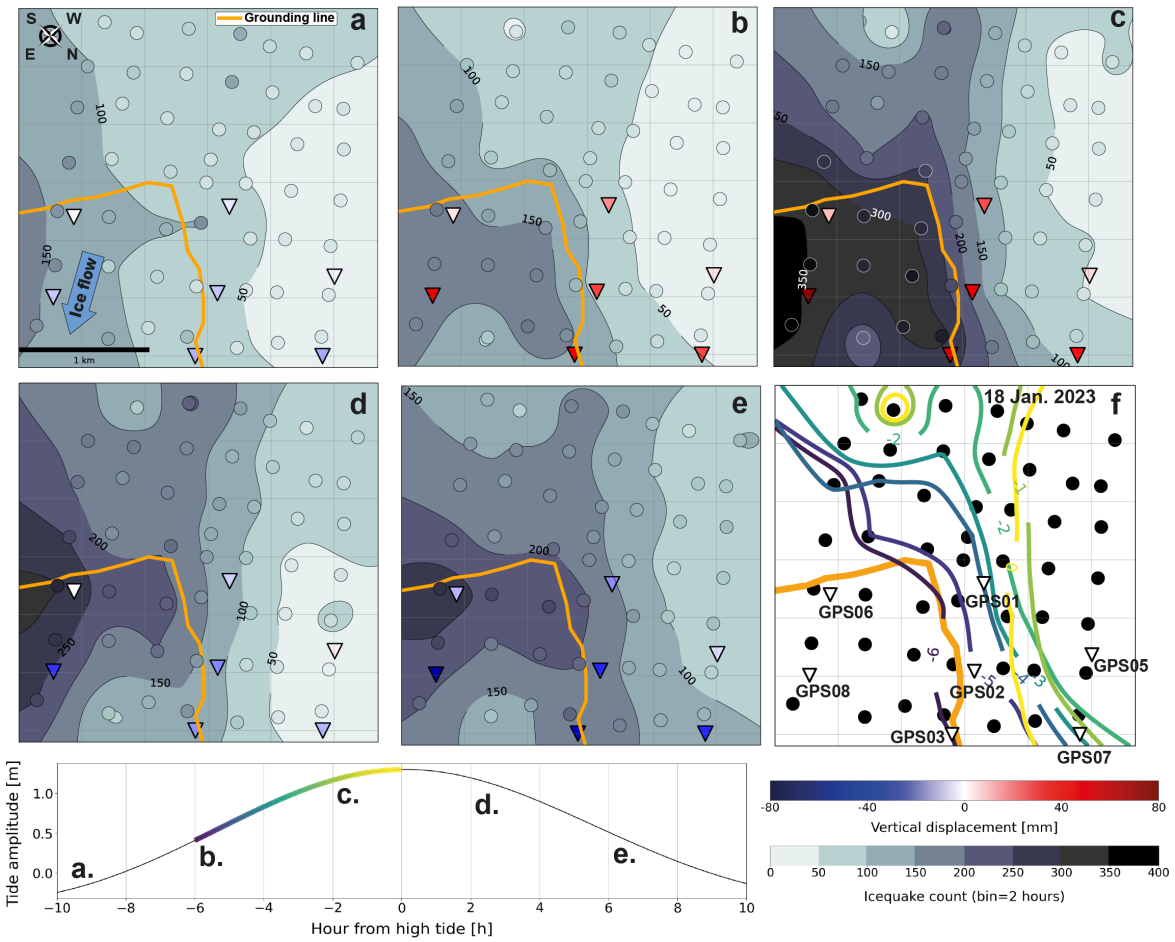

Figure 5.3: (a) to (e): Spatial distribution of icequake activity across the dense seismic array during a tidal cycle. The maps are derived from kriging-based interpolation of icequake occurrence rates, averaged over seven consecutive tidal cycles from January 17 to 24, 2023. Icequake occurrence rates are expressed as the average number of events per 2-hour interval. Darker shades correspond to higher icequake occurrence rates. Each panel represents a 2-hour interval within the 12-hour window leading up to and following high tide. The corresponding time slot is reported on the tidal amplitude graph, reconstructed from the seven consecutive tidal cycles. For each window, the GNSS stations are colored according to the measured vertical displacement. (f) contour of the average icequake activity for each hour from mid-rising to high tide observed on a single day (Jan. 18, 2023). Each color corresponds to one hour from -6h to 0h, relative to high tide, as reported on the tidal amplitude graph.

shear margin, clusters with reliable depth estimates are generally deeper, ranging from 800 m to 1,300 m. Additionally, we locate clusters upstream of the dense array. Some of these clusters are aligned along the glacier flow and associated with depths greater than 1,300m. The other clusters are shallower, at maximum 660 m depth, and aligned perpendicular to the flow. The estimated source depths are generally consistent with the broad bedrock topographic trends outlined in previous radar surveys conducted in

the area (Le Meur et al., 2014), but tend to be larger by a few hundred meters. Despite reliable identification of both P- and S-wave arrivals, the depth determinations remain uncertain due to poor constraints on seismic velocities and the fact that most event clusters are located outside the array aperture. This uncertainty explains the likely overestimation of source depths. We explore the trade-off between the depth estimate and the seismic velocities, which shows that the depth can vary several hundred meters depending on the (Vp, Vs) couple chosen (see Fig. C.1, 7.5.2). We further show that the overestimation can be mitigated by inferring seismic velocities that fall outside the typical range reported for glacier ice , and particularly by using slower shear velocities (e.g., 1400m/s) than investigated in the present study. It emphasizes the need for independent measurements of seismic velocities to better constrain the stick-slips and therefore the bedrock depth estimates.

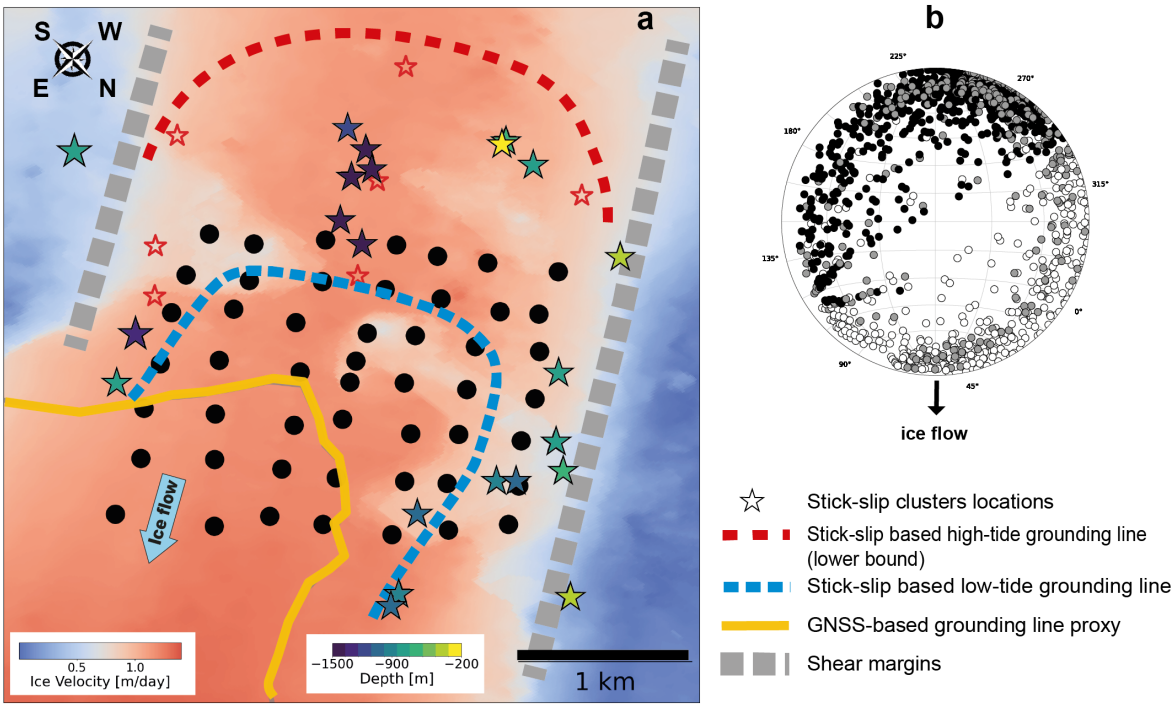

Figure 5.4: Stick-slip clusters location. (a) Map showing the locations of 29 detected stick-slip clusters (stars), overlaid on the ice surface horizontal velocity map from Provost et al. (2024). Clusters are color-coded by their depths. Red stars indicate clusters with poorly resolved depths. The continuous orange line represents the "geodetic" grounding line from Le Meur et al. (2014). The detected stick-slip clusters allow to define a grounding zone bounded by a low and a high tide grounding line, indicated by the blue and red dotted lines, respectively. (b) Lower hemisphere stereonet representing the upward (black circles) and downward (white circles) first P-wave motion over the whole network. Grey circles indicate unsure polarisation.

Stick-slip occurrence

To investigate the dynamics of stick-slip events over tidal cycles and identify patterns in their activation, we first analyse the number of clusters active at the same time during the deployment period (Fig. 5.5a) and then quantify four key parameters variation along a virtual single tide cycle: number of active clusters (Fig. 5.5b), event counts (Fig. 5.5c), inter-event time (Fig. 5.5d), and event amplitude (Fig. 5.5e). In each case, we focus on the period from 17 to 24 January 2023, and values are averaged over 30-minute bins, and presented over a single 24-hours tidal cycle.

We observe that the activation of the clusters is clearly modulated by the tides (Fig. 5.5a). Over the whole week of the time series, we observe peaks of simultaneous (5 to 7) active clusters increasing from low to rising tides, then rapidly decreasing from high to falling tides (below 2). When averaged over the 8 days (Fig. 5.5b) the number of simultaneous active clusters peaks at more than 4 at rising tides and decreases to 1 at falling tides. The associated total number of stick-slip events per 30 min (Fig. 5.5c) shows a rather similar trend, which culminates at 600 events during rising tides, decreases at high tide, and is the lowest during falling tide (at about 100 events). 80% of the clusters exhibit a clear tidal pattern while the remaining, mostly located on the east shear margin, show relatively constant event counts across the tidal cycle. The icequake activity presented as the red curve on the same diagram displays a clearly different pattern with a bimodal distribution, with a first peak at rising tide and a second at falling tide, as already shown in more details on Fig. 8b from Le Bris et al. (2025). The average inter-event time (IET) between stick-slip events typically ranges between 4 and 8 minutes (Fig. 5.5d), with a slight decrease during the falling-to-low tide phase, reaching values below 4 minutes. This trend suggests a rather stable activity with a slight acceleration of stick-slip occurrence as the tide recedes. It is consistent with the surface GNSS measurements that show an horizontal acceleration of the glacier during falling tide (Fig. 11 from Le Bris et al. (2025)). No systematic correlation is found between inter-event times and spatial location. We quantify the mean event amplitude over 30-minutes bins, by extracting the maximum of the envelope of all the events within the time window and across all stations. We then calculate the average amplitude to represent the event as viewed by the full network. To decouple amplitude variation from events occurrence, we normalize the amplitudes by the total number of events in the 30-minutes bin. Figure 5.5e clearly shows that stick-slip amplitudes vary with tides: they increase during rising tide, peak at high tide, and decrease during falling tide. This observation is consistent across all clusters. The rather stable inter-event times and the larger number of events at rising tide suggest that more energy is released per event at high tide to accommodate the ice flow.

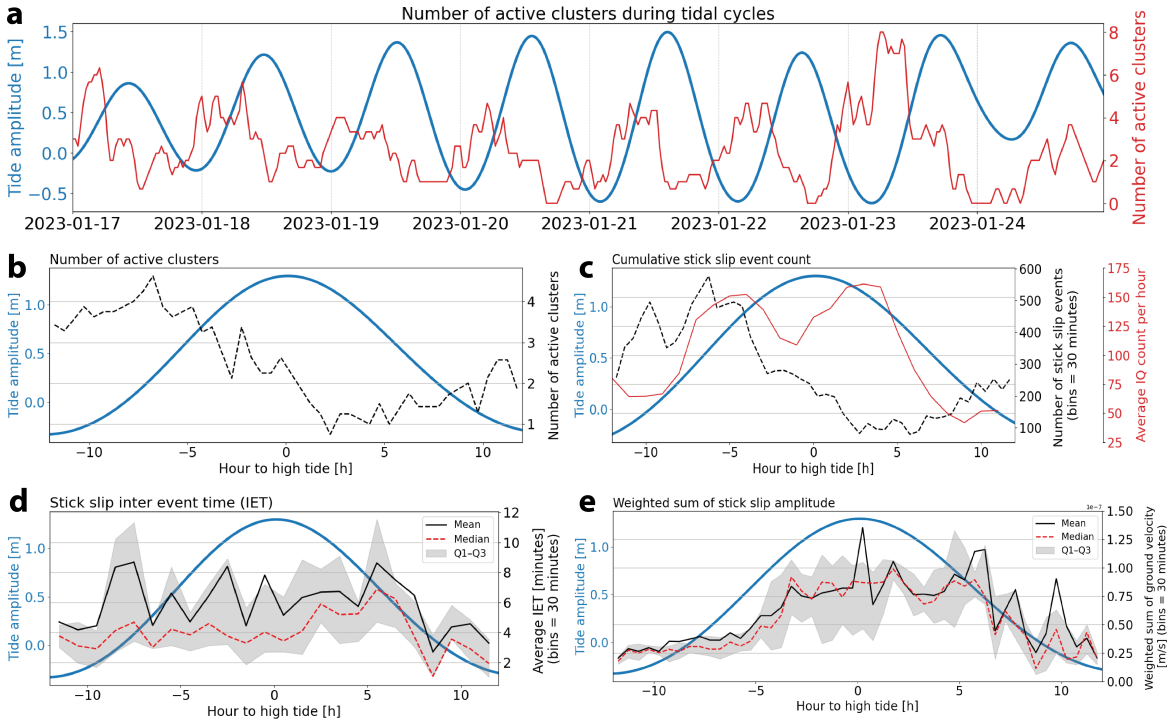

Figure 5.5: Stick-slip activity relative to tide. (a) Time series of the number of active stick-slip clusters (red curve) over the period 17–24 January 2023, together with the tide amplitude (blue curve). (b) number of active clusters (black curve) folded over a representative 24-hour tidal cycle, divided into 30-minute bins. The x-axis represents time relative to high tide, from –12 to +12 hours and tidal amplitude is plotted as a blue curve. Values from all clusters are concatenated. (c) Total number of stick-slip events from all clusters along with the average icequake activity rate (in count per hour, red curve). (d) stick-slip inter-event time (IET). (e) event amplitudes (ground velocity, in m/s). For IET and event amplitudes, the mean (black curve), median (red dotted curve), and interquartile range (25th–75th percentiles displayed in grey shading) are shown.

Stick-slip focal mechanism

We analyse the focal mechanism of each cluster by locating compressional (up) or dilatational (down) motions across the seismic network, which in turn allows identification of the nodal planes and fault geometry (vertical strike-slip, normal, reverse, or oblique). To do so, we stacked the waveforms of all events within each cluster across all seismic nodes of the dense array, in order to make the P-wave first motions more visible. Three analysts independently identified the first motions, classified as “up,” “down,” or “uncertain”. For each cluster, the identifications were then combined with unanimity in the agreement on the “up” or “down” motion provided by the 3 analysts. When analyzing P-wave first motions for fault mechanism determination, the ideal scenario is a full azimuthal and incidence angle coverage around the seismic source. Here, we are unfortunately limited by partial azimuthal and inclination coverage of the seismic sources relative to the stations, since most of them occur at the periphery of the

network, thus impeding to cover the whole azimuth/inclination hemisphere and hence resolving the full focal mechanisms. To overcome this limitation, we make the hypothesis that all clusters have similar focal mechanisms and merge all the compressional and dilatational wave motions into a single virtual source displayed in the stereonet Fig. 5.4b. It allows for a more complete azimuth and incidence range to be covered. We obtain a clear two-quadrant mechanism, with compressional upward first motions southward and dilatational downward first motions northward in the lower hemisphere. This coherent pattern confirms our initial hypothesis that all stick-slip clusters share a similar focal mechanism (for individual stereonets, see Fig. C.2, 7.5.2). At first approximation, such quadrant configuration is compatible with a horizontal strike-slip faulting and an along-flow displacement. We observe a slight obliquity between the azimuth of the vertical focal plane and the flow direction that could likely reflect departure from a flat and horizontal bedrock hypothesis, such as dipping and laterally-varying structures.

5.2.6 Discussion

Surface icequakes as a proxy for grounding line migration

During rising tide, we observe that the zone of intense surface icequake activity migrates landward, opposite to the direction of ice flow (Fig. 5.3). These icequakes being the brittle response to the tide-induced flexure of the glacier at its GZ (Le Bris et al., 2025), this suggests that the flexure moves upstream during rising tides. We quantify that the upstream migration of icequake activity at the glacier surface occurs at an apparent velocity ranging from 0.1 to 0.3 m/s. This velocity is controlled by the amplitude of the tidal flexure of the glacier but also by the bedrock slope, which is poorly constrained in our region. The same order of magnitude has been observed by Rignot et al. (2024) at the Thwaites Glacier with grounding line migration velocity of 0.5 m/s. Assuming that such flexure is closely related to the seawater intrusion at its base (Gadi et al., 2023; Rack et al., 2017; Robel et al., 2017; Walker et al., 2013), one can deduce that the minimum horizontal distance of seawater intrusion observed beneath the Astrolabe Glacier GZ is 3 km, the approximate length of the array. We could expect seawater to travel greater distance landward, depending on the topography of the bed, which is unknown. Such value is compatible with other studies revealing either tidal flexuring observations several kilometers beyond the grounding line (uplift visible up to a cm-scale) (Drews et al., 2021) or grounding line migration at a kilometer-scale over tidal cycles (Chen et al., 2023; Ciracì et al., 2023; Millan et al., 2020). Our ability to constrain the intrusion distance from tidal flexure observation is however limited not only by the spatial extent of the seismic network, but more critically by the fact that the surface flexure is a proxy that may sign with some offset with the processes occurring directly at the glacier base.

A new delineation of the grounding zone based on stick-slip clusters

Using stick-slip clusters of events at the base of the glacier, we show that we can constrain the true mechanical grounding line position and its temporal migration. It is

broadly accepted that stick-slip events originate from basal friction and accommodate sliding at the ice-bedrock interface or on bedrock asperities, either at the glacier base or along the lateral shear margins where differential motion occurs. In principle, stick-slip sources are expected to occur upstream of the grounding line where the glacier is expected to be at least partially grounded, the glacier being fully floating downstream of the GL. However, in our observations, such events are absent directly beneath the dense array (supposedly at least partially grounded) and instead appear significantly upstream of it (Fig. 5.4). Consequently, this suggests that the actual grounding line may lie farther inland from the "geodetic", flexure-induced, grounding line proposed by Le Meur et al. (2014). The activation pattern of stick-slip clusters (Fig. 5.5a) further supports this interpretation: maximum clusters activities are observed at rising tides, when enough stress has been accumulated, then clusters deactivate at high tide, consistent with ice surrection and seawater intrusion reducing bed-ice contact. Stick-slip clusters reactivate during low and rising tides, when renewed contact reestablishes basal friction and will allow the glacier flow to start a new cycle of shear stress concentration at some pinning points of the ice-bedrock interface. Based on these observations, we delineate a new grounding zone using stick-slip activity (Fig. 5.4a), bounded by a lower (downstream) limit (blue dashed line Fig. 5.4a) at low tide (when clusters are active) and an upper (upstream) limit (red dashed line Fig. 5.4a) at high tide (when they are absent). This upper limit is conservative since it could extend further inland but is limited by our ability to detect stick-slip activity at larger distances from the node array. This stick-slip derived grounding zone shows a clear offset relative to both the previously proposed "geodetic" grounding line and the position inferred from tidal-induced icequake activity. Importantly, stick-slip analysis maps the mechanical grounding line, defined by direct ice-bedrock contact, rather than the flexural grounding line seen from the surface of the glacier or from space. While the flexural grounding line is a good proxy that reflects the surface bending, it is inherently offset from the true basal mechanical boundary.

Constraining grounding zone dynamics

In accordance with observations from surface icequakes and stick-slip events, we propose in Figure 5.6, a simplified cartoon illustrating the grounding zone dynamics at a daily tidal cycle scale: as the tide begins to rise, it lifts up the floating part of the glacier inducing seawater to infiltrate the subglacial cavity. This transitional phase may destabilize the ice-bedrock interface by changing its state of effective pressure and thus triggering stick-slip sources by releasing the accumulated stress at the bedrock on sub-horizontal fault planes. At the same time, the tide-induced bending of the glacier generates an extensional state of stress and numerous icequakes at the surface, migrating landward together with the flexure migration. At high tide, seawater intrusion has reduced friction and deactivated most of the stick-slip sources by lubrificating or opening the ice-bedrock interface. The stick-slip activity becomes concentrated in only a few locations, still seismically accommodating the glacier horizontal flow, with less frequent but more energetic events. During falling tide, stick-slip activity is minimal.

This suggests that the interface is still lubricated from the preceding high tide and/or that the accumulated stress is not yet high enough to generate seismic events. It allows for smoother, aseismic basal and lateral sliding with reduced resistance from bedrock asperities. As the system reaches low tide, seawater has drained toward the cavity, leading to a reduction in lubrication of the interface and starting a new cycle of increased basal contacts resulting in a new cycle of stress accumulation and in a higher rate of small stick-slip events.

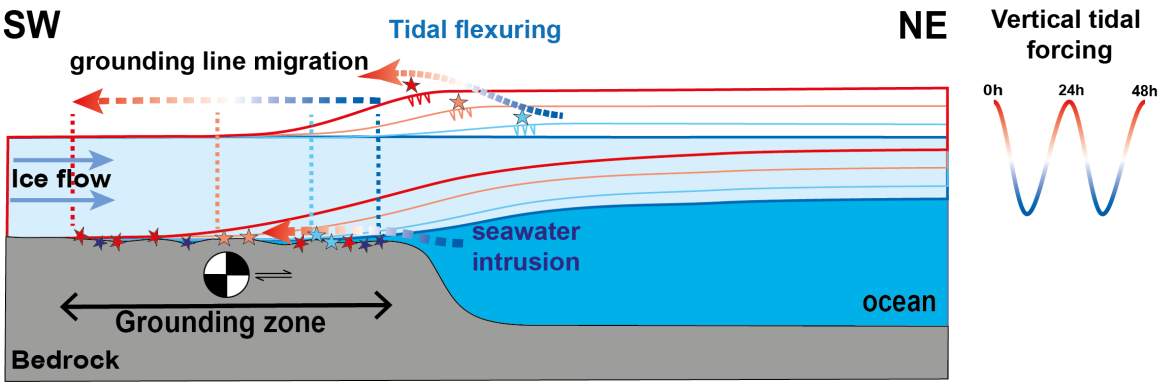

Figure 5.6: Cartoon of the seismic observations and interpretation of grounding zone dynamics during a tidal cycle. It includes the surface icequakes generated by the tidal flexure, the grounding line migration and seawater intrusion seen by the basal stick-slip events. Note that the vertical movement is not to scale.

Tracking grounding line retreat using seismology

Overall, both surface icequakes and stick-slip clusters provide constraints on grounding zone dynamics. Surface icequakes, driven by tidal flexure, migrate landward in response to grounding line motion. It can help mapping grounding line position from surface activity although with a systematic offset relative to its actual location at the ice base. At the ice-bedrock interface, daily tidal cycles modulate grounding line migration through seawater intrusion, which governs the activation, deactivation, and magnitude of stick-slip events. Following such observations, we propose that the monitoring of stick-slip clusters could offer a direct means of tracking grounding line retreat over long timescales. This is of particular importance considering the first-order control of the basal friction and of pinning points on the coastal glacier stability (e.g., Pirli et al., 2018). Unlike geodetic methods, which are limited to surface observations, recording of seismicity captures processes over the whole ice column down to the glacier base, at high spatial and temporal resolution. Once clusters are identified and located, a monitoring strategy may focus on a single or a little number of active clusters using a reduced but efficient seismic setup: a little number of surface stations may be indeed enough to monitor a cluster activity over long time periods. The eventual disappearance of stick-slip clusters could sign a grounding line retreat and/or a basal melting and ice thinning. This makes the approach a low-cost, low-maintenance, yet powerful

tool for multi-annual monitoring of grounding line retreat.

5.2.7 Conclusion

We describe the dynamic of the coastal Astrolabe Glacier at its GZ in response to consecutive tidal cycles, capturing fine-scale spatial and temporal variability of cryoseismic events occurring both at the surface and at the ice-bedrock interface. Our observations show that surface brittle deformation migrates landward during rising tide, suggesting that tidal flexuring propagates inland in direct correlation with grounding line migration and associated seawater intrusion. These icequakes may thus serve as a strong proxy for monitoring grounding line migration on daily timescales. In addition, we also detect and locate stick-slip clusters at the ice-bedrock interface, activated and modulated by the tidal cycle: numerous clusters of low-energy events occur during low tides, while fewer but higher-energy events are concentrated at high tides. This pattern aligns with seawater intrusion during rising tides, reducing basal friction and/or removing the direct contact between ice and bedrock, and increased basal friction rates at receding tides when seawater is retreating. Together, these results provide new insights into the high temporal and spatial resolution of grounding line migration driven by tidal, flexure-induced glacier deformation. This deformation is detected by surface icequakes and basal stick-slips, the latter of which show a clear upstream offset and underlie the actual mechanical grounding line. Such observations are valuable for constraining future models of glacier and grounding line dynamics under tidal forcing. They will also become crucial for monitoring Antarctic ice sheet vulnerability to warm water intrusion at grounding zones of outlet glaciers, and particularly for constraining the tidal pumping effect which may enhance ocean-ice interaction and the subsequent basal melting.

5.2.8 Acknowledgements and Data Availability

The SEIS-ADELICE project benefited from the support of the French Polar Institute Paul-Émile Victor (IPEV) for the program #1214, from the French CNRS-INSU SYSTER and LEFE-IMAGO programs, from the Grenoble University UGA-IRGA funding, for the project NODES-ADELICE supported by the French National Research Agency (ANR) in the framework of the "Investissements d'avenir" program (ANR-15-IDEX-02), from the LabEx OSUG@2020 (Investissements d'avenir – ANR10 LABX56) for the project DAS-ADELICE, and from IGE Grenoble. We are grateful to EPOS-France (European Plate Observing System $https://www.epos-france.fr/$) for the data management. Seismic nodes used in this study have been provided by the "Plateforme instrumentale sismologique" of EOST and complemented by nodes from IPGP (Institut de Physique du Globe de Paris). Thanks to Louis Grauwin, Enzo Tahon, Léonard Barthélémy, Arnaud Reboud, Tom Dumouch for their efficient help in the field work.

Thanks to Pierre Rizzardo from ENSA Chamonix for his help and for securing the January 2023 field work on the Astrolabe Glacier. Thanks to P. Techine, M. Calzas and L. Testut for providing access to the tide gauge data managed by the NIVMER/ROSAME project.

The SEIS-ADELICE seismic data are available at the RESIF data center under the FDSN network code ZR (Barruol et al. 2023). Raw and processed GNSS data acquired on the Astrolabe Glacier GZ are available under a Creative Commons Attribution 4.0 International license in Togaibekov et al. (2024). Tide gauge data, managed by the NIVMER/ ROSAME project (Calzas et al., 1992), are available at *https* : *//doi.org*/10.17183/*REFMAR*#108. Seismic data were processed using ObsPy version 1.4.0 (Beyreuther et al., 2010; The ObsPy Development Team, 2022), available under the ObsPy license at *https* : *//docs.obspy.org/*. Figures were made with Matplotlib version 3.5.3 (Caswell et al., 2020; Hunter, 2007), available under the Matplotlib license at *https* : *//matplotlib.org/*. All data and scripts used to generate the figures and results in this study are openly available under a Creative Commons Attribution 4.0 International license.

5.3 Outcomes and outlook

In this chapter, we showed that seismic observations provide an effective way to track daily grounding line migration at high temporal resolution. More specifically, our results demonstrate that the tidal response recorded at the glacier surface can be used to monitor grounding zone dynamics continuously at sub-daily timescales. However, the observed seismic activity reflects surface flexure rather than the mechanical grounding line itself, which lies at the ice–bed interface. Consequently, a horizontal offset exists between the "geodetic" grounding line mapped from surface deformation and the "mechanical" grounding line at the glacier base. At the glacier bed, we found that basal stick-slip events are also modulated by tidal forcing and provide information on the state of the ice–bedrock interface. These events exhibit tidally driven cycles of activation and deactivation, consistent with seawater intrusion extending inland during high tides. These results are promising, as they help overcome the current limitations of temporal resolution in monitoring such processes.

A limitation remains, however. The depth and position of the stick-slip clusters are affected by uncertainties in the compressional and shear seismic velocities and the limited aperture of the network which prevent good accuracy on location of basal sources. As a result, asperities of the bedrock over which there is stick-slip activity remain only partially constrained. Future seismic imaging will help refine the local velocity structure and improve depth accuracy.

Looking ahead, extending seismic deployments over longer periods (e.g., several months to a year) would allow continuous monitoring of grounding line migration over

seasonal and interannual tidal cycles. Even a sparse network of seismic stations could be sufficient to track the activation of basal clusters through time, potentially revealing a progressive retreat of the grounding line. If basal seismicity were to permanently deactivate in a given area, it could indicate a lasting decoupling between the ice and bedrock, meaning that the area has transitioned to a fully floating state. Future studies should also test the applicability of this approach to other larger Antarctic outlet glaciers. The Astrolabe Glacier, being relatively narrow and confined within a fjord, provides favorable conditions for dense array coverage of the grounding zone. Applying this method to wider or less confined glaciers would help determine how glacier geometry and bed conditions influence the detectability of short-term grounding line migration from seismic data. Such comparative analyses will help assess the generality and scalability of cryoseismic monitoring of grounding zones across Antarctica.

In the next chapter, we shift our focus from the grounding zone to the lateral shear margin of the Astrolabe Glacier, where we continue to use seismic observations from a dense array to investigate how stress is accommodated within this region where there is important deformation between flowing and stable ice. Stick-slip events, in particular, will again serve as indicators of the mechanical coupling between the glacier and the lateral rock wall of the fjord.

CHAPTER 6

Investigation on the seismic signature of Astrolabe Glacier shear margin

Contents

6.1 Ice dynamics at shear margins of outlet glaciers 118

6.2 Data acquisition 119

6.2.1 2025 dense array configuration and deployment 119

6.2.2 Quality of the data and first observations 119

6.3 Dynamic framework of the shear margin 123

6.4 Stick-slip clusters identification 126

6.4.1 Detection and location of stick-slip clusters 126

6.4.2 Focal mechanisms 127

6.5 Spatial and temporal analysis of stick-slip clusters activity 130

6.5.1 Tidal influence on stick-slip clusters 130

6.5.2 Lateral and depth distribution and comparison with radar data 132

6.6 Outcomes and outlook 136

6.1 Ice dynamics at shear margins of outlet glaciers

Shear margins are narrow transition zones that separate the fast-flowing ice stream from stable or slow-moving ice or rocky valley walls. They accommodate strong velocity gradients and cumulative shear strains, and thus provide a major source of lateral drag that counteracts ice flow (Echelmeyer et al., 1994; Minchew et al., 2018). This lateral resistance has a fundamental control on ice stream dynamics, yet it remains poorly constrained by direct observations (Morlighem et al., 2010).

Deformation within shear margins can occur through two distinct but complementary mechanisms. At the ice-ice interface, shear can be initially accommodated by ductile deformation but may transition to brittle failure when the brittle strength of the ice is exceeded. It produces crevasse fields well visible at the surface of the glaciers (Jennings & Hambrey, 2021). At the lateral ice-bedrock interface, shear is expected to be controlled by frictional contact with valley walls. Displacement can be accommodated by a stick-slip mechanism, similar to basal sliding over the bedrock, but with steeply dipping planes. Both mechanisms involve shear stresses acting in opposite directions along a plane. Ice-ice deformation may proceed aseismically through creep, and seismically through icequakes from crevasse formation while ice-bedrock friction produces impulsive stick-slip like seismic signals (Hudson et al., 2020). Because shear margins must accommodate the velocity contrast between fast-moving ice (meters per day) and stable ice or rock, they play a crucial role in regulating the overall motion of confined glaciers. These boundaries generate flow resistance and can compensate for basal weakening, thereby stabilizing the glacier against acceleration (Van der Veen et al., 2011) and participating in the overall buttressing effect. Understanding how this resistance is laterally and vertically partitioned between ductile, brittle, and frictional processes is therefore essential.

Regarding the Astrolabe Glacier, which flows within a fjord, the ice stream is laterally constrained by valley walls. In 2025, a dense seismic array (A3) was deployed over the west lateral shear margin of the glacier to capture deformation at the interface between fast-flowing ice and the surrounding slow moving ice. This configuration aimed at characterizing both the shear-zone induced crevasse-related seismicity and the frictional stick-slip events associated with ice-bedrock contact. By locating these events, we can also infer information on the underlying bedrock topography and lateral boundary conditions. While GNSS and satellite interferometry quantify the surface absolute velocity field and therefore the actual velocity gradient across the shear-zone, seismic data may reveal how stresses are locally accommodated through brittle failure and frictional sliding. In this chapter, we build on previous analyses of basal seismicity at the grounding zone to investigate the seismic signature of the shear margin, evaluate its sensitivity to tidal forcing, and assess the role of lateral drag in modulating glacier dynamics.

6.2 Data acquisition

6.2.1 2025 dense array configuration and deployment

In January 2025, a total of 44 seismic nodes were deployed across the Astrolabe Glacier west lateral shear margin, using *SmartSolo* IGU-16HR 3 component nodes. Figure 6.1 presents the map of the deployment with location of the seismic nodes, along with the GNSS stations from the GLACIOCLIM network and an additional short period seismic data recorder (Digos DataCube, AST16). The array configuration follows the "Square-Triangle" method of Mordret & Grushin (2025), with an average inter-station spacing of approximately 150 m. This configuration ensures a good azimuthal coverage and thus a better source location resolution. Sensors recorded continuously at a sampling rate of 500 Hz over a period of 12 to 15 days.

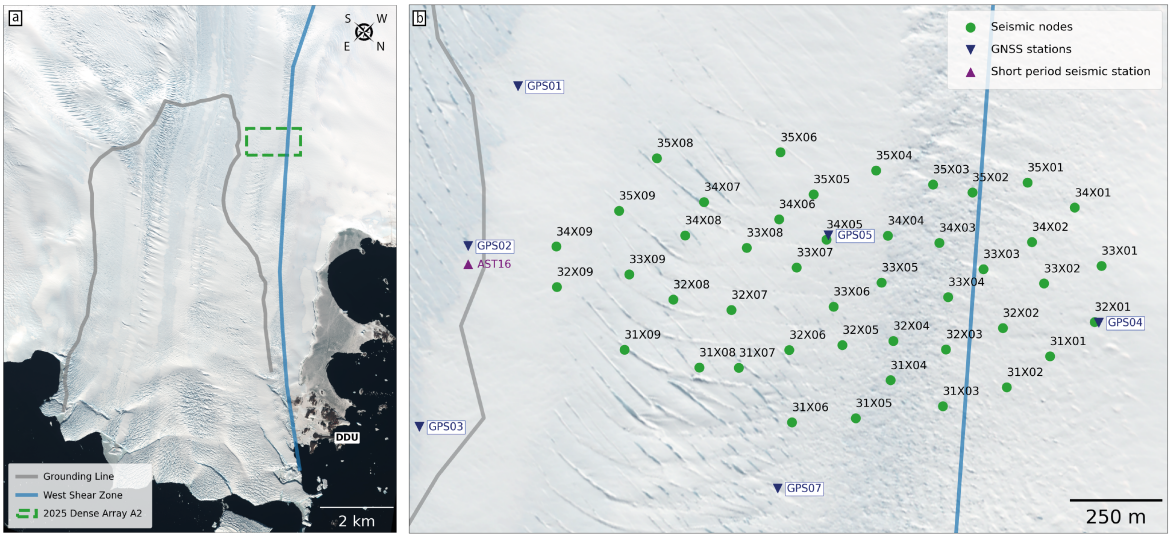

Figure 6.1: Map of the January 2025 dense seismic array deployed over the west lateral shear zone of the Astrolabe Glacier for 15 days. GNSS stations are deployed within and around the dense array as part of the GLACIOCLIM observatory. The shear margin, accommodating a left-lateral shearing, and whose delineation is based on surface velocity gradient, is represented by the blue line. Grounding line position is represented by the grey line.

6.2.2 Quality of the data and first observations

An effective way to assess the quality and stability of seismic data is through the computation of seismic power, which provides a quantitative measure of how the seismic energy levels are distributed in frequency and how they vary during the deployment. In this study, spectrograms were calculated using Welch's method, which averages periodograms from overlapping signal segments to reduce variance and noise. Figure

6.2 presents spectrograms from four seismic nodes, over a one-week period. These stations are aligned along a profile approximately perpendicular to the shear zone, extending from stable grounded ice in the northwest to floating ice in the southeast (see their location Fig. 6.3). A dominant feature resides in the vertical lines representing short-time events with a broad spectral content. These events are the so-called icequakes that accommodate the surface brittle deformation and on which we focused our study in Chapter 4. A marked increase in energy is observed between 16 and 17 January 2025, spanning all frequencies but most pronounced within the 150-225 Hz band, where power levels rise from approximately –120 dB on 15 January to –90 dB on 16 January. This increase coincides with a period of severe weather conditions at DDU, including precipitation and strong winds reaching up to 120 km/h. The magnitude of this energy increase varies among stations (e.g., 33x01 and 33x03), suggesting different sensitivities to environmental noise. Such variability likely reflects local factors such as the thickness and state of snow cover around the sensors or micro-topographic bumps shielding the sensors from wind. These observations highlight that variations in local environmental conditions can strongly influence measured energy levels. Consequently, direct comparison of energy amplitudes between stations should be done with caution, as they are not necessarily indicative of differences in seismic activity but also on extremely local physical conditions. An additional feature visible across all stations is a narrow, stable spectral line around 180 Hz. Such lines may originate from electronic interference or from nearby objects vibrating at resonance frequencies. In this case, the amplitude variability of the line, especially its intensification during the storm, suggests a signal likely linked to resonance of bamboo stakes near the sensors rather than electronic noise, which would typically remain constant in amplitude. Finally, below 100 Hz, a clear contrast can be seen between the low background noise ($\sim$ -150 dB) and impulsive seismic signals ($\sim$ -120 dB or higher). At higher frequencies, this contrast diminishes due to overall elevated noise levels. This is consistent with the dominant frequency content of impulsive cryoseismic events, which typically exhibit most of their energy below 50 Hz.

The noise spectra recorded by the seismic nodes show significant spatial variability, particularly across the transition from grounded to floating ice. Figure 6.3 presents the probabilistic power spectral densities (PPSDs) computed from the vertical components of the same seismic nodes as in Figure 6.2 over a single day (Jan. 15, 2025). All nodes display a common energy peak between 3 and 4 seconds, classically associated with secondary microseisms generated by distant ocean swells (Grob et al., 2011; Stutzmann et al., 2009). The amplitude of these secondary microseisms increases progressively by approximately 10 dB from the stable area toward the grounding zone. At shorter periods (<1 s), all stations exhibit low noise levels (around –130 dB), which ensures the detectability of small-amplitude seismic events such as icequakes and stick-slip activity. A distinctive feature, however, emerges at longer periods: a pronounced energy peak centred around 16 seconds appears when approaching the floating ice. This spectral peak is absent at the grounded stations west of the shear zone and intensifies progres-

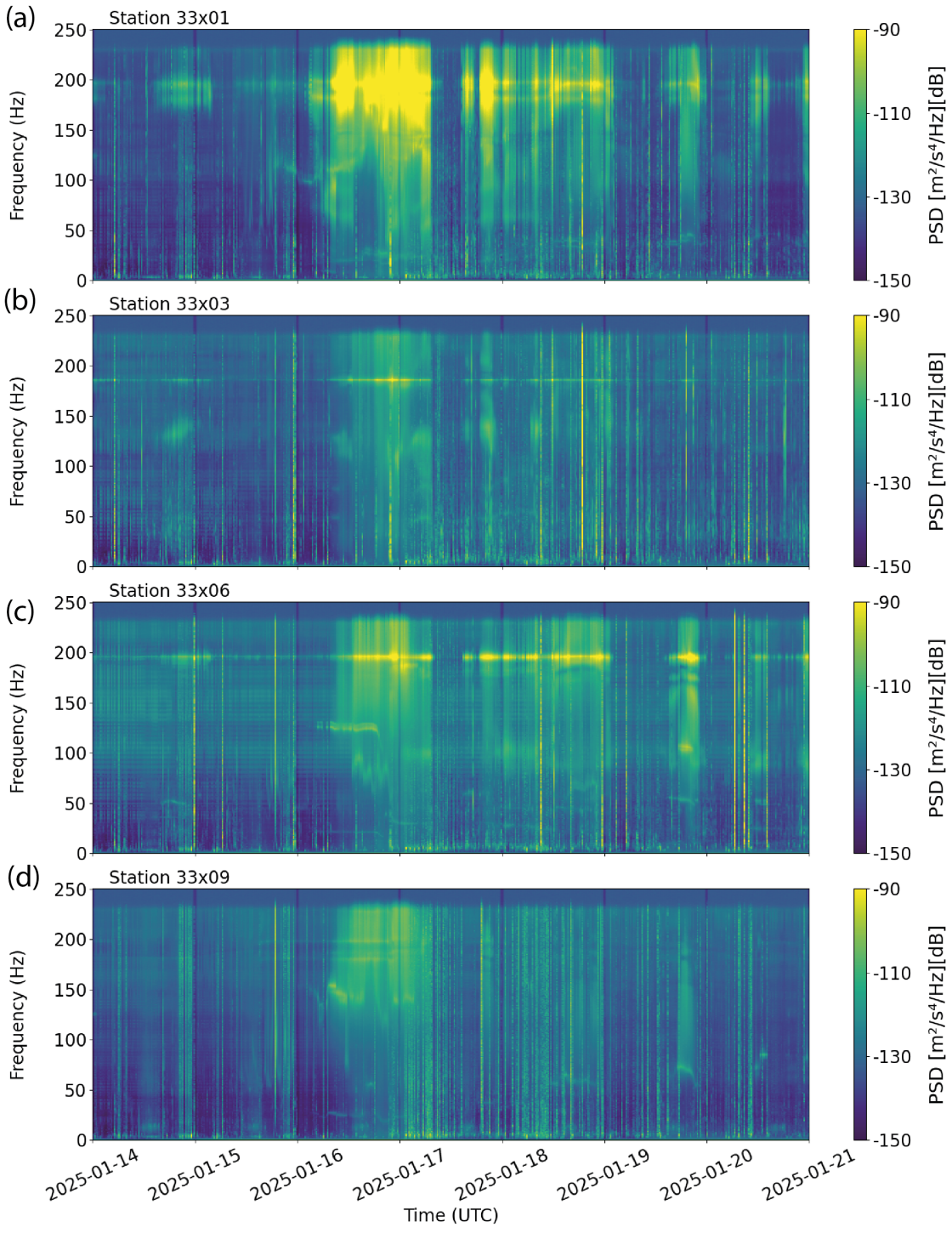

Figure 6.2: Welch's spectrogram of 4 stations (33x01, 33x03, 33x06 and 33x09) across the dense array over 7 days. Note the noise during the two-day long storm (Jan, 16th and Jan, 17th). PSD stands for Power Spectral Density.

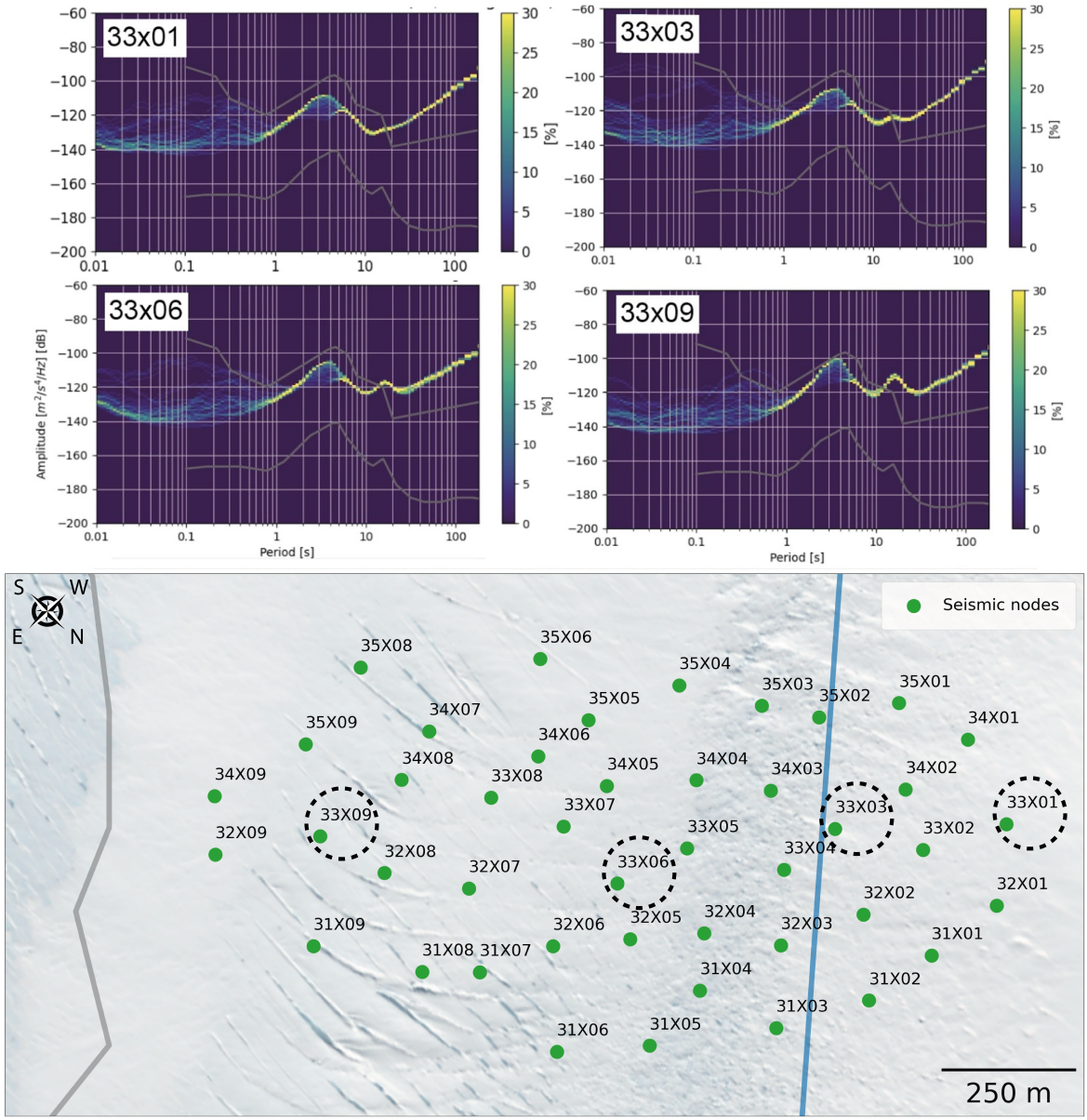

Figure 6.3: PPSD of seismic nodes (vertical components DPZ) deployed in Jan. 2025 across the west lateral shear zone of the Astrolabe Glacier. The 4 presented individual PPSD are calculated for 1 day (Jan. 15, 2025) at 4 stations along a NW-SE trending line perpendicular to the shear zone, from the stable ice (right, node 33X01) to approaching the floating part of the glacier (left, node 33X09). Modified from Barruol et al. (2025).

sively toward the southeast. The amplitude of these long-period spectral peaks exceeds the New High Noise Model (Peterson, 1993), and coincides (or overlap) with the frequency of the primary microseismic peak. These peaks are remarkably stable in both space and time, having also been observed at floating sites where we deployed broadband stations in 2022, and at seismic nodes deployed in 2023 and 2024. This persistent

spectral feature observed at around 16s at stations on or close to the floating tongue of the glacier and systematically absent at grounded stations suggests that the partly floating ice in this region behaves as a resonant system, oscillating at its natural frequency over the subglacial ocean cavity (Okal & MacAyeal, 2006). Understanding and precising the origin of this 16s signal would certainly require some deeper and more quantitative investigations but is beyond the scope of the present study. Note that observing such signals at 16 seconds on short period sensors (such as the *SmartSolo* seismic nodes) is unexpected and demonstrates the quality of the sensors and the high sensitivity in this glacial environment.

6.3 Dynamic framework of the shear margin

Figure 6.4 presents the horizontal displacement map of the western lateral shear margin region. The displacement of the seismic nodes, derived from the change in their GPS positions over the 12-15 day deployment period, provides a first-order view of the ice surface velocity field. During the deployment time, most sensors moved from their initial positions but to different extents. On the west side of the dense array, total displacements remain well below 10 m, while to the east, displacements increase progressively from 10 to 15 m and reach up to 23 m near the glacier fast-flowing region. It aligns well with the shear margin delineated from satellite-derived velocity maps (see blue line, Fig. 6.4). This velocity gradient is also consistent with the data recorded by the 6 GNSS stations during the same period. Located along the central axis of the glacier, stations GPS01, GPS02, and GPS03 show average horizontal velocities between 50 and 60 mm/h, representing 1.2 m/d to 1.4 m/d and therefore 18 to 21 m for the 15 days of the experiment duration. Closer to the shear margin, GPS05 and GPS07 record slightly lower velocities of around 42 mm/h, while GPS04, that we temporarily deployed during the 2025 node experiment on the slow-moving ice beyond the margin, displays a markedly lower rate of about 5 mm/h (see also Fig. 6.5d), which corresponds to a displacement of only 0.12 m/d for the more stable slow-moving ice which is a total of 1.8 m for the full experiment duration .

These average values provide a broad preview of ice surface motion, but temporal variations in both horizontal and vertical displacements show modulation in response to tides. Figure 6.5 shows the time series of horizontal velocity for each GNSS station recorded between 10 and 20 January 2025, compared with tidal amplitude. As previously noted, GPS01, GPS02, and GPS03 exhibit similar velocity magnitudes (see Fig. 6.5a, 6.5b and 6.5c, respectively). At GPS01, horizontal velocity variations are strongly correlated with tidal amplitude, with a slight phase lag between the velocity and tidal peaks, most clearly seen between 10 and 15 January. For GPS02 and GPS03, the correlation with tides is less distinct, though periodic increases in velocity often coincide with the falling tide. Stations GPS05 and GPS07, positioned closer to the shear margin, record lower velocities ($35 - 45 mm.h^{-1}$) (Fig. 6.5e and 6.5f, respectively). Here,

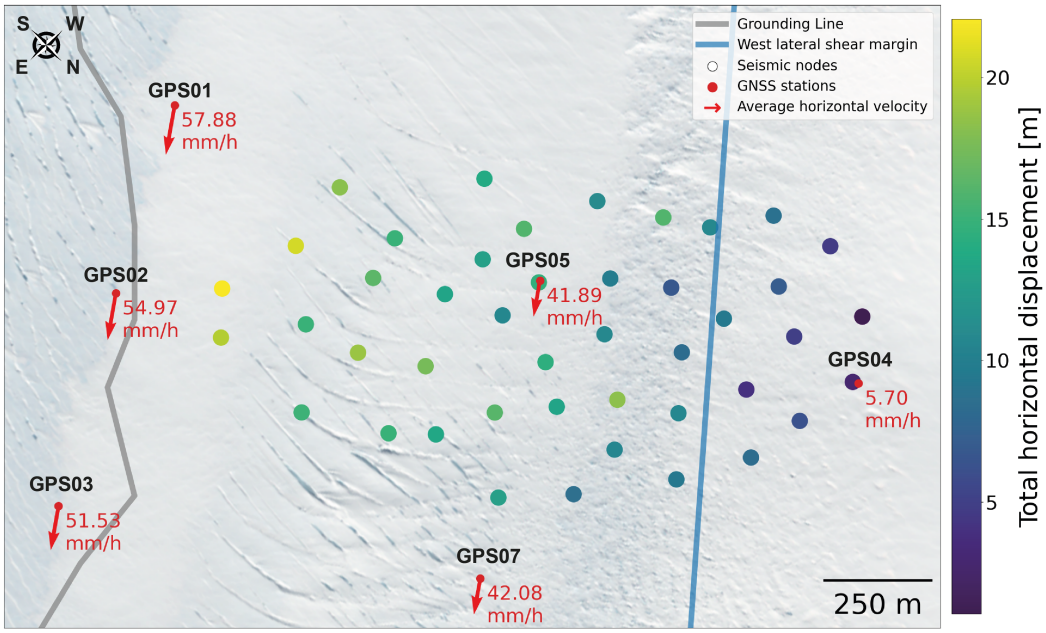

Figure 6.4: Horizontal displacement map of the shear margin area. Seismic nodes are color-coded by their total horizontal displacement (in meters) over the 12 to 15 days of deployment. GNSS stations (red dots) and their average horizontal motion are represented by arrows oriented along the dominant ice-flow direction and annotated with mean horizontal velocities (in millimeters per hour).

tidal control remains still visible, but the modulation is weaker and more synchronous with the tidal peaks, with little or no phase lag. Finally, GPS04, located over the slow-moving ice, shows - as expected - the lowest horizontal velocities ($< 12 mm.h^{-1}$) and only weak correlation with tidal amplitude, visible primarily between 17 and 20 January (Fig. 6.5d). Such observation is consistent with a station positioned beyond the shear margin, where motion is supposedly decoupled from tidal forcing. The FFT analysis reveals spectral peaks at diurnal and semidiurnal frequencies for all GNSS stations, although very weak for GPS04, confirming a sensitivity to tides (see Fig. D.1). Vertical displacement time series display a similar spatial pattern. Stations closer to the floating ice and grounding zone (GPS03, GPS02 and GPS01) exhibit stronger vertical motion, with clear tidal modulation (Fig. 6.6a, 6.6b and 6.6c, respectively). In contrast, stations located closer to the shear margins (GPS05, GPS07) show, though with much smaller amplitude compared to the easternmost stations, sensitivity to tidal forcing Fig. 6.6e and 6.6f, respectively). This lateral variation in the vertical ice displacement illustrates well the general lateral bending and flexuring of the glacier under the tidal sollicitation. FTTs spectra display amplitude peaks at both semidiurnal and diurnal tidal cycles for these stations. For station GPS04, there are also very weak vertical motion variations but the sensitivity to the tide is harder to observe (Fig. 6.6d). Accordingly, there is only a weak amplitude peak at the diurnal tidal cycle in the FFT spectrum (see Fig. D.2).

Overall, both horizontal velocity and vertical displacement show a clear spatial gradient across the study area, marking the transition from fast-flowing glacier ice to slower-moving, grounded ice. These observations also demonstrate that the ice surface motion remains controlled by tidal forcing, particularly near the grounding zone, though weaker tidal modulation persists even over the more stable ice. The key question that follows is how these pronounced horizontal and vertical tidally driven motion gradients and the induced shear strain is accommodated. The next section investigates the seismic response to this mechanical forcing, focusing on stick-slip events, their spatial distribution along the lateral ice-bedrock interface and their temporal characteristics.

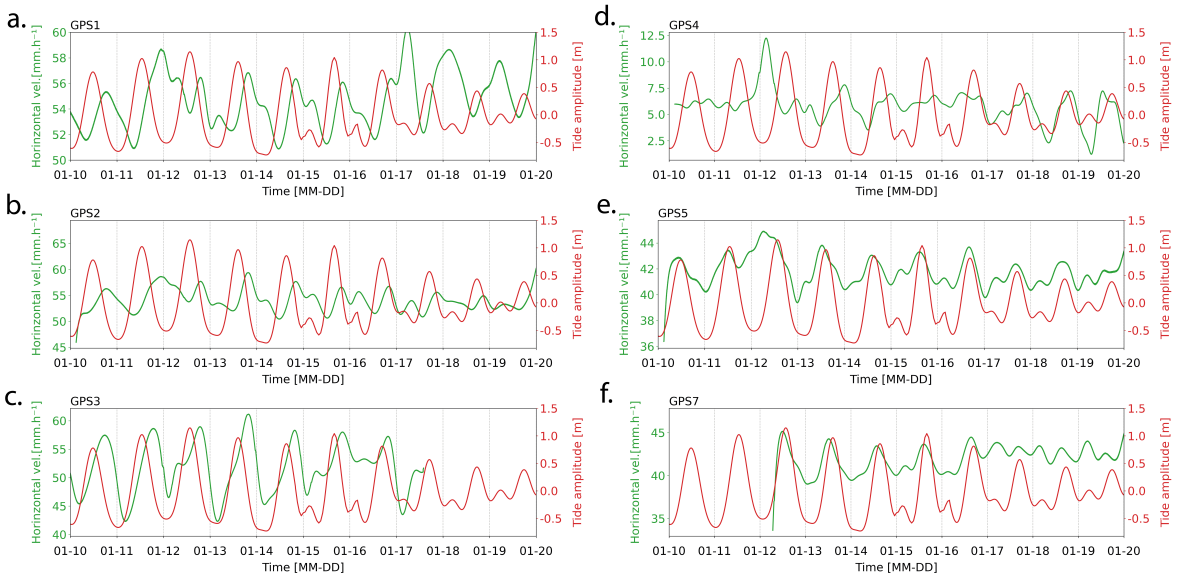

Figure 6.5: Horizontal velocity timeseries (green curve) superposed with tide amplitude (red curve) for 6 GNSS stations (see positions in Fig. 6.4): GPS01 (a), GPS02 (b), GPS03 (c), GPS04 (d), GPS05 (e), GPS07 (f) over the period January 10-20, 2025. Note that the y-axis is not the same for the different panels.

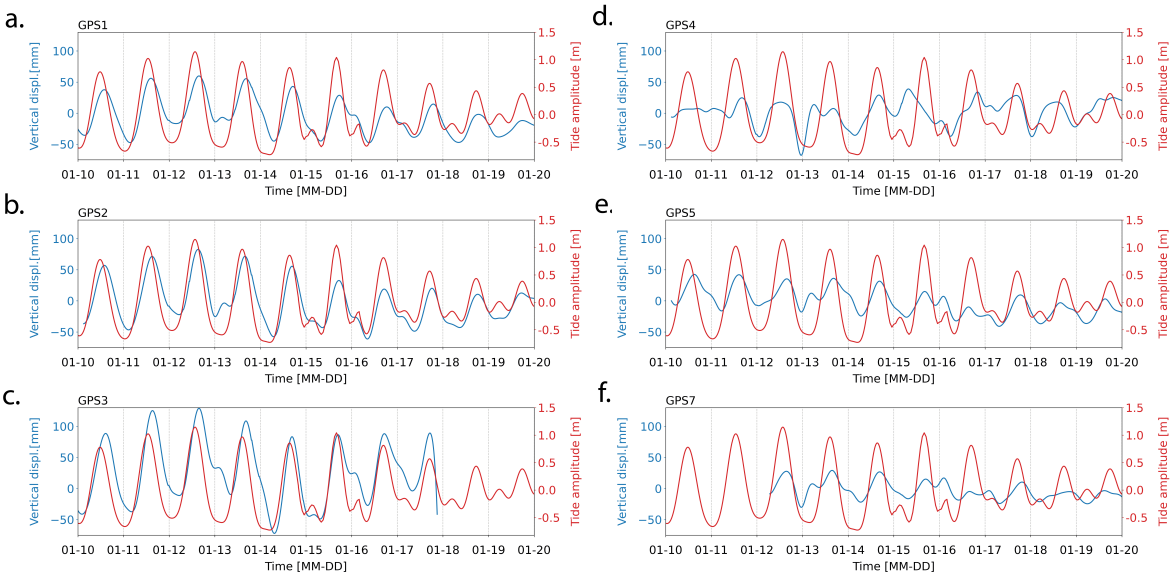

Figure 6.6: Vertical displacement timeseries (blue curve) superposed with tide amplitude (red curve) for GNSS stations GPS01 (a), GPS02 (b), GPS03 (c), GPS04 (d), GPS05 (e), GPS07 (f), over the period January 10-20, 2025.

6.4 Stick-slip clusters identification

6.4.1 Detection and location of stick-slip clusters

We follow the same workflow as described in Chapter 5 for the detection and location of stick-slip clusters. We apply template matching on the continuous seismic records and once all clusters are identified we locate them using QuakeMigrate. Because the station spacing in the 2025 array (A3) is smaller than in the 2023 array (A1), with inter-station distances of respectively approximately 150 m compared to 350 m, the QuakeMigrate algorithm is particularly efficient for cluster localization. Indeed, the shorter spacing allows clear identification of S-wave arrivals across multiple stations without the need of performing waveform stacking. It therefore should improve the accuracy of the events locations and depth estimates.

A total of 16 clusters of stick-slip events are detected (Fig. 6.7). Their coordinates are summarized in Table 6.1, along with the number of detections associated with each cluster. The clusters are spatially distributed into two approximate lines: the first comprising clusters 1 to 9, and the second comprising clusters 10 to 16. The estimated cluster depths range between 450 m and 1000 m from the surface. Clusters 1 to 10 are deeper than 750 m, while clusters 11 to 16 occur at shallower depths, between 450 m and 600 m. Several clusters are located directly beneath the dense array, in contrast to the stick-slip events identified during the A1 deployment (see Chapter 5). This difference is consistent with the positioning of the A3 array above the more grounded

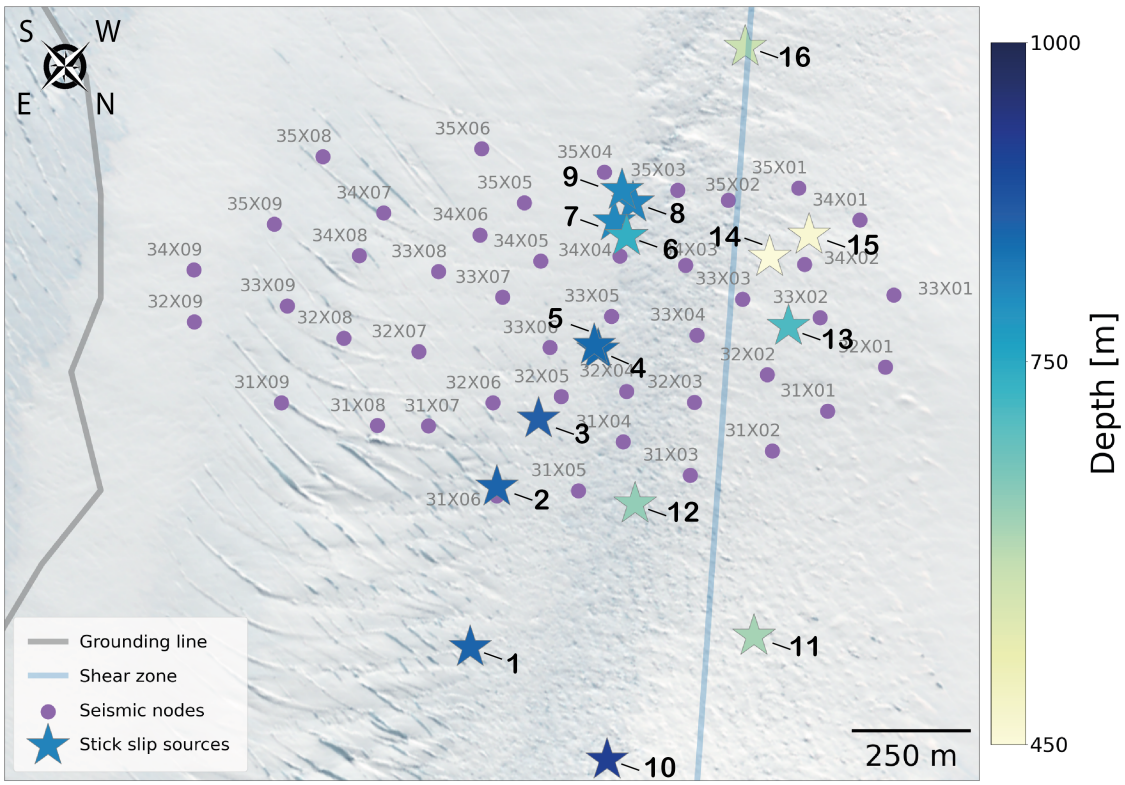

Figure 6.7: Map with location of seismic nodes (purple dots) and stick-slip clusters (stars), colored according to their depth.

part of the glacier and the shear margin, where ice maintains direct contact with the bedrock. In comparison, part of the A1 array extended over the floating section of the glacier, where seawater intrusion likely reduced the ice-bedrock contact area and, consequently, the occurrence of basal stick-slip events. The spatial coverage of the A3 array is smaller than that of A1. Considering both the smaller aperture of the network and the relatively low amplitude of the stick-slip events, detections are therefore limited to a more localized area. The A3 dataset seems to primarily provide a view of basal seismicity associated with ice-bedrock interaction at the shear margin and not stick-slip event that could occur at large distances from the network.

6.4.2 Focal mechanisms

We analyse the focal mechanisms of each stick-slip cluster by identifying compressional (upward) and dilatational (downward) first P-wave motions across the dense array. This approach enables the determination of nodal planes and fault geometries (e.g., strike-slip, normal, reverse, or oblique). To ensure robustness in this analysis, three independent analysts manually picked the polarity of the P-wave first arrivals.

Cluster	Long (°E)	Lat (°N)	Depth (m)	Number of events
1	-66.721251	139.933174	854	385
2	-66.723223	139.927337	856	185
3	-66.723694	139.923766	862	652
4	-66.724075	139.919516	846	108
5	-66.723963	139.919516	846	155
6	-66.72524	139.915038	738	872
7	-66.725599	139.915038	806	950
8	-66.725643	139.913791	812	430
9	-66.725952	139.913809	806	328
10	-66.718	139.931644	920	817
11	-66.718	139.922579	620	221
12	-66.721318	139.92286	640	1990
13	-66.722011	139.911923	712	926
14	-66.723222	139.910506	444	488
15	-66.723065	139.908409	464	366
16	-66.726516	139.905005	580	1425

Table 6.1: Stick-slip clusters detected beneath the Astrolabe Glacier west shear margin using the dense array A3 deployed in Jan. 2025. For each cluster is shown the longitude, latitude, depth and the number of events detected.

Ideally, fault mechanism determination requires full azimuthal and incidence-angle coverage around the seismic source. In our case however, we are limited for some clusters by partial azimuthal and inclination coverage of the seismic sources relative to the stations, as they occur at the periphery of the network. It results in a restricted azimuthal and inclination coverage, preventing a complete resolution of individual focal mechanisms. To overcome this limitation, we assume that all clusters share similar fault mechanisms and combine their first-motion polarities into a single virtual source, represented on a lower-hemisphere stereonet (Fig. 6.8). This approach is justified by the strong consistency observed among most individual stereonets (see Fig. D.3), with the exception of clusters 8 and 10, which display opposite polarity patterns from other clusters and are thus not included in the stereonet. This opposite polarity pattern could reflect local heterogeneity in the stress field, causing a change in the orientation of the rupture, or temporal variations in the basal conditions influencing the behavior of the slip. This hypothesis is supported by the fact that clusters 8 and 9, located next to each other, are not active during the same period.

When all data are combined into a single stereonet, a clear two-quadrant pattern

emerges, characterized by compressional (upward) first motions toward the south and dilatational (downward) motions toward the north. This configuration is consistent with previous results presented in Chapter 5 (see Fig. 5.4b) that could correspond to a strike-slip faulting mechanism on a horizontal plane and the corresponding motion aligned with the glacier flow direction. We find again a slight obliquity between the inferred fault plane and the flow direction.

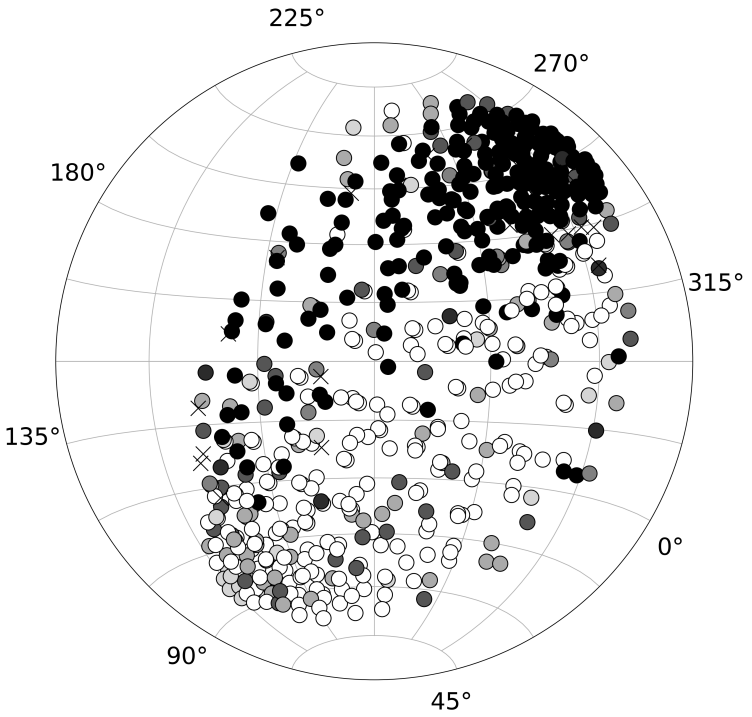

Figure 6.8: Lower hemisphere stereonet (in the same orientation as Fig. 6.7, i.e. with the flow vector pointing along the azimuth N055°E) representing the upward (black circles) and downward (white circles) first P-wave motion of 14 stick-slip clusters (1 to 16 except 8 and 10 which show opposite focal mechanisms). Grey circles indicate unsure first P-wave motion. Crosses indicate no clear waveform for picking the P-wave first motion.

6.5 Spatial and temporal analysis of stick-slip clusters activity

6.5.1 Tidal influence on stick-slip clusters

To place these results in context, similar analyses were presented in Chapter 5, where clusters identified both near the shear margins of the glacier and upstream from dense array A1 exhibited a clear tidal modulation. Those clusters tended to activate preferentially at low and rising tide and to become quiescent at high and falling tide. The cumulative number of stick-slip events observed along the Astrolabe Glacier lateral shear zone followed the same trend as the number of active clusters, peaking at low and rising tide. Event amplitudes, in contrast, were largest at high tide, while inter-event times (IETs) remained relatively constant throughout the tidal cycle.

We apply the same analysis here to the clusters identified using the array A3 (Fig. 6.9), examining variations in the number of active clusters, cumulative event counts across the tidal cycle, inter-event times and event amplitudes. Between 9 and 15 January 2025, when the tidal regime is predominantly diurnal, we observe that stick-slip activity peaks preferentially at low tide, with punctually additional clusters occurring at rising to high tide (e.g., 10–11 January) (Fig. 6.9a). After 15 January, when the tidal regime shifts toward a more mixed semidiurnal pattern, the correlation between tide amplitude and cluster activation becomes less clear. Activity occurs at roughly half the rate observed earlier, suggesting a transition to a different regime. During this latter period, activity is concentrated in clusters 2, 10, 7, 12, 14, and 16, which are spatially distributed across the study area (see Fig. 6.8) and at various depths, indicating no distinct spatial pattern associated with this second regime. When representing these data over a representative tidal cycle (averaged from 9–15 January 2025), we can refine the occurrence analysis and observe that clusters are most active during low, rising, and high tide, and least active during falling tide (Fig. 6.9b). There is no clear interdependence between clusters meaning their activation tends to occur simultaneously, but without a recurring sequential pattern between each other. The cumulative number of stick-slip events (Fig. 6.9c) follows the same trend, with the minimum number of events during falling tide. The inter-event time (IET) remains relatively constant throughout the tidal cycle, generally between 5 and 10 minutes (Fig. 6.9d). A slight increase of the IET (from $\sim$7 minutes to over 10 minutes) occurs near the end of the falling tide. That coincides with a decrease of the vertical ice velocity (see Fig. 6.6), which implies less shear stress to accommodate. The median amplitude of events roughly doubles between low tide and mid-rising tide, and again toward the end of falling tide (Fig. 6.9e). These observations confirm our hypothesis that, during falling tide, the shear stress accumulation is smaller, requiring more time for the shear stress to reach the rupture threshold necessary to trigger a stick-slip (hence the increase IET). By contrast, enhanced number of events and higher event amplitudes during rising and high tide may reflect increased shear stress to accommodate and

more rapid stress loading. Such partitioning is consistent with the vertical velocity being maximum at high tide (see Fig. 6.6). Note that the dynamics is most probably also influenced by simultaneous aseismic deformation processes that modulate stress distribution within the shear margin at different times of the tidal cycle.

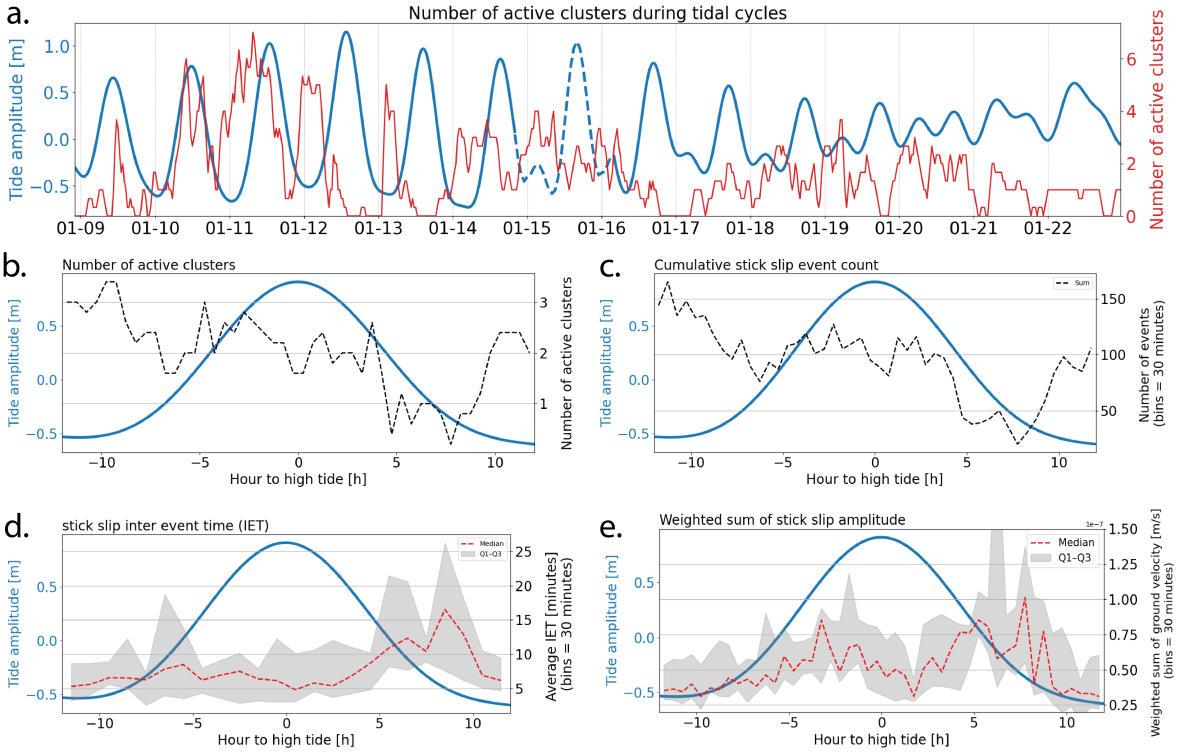

Figure 6.9: Stick-slip activity relative to tide: (a) Time series of the number of active stick-slip clusters (red curve) over the period 9–15 January 2025, together with the tide amplitude (blue curve). (b) Number of active clusters (black curve) folded over a representative 24-hour tidal cycle, divided into 30-minute bins. The x-axis represents time relative to high tide, from –12 to +12 hours and tidal amplitude is plotted as a blue curve. (c) Total number of stick-slip events from all clusters, folded over a representative 24-hour tidal cycle, divided into 30-minute bins. (d) Stick-slip inter-event time (IET), folded over a representative 24-hour tidal cycle, divided into 30-minute bins. (e) Event amplitudes (ground velocity, in m/s), folded over a representative 24-hour tidal cycle, divided into 30-minute bins. For IET and event amplitudes, the median (red dotted curve), and interquartile range (25th–75th percentiles displayed in grey shading) are shown.

These observations confirm that tidal forcing modulates the ice flow (vertical and horizontal displacement), but also the occurrence and characteristics of stick-slip activity along the glacier shear margin. The timing of cluster activation relative to the tidal cycle is broadly consistent with that observed in Chapter 5 for clusters derived from array A1, though subtle differences emerge in inter-event time and amplitude patterns. These variations suggest that the shear margin may operate under locally

variable stress conditions, with differing rupture thresholds compared to clusters located farther upstream beneath the fast-flowing glacier ice.

6.5.2 Lateral and depth distribution and comparison with radar data

We compare, in Figure 6.10a, the position between the stick-slip clusters detected with dense arrays A1 (2023) and A3 (2025), within the shear margin area. In 2023, some source locations extended about 500 meters farther east than the stick-slip clusters inferred from 2025. They also roughly align with the shear margin. The other clusters occurred in the same areas or along the same alignment as those from 2025. No seismic clusters were detected near the grounding zone, and this pattern is consistent across both years. These observations highlight a spatial partitioning of stick-slip activity, concentrated along the shear margin and progressively disappearing toward the main ice-flow area and the lateral extent of the grounding zone on the side of the Astrolabe Glacier. The successive lines of stick-slip clusters can thus be interpreted as marking lateral zones where basal motion is accommodated by frictional (seismic) processes, beyond which the glacier base transitions to aseismic sliding. The absence of seismicity in this sector may indicate a more lubricated interface or an area that is only partially grounded during tidal cycles and daily seawater intrusion.

To constrain the geometry of the ice-bedrock interface and the slope of the seismically active part of the shear margin, we compare the depth distribution of stick-slip clusters with available radar-derived ice thickness data (Fig. 6.10a). Several radar campaigns have previously surveyed the Astrolabe Glacier region. Airborne radar data were collected by NASA using the Warm Ice Sounding Explorer (WISE) during the 2008–09 season (Mouginot et al., 2014). Additional airborne measurements were acquired within the ICECAP project using the High Capability Radar Sounder (HiCARS) in 2008-09 and 2009-10 (Young et al., 2011). Ground-penetrating radar (GPR) profiles were also collected during the 2007-08 field season (Le Meur et al., 2014). Each dataset was processed independently by the respective project teams. Here, we compile ice thickness estimates from all available radar profiles crossing the area of interest around the west lateral shear margin. An overview of the radar data coverage is provided in Fig. D.4.

We project the cluster locations and radar-derived ice thicknesses along a 2D transect parallel to the x-axis (Fig. 6.10b). A polynomial regression curve is fitted to each dataset to visualize the general slope of the ice-bedrock interface. The stick-slip cluster depths reveal a trend consistent with the expected geometry of the lateral margin: shallower depths toward the west (near and above the rocky valley wall) and increasing depth eastward toward the glacier main body and the center of the fjord. Ice thickness inferred from cluster locations increases from just over 400 m at the western margin to

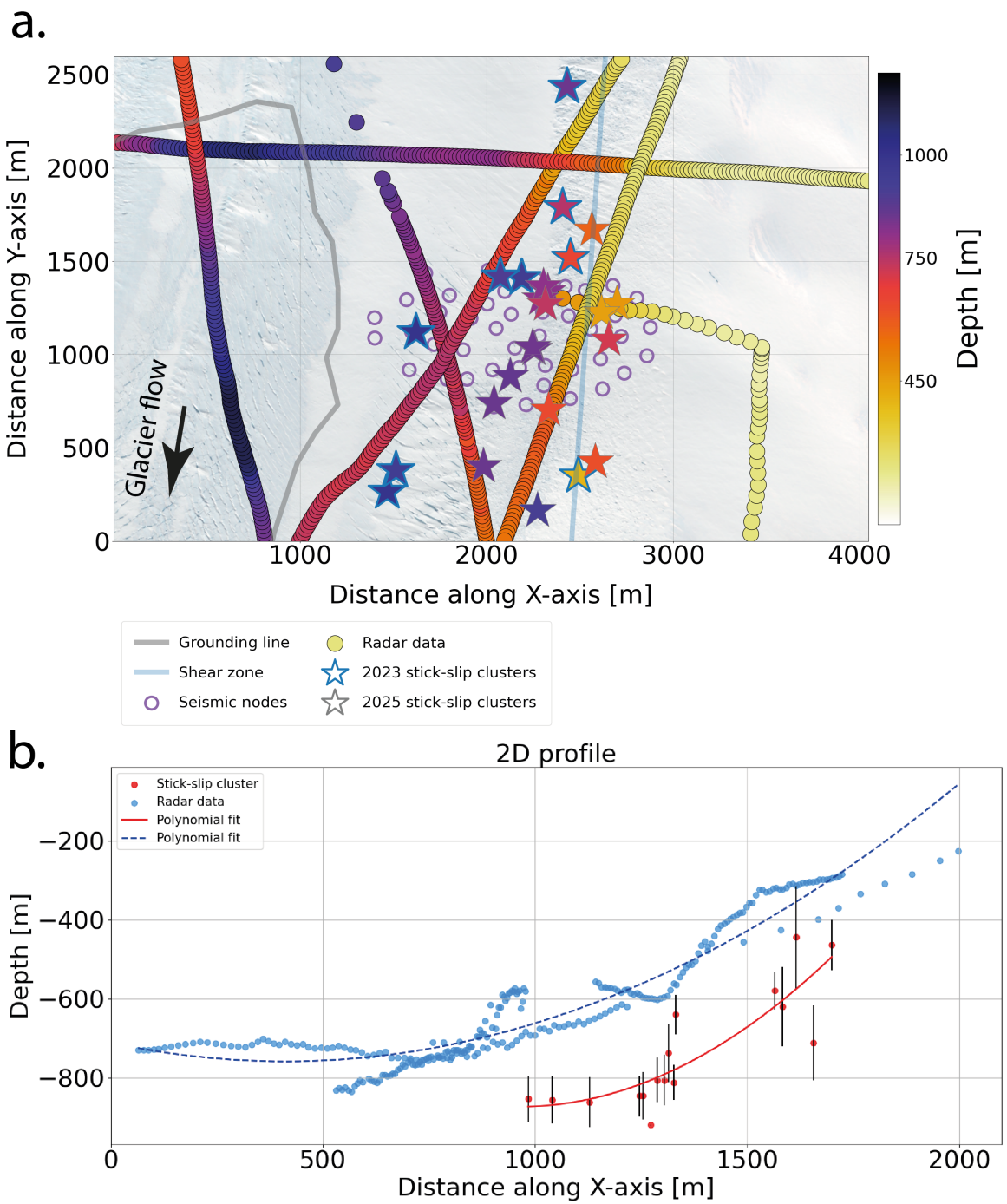

Figure 6.10: (a) Map showing stick-slip clusters locations from 2023 detection (stars with blue edge) and 2025 detection (stars with no edge color), color-coded by their depths. Radar profiles intersecting the seismic node array are represented by dots color-coded according to the associated ice thickness (in meters). The lateral shear margin of the Astrolabe Glacier is outlined in light blue. (b) 2D profile of the ice–bedrock interface depths along the X-axis, approximately perpendicular to the shear margin. Blue dots represent the projection of the radar-derived ice thicknesses on the plane normal to the shear zone, and red dots indicate depths of stick-slip clusters inferred from seismic data, along with their uncertainties (black error bars). Polynomial (degree-2) regression curves are fitted to each dataset to illustrate the general trend of the ice-bedrock interface slope.

about 900 m at the base of the glacier, over a horizontal distance of approximately 715 m, corresponding to an estimated slope of $\sim 35°$. The radar-derived ice thickness data exhibit strong consistency between points as well, allowing a well-fitted polynomial regression. We also observe shallower depths near and above the rocky valley wall and increasing depth eastward. Local discrepancies between intersecting radar lines are visible (typically <100 m at 600, 900, and 1,200 m along the x-axis) but could come from variability along the y-axis. From the radar data, the inferred bedrock slope, over the same section of the profile as for stick-slip clusters (from 1,000 m to 1,700 m along the x-axis), is less steep, around 25°.

We observe a systematic offset of approximately 200-300 m between radar and seismic inferred depths, with stick-slip clusters systematically deeper. Given that radar-derived ice thickness estimates generally have uncertainties below 50 m, and that the results from the different radar campaigns (WISE, HiCARS, and ground-penetrating radar) are mostly consistent, the radar-based values likely represent the most reliable reference for ice thickness in this area. Consequently, the difference most likely originates from uncertainties associated with the seismic depth estimation procedure, which relies mostly on local seismic P- and S-waves velocities. When determining event locations using the QuakeMigrate algorithm, the principal source of uncertainty indeed arises from the assumed values of the compressional (V_P) and shear (V_S) wave velocities. In the present study, depths of the stick-slip clusters were computed by investigating velocity ranges of V_P = 3.5-3.8 $km/s$and V_S = 1.7-1.9 km/s, with the selected velocity pair corresponding to the model that best fits the P- and S-wave arrival times at the seismic nodes. These velocity ranges were chosen based on commonly reported values for glacier ice (Maurel et al., 2016; Wittlinger & Farra, 2012), as no direct measurements of V_P and V_S are available for the Astrolabe Glacier.

We perform a sensitivity analysis over a broader range of V_P and V_S values for two representative clusters (Fig. 6.11). We estimate ice thickness using all possible (V_P,V_S) couples and the measured differential P-S travel time (dt), following Eq. 3.6. We use dt values derived from direct observations at the seismic station located closest to each stick-slip cluster (at its vertical), minimizing potential errors related to ray-path geometry. In these tests, V_P varies between 3.0 and 4.0 km/s and Vs between 1.0 and 2.0 km/s. For the two considered examples, the resulting maps of predicted ice thickness as a function of (V_P,V_S) show that the observed dt values correspond to greater depths than those derived from radar data, when using velocities we set in QuakeMigrate (indicated by the rectangle, Fig. 6.11). In order to make our stick-slip depths matching with the radar-derived thickness, Vs would need to be significantly lower, around 1.40-1.45 km/s. Such shear-wave velocities are notably low compared to what is generally admitted for ice in the literature (Llorens et al., 2020; Wittlinger & Farra, 2012). Our sensitivity tests also show that depth estimates are far more sensitive to changes in V_S than to changes in V_P, indicating that uncertainties in shear-wave velocity dominate the overall depth uncertainty. The very low shear wave velocities

could originate from a pervasive effect of ice damage that could strongly attenuate shear waves. One can hypothesise first that this damage could be inherited from the deformation history of the glacier, and particularly developed when crossing the serac zone upstream the grounding area of the glacier, or more recently induced by the daily tidal displacement of the floating tongue relative to its grounded part. Second, one can also hypothesise that the damage could also be related to the accommodation of the shear displacement at depth. Third, low shear wave velocities could result from seismic anisotropy with low Vs along the vertical direction, induced by intrinsic ice crystals preferred orientation and/or extrensic pervasive ice structure, such as microfracturing.

All in all, these tests seem to point that our current velocity model likely overestimate shear-wave speed leading to an overestimation of cluster depth. These findings emphasize an important limitation of using passive seismic methods to infer subsurface geometry in glacier environments. While the relative depth distribution of stick-slip clusters provides preliminary insights into the structure of the shear margin, absolute depth estimates may remain uncertain without independent velocity or depths constraints.

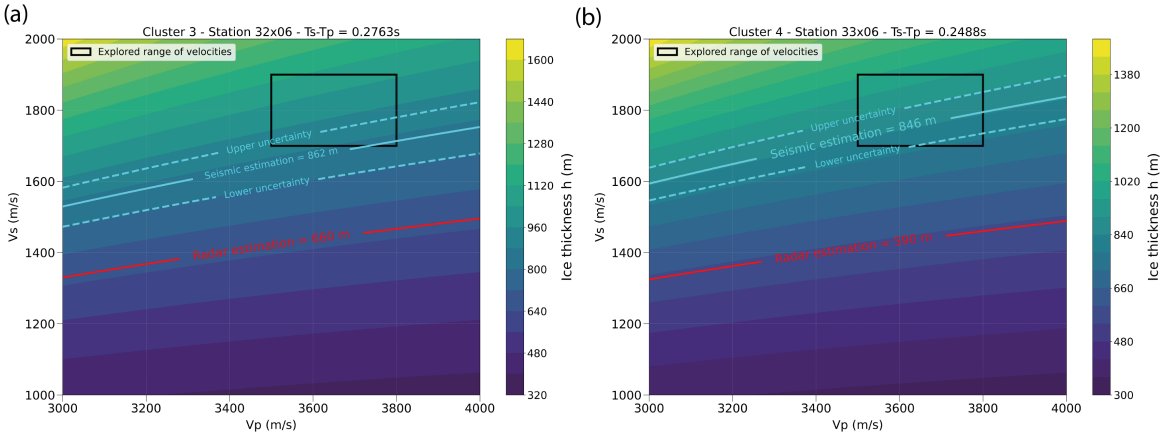

Figure 6.11: (a) Predicted ice thickness as a function of compressional (V_P) and shear (V_S) wave velocities that can explain the measured P-S differential travel time (dt = 0.2763 s) observed at station 32x06, located at the vertical of the source of cluster 3. The black rectangle delineates the velocity domain explored within QuakeMigrate. The solid cyan line represents the cluster depth for the location with best fit to the P- and S- wave arrivals, and the dashed cyan lines indicate the corresponding uncertainty bounds. The red line marks the radar-derived ice thickness estimate, showing that the Vs could be much smaller than investigated. (b) Same as in (a), but for cluster 4 (dt = 0.2488 s), observed from the recorded data at station 33x06.

6.6 Outcomes and outlook

In this chapter, we investigated the dynamics of the west lateral shear margin of the Astrolabe Glacier using a dense seismic array deployed in January 2025, complemented by GNSS measurements. This zone of the glacier experiences strong mechanical stress, resulting from the important velocity gradient between the fast-flowing glacier, advancing at 1 - 1.5 m per day in its central part, and the surrounding stable to slow-moving ice, advancing at about 10 cm per day. Our analysis focused on stick-slip events, accommodating basal and lateral shear stress along this active boundary.

We detected and located 16 stick-slip clusters beneath and in the vicinity of the dense array. These clusters are organized into two along-flow lines and display horizontal strike-slip focal mechanisms. These clusters are present along the western part of the array but clearly absent beneath its eastern part, suggesting a transition to the grounding zone. Their activity rate is modulated by the tidal cycle, with dominant activity during low and rising tides, similar to the stick-slip clusters identified from the 2023 dense array on the glacier grounding zone (see Chapter 5). This timing coincides with periods of larger surface ice velocity, suggesting an increase of the shear to accommodate flow during these phases, promoting seismic slip along the glacier lateral margins.

Comparison between cluster depths and radar-derived ice thickness reveals a persistent overestimation of event depths in the seismic results. This overestimation likely originates from slower V_S values than typically expected for glacier ice. Such velocity anomaly could be a marker of important ice damage at the shear margin induced by strong shear stress. The next step to complete the current analysis would be to investigate the origin of such low shear-wave velocities. A tomographic inversion could be performed to retrieve spatial variations in V_P and V_S across the glacier, to identify structural heterogeneities or damaged zones that may explain these anomalies. In addition, applying shear-wave splitting analysis would allow us to evaluate seismic anisotropy distributed along the wave paths, which could also contribute to the observed low V_S values. Because the shear wave velocity anomaly may arise anywhere within the ice column, processes near the surface should also be investigated. Future analyses should therefore combine surface seismicity together with glacier surface morphology that may inform on the local state of stress. Part of this work has already been carried in Chapter 4, where we analyzed the spatio-temporal distribution of icequake activity over the shear margin. However, we now need improved event localization. This can be achieved through matched-field processing (MFP), whose preliminary outputs will be briefly presented in the next section. The application of MFP to the 2025 dense array remains in an early stage and requires further validation before interpretations. Ultimately, these additional analyses will establish how surface morphology and subsurface velocity anomalies, together with the stick-slip clusters, can shed light on the mechanical behavior and vertical deformation structure of the shear margin.

CHAPTER 7

Thoughts on the deployment and performance of geophysical instrumentation in polar regions

Contents

7.1 Context and scope of the discussion 138

7.2 Contrasted field conditions and logistical challenges across polar regions 139

7.2.1 Climatic constraints on missions 139

7.2.1.1 Antarctica missions 139

7.2.1.2 Greenland missions 140

7.2.2 Logistical architectures: access and operational frameworks . 141

7.2.3 Risk management on the field 144

7.3 Dense seismic arrays: instrumentation strategies and data quality analysis 146

7.3.1 Deployment 147

7.3.2 Recovery 150

7.3.3 Tilting 152

7.3.4 Intercomparison of seismic sources: Astrolabe vs. Isunnguata Sermia 156

7.4 Distributed Acoustic Sensing (DAS): instrumentation strategies and data quality analysis 160

7.4.1 Deployment of optic fiber in Antarctica and Greenland 161

7.4.2 Quality of the data acquired on the Astrolabe Glacier 164

7.4.3 Preliminary analysis and comparison with data acquired on Isunnguata Sermia 166

7.4.4 Can we substitute dense networks with DAS ? 169

7.5 Data acquisition and scientific responsibility 170

7.5.1 From acquisition to valorization 170

7.5.2 Environmental cost and scientific sobriety 171

In this final chapter, we step aside from the previous focus on cryoseismic signatures of the dynamics of the Astrolabe Glacier to address a different but important topic for glaciological studies based on observational data: data acquisition in polar regions. Drawing on my fieldwork experience in Antarctica and Greenland, I discuss strategies for deploying geophysical instruments, particularly seismic instruments, in polar regions, and how site-specific environmental and logistical factors can influence the quality and content of the data collected.

7.1 Context and scope of the discussion

During my doctoral research, I participated in the deployment of geophysical instrumentation across polar glacier margins, including both outlet and land-terminating glaciers. I first took part in the SEIS-ADELICE campaign on the Astrolabe Glacier, spending six weeks at Dumont d'Urville Station (Jan–Feb 2024) to deploy and maintain seismic stations, recover ocean-bottom seismometers, and install a dense array of 50 seismic nodes combined with optical fiber for Distributed Acoustic Sensing (DAS). I later contributed to dense array and DAS deployments on Isunnguata Sermia near Kangerlussuaq, Greenland, within the SLIDE (Livingstone, 2022–2024) and REASSESS (Gimbert, 2024–2029) projects. Both study sites represent highly dynamic environments characterized by strong spatial and temporal variability. Their behavior responds rapidly to external forcings such as abrupt weather changes, melt or snowfall events, and strong winds. This variability demands flexible, reliable, and robust instrumentation strategies, raising a practical question: how can high-quality geophysical observations be achieved in such extreme and rapidly changing environments?

While French polar geophysics has historically focused on Antarctica -thanks to the Dumont d'Urville and Concordia stations and the legacy of pioneering French glaciologists — Greenland has seen comparatively little French geophysical activity. France operates several permanent and seasonal Antarctic bases supported by the Institut Polaire Français Paul-Émile Victor (IPEV), but lacks an equivalent logistical framework in Greenland, where most field campaigns are led by the Geological Survey of Denmark and Greenland (GEUS). This imbalance is unfortunate, as field operations in Greenland are often logistically simpler and less costly: for instance direct flights from Copenhagen to Nuuk or Kangerlussuaq provide easy access to glaciers and ice-sheet margins. Yet, the limited experience means that few established practices exist for conducting geophysical operations in Greenland. A comparison based on field experience in these two polar environments can therefore be useful for sharing ideas on how field strategies can be optimized and adapted to distinct environmental and logistical conditions.

This chapter presents and reflects on the practical and methodological aspects of conducting geophysical fieldwork in polar regions. I first discuss the differences in field

conditions and on-site logistics between Antarctica and Greenland. I then focus on two instrumental approaches that remain relatively new in glaciological applications (and among the first deployed in both regions): dense seismic arrays and Distributed Acoustic Sensing (DAS). I describe the deployment strategies, acquisition setups, and resulting data quality, and compare how environmental and logistical factors specific to each region can influence the observations. Finally, beyond the technical aspects, I raise the topic of the broader ethical and sustainability considerations of conducting geophysical research in threatens polar environments.

7.2 Contrasted field conditions and logistical challenges across polar regions

This section aims to compare the two polar environments not through a narrative of field missions, but as contrasting systems impacting in their own ways scientific activity. The discussion focuses on DDU in Antarctica and Isunnguata Sermia near Kangerlussuaq in Qeqqata, West Greenland. These sites, while both representative of polar environments, expose important differences in climatic and logistical conditions that shape how geophysical instrumentation is carried out.

7.2.1 Climatic constraints on missions

7.2.1.1 Antarctica missions

Field missions in Antarctica are conditioned by the continent's extreme and seasonal climate. Research stations operate under two distinct regimes: the austral summer (from November to late February) and the austral winter during the rest of the year. Personnel overwinter at the bases primarily to maintain infrastructure and ensure that scientific instruments remain operational, allowing the stations to fully function when most research teams arrive in summer. The summer season defines the practical limits of field operations. Because the capacity of each base is restricted and the weather window brief, research projects must be carefully scheduled within a few weeks to a maximum of four months. During this period, teams must complete all deployments, data acquisitions, and recovery operations while coordinating with the logistics timetable of the base. For instance, during the SEIS-ADELICE project, our team worked from early January to mid-February to do maintenance on existing broad band seismic stations, to recover OBSs at sea that were deployed the year before, to deploy a dense array of seismic nodes, and to install a fiber-optic cable for DAS measurements. The tight schedule required pre-field planning: array geometry, node and optic fiber placement, acquisition parameters, energy supply, and data management had to be finalized before departure. Coordination with other scientific groups and with helicopter operations is also essential, as weather delays or overlapping missions often imposed last-minute adjustments. Under such conditions, anticipation becomes a critical success factor.

In terms of climate conditions, DDU benefits from a relatively mild coastal climate influenced by the Southern Ocean. Average temperatures in January are around -1.2°C and in February about -4.4°C (Météoclimat, 1970-2025). But mild temperatures do not necessarily mean easy working conditions. Because we are on the coast, wind storms are occurring regularly, lowering perceived temperatures well below actual values. During storms, wind can reach speeds exceeding 100 km per hour, forcing the suspension of outdoor work for one or more days. Additionally, strong and persistent katabatic winds blow almost every evening. These weather events often produce whiteout conditions, reducing visibility and posing safety risks. Consequently, mission plans must incorporate buffer days to account for unavoidable weather-related interruptions. Over the whole SEIS-ADELICE field work covering four summer seasons (2022-2025), the effective work in the field represents only 50% of the time, due to weather constraints. Sea-ice and iceberg conditions also impose logistical constraints by impacting the base access and operations at sea. During the SEIS-ADELICE project, reaching the base at the end of December has never been a problem but earlier in the season, operations may be strongly delayed and even cancelled. During summer, most sea ice around the base breaks up, improving access by boat, though floating ice and large icebergs can still block specific sites. For instance, in January 2024, one ocean-bottom seismometer could not be recovered for several days because an iceberg was positioned directly above it, forcing the retrieval to be postponed. Choosing the mission period (December or January) thus depends partly on sea-ice state, especially when ocean-based operations are planned. Despite Antarctica being the driest continent, precipitation events can occur in coastal zones. Occasional snowfall or rain may temporarily affect accessibility or helicopter flight plans, while snowdrift accumulation around buildings or instrument boxes requires some shoveling. Overall, the climatic regime at DDU imposes strict "on/off" constraints on scientific activities. Successful missions within this short operational window require extensive pre-planning, flexibility to accommodate weather interruptions, and close coordination with base logistics.

7.2.1.2 Greenland missions

The situation in Greenland presents a distinct set of challenges. Field operations there benefit from a longer season, extending roughly from April to October. But this extended window is characterized by important interannual and intraseasonal variability. Therefore, mission planning depends mainly on short-term weather forecasts and the specific scientific objectives of each campaign. We can divide the field season into three categories: early spring with transition from winter to melt season, summer with mild temperatures and easiest fieldwork conditions and winter transition with declining temperatures and reduced daylight. In April, in Kangerlussuaq, snow begins to melt across both the tundra and glacier surface, though fresh snowfalls of 20-50 cm remain possible. Temperatures vary widely, often ranging from -15°C at night to around 0°C during the day. This diurnal variability results in rapid surface melting under clear skies, yet crevasses and moulins remain snow-filled and hidden, complicating safe

glacier progression. Hydrological activity gradually initiates toward the end of the month and May, as frozen surface streams (bedières) and drainage channels begin to thaw. In the tundra near the glacier tongue, the ground remains frozen, saturating the upper layer of moss and grass with meltwater. Operationally, this period poses comfort and safety challenges, but offers a good window for early-season instrument deployment to capture the start of the meltwater season. By late June, Isunnguata Sermia enters the full melt season, with daily temperatures generally above freezing. In July, daytime temperatures often reach 10°C, and under clear skies the reflective glacier surface can make it feel considerably warmer. Nights rarely refreeze, and continuous melting maintains hydrological networks of moulins and surface channels active. During these months, surface ablation reaches 4-6 m. These conditions allow relatively stable access to the study site but increase the risk of getting trapped in between rapid streams forming at the surface. Storms are not frequent at this period but high winds can be expected and with it temporary cooling of the temperatures. As in Antarctica, katabatic winds often develop in the evening, though generally weaker. From late August onwards, the climate shifts again toward freezing conditions. Nights regularly fall below 0°C, and periods of poor weather become more frequent. Snowfalls, though generally short-lived, may accumulate temporarily and halt field operations. September and October alternate between clear days with residual melting and stormy episodes that can fully paralyze fieldwork for several days. Inter annual variability is high: for instance, October 2025 was marked by persistent high winds preventing data collection, while October 2024 remained mild and sunny (note that the study site in 2025 was higher up on the glacier). In addition, daylight hours decrease rapidly, constraining working time compared to the 24-hour light conditions of high summer.

Overall, the climatic window in Greenland is longer but less predictable than in Antarctica. The choice of deployment period must align with the scientific objectives, whether observing the onset of melt, peak ablation, or refreezing processes. The flexibility of fieldwork in Greenland, where researchers are not bound by the schedule of a permanent base station, offers significant autonomy in planning. Yet it still demands great adaptability to local weather and terrain conditions that can change quickly. Unlike at DDU, where teams can shelter in established facilities during storms, Greenland missions are typically camp-based and thus more directly exposed to weather variability. In both regions, however, climate remains the ultimate constraint, dictating access, safety, and the duration of deployment and data acquisition windows.

7.2.2 Logistical architectures: access and operational frameworks

Accessing the study sites

Reaching the glaciers in both regions involves fundamentally different logistical ap-

proaches. Access to the Astrolabe Glacier in Antarctica first requires reaching DDU, a mission in itself. Scientists and equipment travel aboard the Astrolabe vessel from Hobart, Tasmania, on a six-day journey across the Roaring Forties, Furious Fifties, and Screaming Sixties (i.e., zones of persistent strong winds and rough seas characteristic of the Southern Ocean). All scientific material, including instruments, sensors, and spare parts, must be shipped months in advance from France to Australia before being loaded onto the vessel. Once in DDU, instruments are transported to the glacier by helicopter, which also shuttles researchers daily between the base and field site. This high level of logistical coordination ensures reliable running of the operations but also imposes rigid scheduling. Scientific operations depend on helicopter availability, weather conditions, and the activity of other research teams at the base. Each day of good weather must therefore be optimized for all.

In Greenland, reaching Isunnguata Sermia involves first going to Kangerlussuaq. With a four-and-a-half-hour flight from Copenhagen. There, we can start the preparation at the Kangerlussuaq International Science Support (KISS) facility -a small scientific hub with accommodation for scientists and space for unpacking shipments arriving by air or by sea, organizing material for helicopter transport, testing instruments etc. Once preparations are complete, researchers can access the glacier either by car then foot (one hour and half of driving then about two hours to reach the glacier tongue) or by helicopter, depending on the study site, the volume and weight of equipment to transport. Unlike in Antarctica, where IPEV covers all the logistics, helicopter transport in Greenland must be paid for directly through Air Greenland, making cost optimization a central aspect of mission planning. Heavy or bulky instruments, such as seismic nodes, are usually airlifted, while researchers carry personal bags and lighter equipment on foot if possible. Given the expense and limited helicopter availability, it is generally not feasible to commute daily between KISS and the glacier. Instead, teams establish temporary field camps for the duration of their work (typically one to several weeks) either on the tundra close to the ice or directly on the glacier.

Field organization and team structure

Operating from a base such as DDU offers comfort and logistical security: meals, accommodation, maintenance, and technical support are provided by permanent staff, allowing scientists to concentrate almost exclusively on field instrumentation and measurements (Fig. 7.1a and 7.1b). However, this centralized model constrains flexibility. Helicopter flights run on fixed schedules, and poor weather can abruptly suspend operations, leaving limited room for last-minute adaptation. In Greenland, by contrast, teams are fully autonomous. Camps usually consist of sleeping tents, a mess tent, and a scientific tent. Living conditions are basic, and a significant part of each day is devoted to camp maintenance such as reinforcing tents, managing fuel and water, melting snow when streams freeze, and preparing meals (Fig. 7.1c and 7.1d). This self-sufficiency provides freedom in planning work hours and activities but requires more time, energy,

and risk management.

The size and composition of the team reflect these differences. In Antarctica, the number of participants per project rarely exceeds two or three researchers, determined by the station's accommodation capacity and IPEV coordination of multiple concurrent projects. In Greenland, teams can expand or contract depending on scientific needs and available resources. This flexibility allows for more diverse collaborations, including technical staff, engineers, or communication specialists. It also enables successive missions within the same season, adjusting team size and objectives to weather conditions and available funding.



Figure 7.1: Comparison of field organization between Dumont d'Urville Station (Terre Adélie, East Antarctica) and the Isunnguata Sermia field camp (Kangerlussuaq, Qeqqata, West Greenland). (a) Dumont d'Urville (DDU) base station, showing the various buildings dedicated to daily life and scientific operations. (b) Communal dining hall of DDU where all station members share meals. (c) Field camp setup on Isunnguata Sermia, including sleeping tents, a mess tent, and a science tent in the background. (d) Interior view of the mess tent, where cooking and scientific activities often overlap. Daily logistics and research operations are carried out in parallel on the glacier.

Overall, the contrast between the two systems is significant. Antarctic logistics rely on a centralized, institutionally supported framework that ensures safety and reliability but limits flexibility and freedom. Greenlandic logistics are decentralized, demanding greater planning, self-sufficiency but allowing more adaptable and cost-effective operations. From a scientific point of view, these logistical architectures shape both the sci-

entific ambitions and the timeline of fieldwork. Antarctic projects tend to be intensive, time-constrained campaigns while Greenlandic missions request personal consideration of the risk but provide greater autonomy and adaptability.

7.2.3 Risk management on the field

Conducting fieldwork on glaciers involves exposure to physical and environmental risks. Whether in Antarctica or in Greenland, these hazards can become rapidly dangerous if not properly anticipated and managed. Although both environments share the presence of crevasses and extreme weather, the nature and management of risk differ significantly between sites. Walking on glacier ice presents the most immediate danger. On the Astrolabe Glacier near DDU, crevasses are often wide and deep, plunging into darkness and requiring constant caution (Fig. 7.2a). On Isunnguata Sermia in Greenland, crevasses are generally narrower but numerous. What distinguishes Greenlandic glaciers from East Antarctic glaciers is the recurring presence of bedières and moulins (vertical shafts where surface meltwater drains into the glacier interior). Moulins can reach considerable depth and can be concealed by thin snow bridges (Fig. 7.2b). During summer, when the surface ice is largely free of snow, moulins and crevasses are visible and can be avoided through cautious navigation. The rest of the year, or after fresh snowfall, snow accumulation can conceal crevasses and moulins, greatly increasing the level of risk and requiring progressing on the glacier with a rope. On the Astrolabe Glacier, crevasses are often partially concealed by snow bridges. These latest are not always robust and crossing them often requires some testing beforehand, and always progressing on the glacier with a rope.

In such conditions, proper experience and risk awareness are critical for assessing and managing danger. At DDU, all glacier operations are conducted with a professional mountain guide, as requested by IPEV. Having a mountain guide is very valuable: researchers can focus on their scientific objectives while delegating real-time terrain assessment and route decisions to a dedicated person. The guide also coordinates with the base in case of weather deterioration or evacuation needs. In Greenland, this model is rarely feasible. Employing a professional guide is logistically complex and financially constraining. Instead, field teams receive glacier and rescue training before deployment, learning rope techniques and basic medical skills. Once in the field, risk management becomes the shared responsibility of the team, relying on good communication, experience, and constant assessment of conditions. The autonomy of field operations in Greenland thus comes with increased individual responsibility and workload. Anticipating risks that may arise depending on the time of year, the skills of team members and each person's experience, and having safety plans and rules in place can help to lighten the workload.

Weather represents a second major category of risk. Sudden whiteouts, strong kata-

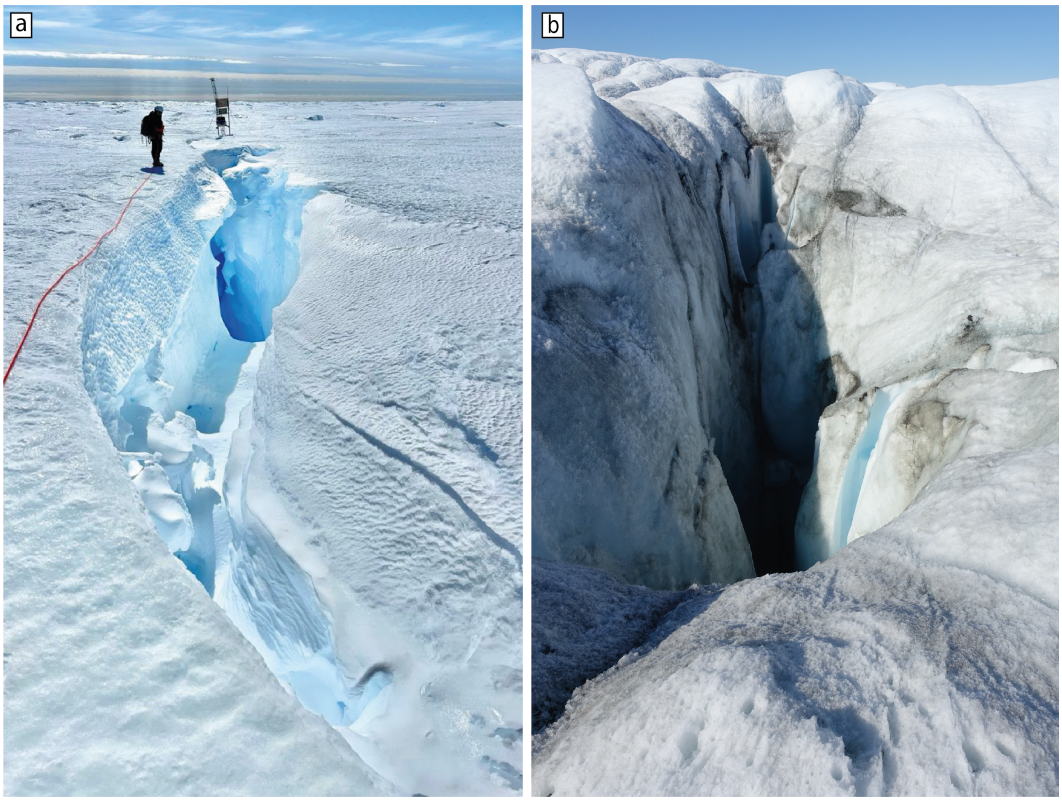

Figure 7.2: Examples of field hazards encountered on glaciers. (a) Large crevasse on the Astrolabe Glacier, partially filled with snow bridges. (b) Moulin on Isunnguata Sermia.

batic winds, and rapid temperature drops are common in both regions. At DDU, these events trigger an established response protocol: if deterioration is anticipated, the helicopter picks up the field team before conditions worsen. If evacuation is not possible, a small emergency shelter can provide temporary refuge. In Greenland, weather management is approached differently. Field camps are situated directly on or near the glacier, providing immediate shelter when conditions change. This proximity improves safety during storms, provided that tents are robust enough. A major difference lies in medical support and evacuation capacity. DDU maintains a small medical unit along with a physician, but serious injuries are difficult to treat locally. Evacuation to Australia can take several days and depends on ship or aircraft schedules. Consequently, field protocols emphasize prevention and risk minimization. In Greenland, emergency response is more flexible. A rescue helicopter based in Kangerlussuaq can reach most field sites rapidly, with transfer to Nuuk's hospital or, if needed, evacuation to Reykjavik or Copenhagen. This relative accessibility allows slightly greater tolerance for risk, though caution remains essential.

Ultimately, scientific ambition must always be weighed against safety considerations. Each deployment decision -whether to cross a crevassed zone, to extend work hours despite deteriorating weather, or to install an instrument further onto unsta-

ble ice- requires a pragmatic balance between scientific value and physical risk. In Antarctica, because it is supervised by IPEV, safety frameworks impose strict limits that sometimes restrict flexibility but ensure security. In Greenland, greater autonomy enables adaptive field strategies but also places the full weight of decision-making on the team. In both contexts, risk management is not only a matter of safety but also a core component of scientific objectives and deployment design: it shapes what can realistically be measured, how far instruments can be deployed, and ultimately how science operates in extreme environments.

7.3 Dense seismic arrays: instrumentation strategies and data quality analysis

Over the past years, dense seismic arrays have appeared as efficient approaches to investigate glacier dynamics. These arrays allow high-resolution sampling of the seismic wavefield, enabling detailed imaging and monitoring of processes within and beneath glaciers (Gimbert et al., 2021; Karplus & Schmandt, 2018; Karplus et al., 2024; Nanni et al., 2021, 2022; Veitch et al., 2021). Recent technology advances have provided the scientific community with compact and lightweight seismic nodes combining into a single casing, a three-component geophone, a data logger, and a battery lasting up to 30-35 days. With such features, they can be deployed in large numbers, often hundreds, across a glacier surface. The resulting datasets provide the dense spatial coverage necessary for both microseismic and ambient noise analyses, offering new insights into glacier structure and dynamic behavior. While the approach is increasingly adopted in glacial environments, large-scale dense arrays remain rare in Greenland and only short-term in Antarctica. To my knowledge, in Greenland, extensive seismic arrays covering hundreds of nodes have not been done before this year, with the project REASSESS. In Antarctica, there have been several major deployments, also very recently, for instance, a 330-node array on Eastwing Glacier lasting for a couple of weeks maximum (Agnew et al., 2025).

Designing an effective dense array requires balancing scientific objectives with practical considerations. The size, density, and duration of each deployment depend strongly on logistical constraints, weather conditions, and prior field experience. Familiarity with a site often leads to more efficient deployments and recoveries, allowing teams to adapt quickly to challenging or unexpected conditions. The network geometry and interstation spacing must also be optimized based on the seismic sources of interest. Likewise, the array location should be selected according to the glacier structural and dynamic features of interest: grounding zones, shear margins, crevassed fields etc. In the following sections, I discuss key aspects of deploying and operating dense seismic arrays on glaciers, drawing on field experience from both Antarctica and Greenland. I focus particularly on how deployment strategies influence data quality, including the

importance of adapting deployment methods to local conditions and logistical planning. I also discuss how seasonal and environmental variability can affect seismic recordings, and how the sensitivity of dense arrays differs between sites depending on local glacier dynamics and dominant seismic sources.

7.3.1 Deployment

The deployment strategy for dense seismic networks in Antarctica and Greenland follows a common operational principle: drilling a hole, placing and orienting the sensor, covering it with slush or snow, and marking the location for recovery (Fig. 7.3). However, specific procedures depend strongly on the environmental conditions, the duration of deployment, and the design of the seismic nodes.

Instrument types and deployment implications

Different brands and models of seismic nodes impose specific logistical and methodological constraints. *SmartSolo* and *Fairfield* nodes are compact "all-in-one" systems integrating the sensor, data logger, and battery in a single parallelepipedic or cylindrical casing (see Fig. 7.3a and 7.3b, respectively). These are straightforward to install, requiring only a single hole of an appropriate diameter. By contrast, *Geospace GSB* systems are in multiple parts, consisting of a separate geophone connected to the acquisition unit (see Fig. 7.3c) and an optional external battery connected by cables. This configuration increases weight and complexity but offers flexibility for long-term deployments. The possibility of connecting multiple batteries in series extends recording duration beyond the one-month autonomy of *SmartSolo* or *Fairfield* nodes to durations up to 6 months.

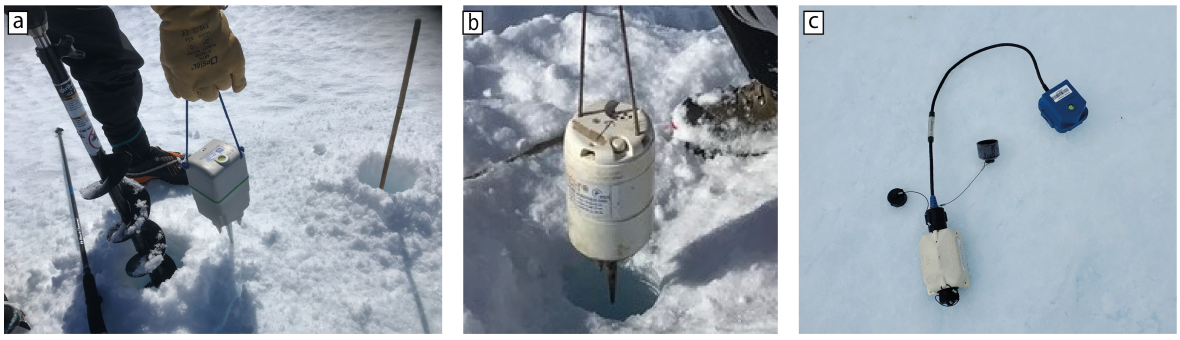

Figure 7.3: Comparison of the instrument types and their design that shape the strategy of deployment. (a) *SmartSolo* IGU-16HR 3C node. (b) Magseis *Fairfield* ZLAND 3-component 5Hz node. (c) *Geospace GSB* 3-channel unit connected to a *Geospace* 5 Hz Geophone 3C.

On the Astrolabe Glacier, short-term dense arrays were deployed for three to four weeks using *SmartSolo* nodes. Their battery autonomy is around 30 days which was

sufficient for the survey durations. The relatively low surface melting at this time of year allows sensors to be buried at shallow depth (around 50 cm), sufficient to protect them from wind-induced noise while maintaining GPS connectivity for time synchronization (Fig. 7.4a). Burying them too deep can cause the GPS signal to be lost under the ice, so the installation depth represents a compromise between protection from external disturbance and technical requirements.

The first dense array experiment on Isunnguata Sermia in April 2023 used *Fairfield* nodes provided by EPOS-SISMOB French national instrumental pool, with a battery life of around 35 days. Sensors were installed at 50 cm depth, as surface melting was just beginning in early May. The key challenge was to anticipate the onset of the melt season so that the instruments would record the transition from stable ice conditions to melting conditions before batteries were empty. For longer summer deployments (July to September for instance), the high ablation rate from surface melting requires deeper holes, typically 1.5 to 2 m, to ensure that the sensors remain embedded in the ice throughout the season. Here, modular systems such as *Geospace GSB* are better fitting: the geophone can be placed at depth, while the data logger and GPS antenna remain near the surface (Fig. 7.4b). This configuration also allows the addition of external batteries for extended autonomy. However, deep drilling requires heavier augers and stronger power tools. Also, transporting the heavier and larger seismic nodes is also impacted (from having the nodes in a backpack, to using sledges or ATVs) and in consequence impact the time it takes to deploy the full network.

Surface conditions also dictate deployment strategy. Highly crevassed areas pose the risk of losing sensors or making recovery difficult or impossible. Similarly, sites near supraglacial lakes or bedières may mean sensors being flooded as surface melting accelerates. Early-season deployments thus involve a degree of uncertainty, since meltwater stream routes and lakes are not yet fully established.

Orientation procedures and marking

Sensor orientation is crucial for seismological data processing. In DDU, the proximity to the South magnetic pole makes magnetic compasses unreliable. During the SEIS-ADELICE project, sensors were oriented using a "gnomon" equipped with a 360° protractor, functioning as a solar compass (Fig. 7.4c). The method requires precalculated solar azimuths for every minute of the day at each node deployment site, allowing true North to be derived from the position of the sun's shadow on the protractor. Although the accuracy is limited to a few degrees, this approach proved efficient under clear-sky conditions, which typically coincide with fieldwork days. Another alternative using the same gnomon has been to use fixed and referenced points such as building, topographic feature or other well positioned instrument and to define their azimuths from the point of interest. This method requires to have points of a well known position and to see them. It proved to be efficient particularly during cloudy

days where the sun was not visible.

In Greenland, where the North magnetic pole is further away, standard compasses can be used, provided a correction for declination is applied (∼25°W near Kangerlussuaq in 2025). Accurate orientation with a compass is difficult once the sensor is positioned in the hole. The most reliable approach is to mount the sensor on a guiding rod, adjust its azimuth once it is at the bottom of the hole, and release it only when properly aligned (Fig. 7.4d). Despite these precautions, orientation uncertainties remain and may necessitate post-processing correction of the recorded seismic data.

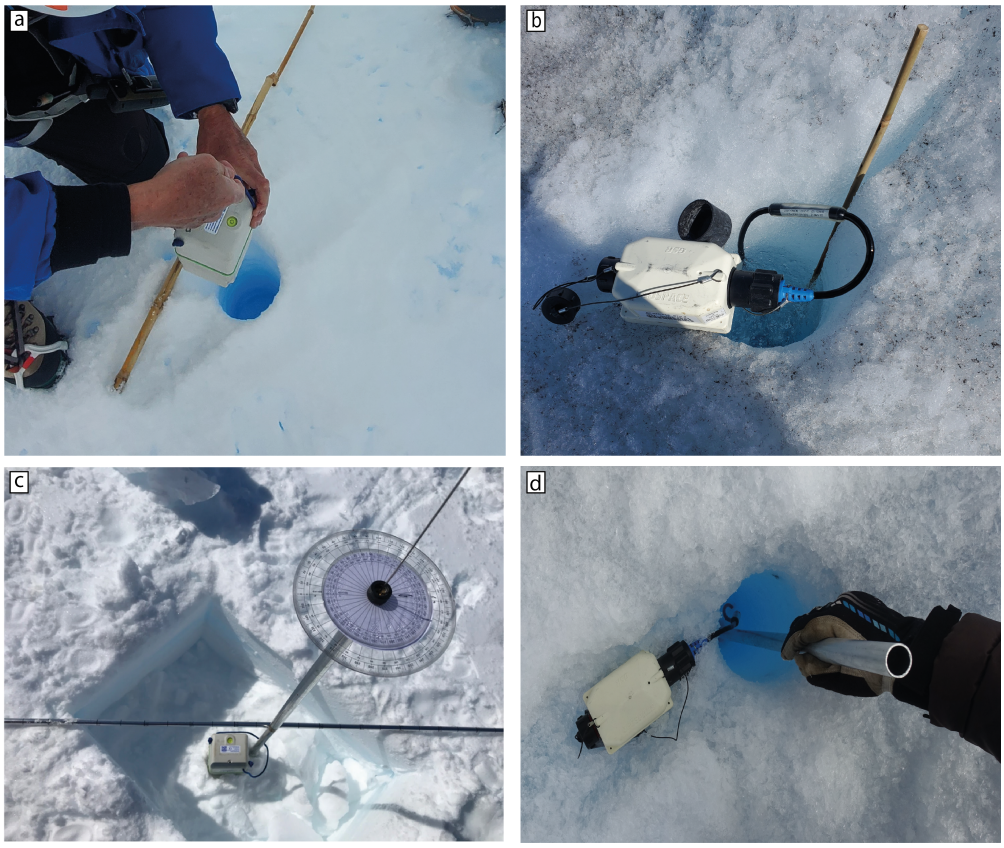

Figure 7.4: Strategies of deployment of seismic nodes on glacier ice. (a) Installation of a *SmartSolo* IGU-16HR 3C node in a drilled borehole approximately 50 cm deep. (b) Setup of a *Geospace GSB* unit connected to a geophone placed at the bottom of a 1 m-deep borehole. The GSB unit remains at the surface to ensure reliable GPS connection; bamboo markers are used to locate the node. (c) Example of a gnomon used to orient seismic nodes toward geographic north. In this case, the sensors were installed in rectangular holes, prior to adopting drilled holes as a more effective solution. (d) Use of a guiding rod to accurately orient the geophone at the bottom of the borehole toward geographic north.

After placement and orientation, each node is covered with slush or snow from drilling. Depending on air temperature, this material may either refreeze, helping

to stabilize the sensor, or melt and compromise its stability and leveling. Bamboo sticks are inserted nearby to facilitate recovery, as sensors unavoidably move along with glacier motion over the deployment period.

Feasibility of long-term deployments

While the deployments I participated in were limited to periods shorter than three months, both environments offer potential for longer-term installations. In Antarctica, modest surface melting could allow year-long operation, provided the nodes are buried deeply enough and equipped with sufficient battery capacity. The main uncertainty lies in the effect of sustained cold on battery performance. In Greenland, extended deployments are more constrained by surface melting. Re-installations may therefore be necessary: for example, deploying in May-June to capture early melt, and again in September to record until next summer. The easy access of the study sites at the margins of the Greenlandic ice cap makes successive maintenance missions feasible. In both cases, accurate knowledge of local ablation rates seems essential for determining optimal installation depth and timing.

7.3.2 Recovery

On the Astrolabe Glacier, the recovery of seismic nodes has so far been relatively straightforward. This is mostly due to the short deployment durations and the limited snow accumulation. The nodes are found using deployment GPS positions and the bamboo sticks placed slightly east of the drilled holes during installation. New positions of seismic nodes are also estimated using glacier surface velocity. We then recover the nodes by cutting a wide rectangle around the expected location with a chainsaw (avoiding direct contact with the node) and finish extraction using an ice axe (Fig. 7.5a and 7.5b).

In Greenland, recovery conditions are more variable and often more challenging, primarily because of unpredictable weather and melt conditions. Between 2023 and 2025, I took part in three recovery campaigns under very different circumstances, each revealing numerous logistical and environmental challenges. During the first recovery in late June 2023, the melting season was unusually late, and many nodes remained trapped beneath 5-10 cm of blue ice despite expectations that they would reappear at the surface. Locating them was further complicated by not having their exact position after one month of moving along with the glacier. Once located, the extraction was slow and physically demanding, requiring use of ice axes and a drill. Interestingly, the onset of strong melting a few days later significantly eased the work, highlighting how timing the mission according to short-term melt forecasts can significantly affect efficiency. Planning so close to the melting period also carries the risk of losing sensors to supraglacial streams or lakes previously not activated; one node, for instance, was found on the edge of a meltwater pond. The second campaign was in late August to

early September 2024. While the sensors were mostly at the surface, they had slid downslope from their original positions as ice melted during summer. For the first few days of the mission, a snowstorm deposited around 40 cm of fresh snow, covering the entire network and complicating matters further (Fig. 7.5c). This made localization particularly difficult, and each recovery required sometimes hours of manual searching. Once again, partial melting later in the week improved visibility, but the process remained slow and unpredictable. The third recovery, in October 2025, was even more complex. We were on a higher part of the glacier where early winter conditions had already set in, with substantial snow accumulation and refreezing. The sensors were completely embedded in solid ice. Both localization and extraction proved difficult, as each node had to be found using metal detectors (Fig. 7.5d) and then carefully freed without damaging cables or connectors. Considering these conditions and additional difficult field conditions, we had to abort the mission. Comparatively, the mission in October 2024 (which I did not take part in) was smoother with better weather conditions (note that the study site was also closer to the margin). These different experiences emphasize the high interannual variability of surface conditions in Greenland and the importance of adaptability.

From these experiences, several points of importance have to be carefully anticipated to enhance recovery success under such unpredictable conditions:

(1) Precise localization: Positioning bamboo sticks, Recco reflectors, or built-in localization systems (e.g., the *Geospace* LHR module) can significantly improve efficiency. Bamboo sticks are light and convenient for short-term deployments but may induce seismic noise due to wind resonance at characteristic frequencies. For longer deployment durations it seems more difficult to consider. During the melting season, they can fall down and progressively be embedded in the ice (due to their darker color, the sun melts the ice around it) and become invisible. Recco reflectors, though more costly, could serve as a good alternative for dense networks. Metal detectors also provide a useful backup, though they require sufficient battery autonomy.

(2) Appropriate Extraction Tools: Chainsaws remain the fastest way to extract nodes frozen into ice but must be handled with caution to avoid damaging the instruments or causing injury. Ice axes offer more precision but are slower. Optimally, sensors should be installed at a depth ensuring they emerge or remain near the surface by the end of the survey, to avoid intensive excavation.

(3) Timing and Forecasting: Careful consideration of the melt-freeze cycle, glacier surface velocity, and short-term weather forecasts is necessary to schedule recoveries at the optimal time: late enough to benefit from melting but early enough to avoid refreezing or snow burial. In summary, operations in Greenland require greater flexibility, adaptability, and good strategy in both localization and extraction.



Figure 7.5: Recovery operations of seismic nodes on glaciers. (a) Extraction of a node deployed on the Astrolabe Glacier using a chainsaw. (b) Removal of residual ice stuck to a seismic node with an ice axe. (c) Example of a node trapped in ice slush after successive melting and snowfall episodes. (d) Search for a snow-covered seismic node using a metal detector.

7.3.3 Tilting

Localized melting around geophysical sensors is a common phenomenon in glacial environments. It occurs because objects such as seismic nodes absorb and transfer more heat than the surrounding ice, through both solar radiation and thermal conduction. Even when air and ice temperatures remain well below freezing, this differential heat transfer can raise the nearby ice to its melting point and create a thin water film around the instrument. If surface melting is occurring simultaneously (e.g., in summer), this thin melt layer can increase into a proper puddle and significantly reduces the mechanical coupling between the sensor and the ice, which is critical for high-quality seismic measurements. When installed, seismic nodes are carefully levelled, oriented to geographic north, and placed tightly in drilled holes to ensure optimal coupling on all three components. Melt-induced decoupling disrupts this configuration. If melting occurs unevenly around the sensor, the node begins to tilt gradually. Once the tilt angle

exceeds a certain threshold, the vertical and horizontal components become unreliable. After refreezing, if refreezing there is, the sensor remains locked in its tilted position until the next melt cycle, potentially degrading data quality for several days or weeks.

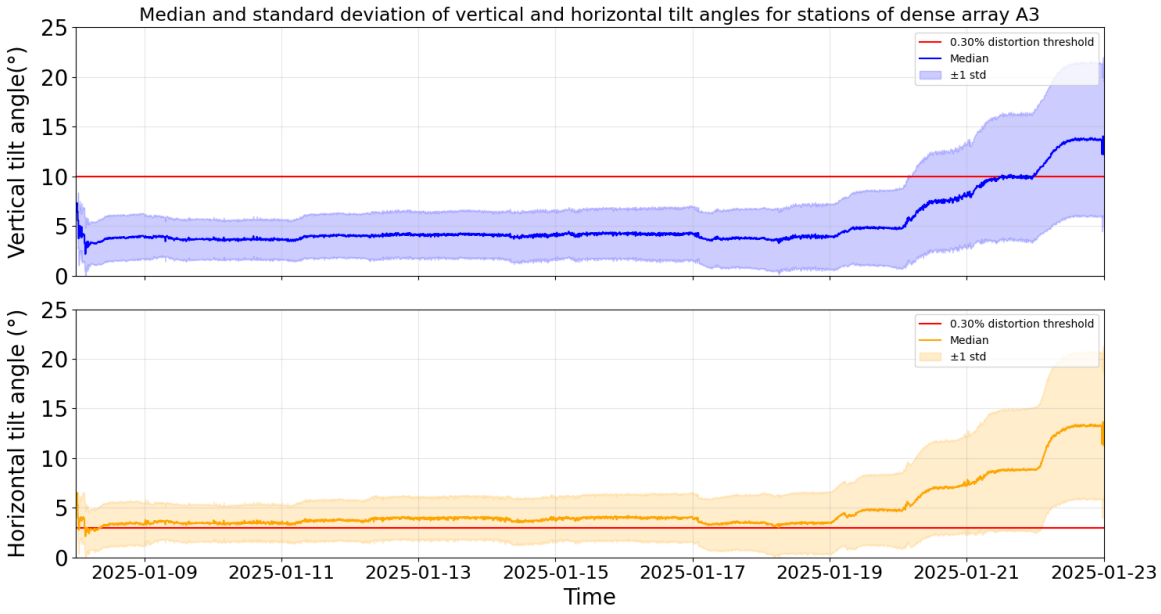

Figure 7.6: Analyses of the tilting on the seismic nodes of dense array A3 deployed in 2025. (top) Median (blue) and standard deviation (light blue) of the vertical tilt angle timeseries during the period Jan. 8, 2025 to Jan. 23, 2025. (bottom) Median (orange) and standard deviation (light orange) of the horizontal tilt angle timeseries during the period Jan. 8, 2025 to Jan. 23, 2025. The red lines represent respectively on the top and bottom plots, the vertical and horizontal tilt angle threshold to ensure a distortion inferior or equal to 0.30% at 12 Hz.

This effect was systematically observed during deployments on both the Astrolabe Glacier and Isunnguata Sermia, although with different magnitudes. On the Astrolabe Glacier, strong solar radiation was sufficient to cause local melting around the sensor casing even in the absence of significant surface melt. Because the drilled holes matched the sensor diameter closely, most nodes installed during the 2024 and 2025 seasons remained nearly upright throughout the deployment. In rare cases, typically on south-facing slopes, more pronounced melting caused partial surface emergence of the sensor and increased tilting. The *SmartSolo* technical documentation specifies that tilt affects both amplitude and phase of recorded signals. For example, a vertical tilt between 0° and 10° and a horizontal tilt between 0° and 3° produces a distortion of the signal of up to 0.30% at 12 Hz. Using the quality-control metadata available for January 2025, we examine the evolution of tilt angles for the dense array A3 (Fig. 7.6). Both vertical and horizontal tilts remain stable from 8 to 20 January. After this period, the vertical tilt increases from about 5° to 13° on average, with a maximum of 23°.

This exceeds the 0.30% distortion threshold, but because the manufacturer does not provide the full distortion-versus-tilt curve, the true impact on recorded waveform is uncertain. Horizontal tilt angles exceed the 3° threshold throughout the all deployment but remain relatively constant. There is no clear explanation for the sudden increase in tilt near the end of the deployment, as the temperature time series does not show marked changes between the two periods. A likely hypothesis is that once melt reaches a certain advanced stage around the sensor, the system becomes mechanically unstable and tilt progresses rapidly. The vertical and horizontal tilt angle timeseries also show that sensors are not perfectly levelled at installation, which is expected given the difficulty of placing an instrument precisely levelled inside a narrow ice borehole without a rigid base. However, the stability of the tilt angle during most of the deployment period is a good indicator that by taking precautions when installing the nodes, we are ensuring stable and satisfactory data quality.



Figure 7.7: Sensor found tilted after being deployed for two months in July and August 2024 on Isunnguata Sermia, western Greenland.

The tilting issue is significantly more pronounced in Greenland, where higher temperatures, stronger solar radiation, and intense summer melting amplify melt-induced decoupling. For this reason, sensors are installed in deeper drilled holes. However, ablation and progressive melt can still expose buried sensors later in the season, leading to severe tilting or even complete inversion (Fig. 7.7).

Power spectral densities (PSDs) from three sensors deployed respectively in spring

2023, summer 2024, and autumn 2024 illustrate the strong seasonal contrast (Fig. 7.8). In spring 2023, limited melting allowed sensors to remain frozen and well aligned inside their holes. In summer 2024, however, extensive surface melt, strong radiation, and imperfect diameter matching between the casing and the drilled holes caused many sensors to tilt completely. PSDs from node 1088 show repeated periods of sharp power decrease on the 3 components of the sensor (dashed line, Fig. 7.8), consistent with the manufacturer's indication that power loss occurs when vertical tilt exceeds 30° and horizontal tilt exceeds 8°. At such tilt angles, the geophone coil reaches its end stop, producing strong amplitude reduction, especially between 5 and 20 Hz. During the early autumn 2024 deployment, tilting is still visible in early September but becomes much less pronounced later in the season as temperatures drop and refreezing stabilizes the sensors. To reduce tilting during the summer 2025 field season, sensors were installed inside PVC protective tubes. This approach significantly limited tilt while maintaining acceptable coupling with the surrounding ice, provided the geophone remained sufficiently deep.

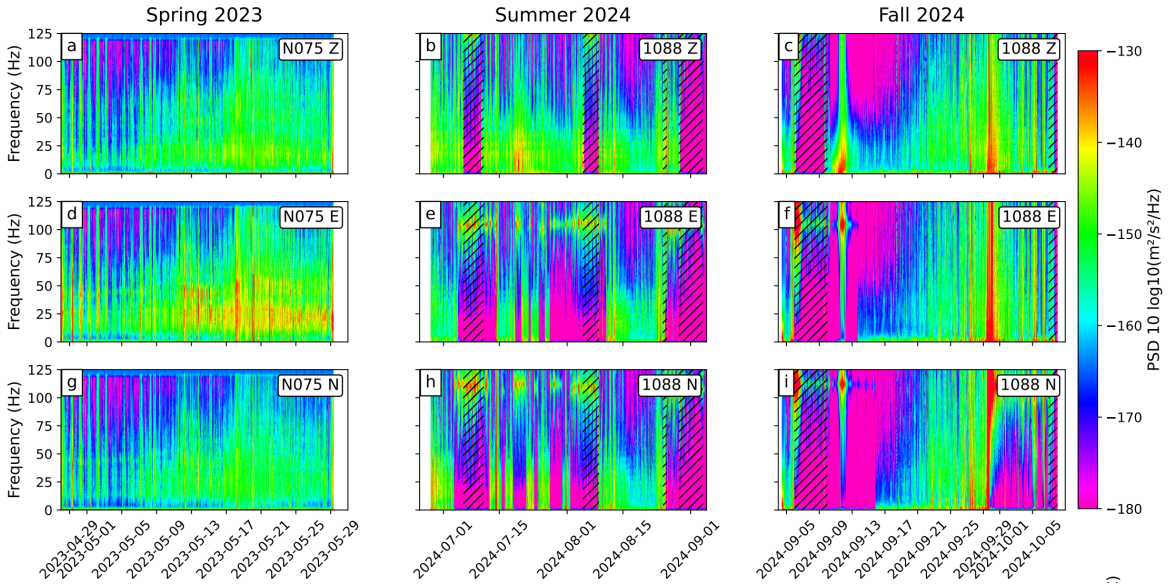

Figure 7.8: Power Spectral Density (PSD) spectrograms on the 3 components of 3 stations from dense arrays deployed in spring 2023 (a, d, g), summer 2024 (b, e, h) and fall 2024 (c, f, i) on Isunnguata Sermia. The hashed area highlights the days where the sensors were classified as significantly tilted on the vertical and horizontal components. Modified from Paris et al. (in prep.)

Overall, in Antarctica, where deployments are shorter and summer melting weaker than in western Greenland, tilt generally remains limited and has a smaller impact on data quality. Nevertheless, for future long-term deployments, protective casings such as PVC tubes should be considered to maintain sensor stability until winter refreezing. Finally, we note that different sensor models respond differently to tilt. *Geospace GSB* nodes show pronounced changes in signal power under large tilting, whereas *Smart-Solo* sensors used in SEIS-ADELICE dense arrays did not show comparable power loss,

some level of waveform distortion is expected, instead.

7.3.4 Intercomparison of seismic sources: Astrolabe vs. Isunnguata Sermia

The Astrolabe Glacier and the Isunnguata Sermia are part of two fundamentally different glaciological systems. The Astrolabe Glacier is a marine-terminating outlet glacier with a floating tongue directly influenced by oceanic processes (currents, tides, storms, swell). In contrast, Isunnguata Sermia is a land-terminating glacier flowing from the Greenland Ice Sheet. These contrasting settings shape their deformation regimes. The Astrolabe Glacier is confined within a 4 km-wide fjord and flows "easily" towards the ocean while experiencing strong lateral shearing on its sides. Both shearing stress and tidal forcing generate brittle ice deformation such as large crevasses at the surface of the glacier. But these crevasses do not cover the full surface of the glacier, instead concentrated in distinct areas like the calving front, the shear margins or over the grounding zone. In comparison, Isunnguata Sermia exhibits smaller but more numerous signs of ice deformation, with a vast dense network of crevasses and a heterogeneous surface topography in response to the more complex bedrock topography over which the glacier flows. The surface topography is also affected by very active surface melting, creating small bumps and hollows.

Because seismic sources are a window into ice deformation, we expect differences in the frequency, depth, and spatial distribution of cryoseismic signals between the two glaciers. We have applied Match Field Processing (MFP) to dense seismic arrays deployed on both glaciers. MFP provides a broad view of seismic sources distribution in time, space and frequency. We use these outputs to investigate the difference between seismic sources in both places. The same processing workflow was applied to both regions of study. For Isunnguata Sermia, three datasets - spring 2023, summer 2024, and autumn 2024, allow an additional examination of seasonal variability.

Seismic sources on the Astrolabe Glacier

Figure 7.9 presents the spatial distribution of seismic sources detected by MFP for the dense arrays deployed in 2023 (A1, Fig. 7.9a) and 2025 (A3, Fig. 7.9b). For both maps, we set the Bartlett Output (BO) threshold to 0.2. The interstation distance of A1 (2023) restricts analysis to frequencies below 3 Hz, which limits the detection of high-frequency cryoseismic signals typically associated with brittle ice deformation. At these frequencies, MFP outputs are more strongly influenced by low-frequency oceanic noise. The shorter interstation distance of A3 (2025) allows analysis in the 4 - 6 Hz band, which is better suited for detecting icequakes and reduces contamination from oceanic microseisms, although the network is closer to the coast. The two arrays sample different dynamic environments: A1 is located over the grounding zone, while A3

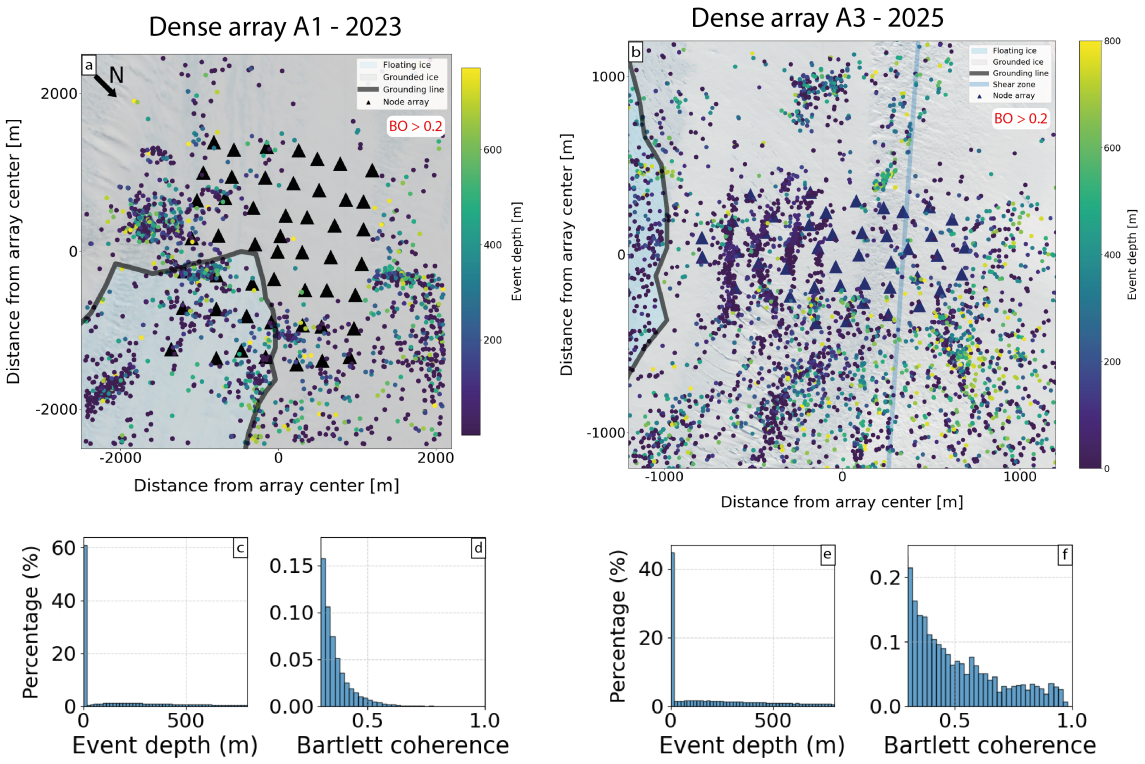

Figure 7.9: Map of source locations, based on Match Field Processing method, for dense arrays deployed on the Astrolabe Glacier. (a) Map of MFP-based event locations for the 2023 array. (b) Map of MFP-based event locations for the 2025 array. For the two maps, the Bartlett output (BO) threshold is set to 0.2. (c) and (d) Histograms of event Bartlett coherence and depth for the 2023 array, respectively. (e) and (f) Histograms of event Bartlett coherence and depth for the 2025 array, respectively.

is positioned over the lateral shear margin. For A1 (2023), most events are located on the floating section and along the lateral shear margins. Notably, few events occur beneath the eastern side of the array, consistent with detections obtained using STA/LTA methods (see chapter 4). For A3 (2025), despite the smaller surface area covered by the array, the method identifies a larger number of events. Some events lie on the partially visible floating tongue (as for A3). Others align in 4 successive shallow lines, parallel to the glacier flow, on the western side of the array. The proximity of A3 to the ocean may explain the higher density of detections to the north. The events located at large depths in the 2025 dataset raise concerns regarding depth resolution. Indeed, radar transects and borehole measurements indicate ice thicknesses of ∼200 m in this area; therefore, deeper inferred events either originate from the underlying bedrock or, more realistically, from poor convergence of the beamforming solution. A more detailed analysis is needed before interpreting source depths quantitatively.

A similarity between the 2023 and 2025 arrays is the negatively skewed distribution

of Bartlett coefficients, and low percentage of high BO values (BO > 0.3) (Fig. 7.9d and Fig. 7.9f, respectively). Low BO value for an event indicates poor coherence across the array. This may come from the highly localized propagation of icequake signals, which do not illuminate the full aperture of the array. In addition, background ocean noise (arriving predominantly from the northeast) produces coherent low-BO arrivals that generate characteristic cones of "false" seismic sources. Depth distributions show that 50-60% of events cluster near the surface (Fig. 7.9c and 7.9e, respectively). It is difficult to assess which of these events are truly occurring at the surface and which are due to the solution not converging well in the beamforming step. Overall, the Astrolabe Glacier results illustrate the challenges of applying MFP in an environment characterised by strong oceanic noise and spatially variable cryoseismic activity. It is difficult to infer the type of seismic activity detected given these results.

Seismic sources on Isunnguata Sermia

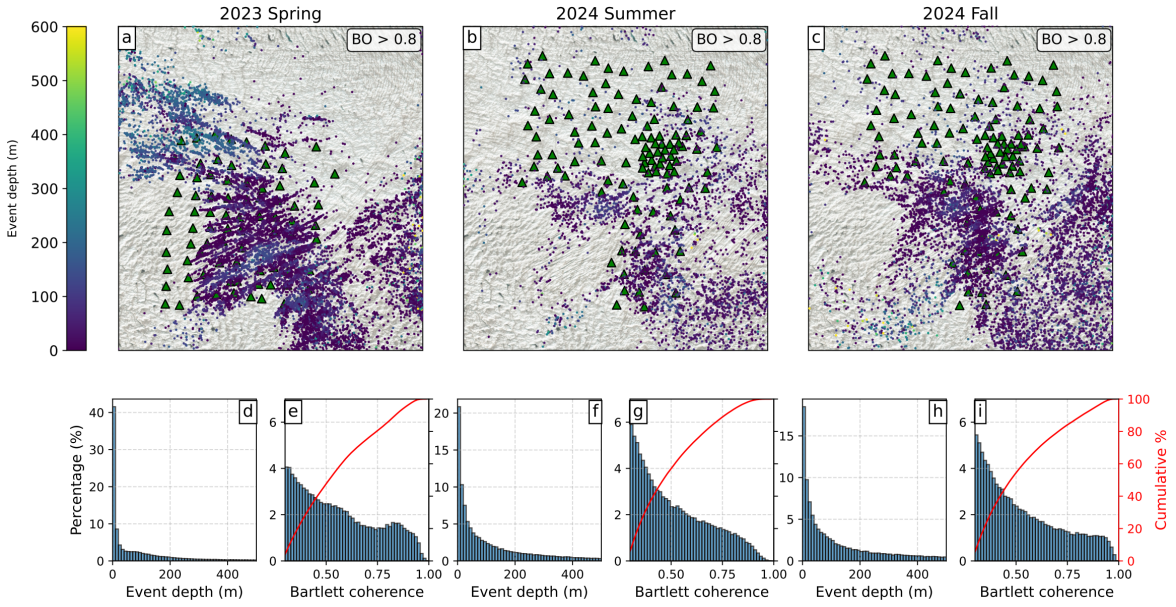

Figure 7.10: Map of source locations, based on Match Field Processing method, for Isunnguata Sermia arrays. (a) Map of MFP-based event locations for the 2023 spring array. (b) Map of MFP-based event locations for the 2024 summer array. (c) Map of MFP-based event locations for the 2024 fall array. For all three maps, the Bartlett output (BO) threshold is set to 0.8. (d) and (e) Histograms of event Bartlett coherence and depth for the 2023 spring array, respectively. (f), (g), (h) and (i) are the same as (d) and (e) but for the 2024 summer and fall datasets. Modified from Paris et al. (in prep).

The three dense arrays deployed on Isunnguata Sermia in spring 2023, summer 2024, and autumn 2024 have shorter interstation spacing than the 2023 Antarctic array, enabling analysis in the 4 - 6 Hz frequency band. Figure 7.10 shows the MFP source locations (Fig. 7.10a, 7.10b and 7.10c), depth distributions (Fig. 7.10d, 7.10f

and 7.10h), and Bartlett coefficient distribution (Fig. 7.10e, 7.10g and 7.10i) for the three seasonal datasets. For the maps, we use a high Bartlett threshold (BO > 0.8). During spring 2023, events cluster near the surface and align with major crevasse fields trending NE-SW. Deeper events are also identified northwest of the array, following a different orientation pattern (NW-SE). In summer 2024, sources with BO > 0.8 are much less numerous and exhibit no clear spatial pattern. Few events occur within the southern crevasse field or the northwestern region active during spring. Autumn 2024 displays intermediate behaviour. The number of detected sources increases compared to summer, and many events align again along surface crevasses in the southwest, similar to spring 2023.

The proportion of near-surface events, which was $\sim$40% in spring 2023, drops to $\sim$20% in summer 2024 and in autumn 2024. The proportion and shape of the depth distribution for Spring 2023 dataset is close to what was observed for the Antarctic datasets. This could mean that surface events, fewer in proportion in summer and autumn 2024, could be occurring less during melting-related processes. The Bartlett coefficient distribution is also different between spring 2023 and summer and autmun 2024. We notice overall higher proportion of high BO values for the 2024 datasets but a more important decrease of this proportion as BO values get higher. Seasonal variations in BO values have been shown to be controlled by environmental conditions: sensor tilt (substantial during the summer 2024 deployment) and hydrological noise both degrade signal coherence (Paris et al., in prep). Hydrological noise is the dominant factor, which implies that BO variations across seasons are an indicator of noise conditions rather than true seasonal changes in seismic source types.

Comparison between the two glaciers

The most striking contrast between the MFP results from Astrolabe Glacier and Isunnguata Sermia lies in the BO values. BO values in Antarctica remain systematically low, whereas in Greenland, high BO values are frequent. For instance, at Isunnguata Sermia, between 4 % and 6 % of the detected events exhibit BO = 0.3. In contrast, at the Astrolabe Glacier, only about 0.13 % to 0.22 % of events show the same BO value, roughly a thirtyfold difference in the proportion of events. Two main hypotheses may explain this difference. First, background noise characteristics. In Greenland, noise during the melt season is dominated by supraglacial hydrological flow, which is variable but spatially diffuse. In Antarctica, persistent oceanic noise arriving from a preferential direction (NE) may continuously reduce wavefield coherence, producing low BO values even when cryoseismic activity is strong. Second, differences in cryoseismic activity and array geometry. Surface deformation at Isunnguata Sermia is intense and widespread, generating numerous coherent surface events in the 4 - 6 Hz range. Astrolabe Glacier has smoother surface topography, larger but fewer crevasses, and for the A1 array, large interstation spacing. Le Bris et al. (2025) showed that events there are relatively small, making coherent detection across the array more difficult. The

consistency of BO distributions across years in Antarctica suggests that the observed differences are robust and not caused by year-to-year variations in deployment or noise conditions. This comparative analysis is an initial exploration based on the MFP outputs. A more complete study would require detailed investigation of spatial patterns, sensitivity tests on noise influence, and synthetic experiments to quantify how reduced SNR (as seen in summer 2024) affects BO on Antarctica datasets. Such work would help determine how much of the observed contrast results from environmental noise, array geometry, or true differences in ice deformation processes.

7.4 Distributed Acoustic Sensing (DAS): instrumentation strategies and data quality analysis

Distributed Acoustic Sensing (DAS) is a seismic measurement technique that has rapidly developed in geosciences since its emergence around 2010 (Zhan, 2019a). It uses fiber-optic cables as continuous sensors to record strain or strain rate in the longitudinal direction of the cable. A DAS interrogator sends laser pulses through the fiber. When the light is traveling through the fiber, it hits natural imperfections within the cable which produce Rayleigh scattering (Fig. 7.11a). Part of this scattering is backscattered toward the start of the cable, where the interrogator is attached. When a seismic wave, such as from an earthquake, passes through the cable, the fiber undergoes stretching and compression. It changes the relative position of these scattering points and modifies the travel time and phase of the backscattered light (Fig. 7.11c). From these phase variations, the local change in fiber length, and the associated local strain rate, can be derived and the seismic wavefield reconstructed. This process is known as optical time-domain reflectometry (Masoudi & Newson, 2016; Zhan, 2019a). The spatial resolution of DAS measurements is determined by the gauge length, typically between 5 and 10 m, which defines the segment of cable over which strain is averaged (Fig. 7.11b). This configuration allows DAS to record seismic wavefields with meter-scale sampling over distances of several kilometers to hundreds of kilometers, providing a level of spatial continuity that is impossible with more conventional seismic arrays. Such technology thus offers great potential for monitoring seismic processes in challenging environments such as glacial or volcanic regions.

In the following section, I describe the deployment of fiber-optic cables and the setup of DAS interrogators in both Antarctica and Greenland. I discuss the logistical and technical challenges of operating in these polar environments and then present an exploratory analysis of DAS data acquired on the Astrolabe Glacier and Isunnguata Sermia. I conclude with a discussion of whether DAS could realistically substitute dense arrays of seismic nodes in glaciological applications.

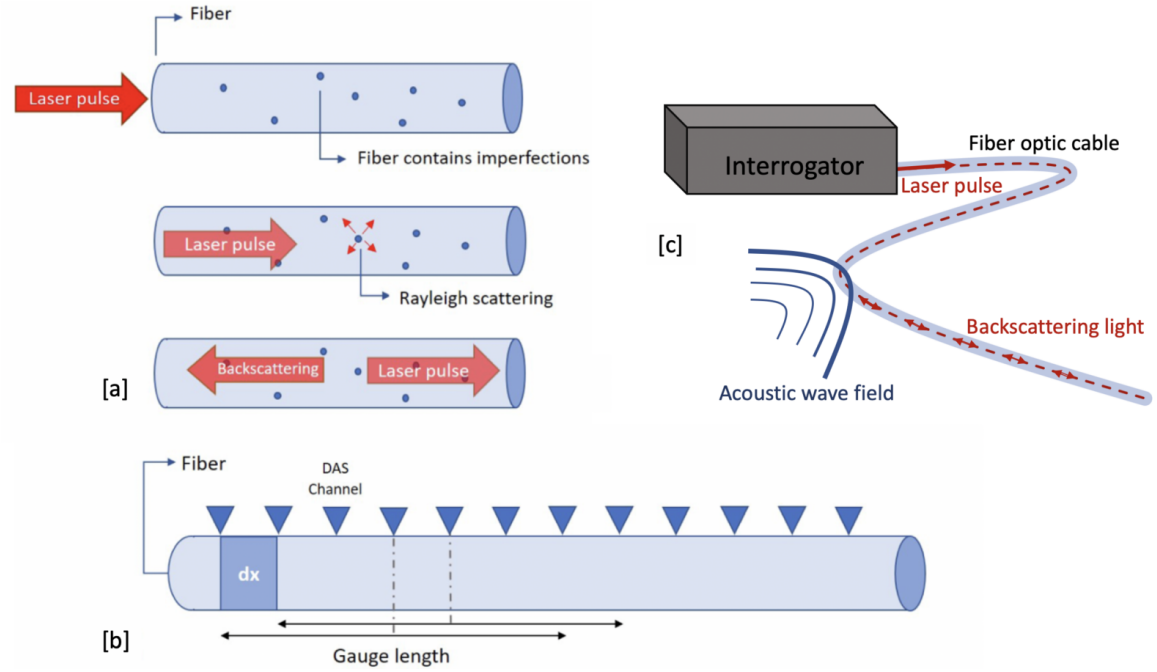

Figure 7.11: (a) Diagram illustrating the principle of DAS technology. The interrogator sends a laser pulse into the cable. Due to natural imperfections in the fibre, Rayleigh scattering occurs. Some of this scattered light is backscattered towards the interrogator (see (c)). (b) The strain rate of each DAS channel, spaced at dx, is determined over a gauge length that functions as a moving average across the fibre optic cable. (c) When strains occur in the optic cable, the backscattered light signal that reaches the interrogator changes. From these changes, the interrogator calculates the strain rate occurring in the cable for each DAS channel. Note that the figure is not to scale. Adapted from Nap (2020).

7.4.1 Deployment of optic fiber in Antarctica and Greenland

Our first experience deploying an optical fiber for DAS measurements was conducted on the Astrolabe Glacier in January 2024. The objective was to install a total of 4 km of optical fiber arranged along two 2-km lines at the glacier surface, over the grounding zone: one linear and one zigzag (Fig. 7.12a and Fig. 7.12c, respectively). The deployment procedure involved laying the fiber directly on the ice surface using a reel dispenser mounted on a sledge (Fig. 7.12f). The operation required a small team: a lead guide defining the safe route, a person pulling the sledge, another ensuring smooth unrolling of the reel, and another person behind to monitor the fiber trajectory using GPS. Because of the rather uniform landscape without clear features, maintaining a straight line was challenging, and continuous corrections were necessary to stay aligned with the planned track. Although the total distance per line was only 2 km, the deployment of each line took a full day to ensure proper cable position. Initially, we were uncertain how well the fiber would couple with the ice. Good coupling is essential to record glacier vibrations while minimizing noise from wind. We considered digging a shallow trench to improve coupling but quickly realized that the black fiber absorbed

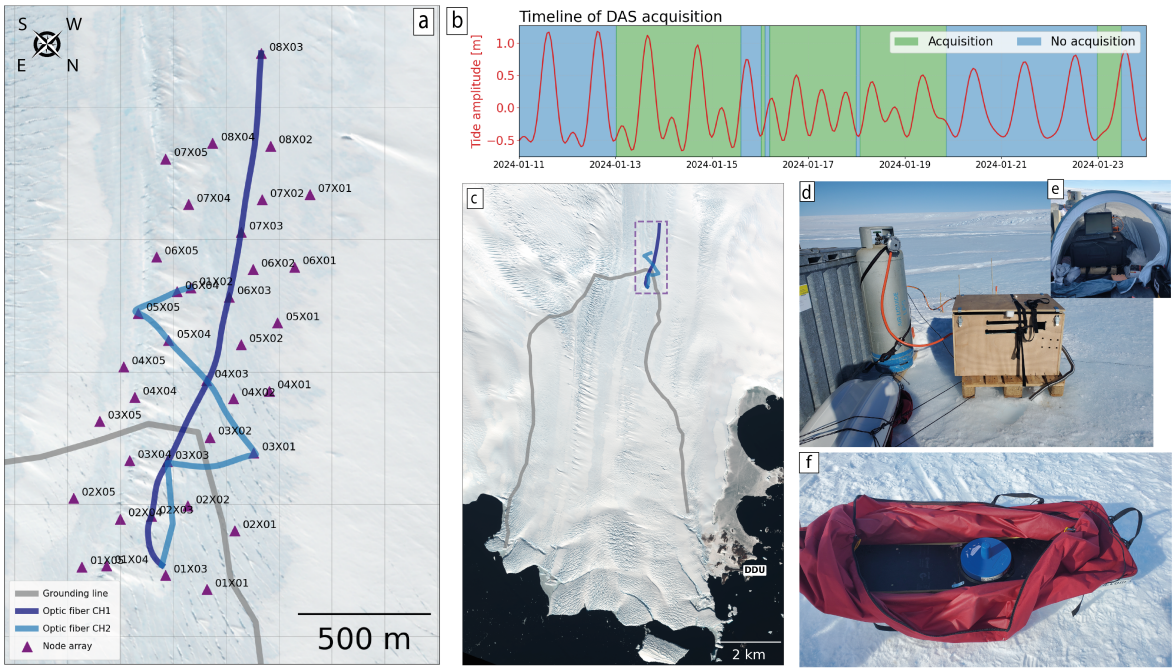

Figure 7.12: Deployment of the Distributed Acoustic Sensing (DAS) system on the Astrolabe Glacier in January 2024. (a) Map showing the location of the seismic node array A2 (purple triangles) and the two optical fiber lines: CH1 (straight, dark blue) and CH2 (zig-zag, light blue). (b) Timeline of DAS data acquisition periods (in green) and downtime (in blue), overlaid with the tidal amplitude measured at DDU tide gauge (red curve). (c) Overview of the array and fiber layout on the Astrolabe Glacier, located over the grounding zone. (d) Power supply system for the DAS computer: a propane-fuelled generator is kept in a ventilated wooden box to prevent overheating. (e) DAS interrogator unit stored within a metal box and protected from drifting snow by a tent cover. (f) Fiber-deployment setup using a reel dispenser mounted on a sledge for cable unwinding.

sufficient solar radiation to melt the ice at its contact and to become progressively welded and coupled into the ice. We observed in the field that within three hours, the fiber was self-embedded by about 5 cm, which provided natural coupling without further manual effort. Punctually, large surface crevasses generated coupling issues: where the fiber crossed open fractures, it was left hanging in the air, swinging with the wind. Some practical issues arose during deployment. The first end of the second fiber accidentally broke and was then dragged along by the sledge over ∼200 m. This required a change in the line geometry and led to a section of the cable entangled, resulting in approximately 300 m of unusable data. The DAS unit was stored in a tent itself installed in a metallic box to protect it from wind and snow drift (Fig. 7.12e). The main technical challenge concerned continuous power supply for the DAS unit. Because the instrument required uninterrupted operation, we used a propane-powered generator and large gas tanks that were expected to provide several days of autonomy (Fig. 7.12d). However, maintaining stable functioning in cold and windy conditions proved difficult. The generator had to be enclosed (in a wooden box) to protect it

from snowdrifts, yet too much insulation caused overheating. Furthermore, the low temperatures likely affected the gas pressure, causing repeated shutdowns. Because we were not present everyday on the glacier (due to logistics and weather constraints), we could not check the state of the generator and it was difficult to establish a strong diagnosis on why it turned off. As a result, a total of 162 hours of data were recorded over ten days (Fig. 7.12b).

Building on this experience, a DAS experiment was conducted on Isunnguata Sermia (Fig. 7.13a and Fig. 7.13b). The objective was to deploy two 1-km fiber sections, arranged perpendicularly. The topography of Isunnguata Sermia is much rougher than that of the Astrolabe Glacier, with numerous small bumps and hollows (from differential surface melting) and supraglacial meltwater streams. As a result, using a sledge-mounted reel was impractical. Instead, the fiber was deployed using a backpack-mounted reel dispenser, which allowed better mobility across the uneven surface (Fig. 7.13c). Although this method was physically demanding, the shorter cable length (1 km per line, $\sim$30 kg total weight) made it feasible. Maintaining straight trajectories proved as difficult as in Antarctica, as the local topography constantly deviated the intended direction. In several places, the fiber was left partially suspended across small crests or melt channels, preventing good local coupling. Shallow trenches were cut with a chainsaw to improve contact where possible, and over time the fiber naturally settled into the ice through melting and refreezing. In Greenland, the power system was more robust and stable thanks to our continuous presence on the glacier. The DAS interrogator, stored also in a tent (Fig. 7.13d), was supplied by a system of solar panels, batteries, and a gasoline generator. Continuous monitoring and regular refueling were possible. As a result of this continuous system monitoring, the DAS recorded data during a four-month period (July to October 2024), with several weeks of continuous recordings (Fig. 7.13e).

Both deployments revealed that surface DAS installations on glaciers are feasible but extremely sensitive to environmental conditions. On blue ice, self-embedding through solar heating can ensure adequate coupling without trenching, whereas in melting environments, irregular topography and surface ablation introduce strong coupling variability along the fibre. Reliable and autonomous power supply remains one of the major challenges for long-term DAS experiments in polar regions. Future deployments should consider more robust power systems and more continuous monitoring of the acquisition (small camp on the Astrolabe Glacier for instance).

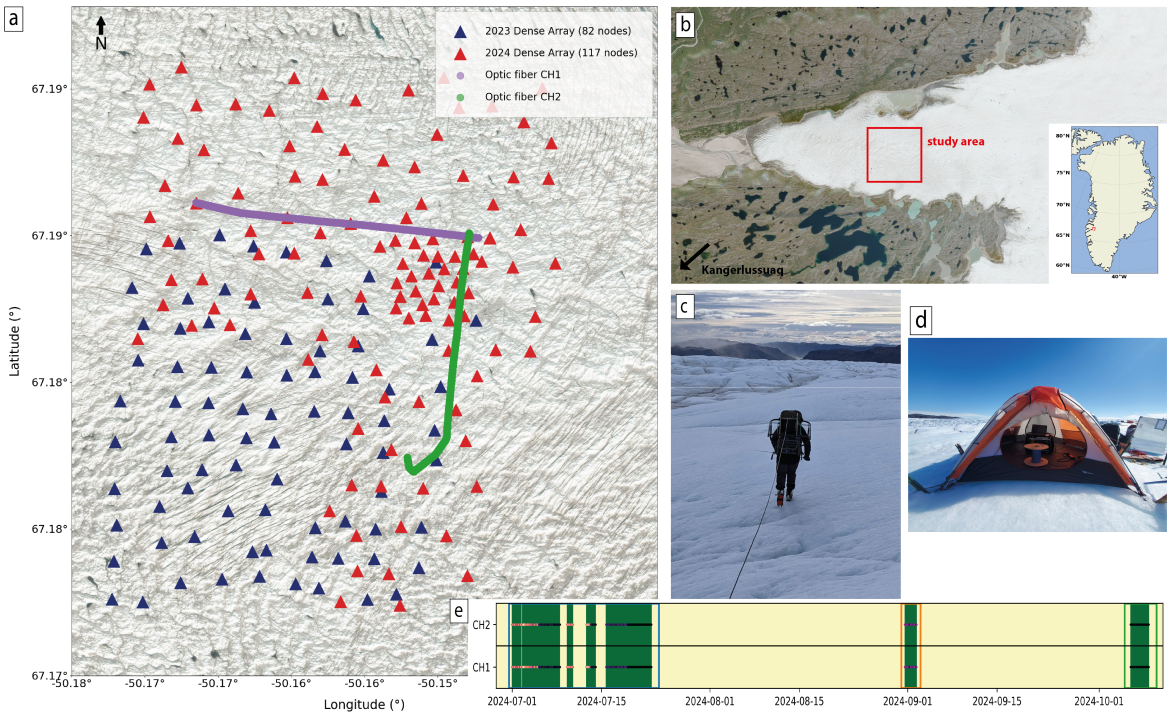

Figure 7.13: Deployment of the Distributed Acoustic Sensing (DAS) system on Isunnguata Sermia, western Greenland, in July 2024. (a) Map showing the location of the seismic node arrays deployed in 2023 (blue triangles) and 2024 (red triangles) and the two optical fiber lines: CH1 (purple line) and CH2 (green line). (b) Overview of the study area on Isunnguata Sermia, near Kangerlussuaq, Qeqqata, Greenland. (c) Fiber-deployment setup using a reel dispenser attached to a backpack for cable unwinding. (d) DAS interrogator unit stored in a tent to protect it from wind and precipitations. (e) Timeline of DAS data acquisition periods (green) and downtime (beige) for the two fibers CH1 (bottom) and CH2 (top).

7.4.2 Quality of the data acquired on the Astrolabe Glacier

The DAS system was configured with a gauge length of 10 m and a sampling frequency of 500 Hz. We obtained a total of 161 hours of recording across two channels, corresponding to approximately 2 TB of data. Figure 7.14a and 7.14b respectively present 30-minute of DAS sections showing signal amplitude along the fiber-optic cables for channels CH1 (linear fibre) and CH2 (zig-zag fibre).

On both CH1 and CH2, several segments display high-amplitude zones, indicating very low signal-to-noise ratios (SNR). These segments correspond to regions of poor coupling between the cable and the ice, which makes the fiber highly sensitive to external disturbances such as wind or swinging across crevasses. Indeed, some of these noisy sections spatially coincide with the locations of crevasse fields identified during the deployment. The beginning of the record is also typically noisy, as the optic fiber starts with several meters stored within the protective box. In contrast, low-amplitude zones suggest good mechanical coupling between the ice and the cable. These observations

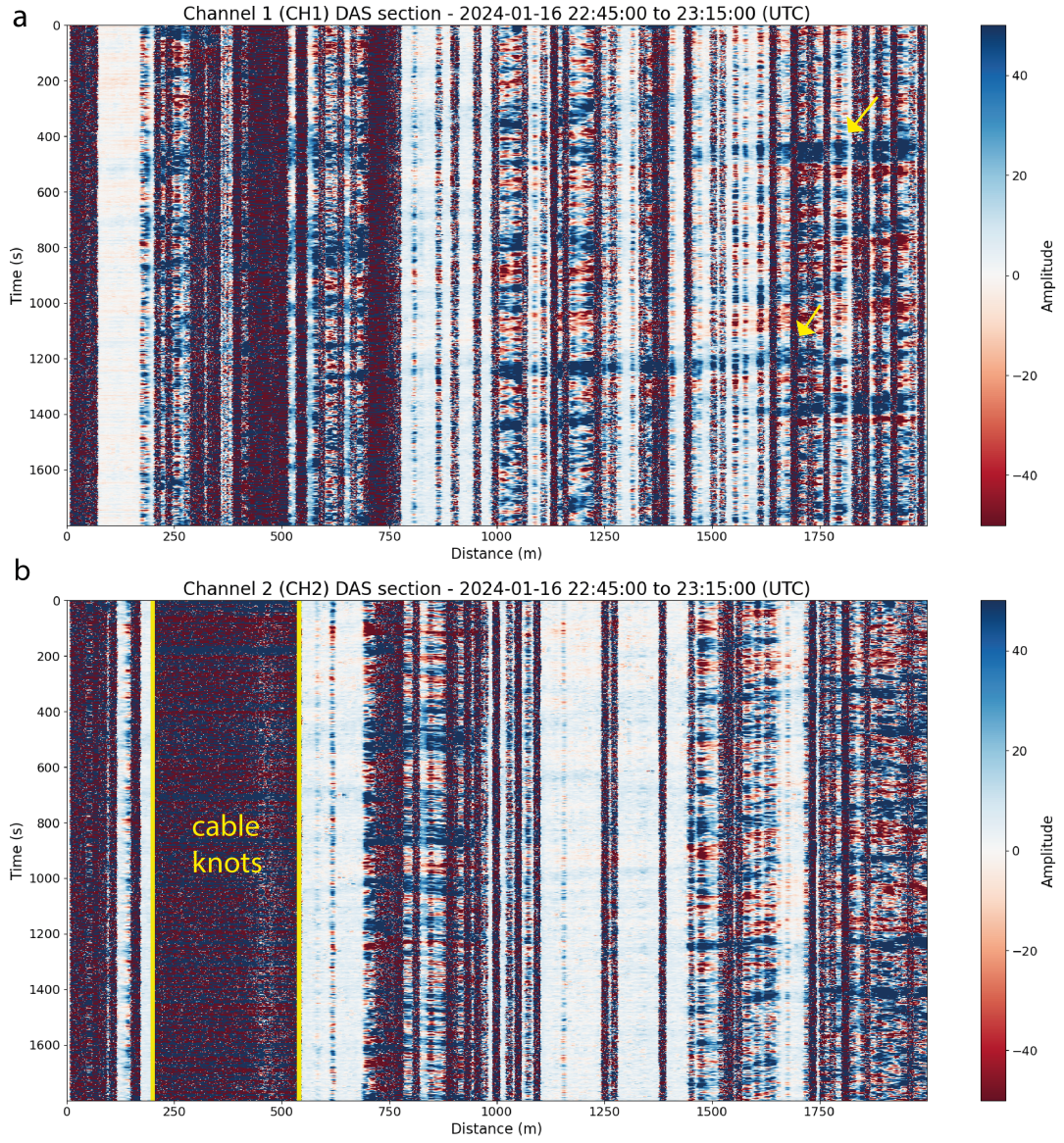

Figure 7.14: DAS sections of signal amplitudes over 30 minutes along the full length of the two optic fibers CH1 (a) and CH2 (b). The yellow arrows point to long transects of coherent noise propagating along the cable. The section delimited by two yellow lines is where the optic fiber cable was entangled and could not be properly deployed.

demonstrate that data quality is not homogeneous along the cable length. Consequently, the expected advantage of DAS (i.e., continuous seismic field measurements over long distances) is reduced, and the record instead alternates between segments of high and low data quality. Raster plots of DAS amplitude, as shown in Figure 7.14, are useful for visually identifying these segments and selecting portions of the cable reliable for future analysis.

Within the CH1 section, a coherent wavefield can be observed propagating from the end of the cable (at a distance of 2000 m) toward approximately 200 m (see yellow arrows, Fig. 7.14a). This signal, characterized by alternating positive and negative amplitude phases, differs from noise-dominated segments by its spatial coherence over distance. While its origin remains uncertain at this preliminary stage, it may indicate long-period deformation processes along the transect. For channel 2 (CH2), approximately 300 m of the cable was damaged and consists of entangled sections of cable, and is clearly visible on the DAS section, enclosed between two vertical yellow lines in Figure 7.14b. Similar to CH1, some coherent, long-period wavefield patterns can be identified. In both cases, thorough data processing is required to isolate reliable sections of the cable by removing portions affected by excessive noise. Once these corrections are applied, we can perform a more robust analysis of the coherent wavefield patterns, and other signals recorded, and have a better understanding of their physical origin.

7.4.3 Preliminary analysis and comparison with data acquired on Isunnguata Sermia

To assess the quality of the DAS data, but also to accurately locate the fibre and its optical distance to the DAS, we look at hammer shots (tap tests) that were performed along the optical fiber cable. The impact was generated using a hammer and a metal plate. Figure 7.15 illustrates the recorded signals on both the seismic nodes of dense array A2 and the zigzag optical fiber (CH2). We compare ground velocity recorded by the nodes with strain measurements along the fiber. On the dense node array (Fig. 7.15a), the hammer shot produces a clear signal visible across most seismic nodes, with wave propagation observable over a distance of approximately 1500 m. In contrast, the same event recorded by the fiber (Fig. 7.15b) shows a shorter propagation distance. The black arrow marks the impact position along the cable. The signal propagates only toward the end of the cable, while the opposite direction (toward the cable start and the DAS) is dominated by noise, likely caused by poor coupling between the cable and the ice. On the propagating side, the coherent signal remains visible for only about 150 m, considerably shorter than the node array record, suggesting a rather poor coupling at the time of the shot (sunny afternoon, perhaps generating melt around the fiber). We then compare the waveforms recorded at the node closest to the hammer shot (03x01) with the optical channel closest to the hammer shot. Despite the shorter wavefield propagation observed on DAS data, the normalized waveforms from both instruments are very similar (Fig. 7.15c). The DAS trace exhibits slightly higher noise but reveals a clearer second arrival, likely corresponding to a Rayleigh wave, following the first arrival (P wave). This can be attributed to the directional sensitivity of the DAS system, which records strain exclusively along the fiber axis, a horizontal component. Whereas the seismic trace for the node data presented here corresponds to the vertical component. Such geometry makes the DAS more sensitive to surface waves,

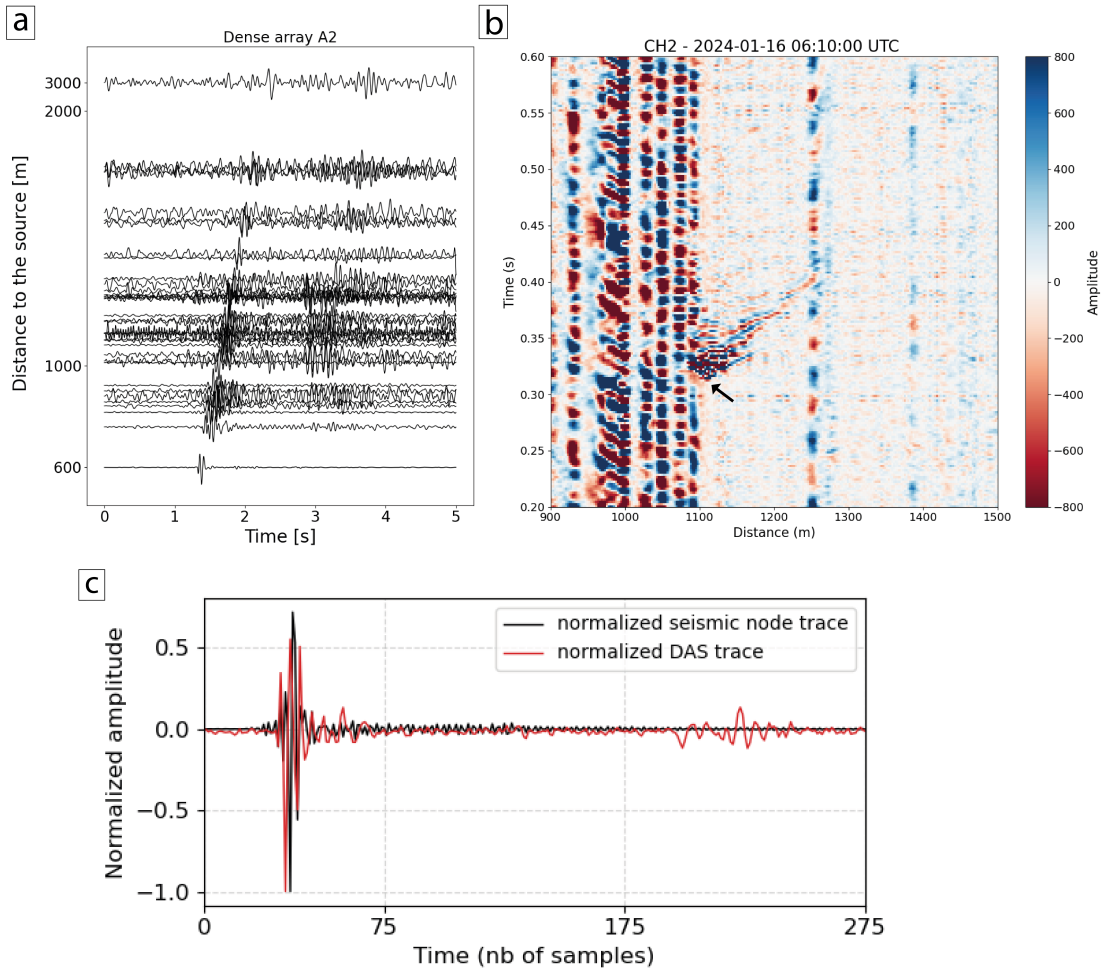

Figure 7.15: Hammer shot near the dense array A2 and the optic fibers. (a) Active seismic hammer shot seen on seismic nodes of the dense array A2. The hammer shot was performed near seismic node 03x01 on 16, Jan 2024 at 06:10:00 (UTC). Seismic waveforms are from the vertical component and filtered between 5 and 20 Hz. (b) DAS record of the hammer shot on the zigzag fiber CH2. The black arrow indicates where the shot was performed along the cable. We observe propagation of the signal at around 150 m on one side, and the signal being lost in noise on the other side. (c) Comparison of the waveform on seismic node 03x01 (vertical component) (black) and strain record the DAS channel next to the node (red). Note that amplitudes are normalized.

particularly under this experimental setup.

A similar experiment was conducted on Isunnguata Sermia during the summer 2024 campaign. Figure 7.16a shows a section of the record from a single hammer shot near node 1104, observed on the vertical component of the seismic nodes. Figure 7.16b presents the same event recorded by the DAS. The seismic waves generated by the impact are visible but propagates only to approximately 25 m from the source. The dis-

tance of propagation of the hammer shot is significantly shorter than on the Astrolabe Glacier. Comparison of the waveforms from node 1104 and the closest DAS channel (Fig. 7.16c) shows very similar shapes, characterized by a strong, short-duration wave packet followed by a brief coda. However, the noise level in the DAS data is significantly higher compared to the seismic trace. This observation, along with the short propagation distance of the signal, suggests a poor coupling between the fiber and the ice on Isunnguata Sermia, compared to the Astrolabe Glacier. This is consistent with surface topography and weather conditions that could affect the fiber-ice coupling and noise level.

The fact that the propagation of the hammer shot is shorter on the DAS data than on a dense array has been observed in several cases of using DAS on glacial environments and has been discussed by Kennett et al. (2024). When the seismic source is very close to the cable, the recorded strain field is influenced by steep spatial gradients, direct and reflected body waves, surface waves, and broadside arrivals. These effects interact with instrumental factors such as finite gauge length, fiber orientation, and mechanical coupling, which together govern the recorded signal. In such near-field conditions, the fiber effectively senses mechanical energy over only a limited segment. Moreover, when the impact generates waves with broadside or vertical incidence, the horizontally deployed fiber experiences only a fraction of the strain energy, further reducing the observed amplitude and apparent propagation distance.

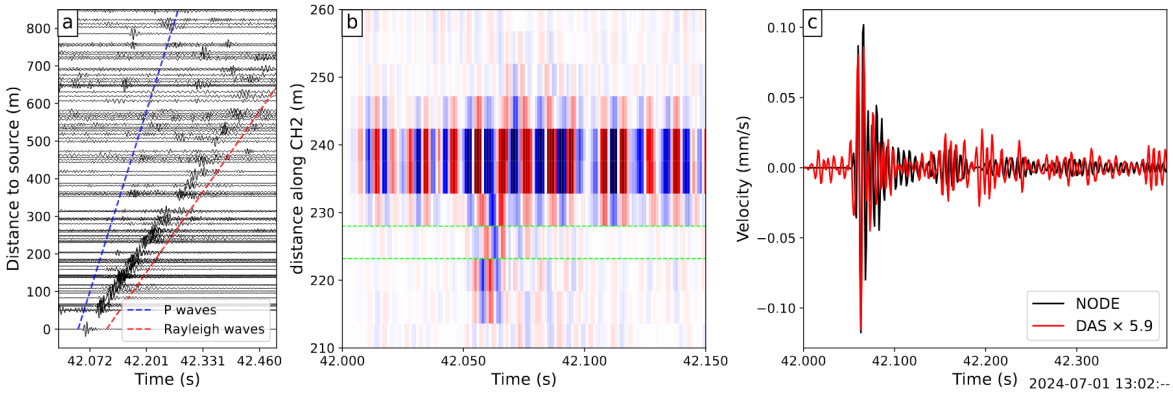

Figure 7.16: (a) Vertical component of dense array seismic traces of a hammer shot close to node 1104 (from the 2024 dense array deployed on Isunnguata Sermia). (b) DAS section for the same event. The light green box shows the channel closest to node 1104. (c) Comparison between the waveforms of node 1104 and the DAS channel in the light green box in (b). Adapted from Paris et al. (in prep)

7.4.4 Can we substitute dense networks with DAS ?

Distributed Acoustic Sensing (DAS) has emerged as a promising method for recording seismic waves through an optical fibre, providing potential metre-scale sampling over several kilometres. This dense spatial sampling allows the observation of seismic events and their propagation at high frequencies, often unresolved by seismic nodes because of their larger inter-station spacing. The ability to deploy several kilometres of fibre has brought suggestions that DAS could substitute dense nodal arrays in regions that are difficult to access. This raises the question of whether DAS can realistically replace seismic nodes in glaciological applications. The strongest advantage of DAS is its spatial density and continuity. With gauge lengths of a few metres, a 2-km fibre produces about 2,000 measurement points. Such density exceeds what is feasible with individual seismic nodes, which would require important manpower and time to deploy for large dense arrays. For large-scale monitoring applications (from kilometres to tens of kilometres), DAS provides both long-distance coverage and high spatial resolution that is difficult to obtain with geophones.

However, despite these advantages, DAS does not measure the same physical quantity as a geophone. It records strain rate along the fibre direction, whereas geophones measure three-component ground motion (vertical, east, and north) and has the ability to monitor large surface areas. The geophones are sensitive to P-, SV-, and SH-phase arrivals. This difference introduces several limitations. First, DAS is primarily sensitive to waves travelling parallel to the cable. Events arriving with wavefronts perpendicular to the fibre may be weakly recorded or entirely missed, reducing the accuracy of event localisation and creating detection biases toward certain azimuths or distances. Dense arrays, by contrast, provide full azimuthal coverage. The two systems sample the seismic wavefield differently, making their outputs not always directly comparable. In practice, some events are more easily detected with DAS, while others are better captured by seismic nodes. In addition, a single DAS channel typically has a much lower signal-to-noise ratio (SNR) than a co-located geophone. Noise from poor cable-ice coupling and wind can further reduce the SNR, limiting the usefulness of individual optical channels as true seismic sensors. For this reason, DAS alone is usually insufficient for comprehensive event detection and robust source localisation, while dense arrays alone cannot achieve kilometre-scale sampling at metre spacing. Second, DAS acquisitions generate very large data volumes which becomes also a challenge for storage and long-term archiving. Finally, DAS interrogators remain energy-consuming, expensive, and dependent on continuous power supply, conditions that are difficult to maintain in remote polar environments. In contrast, seismic nodes are compact, low-power, and robust, making them easier to deploy autonomously for long periods.

Several strategies can mitigate DAS limitations. Introducing geometric complexity into the cable layout, such as loops, L-shapes, or perpendicular branches, helps improve azimuthal sensitivity. Combining surface and borehole DAS deployments also increases directional coverage and provides access to deep ice properties (Booth et al.,

2020). Data quality can be further improved by enhancing cable coupling and reducing environmental noise, for example by burying the fibre, avoiding exposed crests, or isolating it from wind and meltwater streams. These approaches help narrow the gap between DAS and traditional arrays but do not eliminate it. Given current technological constraints, DAS cannot yet fully replace dense seismic arrays, and seismic nodes cannot provide the spatial continuity that DAS offers. A combined and synchronous approach currently yields the best scientific return: nodes provide accurate, three-component measurements for phase identification and precise localisation, while DAS offers continuous, high-resolution sampling to image structures, track dispersion, and detect fine-scale ice motion.

7.5 Data acquisition and scientific responsibility

The previous sections have focused on the logistical and technical aspects of seismological instrumentation in polar environments: how sensors are deployed under difficult weather conditions and how data quality can be affected by environmental constraints. However, beyond these operational aspects, it is necessary to consider the broader implications and responsibilities of such scientific activity. Field research in Antarctica and Greenland represents a considerable human and institutional effort, but it also raises questions about how the data collected are used, shared, and justified in light of their environmental and ethical implications. This section aims to open a discussion on the value and impact of data acquisition in polar research.

7.5.1 From acquisition to valorization

Geophysical instrumentation missions in polar regions involve important human, material, and logistical investment. Each deployment requires international travel, complex coordination, and often weeks of field operations under harsh and unpredictable conditions. The commitment of researchers and technical staff in such environments creates a scientific responsibility: to ensure that the data collected through these efforts are fully exploited, properly stored, and made accessible for future use.

Maximizing the scientific contribution of field campaigns implies looking beyond the scope of individual projects. The uncertain nature of polar fieldwork, and the limited time windows available for deployment, make it essential to anticipate the scientific lifecycle of the data, from acquisition to dissemination. This includes the implementation of robust data processing routines, the creation of thorough metadata documentation, and the establishment of reliable archiving strategies.

The application of the FAIR principles (Findability, Accessibility, Interoperability, and Reusability) provides a framework for this process. These principles encourage the

creation of datasets that remain useful in the long term, both within and beyond the original research team. In practice, this means uploading field data to global repositories (for instance, Epos-France for French seismological data), documenting the data acquisition field campaign, detailing the instrument settings, and processing steps, and ensuring that metadata and code are publicly available. Such transparency increases the reproducibility of results and enables the integration of observational data into broader multidisciplinary studies. Despite growing awareness, a proportion of polar geophysical datasets remain underused. They are often stored locally or forgotten after project completion. This is a missed opportunity, especially given the involvement of scientists for the acquisition of these datasets, and the financial and environmental costs associated. To prevent this, establishing a data management plan should be a standard requirement of every field program, as a main component of the research process within a project.

The concept of valorization must therefore be understood in a broad sense. It is more than production of scientific publications and includes training, sharing, and interdisciplinary integration. Training early-career scientists in data reuse and documentation practices is one of the most effective ways to promote sustainability in polar research. Likewise, sharing code, processing workflows, and calibration protocols facilitates transparency and strengthens collaborative networks. Ultimately, the objective is to transform the heavy logistical investment of polar field campaigns into collective scientific resources. When datasets are properly archived and openly shared, each mission contributes not only to its immediate research question but also to a long-term, cumulative effort to document the dynamics of polar regions.

7.5.2 Environmental cost and scientific sobriety

Despite their fundamental contribution to climate research, scientific polar missions have an important environmental footprint. The carbon emission associated with long-distance air and sea travels, helicopter transport, heavy equipment shipment, and energy-intensive field operations is considerable. This reality confronts polar scientists with a paradox: studying climate change in some of the most fragile environments on Earth often involves carbon-intensive expeditions that contribute to the very problem being investigated.

Acknowledging this paradox does not rule out the necessity of field research, but it rather calls for a new way of doing science in polar regions, with sobriety. The idea, increasingly discussed in recent conferences and position papers (e.g., CNRS 2022, Science en transition), is not to abandon fieldwork but to rethink how it is organized. Several strategies can help reduce the environmental impact of polar research while maintaining its scientific value.

First, mutualization of logistics and equipment across research teams and national programs can help reduce the number of campaigns and associated logistics costs. Instead of multiple small missions, a single coordinated expedition combining different scientific objectives can optimize transport and energy use. Second, coordination at the international level can prevent unnecessary duplication of measurements. Many regions of Antarctica and Greenland are already covered by existing geophysical observations. A careful review of available data before planning new missions can identify where re-measurement is truly justified and where data reuse would be sufficient. This approach requires efficient data sharing mechanisms, another reason why FAIR and open data policies are essential to a low-impact scientific approach. Third, ethical planning should become a formal stage in project preparation. Researchers and institutions must be encouraged, when writing proposals for projects, to ask whether it is essential to acquire a particular set of data or can the scientific question be answered using existing datasets. Estimating the carbon emissions of each campaign, even approximately, would also be a valuable practice. Such assessments could inform decisions about mission design, justify the need for mutualized logistics, and promote the development of low carbon emission strategies when doing polar research.

Conclusion & Perspectives

This thesis aimed to characterize the short-term dynamics of the Astrolabe Glacier using high-resolution seismic observations. The research relied on identifying, detecting and locating cryoseismic sources, analyzing their temporal and spatial variability and link the activity regimes to processes controlling outlet glacier dynamics.

For marine-terminating outlet glaciers, seismic sources may originate from several interfaces: the ice–ocean boundary (e.g., calving, sea-ice interactions), the ice–bedrock interface (e.g., basal slip, subglacial hydrology), or within the ice body itself (e.g., crevassing). Each of these processes generates signals with distinct spectral and waveform characteristics. Consequently, no single analysis method can be universally applied; techniques must be adapted to the type of source and waveform complexity, what has been done during this thesis. The approach adopted combines classical detection techniques - such as STA/LTA and template matching — with statistical analyses of event occurrence. This dual approach provides robust temporal and spatial characterization of glacier seismic activity patterns.

At the glacier surface, we demonstrated that brittle deformation revealed by seismic activity at the Astrolabe Glacier is strongly modulated by tides, from monthly to sub-daily cycles. The most common pattern includes one or two peaks of seismicity per diurnal cycle, with variations depending on the observation period and sensor location. Within the grounding zone, surface icequake activity is particularly intense over the floating part of the glacier, occurring preferentially during rising tide, whereas the grounded section shows lower seismicity concentrated during falling tide. This spatial partitioning of brittle deformation is consistent with the position of the "geodetic" grounding line. GNSS observations support this interpretation, capturing vertical displacements associated with the transition between grounded and floating states. Overall, tidal flexure of the floating ice tongue induces stress variations that generate brittle deformation. Icequake activity thus serves as a sensitive proxy for mapping the grounding zone and tracking the migration of tidal flexure at sub-daily timescales.

At the glacier base, clusters of stick-slip events were located and interpreted as cycles of stress accumulation and frictional sliding of the ice flowing over bedrock asperities. Their activation at low and rising tide, followed by quiescence at high and falling tide, indicates modulation of the basal sliding by seawater intrusion beneath the glacier. The spatial distribution of these clusters constrains the position of the mechanical grounding zone at the base of the glacier, which is offset from the geodetic grounding zone inferred from surface tidal flexure. These observations highlight the

tidal control on the mechanical state of the ice–bed interface: tide-induced vertical motion of the floating ice generates seawater intrusion, the interface transitions from frictional to a more lubricated sliding, reducing basal seismicity.

To push further our analysis on the seismic accommodation of ice deformation at outlet glaciers, we shifted our focus on the shear margin of the Astrolabe Glacier, near the grounding zone. We identified and located stick-slip clusters along the lateral ice-bedrock interface. Their spatial distribution underline where the relative motion of ice is seismically accommodated by sliding over the bedrock. This emphasizes the mechanical coupling between the glacier and the fjord valley walls, which plays a key role in accommodating stress at the margin.

These results demonstrate that seismology and dense seismic networks in particular provide powerful means to resolve glacier dynamics at sub-daily timescales. Their high temporal resolution enables the monitoring of variations in icequake and stick-slip activity linked to tidal forcing, while their spatial coverage allows mapping of deformation patterns and interface states over hundreds of meters to a few kilometers. This combination of spatial and temporal sensitivity enables us to infer the positions of both "geodetic" and "mechanical" grounding zones. In particular, our results show that grounding line migration can be tracked on a continuous basis and at unprecedented temporal resolution, usually inaccessible from traditional observation methods. On a methodological point of view, our icequakes and stick-slip detection catalogs could provide a robust ground truth to benchmark automatic machine learning methods for detection and clustering (e.g., Rimpot et al., 2025), which could likely unveil other types of cryoseismic events such as short-period tremors or long period glacial earthquakes.

The conducted work establishes a groundwork from which broader research perspectives can be developed. We underline below five, non exhaustives, perspectives for future investigations:

1. From observations on a single study-site to larger scale scientific implications

Compared to other remote and large outlet glaciers of Antarctica, the Astrolabe Glacier, with its moderate size and logistical accessibility, can be regarded as a "natural laboratory" for testing dense seismic array methods. These favorable conditions enabled high-resolution observations of grounding zone dynamics. We established a new approach for analyzing seismic events induced by these dynamics and for tracking short-term grounding line migration. The next step is to evaluate whether this approach can be generalized to other marine-terminating outlet glaciers. Applying it to sites with different geometries, basal conditions, and hydrological regimes would help determine how such factors influence local cryoseismicity, as well as the seismic detectability and behavior of grounding line migration. Comparative analyses across

multiple glaciers could reveal common physical mechanisms, such as the role of subglacial hydrology and cavity formation in modulating stick-slip activity, and establish a framework for continent-scale monitoring of grounding zone processes.

2. Long-term monitoring of basal slip as an environmental proxy for grounding line retreat and glacier stability.

One important conclusion of this work is that stick-slip may serve as a potential proxy for assessing grounding line retreat and glacier stability. The next central question is whether basal slip can reliably indicate grounding line retreat and changes in basal mechanical conditions over longer timescale. Addressing this requires long-term seismic monitoring to objectively evaluate the temporal evolution of basal slip processes. Extending deployments over seasonal and interannual timescales would provide continuous observations of grounding line migration and basal dynamics. Developing a monitoring framework based on the basal slip, however, necessitates overcoming several limitations. Reliable event depth estimates is needed to fully capture the grounding zone state and to link stick-slip cluster distribution with basal asperities. Achieving this depends on better constraints on the glacier internal seismic velocity structure and improved knowledge of the underlying bed topography. From a logistical perspective, we have discussed how Greenland presents more accessible settings for year-round observations, whereas Antarctic sites such as the Astrolabe Glacier - despite their major environmental interest - require heavier preparation to develop comparable long-term records.

3. Seismic imaging and wave propagation characterization

Building on the need for stronger observational constraints to develop a reliable monitoring strategy for grounding line retreat, seismic imaging represents a crucial next step. High-resolution imaging of the bedrock geometry, beneath both the grounded and floating ice, is of major importance for improving our knowledge on glacier stability but also for the potential impact of ocean water masses underneath. To constrain ice geometry from the surface seismological observations, seismic wave propagation within the ice and at the interfaces must be more accurately modeled and constrained. During the analysis of our seismic sources, we observed inconsistencies in the source depths that could be induced by unconstrained P- and S-wave velocities, suggesting anomalously low S-wave speeds. Future work should determine whether these anomalies reflect strong heterogeneities in the subglacial bedrock or unusual ice properties such as enhanced fracturing, fabric anisotropy, or variations in ice temperature that may significantly affect seismic wave propagation. This line of research forms the objective of a new PhD starting in 2025 at ITES Strasbourg.

4. Connecting observations to modeling: toward a better understanding of physical processes at play

Another perspective in which this work could be extended is to connect our seismic observations with models of outlet glacier ice deformation. Such integration would help translate observed seismic signatures into quantitative physical parameters, bridging the gap between field-based observations and theoretical modeling. A first step would be to numerically reproduce the tidally modulated brittle deformation and the spatial partitioning of stress observed over the grounding zone. This would enable a more robust assessment of ice rheology, stress accommodation, and the long-term mechanical stability of grounding zones under periodic tidal forcing. A second step concerns the modeling of basal stick-slip processes at the ice–bedrock interface. The goal would be to reconstruct seismic cycles in connection with tidal dynamics, i.e., identifying coseismic, inter-seismic, and aseismic phases, and to determine the rupture thresholds controlling stick-slip activation while considering the effect of water pressurization at the ice–bedrock interface. Using the amplitude and occurrence of basal clusters, it may be possible to quantitatively estimate stress accumulation and release patterns at the ice–bed interface during tidal cycles. By integrating seismic and modeling approaches, we could better quantify the stress–strain relationships controlling glacier sliding and surface brittle deformation, thereby improving our physical understanding of how marine-terminating glaciers mechanically respond to oceanic forcing.

5. Exploring calving-related seismicity and glacier front dynamics as a proxy for ice mass balance

While this thesis focused on the grounding zone and shear margin of the Astrolabe Glacier, calving remains one of the main contributors to ice mass loss in marine-terminating outlet glaciers. Monitoring calving activity is therefore essential for constraining the overall ice mass balance and evaluating its relative contribution to ice loss compared to basal melting (which should also be monitored, for instance through continuous radar technologies such as ApRes). Satellite observations currently provide large-scale assessments of calving front positions and ice volume changes over seasonal to interannual timescales. However, they lack the temporal resolution needed to capture short-term variability and the mechanical processes triggering individual calving events. This limitation raises a key question: can seismic observations provide near-continuous monitoring of calving activity and help quantify its contribution to ice mass loss? By using dense seismic arrays or Distributed Acoustic Sensing (DAS), for example, it would be interesting to determine how well it is possible to detect and locate calving events, characterize their timing, frequency, and magnitude, and investigate how they are modulated by external forcings such as tides or ocean swells. Extending seismic monitoring to glacier fronts would therefore open new perspectives for studying the coupling between mechanical failure, environmental forcing, and ice mass loss at high temporal resolution. Ultimately, such observations could complement satellite

data, improving estimates of calving fluxes and contributing to more accurate evaluations of Antarctica's ice mass balance. However, deploying instruments near calving fronts presents significant challenges, as these regions are highly fractured and unstable, making long-term station installation on the glacier front difficult. Alternative strategies could include placing sensors on stable icy or rocky outcrops close to the glacier front — such as Curie Island at the Astrolabe Glacier — or deploying ocean-bottom seismometers or hydroacoustic floats (e.g., Mermaid types), with geometries optimized for accurate seismic source localization.

Bibliography

Agnew, R.S., Pearce, E., Karplus, M., Ranganathan, M., Hoffman, A.O., Hunt, M., Pretorius, A., Shanly, S.E., Beres, M., Pradhan, K.K., Seldon, Y., Booth, A.D., Clark, R.A., Jan Young, T., 2025. Active and Passive Seismic Surveys over the Grounding Zone of Eastwind Glacier, Antarctica. Seismological Research Letters doi:10.1785/0220250024.

Albrecht, T., Martin, M., Haseloff, M., Winkelmann, R., Levermann, A., 2011. Parameterization for subgrid-scale motion of ice-shelf calving fronts. The Cryosphere 5, 35–44. doi:10.5194/tc-5-35-2011.

Allen, R.V., 1978. Automatic earthquake recognition and timing from single traces. Bulletin of the Seismological Society of America 68, 1521–1532. doi:10.1785/BSSA0680051521.

Alley, R.B., 1993. In search of ice-stream sticky spots. Journal of Glaciology 39, 447–454. doi:10.3189/S0022143000016336.

Allstadt, K., Malone, S.D., 2014. Swarms of repeating stick-slip icequakes triggered by snow loading at Mount Rainier volcano. Journal of Geophysical Research: Earth Surface 119, 1180–1203. doi:10.1002/2014JF003086.

Amundson, J.M., Truffer, M., Lüthi, M.P., Fahnestock, M., West, M., Motyka, R.J., 2008. Glacier, fjord, and seismic response to recent large calving events, Jakobshavn Isbræ, Greenland. Geophysical Research Letters 35. doi:10.1029/2008GL035281.

An, L., Rignot, E., Chauche, N., Holland, D.M., Holland, D., Jakobsson, M., Kane, E., Wood, M., Klaucke, I., Morlighem, M., Velicogna, I., Weinrebe, W., Willis, J.K., 2019. Bathymetry of Southeast Greenland From Oceans Melting Greenland (OMG) Data. Geophysical Research Letters 46, 11197–11205. doi:10.1029/2019GL083953.

Anandakrishnan, S., Alley, R.B., 1997. Tidal forcing of basal seismicity of ice stream C, West Antarctica, observed far inland. Journal of Geophysical Research: Solid Earth 102, 15183–15196. doi:10.1029/97JB01073.

Anandakrishnan, S., Bentley, C.R., 1993. Micro-earthquakes beneath Ice Streams and C, West Antarctica: observations and implications. Journal of Glaciology 39, 455–462. doi:10.3189/S0022143000016348.

Anandakrishnan, S., Voigt, D.E., Alley, R.B., King, M.A., 2003. Ice stream D flow speed is strongly modulated by the tide beneath the Ross Ice Shelf. Geophysical Research Letters 30. doi:10.1029/2002GL016329.

Aster, R.C., Winberry, J.P., 2017. Glacial seismology. Reports on Progress in Physics. Physical Society (Great Britain) 80, 126801. doi:10.1088/1361-6633/aa8473.

Aðalgeirsdóttir, G., Smith, A.M., Murray, T., King, M.A., Makinson, K., Nicholls, K.W., Behar, A.E., 2008. Tidal influence on Rutford Ice Stream, West Antarctica: observations of surface flow and basal processes from closely spaced GPS and passive seismic stations. Journal of Glaciology 54, 715–724. doi:10.3189/002214308786570872.

Bannister, S., Kennett, B.L., 2002. Seismic activity in the Transantarctic Mountains - Results from a broadband array deployment. Terra Antarctica 9, 41–46.

Barcheck, C.G., Tulaczyk, S., Schwartz, S.Y., Walter, J.I., Winberry, J.P., 2018. Implications of basal micro-earthquakes and tremor for ice stream mechanics: Stick-slip basal sliding and till erosion. Earth and Planetary Science Letters 486, 54–60. doi:10.1016/j.epsl.2017.12.046.

Barruol, G., Cordier, E., Bascou, J., Fontaine, F.R., Legrésy, B., Lescarmontier, L., 2013. Tide-induced microseismicity in the Mertz glacier grounding area, East Antarctica. Geophysical Research Letters 40, 5412–5416. doi:10.1002/2013GL057814.

Barruol, G., Le Bris, T., Zigone, D., Gimbert, F., Le Meur, E., Togaibekov, A., Lombardi, D., Maggi, A., Bès de Berc, M., Bernard, A., Operto, L., Daniel, R., Dumouch, T., Besançon, S., Crawford, W., Mordret, A., 2025. Cryoseismic activity and dynamics of the Astrolabe Coastal Glacier, East Antarctica - The SEIS-ADELICE project (2020-2025). Seismica .

Bartholomaus, T.C., Amundson, J.M., Walter, J.I., O'Neel, S., West, M.E., Larsen, C.F., 2015a. Subglacial discharge at tidewater glaciers revealed by seismic tremor. Geophysical Research Letters 42, 6391–6398. doi:10.1002/2015GL064590.

Bartholomaus, T.C., Larsen, C.F., West, M.E., O'Neel, S., Pettit, E.C., Truffer, M., 2015b. Tidal and seasonal variations in calving flux observed with passive seismology. Journal of Geophysical Research: Earth Surface 120, 2318–2337. doi:10.1002/2015JF003641.

Barzycka, B., Grabiec, M., Błaszczyk, M., Ignatiuk, D., Laska, M., Hagen, J.O., Jania, J., 2020. Changes of glacier facies on Hornsund glaciers (Svalbard) during the decade 2007–2017. Remote Sensing of Environment 251, 112060. doi:10.1016/j.rse.2020.112060.

Bassis, J.N., 2011. The statistical physics of iceberg calving and the emergence of universal calving laws. Journal of Glaciology 57, 3–16. doi:10.3189/002214311795306745.

Bassis, J.N., Fricker, H.A., Coleman, R., Minster, J.B., 2008. An investigation into the forces that drive ice-shelf rift propagation on the Amery Ice Shelf, East Antarctica. Journal of Glaciology 54, 17–27. doi:10.3189/002214308784409116.

Baumhoer, C.A., Dietz, A.J., Dech, S., Kuenzer, C., 2018. Remote Sensing of Antarctic Glacier and Ice-Shelf Front Dynamics—A Review. Remote Sensing 10, 1445. doi:10.3390/rs10091445.

Beaman, R.J., O'Brien, P.E., Post, A.L., Santis, L.D., 2011. A new high-resolution bathymetry model for the Terre Adélie and George V continental margin, East Antarctica. Antarctic Science 23, 95–103. doi:10.1017/S095410201000074X.

Begeman, C.B., Tulaczyk, S., Padman, L., King, M., Siegfried, M.R., Hodson, T.O., Fricker, H.A., 2020. Tidal Pressurization of the Ocean Cavity Near an Antarctic Ice Shelf Grounding Line. Journal of Geophysical Research: Oceans 125, e2019JC015562. doi:10.1029/2019JC015562.

Benn, Åström, J., Zwinger, T., Todd, J., Nick, F.M., Cook, S., Hulton, N.R.J., Luckman, A., 2017. Melt-under-cutting and buoyancy-driven calving from tidewater glaciers : new insights from discrete element and continuum model simulations doi:10.1017/jog.2017.41.

Benn, D., Evans, D.J.A., 2014. Glaciers and Glaciation, 2nd edition. 2 ed., Routledge, London. doi:10.4324/9780203785010.

Benn, D.I., Warren, C.R., Mottram, R.H., 2007. Calving processes and the dynamics of calving glaciers. Earth-Science Reviews 82, 143–179. doi:10.1016/j.earscirev.2007.02.002.

Beyreuther, M., Barsch, R., Krischer, L., Megies, T., Behr, Y., Wassermann, J., 2010. ObsPy: A Python Toolbox for Seismology. Seismological Research Letters 81, 530–533. doi:10.1785/gssrl.81.3.530.

Bindschadler, R., 1983. The Importance of Pressurized Subglacial Water in Separation and Sliding at the Glacier Bed. Journal of Glaciology 29, 3–19. doi:10.3189/S0022143000005104.

Bindschadler, R., Choi, H., Wichlacz, A., Bingham, R., Bohlander, J., Brunt, K., Corr, H., Drews, R., Fricker, H., Hall, M., Hindmarsh, R., Kohler, J., Padman, L., Rack, W., Rotschky, G., Urbini, S., Vornberger, P., Young, N., 2011. Getting around Antarctica: new high-resolution mappings of the grounded and freely-floating boundaries of the Antarctic ice sheet created for the International Polar Year. The Cryosphere 5, 569–588. doi:10.5194/tc-5-569-2011.

Bindschadler, R.A., King, M.A., Alley, R.B., Anandakrishnan, S., Padman, L., 2003. Tidally Controlled Stick-Slip Discharge of a West Antarctic Ice Stream 301.

Bonner, W.N., 1987. Antarctic science and conservation — The historical background. Environment International 13, 19–25. doi:10.1016/0160-4120(87)90039-0.

Booth, A.D., Christoffersen, P., Schoonman, C., Clarke, A., Hubbard, B., Law, R., Doyle, S.H., Chudley, T.R., Chalari, A., 2020. Distributed Acoustic Sensing of Seismic Properties in a Borehole Drilled on a Fast-Flowing Greenlandic Outlet Glacier. Geophysical Research Letters 47, e2020GL088148. doi:10.1029/2020GL088148.

Brenguier, F., Shapiro, N., Campillo, M., Ferrazzini, V., Duputel, Z., Coutant, O., Nercessian, A., 2008. Towards forecasting volcanic eruptions using seismic noise. Nature Geoscience 1, 126–130. doi:10.1038/ngeo104.

Brunt, K.M., Fricker, H.A., Padman, L., Scambos, T.A., O'Neel, S., 2010. Mapping the grounding zone of the Ross Ice Shelf, Antarctica, using ICESat laser altimetry. Annals of Glaciology 51, 71–79. doi:10.3189/172756410791392790.

Brunt, K.M., Neumann, T.A., Smith, B.E., 2019. Assessment of ICESat-2 Ice Sheet Surface Heights, Based on Comparisons Over the Interior of the Antarctic Ice Sheet. Geophysical Research Letters 46, 13072–13078. doi:10.1029/2019GL084886.

Calzas, M., Techine, P., Testut, L., 1992. Nivmer doi:10.18142/135.

Carmichael, J.D., Pettit, E.C., Hoffman, M., Fountain, A., Hallet, B., 2012. Seismic multiplet response triggered by melt at Blood Falls, Taylor Glacier, Antarctica. Journal of Geophysical Research: Earth Surface 117. doi:10.1029/2011JF002221.

Carr, J.R., Stokes, C.R., Vieli, A., 2013. Recent progress in understanding marine-terminating Arctic outlet glacier response to climatic and oceanic forcing: Twenty years of rapid change. Progress in Physical Geography: Earth and Environment 37, 436–467. doi:10.1177/0309133313483163.

Catania, G.A., Stearns, L.A., Moon, T.A., Enderlin, E.M., Jackson, R.H., 2020. Future Evolution of Greenland's Marine-Terminating Outlet Glaciers. Journal of Geophysical Research: Earth Surface 125, e2018JF004873. doi:10.1029/2018JF004873.

Charrassin, R., Millan, R., Rignot, E., Scheinert, M., 2025. Bathymetry of the Antarctic continental shelf and ice shelf cavities from circumpolar gravity anomalies and other data. Scientific Reports 15, 1214. doi:10.1038/s41598-024-81599-1.

Chen, G., 1999. GPS kinematic positioning for the airborne laser altimetry at Long Valley, California. Thesis. Massachusetts Institute of Technology.

Chen, H., Rignot, E., Scheuchl, B., Ehrenfeucht, S., 2023. Grounding Zone of Amery Ice Shelf, Antarctica, From Differential Synthetic-Aperture Radar Interferometry. Geophysical Research Letters 50, e2022GL102430. doi:10.1029/2022GL102430.

Christmann, J., Helm, V., Khan, S.A., Kleiner, T., Müller, R., Morlighem, M., Neckel, N., Rückamp, M., Steinhage, D., Zeising, O., Humbert, A., 2021. Elastic deformation plays a non-negligible role in Greenland's outlet glacier flow. Communications Earth & Environment 2, 232. doi:10.1038/s43247-021-00296-3.

Christmann, J., Plate, C., Müller, R., Humbert, A., 2016. Viscous and viscoelastic stress states at the calving front of Antarctic ice shelves. Annals of Glaciology 57, 10–18. doi:10.1017/aog.2016.18.

Ciracì, E., Rignot, E., Scheuchl, B., Tolpekin, V., Wollersheim, M., An, L., Milillo, P., Bueso-Bello, J.L., Rizzoli, P., Dini, L., 2023. Melt rates in the kilometer-size grounding zone of Petermann Glacier, Greenland, before and during a retreat. Proceedings of the National Academy of Sciences 120, e2220924120. doi:10.1073/pnas.2220924120.

Constantino, R.R., Tinto, K.J., 2023. Cook Ice Shelf and Ninnis Glacier Tongue Bathymetry From Inversion of Operation Ice Bridge Airborne Gravity Data. Geophysical Research Letters 50, e2023GL103815. doi:10.1029/2023GL103815.

Cooley, J., Winberry, P., Koutnik, M., Conway, H., 2019. Tidal and spatial variability of flow speed and seismicity near the grounding zone of Beardmore Glacier, Antarctica. Annals of Glaciology 60, 37–44. doi:10.1017/aog.2019.14.

Cressie, N., 1993. Statistics for spatial data. volume Wiley Series in Probability and Statistics.

Cuffey, K.M., Paterson, W.S.B., 2010. The Physics of Glaciers. Academic Press.

Danesi, S., Bannister, S., Morelli, A., 2007. Repeating earthquakes from rupture of an asperity under an Antarctic outlet glacier. Earth and Planetary Science Letters 253, 151–158. doi:10.1016/j.epsl.2006.10.023.

Davison, B.J., Hogg, A.E., Gourmelen, N., Jakob, L., Wuite, J., Nagler, T., Greene, C.A., Andreasen, J., Engdahl, M.E., 2023. Annual mass budget of Antarctic ice shelves from 1997 to 2021. Science Advances 9, eadi0186. doi:10.1126/sciadv.adi0186.

Deb, P., Bromwich, D., Orr, A., Sen, A., Clem, K.R., 2025. Recent increase in surface melting of West Antarctic ice shelves linked to Interdecadal Pacific Oscillation. Communications Earth & Environment 6, 99. doi:10.1038/s43247-025-02077-8.

Dinniman, M.S., Asay-Davis, X.S., Galton-Fenzi, B.K., Holland, P.R., Jenkins, A., Timmermann, R., 2016. Modeling Ice Shelf/Ocean Interaction in Antarctica: A REVIEW. Oceanography 29, 144–153.

van Dongen, E.v., Jouvet, G., Walter, A., Todd, J., Zwinger, T., Asaji, I., Sugiyama, S., Walter, F., Funk, M., 2020. Tides modulate crevasse opening prior to a major calving event at Bowdoin Glacier, Northwest Greenland. Journal of Glaciology 66, 113–123. doi:10.1017/jog.2019.89.

Drews, R., Wild, C.T., Marsh, O.J., Rack, W., Ehlers, T.A., Neckel, N., Helm, V., 2021. Grounding-Zone Flow Variability of Priestley Glacier, Antarctica, in a Diurnal

Tidal Regime. Geophysical Research Letters 48, e2021GL093853. doi:10.1029/2021GL093853.

Drouet, A.S., 2012. Dynamique du glacier émissaire des processus à l'application sur un glacier école, Astrolabe, Antarctique de l'Est. Ph.D. thesis. Université Grenoble Alpes, France (141 pages).

Echelmeyer, K.A., Harrison, W.D., Larsen, C., Mitchell, J.E., 1994. The role of the margins in the dynamics of an active ice stream. Journal of Glaciology 40, 527–538. doi:10.3189/S0022143000012417.

Ekström, G., Nettles, M., Abers, G.A., 2003. Glacial Earthquakes. Science 302, 622–624. doi:10.1126/science.1088057.

Enderlin, E.M., Howat, I.M., Jeong, S., Noh, M.J., van Angelen, J.H., van den Broeke, M.R., 2014. An improved mass budget for the Greenland ice sheet. Geophysical Research Letters 41, 866–872. doi:10.1002/2013GL059010.

Enderlin, E.M., Howat, I.M., Vieli, A., 2013. High sensitivity of tidewater outlet glacier dynamics to shape. The Cryosphere 7, 1007–1015. doi:10.5194/tc-7-1007-2013.

Farinotti, D., Huss, M., Fürst, J.J., Landmann, J., Machguth, H., Maussion, F., Pandit, A., 2019. A consensus estimate for the ice thickness distribution of all glaciers on Earth. Nature Geoscience 12, 168–173. doi:10.1038/s41561-019-0300-3.

Flinn, E., 1965. Signal analysis using rectilinearity and direction of particle motion. Proceedings of the IEEE 53, 1874–1876. doi:10.1109/PROC.1965.4462.

Fontaine, F.R., Barruol, G., Kennett, B.L.N., Bokelmann, G.H.R., Reymond, D., 2009. Upper mantle anisotropy beneath Australia and Tahiti from P wave polarization: Implications for real-time earthquake location. Journal of Geophysical Research: Solid Earth 114. doi:10.1029/2008JB005709.

Francis, D., Fonseca, R., Mattingly, K.S., Marsh, O.J., Lhermitte, S., Cherif, C., 2022. Atmospheric Triggers of the Brunt Ice Shelf Calving in February 2021. Journal of Geophysical Research: Atmospheres 127, e2021JD036424. doi:10.1029/2021JD036424.

Freer, B.I.D., Marsh, O.J., Hogg, A.E., Fricker, H.A., Padman, L., 2023. Modes of Antarctic tidal grounding line migration revealed by Ice, Cloud, and land Elevation Satellite-2 (ICESat-2) laser altimetry. The Cryosphere 17, 4079–4101. doi:10.5194/tc-17-4079-2023.

Fretwell, P., Pritchard, H.D., Vaughan, D.G., Bamber, J.L., Barrand, N.E., Bell, R., Bianchi, C., Bingham, R.G., Blankenship, D.D., Casassa, G., Catania, G., Callens, D., Conway, H., Cook, A.J., Corr, H.F.J., Damaske, D., Damm, V., Ferraccioli, F., Forsberg, R., Fujita, S., Gim, Y., Gogineni, P., Griggs, J.A., Hindmarsh,

R.C.A., Holmlund, P., Holt, J.W., Jacobel, R.W., Jenkins, A., Jokat, W., Jordan, T., King, E.C., Kohler, J., Krabill, W., Riger-Kusk, M., Langley, K.A., Leitchenkov, G., Leuschen, C., Luyendyk, B.P., Matsuoka, K., Mouginot, J., Nitsche, F.O., Nogi, Y., Nost, O.A., Popov, S.V., Rignot, E., Rippin, D.M., Rivera, A., Roberts, J., Ross, N., Siegert, M.J., Smith, A.M., Steinhage, D., Studinger, M., Sun, B., Tinto, B.K., Welch, B.C., Wilson, D., Young, D.A., Xiangbin, C., Zirizzotti, A., 2013. Bedmap2: improved ice bed, surface and thickness datasets for Antarctica. The Cryosphere 7, 375–393. doi:10.5194/tc-7-375-2013.

Fricker, H.A., Allison, I., Craven, M., Hyland, G., Ruddell, A., Young, N., Coleman, R., King, M., Krebs, K., Popov, S., 2002. Redefinition of the Amery Ice Shelf, East Antarctica, grounding zone. Journal of Geophysical Research: Solid Earth 107. doi:10.1029/2001JB000383.

Fricker, H.A., Coleman, R., Padman, L., Scambos, T.A., Bohlander, J., Brunt, K.M., 2009. Mapping the grounding zone of the Amery Ice Shelf, East Antarctica using InSAR, MODIS and ICESat. Antarctic Science 21, 515–532. doi:10.1017/S095410200999023X.

Fricker, H.A., Padman, L., 2006. Ice shelf grounding zone structure from ICESat laser altimetry. Geophysical Research Letters 33. doi:10.1029/2006GL026907.

Friedl, P., Weiser, F., Fluhrer, A., Braun, M.H., 2020. Remote sensing of glacier and ice sheet grounding lines: A review. Earth-Science Reviews 201, 102948. doi:10.1016/j.earscirev.2019.102948.

Fromm, T., Schlindwein, V., Helm, V., Fofonova, V., 2023. Observing tidal effects on the dynamics of the Ekström Ice Shelf with focus on quarterdiurnal and terdiurnal periods. Journal of Glaciology , 1–11doi:10.1017/jog.2023.4.

Fukui, K., Sone, T., Strelin, J.A., Torielli, C.A., Mori, J., Fujii, Y., 2008. Dynamics and GPR stratigraphy of a polar rock glacier on James Ross Island, Antarctic Peninsula. Journal of Glaciology 54, 445–451. doi:10.3189/002214308785836940.

Fürst, J.J., Durand, G., Gillet-Chaulet, F., Tavard, L., Rankl, M., Braun, M., Gagliardini, O., 2016. The safety band of Antarctic ice shelves. Nature Climate Change 6, 479–482. doi:10.1038/nclimate2912.

Gadi, R., Rignot, E., Menemenlis, D., 2023. Modeling Ice Melt Rates From Seawater Intrusions in the Grounding Zone of Petermann Gletscher, Greenland. Geophysical Research Letters 50, e2023GL105869. doi:10.1029/2023GL105869.

Gagliardini, O., Cohen, D., Råback, P., Zwinger, T., 2007. Finite-element modeling of subglacial cavities and related friction law. Journal of Geophysical Research: Earth Surface 112. doi:10.1029/2006JF000576.

Gimbert, F., Nanni, U., Roux, P., Helmstetter, A., Garambois, S., Lecointre, A., Walpersdorf, A., Jourdain, B., Langlais, M., Laarman, O., Lindner, F., Sergeant, A., Vincent, C., Walter, F., 2021. A Multi-Physics Experiment with a Temporary Dense Seismic Array on the Argentière Glacier, French Alps: The RESOLVE Project. Seismological Research Letters 92, 1185–1201. doi:10.1785/0220200280.

Goldstein, R.M., Engelhardt, H., Kamb, B., Frolich, R.M., 1993. Satellite radar interferometry for monitoring ice sheet motion: application to an antarctic ice stream. Science (New York, N.Y.) 262, 1525–1530. doi:10.1126/science.262.5139.1525.

Graham, A.G.C., Wåhlin, A., Hogan, K.A., Nitsche, F.O., Heywood, K.J., Totten, R.L., Smith, J.A., Hillenbrand, C.D., Simkins, L.M., Anderson, J.B., Wellner, J.S., Larter, R.D., 2022. Rapid retreat of Thwaites Glacier in the pre-satellite era. Nature Geoscience 15, 706–713. doi:10.1038/s41561-022-01019-9.

Grob, M., Maggi, A., Stutzmann, E., 2011. Observations of the seasonality of the Antarctic microseismic signal, and its association to sea ice variability. Geophysical Research Letters 38. doi:10.1029/2011GL047525.

Gräff, D., Köpfli, M., Lipovsky, B.P., Selvadurai, P.A., Farinotti, D., Walter, F., 2021. Fine Structure of Microseismic Glacial Stick-Slip. Geophysical Research Letters 48, e2021GL096043. doi:10.1029/2021GL096043.

Gräff, D., Lipovsky, B.P., Vieli, A., Dachauer, A., Jackson, R., Farinotti, D., Schmale, J., Ampuero, J.P., Berg, E., Dannowski, A., Kneib-Walter, A., Köpfli, M., Kopp, H., van der Loo, E., Mata Flores, D., Mercerat, D., Moser, R., Sladen, A., Walter, F., Wasser, D., Welty, E., Wetter, S., Williams, E.F., 2025. Calving-driven fjord dynamics resolved by seafloor fibre sensing. Nature 644, 404–412. doi:10.1038/s41586-025-09347-7.

Gudmundsson, G.H., 2007. Tides and the flow of Rutford Ice Stream, West Antarctica. Journal of Geophysical Research: Earth Surface 112. doi:10.1029/2006JF000731.

Hammer, C., Ohrnberger, M., Schlindwein, V., 2015. Pattern of cryospheric seismic events observed at Ekström Ice Shelf, Antarctica. Geophysical Research Letters 42, 3936–3943. doi:10.1002/2015GL064029.

Harland, S.R., Kendall, J.M., Stuart, G.W., Lloyd, G.E., Baird, A.F., Smith, A.M., Pritchard, H.D., Brisbourne, A.M., 2013. Deformation in Rutford Ice Stream, West Antarctica: measuring shear-wave anisotropy from icequakes. Annals of Glaciology 54, 105–114. doi:10.3189/2013AoG64A033.

Helmstetter, A., Nicolas, B., Comon, P., Gay, M., 2015. Basal icequakes recorded beneath an Alpine glacier (Glacier d'Argentière, Mont Blanc, France): Evidence for stick-slip motion? Journal of Geophysical Research: Earth Surface 120, 379–401. doi:10.1002/2014JF003288.

Herring, T.A., King, R.W., Floyd, M.A., McClusky, S.C., 2018. Introduction to GAMIT/GLOBK Massachusetts Institute of Technology.

Hersbach, H., Bell, B., Berrisford, P., Hirahara, S., Horányi, A., Muñoz-Sabater, J., Nicolas, J., Peubey, C., Radu, R., Schepers, D., Simmons, A., Soci, C., Abdalla, S., Abellan, X., Balsamo, G., Bechtold, P., Biavati, G., Bidlot, J., Bonavita, M., De Chiara, G., Dahlgren, P., Dee, D., Diamantakis, M., Dragani, R., Flemming, J., Forbes, R., Fuentes, M., Geer, A., Haimberger, L., Healy, S., Hogan, R.J., Hólm, E., Janisková, M., Keeley, S., Laloyaux, P., Lopez, P., Lupu, C., Radnoti, G., de Rosnay, P., Rozum, I., Vamborg, F., Villaume, S., Thépaut, J.N., 2020. The ERA5 global reanalysis 146, 1999–2049. doi:10.1002/qj.3803.

Hibert, C., Provost, F., Malet, J.P., Maggi, A., Stumpf, A., Ferrazzini, V., 2017. Automatic identification of rockfalls and volcano-tectonic earthquakes at the Piton de la Fournaise volcano using a Random Forest algorithm. Journal of Volcanology and Geothermal Research 340, 130–142. doi:10.1016/j.jvolgeores.2017.04.015.

Hodgson, D.A., Jordan, T.A., De Rydt, J., Fretwell, P.T., Seddon, S.A., Becker, D., Hogan, K.A., Smith, A.M., Vaughan, D.G., 2019. Past and future dynamics of the Brunt Ice Shelf from seabed bathymetry and ice shelf geometry. The Cryosphere 13, 545–556. doi:10.5194/tc-13-545-2019.

Hogg, A.E., Gudmundsson, G.H., 2017. Impacts of the Larsen-C Ice Shelf calving event. Nature Climate Change 7, 540–542. doi:10.1038/nclimate3359.

Holland, D.M., Thomas, R.H., de Young, B., Ribergaard, M.H., Lyberth, B., 2008. Acceleration of Jakobshavn Isbræ triggered by warm subsurface ocean waters. Nature Geoscience 1, 659–664. doi:10.1038/ngeo316.

Hudson, T.S., Brisbourne, A.M., Kufner, S.K., Kendall, J.M., Smith, A.M., 2023a. Array processing in cryoseismology. preprint. Ice sheets/Instrumentation. doi:10.5194/egusphere-2023-657.

Hudson, T.S., Brisbourne, A.M., Walter, F., Gräff, D., White, R.S., Smith, A.M., 2020. Icequake Source Mechanisms for Studying Glacial Sliding. Journal of Geophysical Research: Earth Surface 125, e2020JF005627. doi:10.1029/2020JF005627.

Hudson, T.S., Kufner, S.K., Brisbourne, A.M., Kendall, J.M., Smith, A.M., Alley, R.B., Arthern, R.J., Murray, T., 2023b. Highly variable friction and slip observed at Antarctic ice stream bed. Nature Geoscience , 1–7doi:10.1038/s41561-023-01204-4.

Hudson, T.S., Smith, J., Brisbourne, A.M., White, R.S., 2019. Automated detection of basal icequakes and discrimination from surface crevassing. Annals of Glaciology 60, 167–181. doi:10.1017/aog.2019.18.

Hulbe, C.L., Klinger, M., Masterson, M., Catania, G., Cruikshank, K., Bugni, A., 2016. Tidal bending and strand cracks at the Kamb Ice Stream grounding line, West Antarctica. Journal of Glaciology 62, 816–824. doi:10.1017/jog.2016.74.

Hulbe, C.L., Whillans, I.M., 1994. Evaluation of strain rates on Ice Stream B, Antarctica, obtained using GPS phase measurements. Annals of Glaciology 20, 254–262. doi:10.3189/1994AoG20-1-254-262.

IMBIE team, 2018. Mass balance of the Antarctic Ice Sheet from 1992 to 2017. Nature 558, 219–222. doi:10.1038/s41586-018-0179-y.

IMBIE Team, 2020. Mass balance of the Greenland Ice Sheet from 1992 to 2018. Nature 579, 233–239. doi:10.1038/s41586-019-1855-2.

IPCC, 2021. Climate Change 2021 – The Physical Science Basis: Working Group I Contribution to the Sixth Assessment Report of the Intergovernmental Panel on Climate Change. 1 ed., Cambridge University Press. doi:10.1017/9781009157896.

Jacobs, S.S., Jenkins, A., Giulivi, C.F., Dutrieux, P., 2011. Stronger ocean circulation and increased melting under Pine Island Glacier ice shelf. Nature Geoscience 4, 519–523. doi:10.1038/ngeo1188.

Jenkins, A., Dutrieux, P., Jacobs, S.S., McPhail, S.D., Perrett, J.R., Webb, A.T., White, D., 2010. Observations beneath Pine Island Glacier in West Antarctica and implications for its retreat. Nature Geoscience 3, 468–472. doi:10.1038/ngeo890.

Jenkins, A., Jacobs, S., 2008. Circulation and melting beneath George VI Ice Shelf, Antarctica. Journal of Geophysical Research: Oceans 113. doi:10.1029/2007JC004449.

Jennings, S.J.A., Hambrey, M.J., 2021. Structures and Deformation in Glaciers and Ice Sheets. Reviews of Geophysics 59, e2021RG000743. doi:10.1029/2021RG000743.

Jurkevics, A., 1988. Polarization analysis of three-component array data. Bulletin of the Seismological Society of America 78, 1725–1743. doi:10.1785/BSSA0780051725.

Kanao, M., 2017. Statistics of Seismic Tremors with Harmonic Overtones Recorded at Syowa Station, Antarctica: October 2014-March 2015. International Journal of Geosciences 8, 811–820. doi:10.4236/ijg.2017.86046.

Karplus, M., Schmandt, B., 2018. Preface to the Focus Section on Geophone Array Seismology. Seismological Research Letters 89, 1597–1600. doi:10.1785/0220180212.

Karplus, M.S., Nakata, N., Kaip, G.M., Harder, S.H., Gonzalez, L.F., Booth, A.D., Smith, E.C., Veitch, S.A., Walter, J.I., Christoffersen, P., 2024. Signal characteristics of surface seismic explosive sources near the West Antarctic Ice Sheet divide. Journal of Glaciology 70, e16. doi:10.1017/jog.2024.41.

Kavanaugh, J.L., Clarke, G.K.C., 2001. Abrupt glacier motion and reorganization of basal shear stress following the establishment of a connected drainage system. Journal of Glaciology 47, 472–480. doi:10.3189/172756501781831972.

Kennett, B.L.N., Lai, V.H., Miller, M.S., Bowden, D., Fichtner, A., 2024. Near-source effects on DAS recording: implications for tap tests. Geophysical Journal International 237, 436–444. doi:10.1093/gji/ggae055.

Khazendar, A., Rignot, E., Schroeder, D.M., Seroussi, H., Schodlok, M.P., Scheuchl, B., Mouginot, J., Sutterley, T.C., Velicogna, I., 2016. Rapid submarine ice melting in the grounding zones of ice shelves in West Antarctica. Nature Communications 7, 13243. doi:10.1038/ncomms13243.

Kitanidis, P.K., 1997. Introduction to Geostatistics: Applications in Hydrogeology. Cambridge University Press.

Klein, E., Mosbeux, C., Bromirski, P.D., Padman, L., Bock, Y., Springer, S.R., Fricker, H.A., 2020. Annual cycle in flow of Ross Ice Shelf, Antarctica: contribution of variable basal melting. Journal of Glaciology 66, 861–875. doi:10.1017/jog.2020.61.

Kufner, S.K., Brisbourne, A.M., Smith, A.M., Hudson, T.S., Murray, T., Schlegel, R., Kendall, J.M., Anandakrishnan, S., Lee, I., 2021. Not all Icequakes are Created Equal: Basal Icequakes Suggest Diverse Bed Deformation Mechanisms at Rutford Ice Stream, West Antarctica. Journal of Geophysical Research: Earth Surface 126, e2020JF006001. doi:10.1029/2020JF006001.

Kwok, R., 2010. Satellite remote sensing of sea-ice thickness and kinematics: a review. Journal of Glaciology 56, 1129–1140. doi:10.3189/002214311796406167.

Lagarias, J.C., Reeds, J.A., Wright, M.H., Wright, P.E., 1998. Convergence Properties of the Nelder–Mead Simplex Method in Low Dimensions. SIAM Journal on Optimization 9, 112–147. doi:10.1137/S1052623496303470.

Lamsters, K., Karušs, J., Stūrmane, A., Ješkins, J., Džeriņš, P., 2022. Mapping of large-scale diapir structures at the paleo-ice tongue bed in western Latvia from geophysical investigations and borehole data. Quaternary International 630, 3–16. doi:10.1016/j.quaint.2020.12.003.

Larose, E., Carrière, S., Voisin, C., Bottelin, P., Baillet, L., Guéguen, P., Walter, F., Jongmans, D., Guillier, B., Garambois, S., Gimbert, F., Massey, C., 2015. Environmental seismology: What can we learn on earth surface processes with ambient noise? Journal of Applied Geophysics 116, 62–74. doi:10.1016/j.jappgeo.2015.02.001.

Le Bris, T., Barruol, G., Gimbert, F., Le Meur, E., Zigone, D., Togaibekov, A., Lombardi, D., Bès de Berc, M., Bernard, A., 2025. Spatial and Temporal Variability in Tide-Induced Icequake Activity at the Astrolabe Coastal Glacier, East

Antarctica. Journal of Geophysical Research: Earth Surface 130, e2024JF008054. doi:10.1029/2024JF008054.

Le Meur, E., Sacchettini, M., Garambois, S., Berthier, E., Drouet, A.S., Durand, G., Young, D., Greenbaum, J.S., Holt, J.W., Blankenship, D.D., Rignot, E., Mouginot, J., Gim, Y., Kirchner, D., de Fleurian, B., Gagliardini, O., Gillet-Chaulet, F., 2014. Two independent methods for mapping the grounding line of an outlet glacier – an example from the Astrolabe Glacier, Terre Adélie, Antarctica. The Cryosphere 8, 1331–1346. doi:10.5194/tc-8-1331-2014.

Lesage, P., 2009. Interactive Matlab software for the analysis of seismic volcanic signals. Computers & Geosciences 35, 2137–2144. doi:10.1016/j.cageo.2009.01.010.

Lewandowska, Teisseyre, 1964. Investigations of the ice microtremors on Spitsbergen in 1962. Biul Inf Komisji Wypraw Geof PAN, 37, 1-5 .

Li, T., Dawson, G.J., Chuter, S.J., Bamber, J.L., 2023. Grounding line retreat and tide-modulated ocean channels at Moscow University and Totten Glacier ice shelves, East Antarctica. The Cryosphere 17, 1003–1022. doi:10.5194/tc-17-1003-2023.

Li, Z., Deng, S., 2024. Wave impedance inversion and interpretation of Ground Penetrating Radar (GPR) data for Amery Ice Shelf in East Antarctica. Journal of Applied Geophysics 227, 105418. doi:10.1016/j.jappgeo.2024.105418.

Ligtenberg, S.R.M., van de Berg, W.J., van den Broeke, M.R., Rae, J.G.L., van Meijgaard, E., 2013. Future surface mass balance of the Antarctic ice sheet and its influence on sea level change, simulated by a regional atmospheric climate model. Climate Dynamics 41, 867–884. doi:10.1007/s00382-013-1749-1.

Lindner, F., Laske, G., Walter, F., Doran, A.K., 2019. Crevasse-induced Rayleigh-wave azimuthal anisotropy on Glacier de la Plaine Morte, Switzerland. Annals of Glaciology 60, 96–111. doi:10.1017/aog.2018.25.

Lliboutry, L., 1968. General Theory of Subglacial Cavitation and Sliding of Temperate Glaciers. Journal of Glaciology 7, 21–58. doi:10.3189/S0022143000020396.

Llorens, M.G., Griera, A., Bons, P.D., Gomez-Rivas, E., Weikusat, I., Prior, D.J., Kerch, J., Lebensohn, R.A., 2020. Seismic Anisotropy of Temperate Ice in Polar Ice Sheets. Journal of Geophysical Research: Earth Surface 125, e2020JF005714. doi:10.1029/2020JF005714.

Lombardi, D., Benoit, L., Camelbeeck, T., Martin, O., Meynard, C., Thom, C., 2016. Bimodal pattern of seismicity detected at the ocean margin of an Antarctic ice shelf. Geophysical Journal International 206, 1375–1381. doi:10.1093/gji/ggw214.

Lucas, E.M., Nyblade, A.A., Aster, R.C., Wiens, D.A., Wilson, T.J., Winberry, J.P., Huerta, A.D., 2023. Tidally Modulated Glacial Seismicity at the Foundation Ice Stream, West Antarctica. Journal of Geophysical Research: Earth Surface , e2023JF007172doi:10.1029/2023JF007172.

Lucchitta, B.K., Ferguson, H.M., 1986. Antarctica: Measuring Glacier Velocity from Satellite Images. Science 234, 1105–1108. doi:10.1126/science.234.4780.1105.

MacAyeal, D.R., 1984. Thermohaline circulation below the Ross Ice Shelf: A consequence of tidally induced vertical mixing and basal melting. Journal of Geophysical Research: Oceans 89, 597–606. doi:10.1029/JC089iC01p00597.

MacAyeal, D.R., Okal, E.A., Aster, R.C., Bassis, J.N., 2008. Seismic and hydroacoustic tremor generated by colliding icebergs. Journal of Geophysical Research: Earth Surface 113. doi:10.1029/2008JF001005.

Marsh, O.J., Arthern, R.J., De Rydt, J., 2025. Ocean tides trigger ice shelf rift growth and calving. Nature Communications 16, 6697. doi:10.1038/s41467-025-61796-w.

Marsh, O.J., Price, D., Courville, Z.R., Floricioiu, D., 2021. Crevasse and rift detection in Antarctica from TerraSAR-X satellite imagery. Cold Regions Science and Technology 187, 103284. doi:10.1016/j.coldregions.2021.103284.

Masoudi, A., Newson, T.P., 2016. Contributed Review: Distributed optical fibre dynamic strain sensing. The Review of Scientific Instruments 87, 011501. doi:10.1063/1.4939482.

Massom, R.A., Giles, A.B., Warner, R.C., Fricker, H.A., Legrésy, B., Hyland, G., Lescarmontier, L., Young, N., 2015. External influences on the Mertz Glacier Tongue (East Antarctica) in the decade leading up to its calving in 2010. Journal of Geophysical Research: Earth Surface 120, 490–506. doi:10.1002/2014JF003223.

Massom, R.A., Scambos, T.A., Bennetts, L.G., Reid, P., Squire, V.A., Stammerjohn, S.E., 2018. Antarctic ice shelf disintegration triggered by sea ice loss and ocean swell. Nature 558, 383–389. doi:10.1038/s41586-018-0212-1.

Maurel, A., Mercier, J.F., Montagnat, M., 2016. Critical investigation of calculation methods for the elastic velocities in anisotropic ice polycrystals. The Cryosphere 10, 3063–3070. doi:10.5194/tc-10-3063-2016.

McBrearty, I.W., Zoet, L.K., Anandakrishnan, S., 2020. Basal seismicity of the Northeast Greenland Ice Stream. Journal of Glaciology 66, 430–446. doi:10.1017/jog.2020.17.

Mikesell, T.D., van Wijk, K., Haney, M.M., Bradford, J.H., Marshall, H.P., Harper, J.T., 2012. Monitoring glacier surface seismicity in time and space using Rayleigh waves. Journal of Geophysical Research: Earth Surface 117. doi:10.1029/2011JF002259.

Millan, R., Mouginot, J., Rabatel, A., Morlighem, M., 2022. Ice velocity and thickness of the world's glaciers. Nature Geoscience 15, 124–129. doi:10.1038/s41561-021-00885-z.

Millan, R., Rignot, E., Bernier, V., Morlighem, M., Dutrieux, P., 2017. Bathymetry of the Amundsen Sea Embayment sector of West Antarctica from Operation IceBridge gravity and other data. Geophysical Research Letters 44, 1360–1368. doi:10.1002/2016GL072071.

Millan, R., St-Laurent, P., Rignot, E., Morlighem, M., Mouginot, J., Scheuchl, B., 2020. Constraining an Ocean Model Under Getz Ice Shelf, Antarctica, Using A Gravity-Derived Bathymetry. Geophysical Research Letters 47, e2019GL086522. doi:10.1029/2019GL086522.

Minchew, B.M., Meyer, C.R., Robel, A.A., Gudmundsson, G.H., Simons, M., 2018. Processes controlling the downstream evolution of ice rheology in glacier shear margins: case study on Rutford Ice Stream, West Antarctica. Journal of Glaciology 64, 583–594. doi:10.1017/jog.2018.47.

Minowa, M., Podolskiy, E.A., Sugiyama, S., 2019. Tide-modulated ice motion and seismicity of a floating glacier tongue in East Antarctica. Annals of Glaciology 60, 57–67. doi:10.1017/aog.2019.25.

Mohajerani, Y., Jeong, S., Scheuchl, B., Velicogna, I., Rignot, E., Milillo, P., 2021. Automatic delineation of glacier grounding lines in differential interferometric synthetic-aperture radar data using deep learning. Scientific Reports 11, 4992. doi:10.1038/s41598-021-84309-3.

Montagner, J.P., Mangeney, A., Stutzmann, E., 2020. Seismology and Environment, in: Gupta, H.K. (Ed.), Encyclopedia of Solid Earth Geophysics. Springer International Publishing, Cham, pp. 1–8. doi:10.1007/978-3-030-10475-7_258-1.

Montalbetti, J.F., Kanasewich, E.R., 1970. Enhancement of Teleseismic Body Phases with a Polarization Filter. Geophysical Journal International 21, 119–129. doi:10.1111/j.1365-246X.1970.tb01771.x.

Mordret, A., Grushin, A.G., 2025. Beating the aliasing limit with aperiodic monotile arrays. Physical Review Applied 23, 034021. doi:10.1103/PhysRevApplied.23.034021.

Mordret, A., Mikesell, T.D., Harig, C., Lipovsky, B.P., Prieto, G.A., 2016. Monitoring southwest Greenland's ice sheet melt with ambient seismic noise. Science Advances 2, e1501538. doi:10.1126/sciadv.1501538.

Morlighem, M., Rignot, E., Binder, T., Blankenship, D., Drews, R., Eagles, G., Eisen, O., Ferraccioli, F., Forsberg, R., Fretwell, P., Goel, V., Greenbaum, J.S., Gudmundsson, H., Guo, J., Helm, V., Hofstede, C., Howat, I., Humbert, A., Jokat, W.,

Karlsson, N.B., Lee, W.S., Matsuoka, K., Millan, R., Mouginot, J., Paden, J., Pattyn, F., Roberts, J., Rosier, S., Ruppel, A., Seroussi, H., Smith, E.C., Steinhage, D., Sun, B., Broeke, M.R.v.d., Ommen, T.D.v., Wessem, M.v., Young, D.A., 2020. Deep glacial troughs and stabilizing ridges unveiled beneath the margins of the Antarctic ice sheet. Nature Geoscience 13. doi:10.1038/s41561-019-0510-8.

Morlighem, M., Rignot, E., Seroussi, H., Larour, E., Ben Dhia, H., Aubry, D., 2010. Spatial patterns of basal drag inferred using control methods from a full-Stokes and simpler models for Pine Island Glacier, West Antarctica. Geophysical Research Letters 37. doi:10.1029/2010GL043853.

Motyka, R.J., Truffer, M., Fahnestock, M., Mortensen, J., Rysgaard, S., Howat, I., 2011. Submarine melting of the 1985 Jakobshavn Isbræ floating tongue and the triggering of the current retreat. Journal of Geophysical Research: Earth Surface 116. doi:10.1029/2009JF001632.

Mouginot, J., Rignot, E., Gim, Y., Kirchner, D., Meur, E.L., 2014. Low-frequency radar sounding of ice in East Antarctica and southern Greenland. Annals of Glaciology 55, 138–146. doi:10.3189/2014AoG67A089.

Mouginot, J., Rignot, E., Scheuchl, B., 2019. Continent-Wide, Interferometric SAR Phase, Mapping of Antarctic Ice Velocity. Geophysical Research Letters 46, 9710–9718. doi:10.1029/2019GL083826.

Murphy, B., Yurchak, R., Müller, S., 2024. GeoStat-Framework/PyKrige: v1.7.2. doi:10.5281/zenodo.11360184.

Métaxian, J.P., Araujo, S., Mora, M., Lesage, P., 2003. Seismicity related to the glacier of Cotopaxi Volcano, Ecuador. Geophysical Research Letters 30. doi:10.1029/2002GL016773.

Müller, C., Schlindwein, V., Eckstaller, A., Miller, H., 2005. Singing icebergs. Science (New York, N.Y.) 310, 1299. doi:10.1126/science.1117145.

Nakayama, Y., Cai, C., Seroussi, H., 2021. Impact of Subglacial Freshwater Discharge on Pine Island Ice Shelf. Geophysical Research Letters 48, e2021GL093923. doi:10.1029/2021GL093923.

Nanni, U., Gimbert, F., Roux, P., Lecointre, A., 2021. Observing the subglacial hydrology network and its dynamics with a dense seismic array. Proceedings of the National Academy of Sciences 118, e2023757118. doi:10.1073/pnas.2023757118.

Nanni, U., Roux, P., Gimbert, F., Lecointre, A., 2022. Dynamic Imaging of Glacier Structures at High-Resolution Using Source Localization With a Dense Seismic Array. Geophysical Research Letters 49, e2021GL095996. doi:10.1029/2021GL095996.

Nansen, F., 1897. The new year, 1896, in: Farthest north: Being the record of a voyage of exploration of the ship "Fram" 1893-96 and of a fifteen months' sleigh journey by Dr. Nansen and Lieut. Johansen, Vol. 2. Harper & Brothers, New York, NY, US, pp. 454–486. doi:10.1037/12900-008.

Nap, A., 2020. On the fidelity of Distributed Acoustic Sensing. Master's thesis. ETH Zürich, Switzerland.

Neave, K.G., Savage, J.C., 1970. Icequakes on the Athabasca Glacier. Journal of Geophysical Research (1896-1977) 75, 1351–1362. doi:10.1029/JB075i008p01351.

Nelder, J.A., Mead, R., 1965. A Simplex Method for Function Minimization. The Computer Journal 7, 308–313. doi:10.1093/comjnl/7.4.308.

Nettles, M., Ekström, G., 2010. Glacial Earthquakes in Greenland and Antarctica. Annual Review of Earth and Planetary Sciences 38, 467–491. doi:10.1146/annurev-earth-040809-152414.

Noble, T.L., Rohling, E.J., Aitken, A.R.A., Bostock, H.C., Chase, Z., Gomez, N., Jong, L.M., King, M.A., Mackintosh, A.N., McCormack, F.S., McKay, R.M., Menviel, L., Phipps, S.J., Weber, M.E., Fogwill, C.J., Gayen, B., Golledge, N.R., Gwyther, D.E., Hogg, A.M., Martos, Y.M., Pena-Molino, B., Roberts, J., van de Flierdt, T., Williams, T., 2020. The Sensitivity of the Antarctic Ice Sheet to a Changing Climate: Past, Present, and Future. Reviews of Geophysics 58, e2019RG000663. doi:10.1029/2019RG000663.

Nowicki, S.M.J., Payne, A., Larour, E., Seroussi, H., Goelzer, H., Lipscomb, W., Gregory, J., Abe-Ouchi, A., Shepherd, A., 2016. Ice Sheet Model Intercomparison Project (ISMIP6) contribution to CMIP6. Geoscientific Model Development 9, 4521–4545. doi:10.5194/gmd-9-4521-2016.

Okal, E.A., MacAyeal, D.R., 2006. Seismic Recording on Drifting Icebergs: Catching Seismic Waves, Tsunamis and Storms from Sumatra and Elsewhere. .

Olivier, G., Brenguier, F., Campillo, M., Roux, P., Shapiro, N.M., Lynch, R., 2015. Investigation of coseismic and postseismic processes using in situ measurements of seismic velocity variations in an underground mine. Geophysical Research Letters 42, 9261–9269. doi:10.1002/2015GL065975.

O'Neel, S., Pfeffer, W.T., 2007. Source mechanics for monochromatic icequakes produced during iceberg calving at Columbia Glacier, AK. Geophysical Research Letters 34. doi:10.1029/2007GL031370.

Oppenheimer, M., Glavovic, B., Hinkel, J., van de Wal, R., Magnan, A.K., Abd-Elgawad, A., Cai, R., Cifuentes-Jara, M., Deconto, R.M., Ghosh, T., Hay, J., Isla, F., Marzeion, B., Meyssignac, B., Sebesvari, Z., 2019. Sea Level Rise and Implications for Low Lying Islands, Coasts and Communities .

Osten-Woldenburg, H.V.D., 1990. Icequakes On Ekström Ice Shelf Near Atka Bay, Antarctica. Journal of Glaciology 36, 31–36. doi:10.3189/S0022143000005517.

Padman, L., Siegfried, M.R., Fricker, H.A., 2018. Ocean Tide Influences on the Antarctic and Greenland Ice Sheets. Reviews of Geophysics 56, 142–184. doi:10.1002/2016RG000546.

Paolo, F.S., Fricker, H.A., Padman, L., 2015. Volume loss from Antarctic ice shelves is accelerating | Science.

Parizek, B.R., 2024. Grounding Zones: The "Inland" Dynamic Interface Between Seawater, Outlet Glaciers, Subglacial Meltwater Routing, and Ice-Shelf Processes. Geophysical Research Letters 51, e2024GL110427. doi:10.1029/2024GL110427.

Pattyn, F., 2018. The paradigm shift in Antarctic ice sheet modelling. Nature Communications 9, 2728. doi:10.1038/s41467-018-05003-z.

Pattyn, F., Favier, L., Sun, S., Durand, G., 2017. Progress in Numerical Modeling of Antarctic Ice-Sheet Dynamics. Current Climate Change Reports 3, 174–184. doi:10.1007/s40641-017-0069-7.

Peterson, J.R., 1993. Observations and modeling of seismic background noise. Technical Report 93-322. U.S. Geological Survey. doi:10.3133/ofr93322.

Pirli, M., Hainzl, S., Schweitzer, J., Köhler, A., Dahm, T., 2018. Localised thickening and grounding of an Antarctic ice shelf from tidal triggering and sizing of cryoseismicity. Earth and Planetary Science Letters 503, 78–87. doi:10.1016/j.epsl.2018.09.024.

Pirot, E., Hibert, C., Mangeney, A., 2024. Enhanced glacial earthquake catalogues with supervised machine learning for more comprehensive analysis. Geophysical Journal International 236, 849–871. doi:10.1093/gji/ggad402.

Podolskiy, E.A., Walter, F., 2016. Cryoseismology. Reviews of Geophysics 54, 708–758. doi:10.1002/2016RG000526.

Prakash, A., Zhou, Q., Hattermann, T., Bao, W., Graversen, R., Kirchner, N., 2022. A nested high-resolution unstructured grid 3-D ocean-sea ice-ice shelf setup for numerical investigations of the Petermann ice shelf and fjord. MethodsX 9, 101668. doi:10.1016/j.mex.2022.101668.

Pratt, M.J., Winberry, J.P., Wiens, D.A., Anandakrishnan, S., Alley, R.B., 2014. Seismic and geodetic evidence for grounding-line control of Whillans Ice Stream stick-slip events. Journal of Geophysical Research: Earth Surface 119, 333–348. doi:10.1002/2013JF002842.

Preiswerk, L.E., Walter, F., 2018. High-Frequency (>2 Hz) Ambient Seismic Noise on High-Melt Glaciers: Green's Function Estimation and Source Characterization. Journal of Geophysical Research: Earth Surface 123, 1667–1681. doi:10.1029/2017JF004498.

Pritchard, H.D., Fretwell, P.T., Fremand, A.C., Bodart, J.A., Kirkham, J.D., Aitken, A., Bamber, J., Bell, R., Bianchi, C., Bingham, R.G., Blankenship, D.D., Casassa, G., Christianson, K., Conway, H., Corr, H.F.J., Cui, X., Damaske, D., Damm, V., Dorschel, B., Drews, R., Eagles, G., Eisen, O., Eisermann, H., Ferraccioli, F., Field, E., Forsberg, R., Franke, S., Goel, V., Gogineni, S.P., Greenbaum, J., Hills, B., Hindmarsh, R.C.A., Hoffman, A.O., Holschuh, N., Holt, J.W., Humbert, A., Jacobel, R.W., Jansen, D., Jenkins, A., Jokat, W., Jong, L., Jordan, T.A., King, E.C., Kohler, J., Krabill, W., Maton, J., Gillespie, M.K., Langley, K., Lee, J., Leitchenkov, G., Leuschen, C., Luyendyk, B., MacGregor, J.A., MacKie, E., Moholdt, G., Matsuoka, K., Morlighem, M., Mouginot, J., Nitsche, F.O., Nost, O.A., Paden, J., Pattyn, F., Popov, S., Rignot, E., Rippin, D.M., Rivera, A., Roberts, J.L., Ross, N., Ruppel, A., Schroeder, D.M., Siegert, M.J., Smith, A.M., Steinhage, D., Studinger, M., Sun, B., Tabacco, I., Tinto, K.J., Urbini, S., Vaughan, D.G., Wilson, D.S., Young, D.A., Zirizzotti, A., 2025. Bedmap3 updated ice bed, surface and thickness gridded datasets for Antarctica. Scientific Data 12, 414. doi:10.1038/s41597-025-04672-y.

Pritchard, H.D., Ligtenberg, S.R.M., Fricker, H.A., Vaughan, D.G., van den Broeke, M.R., Padman, L., 2012. Antarctic ice-sheet loss driven by basal melting of ice shelves. Nature 484, 502–505. doi:10.1038/nature10968.

Provost, F., Zigone, D., Le Meur, E., Malet, J.P., Hibert, C., 2024. Surface dynamics and history of the calving cycle of Astrolabe Glacier (Adélie Coast, Antarctica) derived from satellite imagery. The Cryosphere 18, 3067–3079. doi:10.5194/tc-18-3067-2024.

Qamar, A., 1988. Calving icebergs: A source of low-frequency seismic signals from Columbia Glacier, Alaska. Journal of Geophysical Research 93, 6615–6623. doi:10.1029/JB093iB06p06615.

Rack, W., King, M.A., Marsh, O.J., Wild, C.T., Floricioiu, D., 2017. Analysis of ice shelf flexure and its InSAR representation in the grounding zone of the southern McMurdo Ice Shelf. The Cryosphere 11, 2481–2490. doi:10.5194/tc-11-2481-2017.

Reeh, N., Christensen, E.L., Mayer, C., Olesen, O.B., 2003. Tidal bending of glaciers: a linear viscoelastic approach. Annals of Glaciology 37, 83–89. doi:10.3189/172756403781815663.

Reese, R., Gudmundsson, G.H., Levermann, A., Winkelmann, R., 2018. The far reach of ice-shelf thinning in Antarctica. Nature Climate Change 8, 53–57. doi:10.1038/s41558-017-0020-x.

Rignot, Mouginot, J., Scheuchl, B., van den Broeke, M., van Wessem, M.J., Morlighem, M., 2019. Four decades of Antarctic Ice Sheet mass balance from 1979–2017. Proceedings of the National Academy of Sciences 116, 1095–1103. doi:10.1073/pnas.1812883116.

Rignot, E., 2023. Observations of grounding zones are the missing key to understand ice melt in Antarctica. Nature Climate Change 13, 1010–1013. doi:10.1038/s41558-023-01819-w.

Rignot, E., Chauche, N., Gadi, R., Ehrenfeucht, S., Ciraci, E., 2025. Grounding Line Remote Operated Vehicle (GROV) Survey of the Ice Shelf Cavity of Petermann Glacier, Greenland. Geophysical Research Letters 52, e2024GL113400. doi:10.1029/2024GL113400.

Rignot, E., Ciracì, E., Scheuchl, B., Tolpekin, V., Wollersheim, M., Dow, C., 2024. Widespread seawater intrusions beneath the grounded ice of Thwaites Glacier, West Antarctica. Proceedings of the National Academy of Sciences 121, e2404766121. doi:10.1073/pnas.2404766121.

Rignot, E., Jacobs, S., Mouginot, J., Scheuchl, B., 2013. Ice-Shelf Melting Around Antarctica. Science 341, 266–270. doi:10.1126/science.1235798.

Rignot, E., Koppes, M., Velicogna, I., 2010. Rapid submarine melting of the calving faces of West Greenland glaciers. Nature Geoscience 3, 187–191. doi:10.1038/ngeo765.

Rignot, E., Mouginot, J., Morlighem, M., Seroussi, H., Scheuchl, B., 2014. Widespread, rapid grounding line retreat of Pine Island, Thwaites, Smith, and Kohler glaciers, West Antarctica, from 1992 to 2011. Geophysical Research Letters 41, 3502–3509. doi:10.1002/2014GL060140.

Rignot, E., Mouginot, J., Scheuchl, B., 2011a. Antarctic Grounding Line Mapping from Differential Satellite Radar Interferometry. Geophys. Res. Lett. 38. doi:10.1029/2011GL047109.

Rignot, E., Mouginot, J., Scheuchl, B., 2011b. Ice Flow of the Antarctic Ice Sheet. Science 333, 1427–1430. doi:10.1126/science.1208336.

Rimpot, J., Hibert, C., Malet, J.P., Forestier, G., Weber, J., 2025. Self-Supervised Learning Based Clustering Workflow for Exploring Seismological Data From Dense Networks. Journal of Geophysical Research: Machine Learning and Computation 2, e2025JH000958. doi:10.1029/2025JH000958.

Robel, A.A., Tsai, V.C., Minchew, B., Simons, M., 2017. Tidal modulation of ice shelf buttressing stresses. Annals of Glaciology 58, 12–20. doi:10.1017/aog.2017.22.

Roeoesli, C., Helmstetter, A., Walter, F., Kissling, E., 2016. Meltwater influences on deep stick-slip icequakes near the base of the Greenland Ice Sheet: DEEP STICK-SLIP ICEQUAKES OF THE GRIS. Journal of Geophysical Research: Earth Surface 121, 223–240. doi:10.1002/2015JF003601.

Rost, S., Thomas, C., 2002. Array Seismology: Methods and Applications. Reviews of Geophysics 40, 2–1–2–27. doi:10.1029/2000RG000100.

Rousseau, H., Gaume, J., Blatny, L., Lüthi, M.P., 2024. Transition Between Mechanical and Geometric Controls in Glacier Crevassing Processes. Geophysical Research Letters 51, e2024GL108206. doi:10.1029/2024GL108206.

Röthlisberg, H., 1955. Studies in Glacier Physics on the Penny Ice Cap, Baffin Island, 1953: Part III: Seismic Sounding. Journal of Glaciology 2, 539–552. doi:10.3189/002214355793702064.

Röthlisberger, H., 1972. Water Pressure in Intra- and Subglacial Channels. Journal of Glaciology 11, 177–203. doi:10.3189/S0022143000022188.

Röösli, C., Walter, F., Husen, S., Andrews, L.C., Lüthi, M.P., Catania, G.A., Kissling, E., 2014. Sustained seismic tremors and icequakes detected in the ablation zone of the Greenland ice sheet. Journal of Glaciology 60, 563–575. doi:10.3189/2014JoG13J210.

Santin, I., Colucci, R.R., Žebre, M., Pavan, M., Cagnati, A., Forte, E., 2019. Recent evolution of Marmolada glacier (Dolomites, Italy) by means of ground and airborne GPR surveys. Remote Sensing of Environment 235, 111442. doi:10.1016/j.rse.2019.111442.

Schoof, C., 2005. The Effect of Cavitation on Glacier Sliding. Proceedings: Mathematical, Physical and Engineering Sciences 461, 609–627.

Schoof, C., 2007. Ice sheet grounding line dynamics: Steady states, stability, and hysteresis. Journal of Geophysical Research: Earth Surface 112. doi:10.1029/2006JF000664.

Schröder, L., Richter, A., Fedorov, D.V., Eberlein, L., Brovkov, E.V., Popov, S.V., Knöfel, C., Horwath, M., Dietrich, R., Matveev, A.Y., Scheinert, M., Lukin, V.V., 2017. Validation of satellite altimetry by kinematic GNSS in central East Antarctica. The Cryosphere 11, 1111–1130. doi:10.5194/tc-11-1111-2017.

Schulte-Pelkum, V., Blackman, D.K., 2003. A synthesis of seismic P and S anisotropy. Geophysical Journal International 154, 166–178. doi:10.1046/j.1365-246X.2003.01951.x.

Sens-Schönfelder, C., Wegler, U., 2006. Passive image interferometry and seasonal variations of seismic velocities at Merapi Volcano, Indonesia. Geophysical Research Letters 33. doi:10.1029/2006GL027797.

Sergeant, A., Chmiel, M., Lindner, F., Walter, F., Roux, P., Chaput, J., Gimbert, F., Mordret, A., 2020. On the Green's function emergence from interferometry of seismic wave fields generated in high-melt glaciers: implications for passive imaging and monitoring. The Cryosphere 14, 1139–1171. doi:10.5194/tc-14-1139-2020.

Sergeant, A., Mangeney, A., Stutzmann, E., Montagner, J.P., Walter, F., Moretti, L., Castelnau, O., 2016. Complex force history of a calving-generated glacial earthquake derived from broadband seismic inversion. Geophysical Research Letters 43, 1055–1065. doi:10.1002/2015GL066785.

Sergeant, A., Yastrebov, V.A., Mangeney, A., Castelnau, O., Montagner, J.P., Stutzmann, E., 2018. Numerical Modeling of Iceberg Capsizing Responsible for Glacial Earthquakes. Journal of Geophysical Research: Earth Surface 123, 3013–3033. doi:10.1029/2018JF004768.

Sergienko, O.V., MacAyeal, D.R., Bindschadler, R.A., 2009. Stick–slip behavior of ice streams: modeling investigations. Annals of Glaciology 50, 87–94. doi:10.3189/172756409789624274.

Shapiro, N.M., Campillo, M., 2004. Emergence of broadband Rayleigh waves from correlations of the ambient seismic noise. Geophysical Research Letters 31. doi:10.1029/2004GL019491.

Shapiro, N.M., Campillo, M., Stehly, L., Ritzwoller, M.H., 2005. High-resolution surface-wave tomography from ambient seismic noise. Science (New York, N.Y.) 307, 1615–1618. doi:10.1126/science.1108339.

Shepherd, A., Wingham, D., Rignot, E., 2004. Warm ocean is eroding West Antarctic Ice Sheet. Geophysical Research Letters 31. doi:10.1029/2004GL021106.

Smith, A.M., 2006. Microearthquakes and subglacial conditions. Geophysical Research Letters 33. doi:10.1029/2006GL028207.

Smith, E.C., Baird, A.F., Kendall, J.M., Martín, C., White, R.S., Brisbourne, A.M., Smith, A.M., 2017. Ice fabric in an Antarctic ice stream interpreted from seismic anisotropy. Geophysical Research Letters 44, 3710–3718. doi:10.1002/2016GL072093.

Smith, E.C., Smith, A.M., White, R.S., Brisbourne, A.M., Pritchard, H.D., 2015. Mapping the ice-bed interface characteristics of Rutford Ice Stream, West Antarctica, using microseismicity. Journal of Geophysical Research: Earth Surface 120, 1881–1894. doi:10.1002/2015JF003587.

Stanton, T.P., Shaw, W.J., Truffer, M., Corr, H.F.J., Peters, L.E., Riverman, K.L., Bindschadler, R., Holland, D.M., Anandakrishnan, S., 2013. Channelized Ice Melting in the Ocean Boundary Layer Beneath Pine Island Glacier, Antarctica. Science 341, 1236–1239. doi:10.1126/science.1239373.

Stephenson, S.N., 1984. Glacier Flexure and the Position of Grounding Lines: Measurements By Tiltmeter on Rutford Ice Stream, Antarctica. Annals of Glaciology 5, 165–169. doi:10.3189/1984AoG5-1-165-169.

Stuart, G., Murray, T., Brisbourne, A., Styles, P., Toon, S., 2005. Seismic emissions from a surging glacier: Bakaninbreen, Svalbard. Annals of Glaciology 42, 151–157. doi:10.3189/172756405781812538.

Stutzmann, E., Schimmel, M., Patau, G., Maggi, A., 2009. Global climate imprint on seismic noise. Geochemistry, Geophysics, Geosystems 10, 2009GC002619. doi:10.1029/2009GC002619.

Thelen, W.A., Allstadt, K., Angelis, S.D., Malone, S.D., Moran, S.C., Vidale, J., 2013. Shallow repeating seismic events under an alpine glacier at Mount Rainier, Washington, USA. Journal of Glaciology 59, 345–356. doi:10.3189/2013JoG12J111.

Thomas, R., Rignot, E., Casassa, G., Kanagaratnam, P., Acuña, C., Akins, T., Brecher, H., Frederick, E., Gogineni, P., Krabill, W., Manizade, S., Ramamoorthy, H., Rivera, A., Russell, R., Sonntag, J., Swift, R., Yungel, J., Zwally, J., 2004. Accelerated Sea-Level Rise from West Antarctica. Science 306, 255–258. doi:10.1126/science.1099650.

Tinto, K.J., Bell, R.E., 2011. Progressive unpinning of Thwaites Glacier from newly identified offshore ridge: Constraints from aerogravity. Geophysical Research Letters 38. doi:10.1029/2011GL049026.

Tinto, K.J., Padman, L., Siddoway, C.S., Springer, S.R., Fricker, H.A., Das, I., Caratori Tontini, F., Porter, D.F., Frearson, N.P., Howard, S.L., Siegfried, M.R., Mosbeux, C., Becker, M.K., Bertinato, C., Boghosian, A., Brady, N., Burton, B.L., Chu, W., Cordero, S.I., Dhakal, T., Dong, L., Gustafson, C.D., Keeshin, S., Locke, C., Lockett, A., O'Brien, G., Spergel, J.J., Starke, S.E., Tankersley, M., Wearing, M.G., Bell, R.E., 2019. Ross Ice Shelf response to climate driven by the tectonic imprint on seafloor bathymetry. Nature Geoscience 12, 441–449. doi:10.1038/s41561-019-0370-2.

Tulaczyk, S., Kamb, W.B., Engelhardt, H.F., 2000. Basal mechanics of Ice Stream B, west Antarctica: 2. Undrained plastic bed model. Journal of Geophysical Research: Solid Earth 105, 483–494. doi:10.1029/1999JB900328.

Turner, J., Anderson, P., Lachlan-Cope, T., Colwell, S., Phillips, T., Kirchgaessner, A., Marshall, G.J., King, J.C., Bracegirdle, T., Vaughan, D.G., Lagun, V., Orr, A., 2009a. Record low surface air temperature at vostok station, antarctica 114. doi:10.1029/2009JD012104.

Turner, J., Bindschadler, R., Convey, P., Di Prisco, G., Fahrbach, E., Gutt, J., Hodgson, D., Mayewski, P.A., Summerhayes, C.P., 2009b. Antarctic climate change and the environment: a contribution to the international polar year 2007 - 2008.

VanWormer, D., Berg, E., 1973. Seismic Evidence for Glacier Motion. Journal of Glaciology 12, 259–265. doi:10.3189/S002214300003207X.

Vaughan, D.G., 1994. Investigating tidal flexure on an ice shelf using kinematic GPS. Annals of Glaciology 20, 372–376. doi:10.3189/1994AoG20-1-372-376.

Vaughan, D.G., 1995. Tidal flexure at ice shelf margins. Journal of Geophysical Research: Solid Earth 100, 6213–6224. doi:10.1029/94JB02467.

van der Veen, C.J., 1998. Fracture mechanics approach to penetration of bottom crevasses on glaciers. Cold Regions Science and Technology 27, 213–223. doi:10.1016/S0165-232X(98)00006-8.

van der Veen, C.J., 2002. Calving glaciers. Progress in Physical Geography 26, 96–122. doi:10.1191/0309133302pp327ra.

Van der Veen, C.J.V.D., Plummer, J.C., Stearns, L.A., 2011. Controls on the recent speed-up of Jakobshavn Isbræ, West Greenland. Journal of Glaciology 57, 770–782. doi:10.3189/002214311797409776.

Veitch, S.A., Karplus, M., Kaip, G., Gonzalez, L.F., Amundson, J.M., Bartholomaus, T.C., 2021. Ice thickness estimates of Lemon Creek Glacier, Alaska, from active-source seismic imaging. Journal of Glaciology 67, 824–832. doi:10.1017/jog.2021.32.

Vieli, A., 2011. Tidewater Glaciers, in: Encyclopedia of Snow, Ice and Glaciers. Springer, Dordrecht, pp. 1175–1179. doi:10.1007/978-90-481-2642-2_579.

Wadhams, P., 2014. Ice in the Ocean. CRC Press, London. doi:10.1201/9781482283082.

Walker, R.T., Parizek, B.R., Alley, R.B., Anandakrishnan, S., Riverman, K.L., Christianson, K., 2013. Ice-shelf tidal flexure and subglacial pressure variations. Earth and Planetary Science Letters 361, 422–428. doi:10.1016/j.epsl.2012.11.008.

Walter, F., Clinton, J.F., Deichmann, N., Dreger, D.S., Minson, S.E., Funk, M., 2009. Moment Tensor Inversions of Icequakes on Gornergletscher, Switzerland. Bulletin of the Seismological Society of America 99, 852–870. doi:10.1785/0120080110.

Walter, F., Roux, P., Roeoesli, C., Lecointre, A., Kilb, D., Roux, P.F., 2015a. Using glacier seismicity for phase velocity measurements and Green's function retrieval. Geophysical Journal International 201, 1722–1737. doi:10.1093/gji/ggv069.

Walter, J.I., Svetlizky, I., Fineberg, J., Brodsky, E.E., Tulaczyk, S., Grace Barcheck, C., Carter, S.P., 2015b. Rupture speed dependence on initial stress profiles: Insights from glacier and laboratory stick-slip. Earth and Planetary Science Letters 411, 112–120. doi:10.1016/j.epsl.2014.11.025.

WCRP Global Sea Level Budget Group, 2018. Global sea-level budget 1993–present. Earth System Science Data 10, 1551–1590. doi:10.5194/essd-10-1551-2018.

Weaver, C.S., Malone, S.D., 1979. Seismic Evidence for Discrete Glacier Motion at the Rock–Ice Interface. Journal of Glaciology 23, 171–184. doi:10.3189/S0022143000029816.

Weertman, J., 1957. On the Sliding of Glaciers. Journal of Glaciology 3, 33–38. doi:10.3189/S0022143000024709.

van Wessem, J.M., van de Berg, W.J., Noël, B.P.Y., van Meijgaard, E., Amory, C., Birnbaum, G., Jakobs, C.L., Krüger, K., Lenaerts, J.T.M., Lhermitte, S., Ligtenberg, S.R.M., Medley, B., Reijmer, C.H., van Tricht, K., Trusel, L.D., van Ulft, L.H., Wouters, B., Wuite, J., van den Broeke, M.R., 2018. Modelling the climate and surface mass balance of polar ice sheets using RACMO2 – Part 2: Antarctica (1979–2016). The Cryosphere 12, 1479–1498. doi:10.5194/tc-12-1479-2018.

Wild, C.T., Snow, T., Dotto, T.S., Davis, P.E.D., Tyler, S., Scambos, T.A., Pettit, E.C., Heywood, K.J., 2025. Thwaites Eastern Ice Shelf cavity observations reveal multiyear sea ice dynamics and deepwater warming in Pine Island Bay, West Antarctica. Ocean Science 21, 2605–2629. doi:10.5194/os-21-2605-2025.

Wille, J.D., Favier, V., Gorodetskaya, I.V., Agosta, C., Kittel, C., Beeman, J.C., Jourdain, N.C., Lenaerts, J.T.M., Codron, F., 2021. Antarctic Atmospheric River Climatology and Precipitation Impacts. Journal of Geophysical Research: Atmospheres 126, e2020JD033788. doi:10.1029/2020JD033788.

Winberry, J., Anandakrishnan, S., Wiens, D.A., Alley, R.B., 2013. Nucleation and seismic tremor associated with the glacial earthquakes of Whillans Ice Stream, Antarctica. Geophysical Research Letters 40, 312–315. doi:10.1002/grl.50130.

Winberry, J.P., Anandakrishnan, S., Alley, R.B., 2009. Seismic observations of transient subglacial water-flow beneath MacAyeal Ice Stream, West Antarctica. Geophysical Research Letters 36, L11502. doi:10.1029/2009GL037730.

Winder, T., Bacon, C.A., Smith, J.D., Hudson, T.S., White, R.S., 2025. QuakeMigrate: a Python Package for Automatic Earthquake Detection and Location Using Waveform Migration and Stacking (preprint) .

Wittlinger, G., Farra, V., 2012. Observation of low shear wave velocity at the base of the polar ice sheets: evidence for enhanced anisotropy. Geophysical Journal International 190, 391–405. doi:10.1111/j.1365-246X.2012.05474.x.

Wolf, L.W., Davies, J.N., 1986. Glacier-generated earthquakes from Prince William Sound, Alaska. Bulletin of the Seismological Society of America 76, 367–379. doi:10.1785/BSSA0760020367.

Wåhlin, A., Alley, K.E., Begeman, C., Hegrenæs, , Yuan, X., Graham, A.G.C., Hogan, K., Davis, P.E.D., Dotto, T.S., Eayrs, C., Hall, R.A., Holland, D.M., Kim, T.W., Larter, R.D., Ling, L., Muto, A., Pettit, E.C., Schmidt, B.E., Snow, T., Stedt, F., Washam, P.M., Wahlgren, S., Wild, C., Wellner, J., Zheng, Y., Heywood, K.J., 2024. Swirls and scoops: Ice base melt revealed by multibeam imagery of an Antarctic ice shelf. Science Advances 10, eadn9188. doi:10.1126/sciadv.adn9188.

Yan, P., Holland, D.M., Tsai, V.C., Vaňková, I., Xie, S., 2024. Tidally Modulated Glacial Slip and Tremor at Helheim Glacier, Greenland. Geophysical Research Letters 51, e2023GL105342. doi:10.1029/2023GL105342.

Zhan, Z., 2019a. Distributed Acoustic Sensing Turns Fiber-Optic Cables into Sensitive Seismic Antennas. Seismological Research Letters 91, 1–15. doi:10.1785/0220190112.

Zhan, Z., 2019b. Seismic Noise Interferometry Reveals Transverse Drainage Configuration Beneath the Surging Bering Glacier. Geophysical Research Letters 46, 4747–4756. doi:10.1029/2019GL082411.

Zoet, L.K., Anandakrishnan, S., Alley, R.B., Nyblade, A.A., Wiens, D.A., 2012. Motion of an Antarctic glacier by repeated tidally modulated earthquakes. Nature Geoscience 5, 623–626. doi:10.1038/ngeo1555.

Zwally, H.J., Abdalati, W., Herring, T., Larson, K., Saba, J., Steffen, K., 2002. Surface Melt-Induced Acceleration of Greenland Ice-Sheet Flow. Science 297, 218–222. doi:10.1126/science.1072708.

List of Figures

1.1 An orthographic projection of NASA's Blue Marble data set (1 km resolution global satellite composite). MODIS observations of polar sea ice were combined with observations of Antarctica made by the National Oceanic and Atmospheric Administration's AVHRR sensor-the Advanced Very High Resolution Radiometer. 2

1.2 (a) Bed topography and (b) Surface elevation, in metres above sea level, and (c) Ice thickness in metres of Antarctica from Bedmap3 (Pritchard et al., 2025). 4

1.3 Complete map of ice motion in Antarctica, with speed colored on a logarithmic scale from brown (less than 1 m/year) to red (more than 3 km/year) and flow direction indicated by colored lines and showing the flow pattern of ice across the continent (Mouginot et al., 2019). 5

1.4 Illustration of the mass balance components and their key processes to assess the ice mass balance of ice sheets. Adapted from Nowicki et al. (2016). . . . 6

1.5 (left) Discovery of Adélie Land by Jules Dumont d'Urville. Picture from "Voyage illustré dans les cinq parties du monde" by Adolphe Joanne, published around 1850. (right) Picture of two scientists looking at the icebergs in front of the Astrolabe Glacier from Curie island, in Terre Adélie. Picture from the 2024 SEIS-ADELICE campaign in Dumont d'Urville. 7

1.6 Schematic representation of 2 major marine-terminating glacier morphology: (a) Marine-terminating glacier with a floating terminus. (b) Marine-terminating glacier with a grounded terminus. The grounding line, indicated in panel (a), is the virtual limit from the glacier being grounded on the bedrock to floating on the ocean. The two sketches are not to scale. A similar thickness can be expected between the front of the floating glacier and the grounded glacier. 10

1.7 (a) Schematic representation of the key structural features of a grounding zone. F is the landward limit of ice flexure from tidal movement. G is the latest point of contact between the ice and the ground, i.e. the grounding line. I_b is the break-in-slope. I_m is the local elevation minimum and H is the landward limit of the hydrostatic zone of free-floating ice. It corresponds also to the seaward limit of ice flexure. Note that the distance between F, G, I_b, I_m and H depends on local ice thickness and properties, and local bedrock topography and properties. Adapted from Fricker et al. (2009). (b) Schematic representation of a grounding zone showing migration of the grounding line position (G) between high tide (Gmax) and low tide (Gmin) across a simplified semidiurnal tidal cycle over 24 hours. Adapted from Freer et al. (2023). 11

1.8 Schematic representation of key processes leading to rapid ice loss at marine-terminating glaciers. Modified from Pattyn et al. (2017). 12

1.9 Overview of cryoseismic sources in a marine-terminating glacier environment. These sources come from processes at the glacier ice-bedrock, glacier ice - slow moving ice, glacier ice - ocean, and iceberg-ocean interfaces. 24

1.10 Example of icequake cryoseismicity recorded by a broadband seismic station deployed on the surface of the Astrolabe Glacier, a marine-terminating outlet glacier with a floating terminus in Terre Adélie, East Antarctica. The icequake was recorded on Jan. 18, 2022 by station AST08, positioned near the grounding zone. (a) Three-component seismogram (Vertical, East, North) of an icequake event, lasting approximately 1 second. (b) Three-hour segment of continuous seismic data highlighting the numerous high-amplitude icequakes. For both panels, the instrumental response is removed and a bandpass filtered between 10 Hz and 50 Hz is applied. (c) Frequency analysis of the vertical component of the event shown in (a) using Fast Fourier Transform (FFT), revealing dominant spectral energy between 10 Hz and 30 Hz, with energy extending up to 60 Hz. 26

1.11 Example of a "stick-slip" event recorded on Jan. 16, 2023 by a seismic node (07x04, dense array A1) deployed on the surface of the Astrolabe Glacier, a marine-terminating outlet glacier with a floating terminus in Terre Adélie, East Antarctica. (a) Three-component seismogram (Vertical, East, North) of a "stick-slip" event, lasting 0.6 seconds. (b) Six-hour segment of continuous seismic data highlighting the high number of "stick-slip" events. For both panels, the instrumental response is removed and a bandpass filtered between 10 Hz and 200 Hz is applied. (c) Frequency analysis of the vertical component of the event shown in (a) using Fast Fourier Transform (FFT), revealing dominant spectral energy between 10 Hz and 225 Hz. 28

1.12 Example of a calving event recorded by a seismic station near the front of the Astrolabe Glacier, a marine-terminating outlet glacier with a floating terminus in Terre Adélie, East Antarctica. The broadband seismic station AST14 was installed on Curie Island, located in the Pointe Géologique Archipelago near the French research station Dumont d'Urville. (a) Seismic waveform of the calving event recorded on the three components (Vertical, East, North). The event occurred on Jan. 18 2024 at 03:18:52 UTC. (b) Spectrogram for the corresponding time window, showing the signal energy distribution. (c) Frequency content spectrum using a Fast Fourier Transform (FFT), showing the spectral characteristics of the event. The calving signal lasts approximately 10 seconds, with dominant energy between 3 Hz and 5 Hz and broader energy extending from approximately 1 Hz to 20 Hz. Note that the instrument response has been removed on all plots. 31

2.1 (a) Map of Antarctica highlighting the location of Wilkes Land (light green) and Terre Adélie (red). The positions of the French research stations Dumont d'Urville (DDU) and Concordia (a joint French–Italian station) are also indicated. (b) Detailed map of the Pointe Géologie Archipelago, showing the scientific and logistical bases Cap Prud'Homme (CPH) and DDU, and Curie and Gouverneur islands. 37

2.2 (a) High-resolution satellite image of the Astrolabe Glacier, acquired by Pleiades on 10th January, 2025. The position of the grounding line from (Le Meur et al., 2014) is displayed in light grey. (b) Surface ice velocity map of the Astrolabe Glacier (Provost et al., 2024). The map highlights a sharp lateral velocity gradient between the slow-moving ice (in purple) and the fast-flowing glacier (in blue), indicating the location of shear margins, and a distinct acceleration near the glacier front, associated with active calving processes. . . 38

2.3 Surface imagery of the Astrolabe Glacier with zoom-ins on visible features hinting at distinct glacier structural elements. (1) Heavily crevassed calving front. (2) Right lateral shear margin showing important surface deformation. (3) Central glacier zone exhibiting complex surface crevassing. (4) Left lateral shear margin characterized by two intersecting crevasse fields, where a secondary ice flow is merging with the shear margin. (5) Upper right lateral shear margin, featuring narrow, linear crevasses adjacent to a more chaotic, heavily deformed surface. The background image is a Pleiades satellite acquisition from January 10, 2025. 39

2.4 Thirty days of sea-level records from the DUMON tide gauge at DDU. The data capture two spring tides and two neap tides within a monthly tidal cycle (from 2022, December 21th to 2023, January 20th). The daily tidal cycle predominantly follows a mixed diurnal pattern, characterized by a dominant tidal amplitude of $\sim 1.5 - 2m$ (low to high) and a secondary amplitude peak of $\sim 20cm$. Occasional diurnal cycles are also observed (e.g., on days 27–29). 40

2.5 Map of seismic deployments conducted during the SEIS-ADELICE project (2020-2025). 43

3.1 Influence of STA/LTA parameters on the detection of an icequake. (a) Waveform of an icequake recorded on the vertical component.(b) Comparison between different STA/LTA parameters. The trigger-on and trigger-off thresholds are set to 5 and 2, respectively. Black curve: STA=0.5 s, LTA=5 s. The ratio rises well above the trigger-on threshold and drops below the trigger-off threshold at the end of the event, correctly capturing its duration. Purple curve: STA=0.9 s, LTA=5 s. The ratio barely exceeds the trigger-on threshold and decays too slowly, failing to match the actual event duration. This occurs because the STA window is longer than the event itself, reducing sensitivity. Green curve: STA=0.5 s, LTA=1 s. The ratio never reaches the trigger-on threshold. Here, the LTA window is too short, so background noise is strongly influenced by the signal itself. Both the STA and LTA amplitudes are increasing, keeping the ratio curve below the threshold and preventing proper detection. Parameters of the black curve are those kept for the detections of icequakes in future analyses. The icequake waveform shown for example is from station 01x07 of dense array A1. 48

3.2 Icequake detection at station 01x07, on 18th January, 2023. (a) Vertical seismogram, filtered between 10 and 100 Hz, showing the numerous icequakes appearing as impulsive events. (b) Zoom on 10 minutes-long seismogram of the vertical component, displaying the detected icequakes marked by the red dotted lines. (c) Example of a 1 s-long detected icequake with indication of the STA/LTA ratio threshold triggers for the start (green) and the end (purple) of the event. (d) Comparison between the occurrence of icequakes detected at station 01x07 (black curve, in count per hour) and the tide amplitude (red curve, in meters) during the period Jan, 18 to 22. 49

3.3 Template matching applied on seismic data from the node 34x08 of the dense array A3 on Jan. 21, 2025. (a) Template of a “stick-slip” event used for the template matching detector. (b) (bottom) Two hours of seismic records with repetitive “stick-slip” events detected by template matching colored in red. (top) Correlation coefficient for each detection over the seismic record. Only events with a correlation coefficient superior to 0.65 are displayed. 51

3.4 Results of the template-matching detection algorithm applied to station 34X08 (A3) using the template presented in Fig. 3.3a (a) Stack of 150 detected event waveforms (grey curves) for the three seismic components, with the mean seismic trace superimposed (blue curve). (b) Distribution of the correlation coefficients associated with the 150 waveforms shown in (a). Coefficients are distributed into two groups, with events with correlation coefficient above 0.90, translating strong matching with the template and events with correlation coefficient between 0.65 and 0.85 where matching is probably weaker. . 52

3.5 Examples of template-matching detections illustrating the limitations of the method and the importance of manual verification and careful selection of the correlation coefficient threshold. (a) Example of a correctly identified stick-slip event (green curve) that closely matches the mean trace, with a correlation coefficient of 0.96. (b) Example of a false detection (grey curve) with a waveform diverging from the mean trace despite a high correlation coefficient of 0.97. (c) Correctly identified low-amplitude event (red curve) with a correlation coefficient of 0.68; such events would be missed if the threshold was set too high. (d) Seismic trace of a detection (cyan curve) with a low correlation coefficient of 0.68. The background seismic noise is elevated, although some peaks in the signal match well with the mean trace. It shows the difficulty to distinguish between a correct and a false detection, especially when the event amplitude is small. These examples demonstrate the trade-off between minimizing false detections and avoiding missed events, and emphasize the need for a robust approach when aiming to build the most exhaustive event catalogue possible. 53

3.6 Example of a grid-search location using the differential arrival time ($T_S - T_P$) for a stick-slip event recorded by dense array A1. (a) Root Mean Square Error (RMSE) heatmap showing the convergence to a minimum RMSE value and the best-fitting source location (red star). (b) Distance-to-source versus time plot displaying the manually picked P-wave (red) and S-wave (green) arrivals. (c) Scatter plot of P-wave arrival times used for manual picking, with a fitted linear regression providing the slope and corresponding P-wave velocity. (d) Same as (c) for the S-wave arrivals. 56

3.7 Example of QuakeMigrate event location output on dense array A3. (a) Slices through a 3D coalescence map. We see convergence of the coalescence to a local maximum (yellow shades). (b) Seismogram of event waveform ordered by time of arrival, with predicted P-phases indicated in red and S-phases in blue. (c) Maximum coalescence function with a peak corresponding to possible seismic arrivals. 58

3.8 Example of particle motion analysis applied to a three-component seismic record of a stick-slip event (station 01x02, A1). (From top to bottom) First column: full waveform of the event on the three components - vertical (blue), north (red), and east (green). Second column: zoom on the P-wave onset for each component. Third column: amplitude ratios between the North-Vertical, East-Vertical, and East-North components. The resulting ellipses provide information on the azimuth and incidence angle of the incoming wave, offering an estimate of the source position relative to the station. 61

4.1 Map of the seismic nodes positions for the dense arrays A2 (left) and A3 (right). For position of the arrays on the glacier, see Fig. 2.5, Chapter 2. . . 89

4.2 Comparison of the correlation between the mean icequake activity rate (in count per hour) and tide amplitude (red) for the dense arrays A1 ((a), in blue), A2 ((b), in purple) and A3 ((c), in green). The 25-75% and 10-90% percentiles are presented in light colors. Note the y-axis are different for each panel. 91

4.3 (a) From left to right. Histogram of icequake activity rates (in count per hour) for all stations of dense array A1 (blue), dense array A2 (purple), both deployed over the grounding zone and dense array A3 (green) deployed over the shear margin. (b) Map of the hourly average icequake activity (color-coded in red, indicating the average icequake count per hour) recorded at each station of the seismic dense arrays A1 (blue circle), A2 (purple circle) and A3 (green circle) during their respective periods of deployment. 93

5.1 2023 seismic deployment on the Astrolabe Glacier, East Antarctica. (a) Map of the Astrolabe Glacier region, near the French base station Dumont d'Urville (DDU). The background image is a Pleiades satellite acquisition from January 10, 2025. The dotted black rectangle indicates the locations of the 2023 dense seismic array and includes the GNSS permanent stations (white triangles) and the DUMG reference station. The orange line represents the "geodetic" grounding line as estimated by Le Meur et al. (2014). (b) Location of the study area along the East Antarctica coast. (c) Close-up view of the 2023 deployment: 50 seismic nodes (black dots) installed across the grounding zone. 100

5.2 Stick-slip detection and location procedure. (a) Stacked waveform (red) from a cluster of stick- slip events (cluster 15), as observed at station 03x01 on the three components. Individual normalized waveforms from the cluster (150 traces) are shown in grey, highlighting the high waveform similarity within the cluster. (b) Eight-hour window of continuous seismic data on Jan. 28, 2023 from four stations (03x01, 02x02, 01x01, and 01x02), on the vertical component, during a period of activity for cluster 15. Red segments indicate individual detections identified via template matching with the selected cluster template. Amplitudes are independently normalized for each station. (c) Waveforms of a single event from cluster 15 (vertical component) recorded at the 50 stations plotted as a function of epicentral distance from the cluster source location. Seismograms are filtered between 25 and 100Hz. (d) Location of cluster 15 based on QuakeMigrate (Winder et al., 2025). Normalised coalescence value represents how well seismic arrivals from all stations "stack" coherently at a given point in the 3D grid. (e) Stacked waveforms of 767 events from cluster 15 (vertical component) at the 50 stations plotted as a function of epicentral distance from the cluster source location. Seismograms are filtered between 25 and 100Hz. (f) Refined location of cluster 15 from grid search. RMSE value is based on the difference between observed and modeled time arrival of P and S waves from manual picking. 104

5.3 (a) to (e): Spatial distribution of icequake activity across the dense seismic array during a tidal cycle. The maps are derived from kriging-based interpolation of icequake occurrence rates, averaged over seven consecutive tidal cycles from January 17 to 24, 2023. Icequake occurrence rates are expressed as the average number of events per 2-hour interval. Darker shades correspond to higher icequake occurrence rates. Each panel represents a 2-hour interval within the 12-hour window leading up to and following high tide. The corresponding time slot is reported on the tidal amplitude graph, reconstructed from the seven consecutive tidal cycles. For each window, the GNSS stations are colored according to the measured vertical displacement. (f) contour of the average icequake activity for each hour from mid-rising to high tide observed on a single day (Jan. 18, 2023). Each color corresponds to one hour from -6h to 0h, relative to high tide, as reported on the tidal amplitude graph. 106

5.4 Stick-slip clusters location. (a) Map showing the locations of 29 detected stick-slip clusters (stars), overlaid on the ice surface horizontal velocity map from Provost et al. (2024). Clusters are color-coded by their depths. Red stars indicate clusters with poorly resolved depths. The continuous orange line represents the "geodetic" grounding line from Le Meur et al. (2014). The detected stick-slip clusters allow to define a grounding zone bounded by a low and a high tide grounding line, indicated by the blue and red dotted lines, respectively. (b) Lower hemisphere stereonet representing the upward (black circles) and downward (white circles) first P-wave motion over the whole network. Grey circles indicate unsure polarisation. 107

5.5 Stick-slip activity relative to tide. (a) Time series of the number of active stick-slip clusters (red curve) over the period 17–24 January 2023, together with the tide amplitude (blue curve). (b) number of active clusters (black curve) folded over a representative 24-hour tidal cycle, divided into 30-minute bins. The x-axis represents time relative to high tide, from –12 to +12 hours and tidal amplitude is plotted as a blue curve. Values from all clusters are concatenated. (c) Total number of stick-slip events from all clusters along with the average icequake activity rate (in count per hour, red curve). (d) stick-slip inter-event time (IET). (e) event amplitudes (ground velocity, in m/s). For IET and event amplitudes, the mean (black curve), median (red dotted curve), and interquartile range (25th–75th percentiles displayed in grey shading) are shown. 109

5.6 Cartoon of the seismic observations and interpretation of grounding zone dynamics during a tidal cycle. It includes the surface icequakes generated by the tidal flexure, the grounding line migration and seawater intrusion seen by the basal stick-slip events. Note that the vertical movement is not to scale. . 112

6.1 Map of the January 2025 dense seismic array deployed over the west lateral shear zone of the Astrolabe Glacier for 15 days. GNSS stations are deployed within and around the dense array as part of the GLACIOCLIM observatory. The shear margin, accommodating a left-lateral shearing, and whose delineation is based on surface velocity gradient, is represented by the blue line. Grounding line position is represented by the grey line. 119

6.2 Welch's spectrogram of 4 stations (33x01, 33x03, 33x06 and 33x09) across the dense array over 7 days. Note the noise during the two-day long storm (Jan, 16th and Jan, 17th). PSD stands for Power Spectral Density. 121

6.3 PPSD of seismic nodes (vertical components DPZ) deployed in Jan. 2025 across the west lateral shear zone of the Astrolabe Glacier. The 4 presented individual PPSD are calculated for 1 day (Jan. 15, 2025) at 4 stations along a NW-SE trending line perpendicular to the shear zone, from the stable ice (right, node 33X01) to approaching the floating part of the glacier (left, node 33X09). Modified from Barruol et al. (2025). 122

6.4 Horizontal displacement map of the shear margin area. Seismic nodes are color-coded by their total horizontal displacement (in meters) over the 12 to 15 days of deployment. GNSS stations (red dots) and their average horizontal motion are represented by arrows oriented along the dominant ice-flow direction and annotated with mean horizontal velocities (in millimeters per hour). 124

6.5 Horizontal velocity timeseries (green curve) superposed with tide amplitude (red curve) for 6 GNSS stations (see positions in Fig. 6.4): GPS01 (a), GPS02 (b), GPS03 (c), GPS04 (d), GPS05 (e), GPS07 (f) over the period January 10-20, 2025. Note that the y-axis is not the same for the different panels. . . 125

6.6 Vertical displacement timeseries (blue curve) superposed with tide amplitude (red curve) for GNSS stations GPS01 (a), GPS02 (b), GPS03 (c), GPS04 (d), GPS05 (e), GPS07 (f), over the period January 10-20, 2025. 126

6.7 Map with location of seismic nodes (purple dots) and stick-slip clusters (stars), colored according to their depth. 127

6.8 Lower hemisphere stereonet (in the same orientation as Fig. 6.7, i.e. with the flow vector pointing along the azimuth N055°E) representing the upward (black circles) and downward (white circles) first P-wave motion of 14 stick-slip clusters (1 to 16 except 8 and 10 which show opposite focal mechanisms). Grey circles indicate unsure first P-wave motion. Crosses indicate no clear waveform for picking the P-wave first motion. 129

6.9 Stick-slip activity relative to tide: (a) Time series of the number of active stick-slip clusters (red curve) over the period 9–15 January 2025, together with the tide amplitude (blue curve). (b) Number of active clusters (black curve) folded over a representative 24-hour tidal cycle, divided into 30-minute bins. The x-axis represents time relative to high tide, from –12 to +12 hours and tidal amplitude is plotted as a blue curve. (c) Total number of stick-slip events from all clusters, folded over a representative 24-hour tidal cycle, divided into 30-minute bins. (d) Stick-slip inter-event time (IET), folded over a representative 24-hour tidal cycle, divided into 30-minute bins. (e) Event amplitudes (ground velocity, in m/s), folded over a representative 24-hour tidal cycle, divided into 30-minute bins. For IET and event amplitudes, the median (red dotted curve), and interquartile range (25th–75th percentiles displayed in grey shading) are shown. 131

6.10 (a) Map showing stick-slip clusters locations from 2023 detection (stars with blue edge) and 2025 detection (stars with no edge color), color-coded by their depths. Radar profiles intersecting the seismic node array are represented by dots color-coded according to the associated ice thickness (in meters). The lateral shear margin of the Astrolabe Glacier is outlined in light blue. (b) 2D profile of the ice–bedrock interface depths along the X-axis, approximately perpendicular to the shear margin. Blue dots represent the projection of the radar-derived ice thicknesses on the plane normal to the shear zone, and red dots indicate depths of stick-slip clusters inferred from seismic data, along with their uncertainties (black error bars). Polynomial (degree-2) regression curves are fitted to each dataset to illustrate the general trend of the ice-bedrock interface slope. 133

6.11 (a) Predicted ice thickness as a function of compressional (V_P) and shear (V_S) wave velocities that can explain the measured P-S differential travel time (dt = 0.2763 s) observed at station 32x06, located at the vertical of the source of cluster 3. The black rectangle delineates the velocity domain explored within QuakeMigrate. The solid cyan line represents the cluster depth for the location with best fit to the P- and S- wave arrivals, and the dashed cyan lines indicate the corresponding uncertainty bounds. The red line marks the radar-derived ice thickness estimate, showing that the Vs could be much smaller than investigated. (b) Same as in (a), but for cluster 4 (dt = 0.2488 s), observed from the recorded data at station 33x06. 135

7.1 Comparison of field organization between Dumont d'Urville Station (Terre Adélie, East Antarctica) and the Isunnguata Sermia field camp (Kangerlussuaq, Qeqqata, West Greenland). (a) Dumont d'Urville (DDU) base station, showing the various buildings dedicated to daily life and scientific operations. (b) Communal dining hall of DDU where all station members share meals. (c) Field camp setup on Isunnguata Sermia, including sleeping tents, a mess tent, and a science tent in the background. (d) Interior view of the mess tent, where cooking and scientific activities often overlap. Daily logistics and research operations are carried out in parallel on the glacier. 143

7.2 Examples of field hazards encountered on glaciers. (a) Large crevasse on the Astrolabe Glacier, partially filled with snow bridges. (b) Moulin on Isunnguata Sermia. 145

7.3 Comparison of the instrument types and their design that shape the strategy of deployment. (a) *SmartSolo* IGU-16HR 3C node. (b) Magseis *Fairfield* ZLAND 3-component 5Hz node. (c) *Geospace GSB* 3-channel unit connected to a *Geospace* 5 Hz Geophone 3C. 147

7.4 Strategies of deployment of seismic nodes on glacier ice. (a) Installation of a *SmartSolo* IGU-16HR 3C node in a drilled borehole approximately 50 cm deep. (b) Setup of a *Geospace GSB* unit connected to a geophone placed at the bottom of a 1 m-deep borehole. The GSB unit remains at the surface to ensure reliable GPS connection; bamboo markers are used to locate the node. (c) Example of a gnomon used to orient seismic nodes toward geographic north. In this case, the sensors were installed in rectangular holes, prior to adopting drilled holes as a more effective solution. (d) Use of a guiding rod to accurately orient the geophone at the bottom of the borehole toward geographic north. 149

7.5 Recovery operations of seismic nodes on glaciers. (a) Extraction of a node deployed on the Astrolabe Glacier using a chainsaw. (b) Removal of residual ice stuck to a seismic node with an ice axe. (c) Example of a node trapped in ice slush after successive melting and snowfall episodes. (d) Search for a snow-covered seismic node using a metal detector. 152

7.6 Analyses of the tilting on the seismic nodes of dense array A3 deployed in 2025. (top) Median (blue) and standard deviation (light blue) of the vertical tilt angle timeseries during the period Jan. 8, 2025 to Jan. 23, 2025. (bottom) Median (orange) and standard deviation (light orange) of the horizontal tilt angle timeseries during the period Jan. 8, 2025 to Jan. 23, 2025. The red lines represent respectively on the top and bottom plots, the vertical and horizontal tilt angle threshold to ensure a distortion inferior or equal to 0.30% at 12 Hz. 153

7.7 Sensor found tilted after being deployed for two months in July and August 2024 on Isunnguata Sermia, western Greenland. 154

7.8 Power Spectral Density (PSD) spectrograms on the 3 components of 3 stations from dense arrays deployed in spring 2023 (a, d, g), summer 2024 (b, e, h) and fall 2024 (c, f, i) on Isunnguata Sermia. The hashed area highlights the days where the sensors were classified as significantly tilted on the vertical and horizontal components. Modified from Paris et al. (in prep.) 155

7.9 Map of source locations, based on Match Field Processing method, for dense arrays deployed on the Astrolabe Glacier. (a) Map of MFP-based event locations for the 2023 array. (b) Map of MFP-based event locations for the 2025 array. For the two maps, the Bartlett output (BO) threshold is set to 0.2. (c) and (d) Histograms of event Bartlett coherence and depth for the 2023 array, respectively. (e) and (f) Histograms of event Bartlett coherence and depth for the 2025 array, respectively. 157

7.10 Map of source locations, based on Match Field Processing method, for Isunnguata Sermia arrays. (a) Map of MFP-based event locations for the 2023 spring array. (b) Map of MFP-based event locations for the 2024 summer array. (c) Map of MFP-based event locations for the 2024 fall array. For all three maps, the Bartlett output (BO) threshold is set to 0.8. (d) and (e) Histograms of event Bartlett coherence and depth for the 2023 spring array, respectively. (f), (g), (h) and (i) are the same as (d) and (e) but for the 2024 summer and fall datasets. Modified from Paris et al. (in prep). 158

7.11 (a) Diagram illustrating the principle of DAS technology. The interrogator sends a laser pulse into the cable. Due to natural imperfections in the fibre, Rayleigh scattering occurs. Some of this scattered light is backscattered towards the interrogator (see (c)). (b) The strain rate of each DAS channel, spaced at dx, is determined over a gauge length that functions as a moving average across the fibre optic cable. (c) When strains occur in the optic cable, the backscattered light signal that reaches the interrogator changes. From these changes, the interrogator calculates the strain rate occurring in the cable for each DAS channel. Note that the figure is not to scale. Adapted from Nap (2020). 161

7.12 Deployment of the Distributed Acoustic Sensing (DAS) system on the Astrolabe Glacier in January 2024. (a) Map showing the location of the seismic node array A2 (purple triangles) and the two optical fiber lines: CH1 (straight, dark blue) and CH2 (zig-zag, light blue). (b) Timeline of DAS data acquisition periods (in green) and downtime (in blue), overlaid with the tidal amplitude measured at DDU tide gauge (red curve). (c) Overview of the array and fiber layout on the Astrolabe Glacier, located over the grounding zone. (d) Power supply system for the DAS computer: a propane-fuelled generator is kept in a ventilated wooden box to prevent overheating. (e) DAS interrogator unit stored within a metal box and protected from drifting snow by a tent cover. (f) Fiber-deployment setup using a reel dispenser mounted on a sledge for cable unwinding. 162

7.13 Deployment of the Distributed Acoustic Sensing (DAS) system on Isunnguata Sermia, western Greenland, in July 2024. (a) Map showing the location of the seismic node arrays deployed in 2023 (blue triangles) and 2024 (red triangles) and the two optical fiber lines: CH1 (purple line) and CH2 (green line). (b) Overview of the study area on Isunnguata Sermia, near Kangerlussuaq, Qeqqata, Greenland. (c) Fiber-deployment setup using a reel dispenser attached to a backpack for cable unwinding. (d) DAS interrogator unit stored in a tent to protect it from wind and precipitations. (e) Timeline of DAS data acquisition periods (green) and downtime (beige) for the two fibers CH1 (bottom) and CH2 (top). 164

7.14 DAS sections of signal amplitudes over 30 minutes along the full length of the two optic fibers CH1 (a) and CH2 (b). The yellow arrows point to long transects of coherent noise propagating along the cable. The section delimited by two yellow lines is where the optic fiber cable was entangled and could not be properly deployed. 165

7.15 Hammer shot near the dense array A2 and the optic fibers. (a) Active seismic hammer shot seen on seismic nodes of the dense array A2. The hammer shot was performed near seismic node 03x01 on 16, Jan 2024 at 06:10:00 (UTC). Seismic waveforms are from the vertical component and filtered between 5 and 20 Hz. (b) DAS record of the hammer shot on the zigzag fiber CH2. The black arrow indicates where the shot was performed along the cable. We observe propagation of the signal at around 150 m on one side, and the signal being lost in noise on the other side. (c) Comparison of the waveform on seismic node 03x01 (vertical component) (black) and strain record the DAS channel next to the node (red). Note that amplitudes are normalized. 167

7.16 (a) Vertical component of dense array seismic traces of a hammer shot close to node 1104 (from the 2024 dense array deployed on Isunnguata Sermia). (b) DAS section for the same event. The light green box shows the channel closest to node 1104. (c) Comparison between the waveforms of node 1104 and the DAS channel in the light green box in (b). Adapted from Paris et al. (in prep) 168

B.1 Tide amplitude, tide velocity, icequake rate and spectral energy at AST01 for the period January 16 to 29, 2022. Top plot: Number of detected seismic events (black curve) per hour compared with tide amplitude (red curve) and tide vertical velocity (blue curve). Bottom plot: Spectrogram of seismic energy alongside tide amplitude (red curve). Spectrogram is generated using the Logarithmic Power Spectral Density (LPSD) method on the vertical (Z) component of the data, with 10-minute windows covering the 1-100 Hz frequency range. Welch's method is applied on 10-second segments within each window, and the mean power is computed and converted to decibels (dB). The instrumental response is removed. 227

B.2 Tide amplitude, tide velocity, icequake rate and spectral energy at AST04 for the period January 16 to 29, 2022. Top plot: Number of detected seismic events (black curve) per hour compared with tide amplitude (red curve) and tide vertical velocity (blue curve). Bottom plot: Spectrogram of seismic energy alongside tide amplitude (red curve). Spectrogram is generated using the Logarithmic Power Spectral Density (LPSD) method on the vertical (Z) component of the data, with 10-minute windows covering the 1-100 Hz frequency range. Welch's method is applied on 10-second segments within each window, and the mean power is computed and converted to decibels (dB). The instrumental response is removed. 228

B.3 Tide amplitude, tide velocity, icequake rate and spectral energy at AST06 for the period January 16 to 29, 2022. Top plot: Number of detected seismic events (black curve) per hour compared with tide amplitude (red curve) and tide vertical velocity (blue curve). Bottom plot: Spectrogram of seismic energy alongside tide amplitude (red curve). Spectrogram is generated using the Logarithmic Power Spectral Density (LPSD) method on the vertical (Z) component of the data, with 10-minute windows covering the 1-100 Hz frequency range. Welch's method is applied on 10-second segments within each window, and the mean power is computed and converted to decibels (dB). The instrumental response is removed. 228

B.4 Tide amplitude, tide velocity, icequake rate and spectral energy at AST08 for the period January 16 to 29, 2022. Top plot: Number of detected seismic events (black curve) per hour compared with tide amplitude (red curve) and tide vertical velocity (blue curve). Bottom plot: Spectrogram of seismic energy alongside tide amplitude (red curve). Spectrogram is generated using the Logarithmic Power Spectral Density (LPSD) method on the vertical (Z) component of the data, with 10-minute windows covering the 1-100 Hz frequency range. Welch's method is applied on 10-second segments within each window, and the mean power is computed and converted to decibels (dB). The instrumental response is removed. 229

B.5 Tide amplitude, tide velocity, icequake rate and spectral energy at AST09 for the period January 16 to 29, 2022. Top plot: Number of detected seismic events (black curve) per hour compared with tide amplitude (red curve) and tide vertical velocity (blue curve). Bottom plot: Spectrogram of seismic energy alongside tide amplitude (red curve). Spectrogram is generated using the Logarithmic Power Spectral Density (LPSD) method on the vertical (Z) component of the data, with 10-minute windows covering the 1-100 Hz frequency range. Welch's method is applied on 10-second segments within each window, and the mean power is computed and converted to decibels (dB). The instrumental response is removed. 229

B.6 Comparison between the hourly occurrence rate of MFP-located seismic events (black curve) and tidal amplitudes (red curve) over the period January 17–24, 2023. No clear correlation is observed between the timing of seismic activity and the tidal cycle. 230

B.7 Two examples of icequakes recorded across multiple seismic stations. (Top panels) Normalized waveforms observed at different stations. (Bottom panels) Map showing the locations of the stations used for the waveform examples (red dots) within the dense seismic array (black dots), along with the estimated seismic source location (yellow star). We observe a significant variability in waveforms, making it difficult to accurately pick P- and S-wave arrivals. This results in high location uncertainties, ultimately limiting the reliability of standard localization methods. 230

B.8 Comparison between icequake activity rate (in count per hour) for station 01x07 (A1) and weather parameters: (a) Temperature and (b) Wind speed. Weather data are from MétéoFrance (donneespubliques.meteofrance.fr). 231

C.1 Contour map of depth estimate as a function of P- wave velocity (Vp) and S- wave velocity (Vs) from grid search on cluster 4 (see Table A1, depth estimate: 1000 m) to explain the measured delay between the P- and S-phase arrival times. For each (Vp, Vs) couple, the depth is estimated based on the minimum RMSE value obtained. The black rectangle delineates the velocity domain explored in the present study. Red line indicates the bedrock depth estimate based on radar data, expected to be around 700 m (Le Meur et al., 2014). A clear trade-off is observed between seismic velocities and estimated depth. The diagram shows that the stick-slip depth estimate is more sensitive to variations in Vs than in Vp and that lower shear velocities may reconcile seismic and radar depth estimates. This highlights the importance of improving the seismic velocity structure of the Astrolabe Glacier to better constrain the absolute depth estimates of the stick-slips at the ice-bedrock interface. 235

C.2 Individual stereonets (lower hemisphere) representing the upward (black circles) and downward (white circles) first P-wave motion of each stick-slip cluster detected by the dense seismic node array A1, numbered as in Table C.1. Grey circles indicate unsure polarisation by at least one of the three analysts. 236

D.1 Amplitude Spectral Density (ASD) of horizontal velocity timeseries at six GPS stations, computed using the Welch method. The x-axis shows frequency in cycles per day, and the y-axis shows ASD in mm/h per $\sqrt{}$cycle/day. Peaks near 1 cycle/day and 2 cycles/day indicate, respectively, diurnal and semidiurnal variability in horizontal motion. 237

D.2 Amplitude Spectral Density (ASD) of vertical displacement timeseries at six GPS stations, computed using the Welch method. The x-axis shows frequency in cycles per day, and the y-axis shows ASD in mm per $\sqrt{}$cycle/day. Peaks near 1 cycle/day and 2 cycles/day indicate, respectively, diurnal and semidiurnal variability in horizontal motion. 238

D.3 Individual stereonets for stick-slip clusters detected with dense array A3 (2025) over the shear margin of the Astrolabe Glacier. 239

D.4 Map of the ice thickness estimates inferred from radar data over the Astrolabe Glacier area. The radar dataset includes data from different campaigns. Airborne radar data were collected by NASA using the Warm Ice Sounding Explorer (WISE) during the 2008–09 season (Mouginot et al., 2014). Additional airborne measurements were acquired within the ICECAP project using the High Capability Radar Sounder (HiCARS) in 2008-09 and 2009-10 (Young et al., 2011). Ground-penetrating radar (GPR) profiles were collected during the 2007-08 field season (Le Meur et al., 2014). Each dataset was processed independently by the respective project teams. 240

List of Tables

2.1 Summary of dense arrays of seismic nodes deployed from 2023 to 2025, including surface area, number of nodes, total recording days and sampling rates. Tables with precise localizations of each node of the arrays are given in Tables A2.1, A2.2, A2.3. 43
2.2 Summary of broad band seismic stations (except AST15 and AST16 that are short-period) deployed during the SEIS-ADELICE project, including installation and removal dates, total recording days, instrument types and sampling rates. NT: Nanometrics Trillium 44
2.3 Summary of OBS deployed during the SEIS-ADELICE project, including installation and removal dates, total recording days, instrument types and sampling rates. 44

6.1 Stick-slip clusters detected beneath the Astrolabe Glacier west shear margin using the dense array A3 deployed in Jan. 2025. For each cluster is shown the longitude, latitude, depth and the number of events detected. 128

A.1 Position of seismic nodes of dense array A1 224
A.2 Position of seismic nodes of dense array A2 225
A.3 Position of seismic nodes of dense array A3 226

C.1 Stick-slip clusters detected and located beneath the Astrolabe Glacier grounding zone. For each cluster is shown the initial number of events detected, the final number of events detected after manual screening and the longitude, latitude and depth of the cluster. 234

APPENDIX A

Appendix chapter 2

Node	Lon (°E)	Lat (°N)	Node	Lon (°E)	Lat (°N)
00x00	-66.73992	139.91453	04x04	-66.73877785	139.91798104
01x01	-66.72457	139.92153	04x05	-66.74103639	139.92150546
01x02	-66.72619	139.92819	04x06	-66.74443417	139.92791981
01x03	-66.72774	139.93439	04x07	-66.74614934	139.93418955
01x04	-66.73063756	139.93977583	05x01	-66.7344945	139.89521058
01x05	-66.73291659	139.94393359	05x02	-66.7369037	139.90086906
01x06	-66.73408169	139.95074059	05x03	-66.7395605	139.90529128
01x07	-66.73808703	139.95884978	05x04	-66.7413023	139.90966595
02x01	-66.72668822	139.91534689	05x05	-66.7443031	139.91529416
02x02	-66.72917882	139.92205866	05x06	-66.7471839	139.9195881
02x03	-66.73069127	139.92598134	05x07	-66.748995	139.92618884
02x04	-66.73316181	139.93225152	06x01	-66.7368903	139.89020076
02x05	-66.73550176	139.93638888	06x02	-66.7383167	139.89368944
02x06	-66.73829836	139.94171906	06x03	-66.7410485	139.89780457
02x07	-66.7407784	139.94882624	06x04	-66.74349561	139.90200826
03x01	-66.7294579	139.90900976	06x05	-66.74602407	139.90718905
03x02	-66.7319035	139.91434695	06x06	-66.74849289	139.9142137
03x03	-66.7335194	139.91897112	06x07	-66.75093066	139.91967234
03x04	-66.7366676	139.92372449	07x01	-66.73893489	139.88259274
03x05	-66.7378691	139.92925652	07x02	-66.7418058	139.88835111
03x06	-66.7411706	139.93551224	07x03	-66.74386324	139.89243526
03x07	-66.7438479	139.94179076	07x04	-66.74592212	139.8949105
04x01	-66.73166472	139.9019898	07x05	-66.74855727	139.90125824
04x02	-66.73445808	139.9074966	07x06	-66.75065643	139.90884701
04x03	-66.73693804	139.9127492	07x07	-66.75274387	139.91186366

Table A.1: Position of seismic nodes of dense array A1

Node	**Lon (°E)**	**Lat (°N)**	**Node**	**Lon (°E)**	**Lat (°N)**
21X01	-66.73592375	139.9308964	24X05	-66.74356015	139.9245887
21X02	-66.73714033	139.9311533	25X01	-66.74122121	139.9120839
21X03	-66.73740532	139.9343831	25X02	-66.74147892	139.915571
21X04	-66.7389286	139.9356294	25X03	-66.74245199	139.9178009
21X05	-66.7392931	139.938758	25X04	-66.74330744	139.9196258
22X01	-66.73680447	139.9261313	25X05	-66.74455592	139.9214391
22X02	-66.73835814	139.9270684	26X01	-66.74231168	139.9078887
22X03	-66.73847696	139.930833	26X02	-66.74308658	139.9106813
22X04	-66.73967457	139.9318541	26X03	-66.74330825	139.914855
22X05	-66.74115431	139.9331629	26X04	-66.74447283	139.9161588
23X01	-66.73841726	139.9207369	26X05	-66.74592868	139.9165065
23X02	-66.73964705	139.9228679	27X01	-66.74377965	139.9029037
23X03	-66.73963948	139.9270713	27X02	-66.74467009	139.9063072
23X04	-66.74119668	139.9282463	27X03	-66.74475342	139.9103414
23X05	-66.74237519	139.9294159	27X04	-66.74629143	139.9098797
24X01	-66.73964117	139.9162769	27X05	-66.74789164	139.9104904
24X02	-66.74041386	139.9189504	28X02	-66.74587016	139.9028526
24X03	-66.74151255	139.9209769	28X03	-66.74824809	139.898971
24X04	-66.74231465	139.9245646	28X04	-66.74730644	139.9067365

Table A.2: Position of seismic nodes of dense array A2

Node	Lon (°E)	Lat (°N)	Node	Lon (°E)	Lat (°N)
31X01	-66.720329	139.913086	33X05	-66.724281	139.918015
31X02	-66.720428	139.916290	33X06	-66.724579	139.921188
31X03	-66.721069	139.919998	33X07	-66.725868	139.921371
31X04	-66.722351	139.921417	33X08	-66.727005	139.922913
31X05	-66.722191	139.924515	33X09	-66.728333	139.929413
31X06	-66.723099	139.927628	34X01	-66.722672	139.906128
31X07	-66.724922	139.927963	34X02	-66.722702	139.909454
31X08	-66.725540	139.929794	34X03	-66.724121	139.913788
31X09	-66.727020	139.932571	34X04	-66.725044	139.915894
32X01	-66.720268	139.909668	34X05	-66.725922	139.918900
32X02	-66.721573	139.914169	34X06	-66.727028	139.920303
32X03	-66.722061	139.917633	34X07	-66.728500	139.923111
32X04	-66.723030	139.919754	34X08	-66.728180	139.925293
32X05	-66.723740	139.922272	34X09	-66.729965	139.931702
32X06	-66.724472	139.924927	35X01	-66.723862	139.907349
32X07	-66.726097	139.926056	35X02	-66.724533	139.910278
32X08	-66.727188	139.928345	35X03	-66.725288	139.911804
32X09	-66.729218	139.933258	35X04	-66.726425	139.913895
33X01	-66.721191	139.907166	35X05	-66.726952	139.917725
33X02	-66.721756	139.910522	35X06	-66.728233	139.917618
33X03	-66.722954	139.912766	35X08	-66.730034	139.923584
33X04	-66.722984	139.915497	35X09	-66.729652	139.927399

Table A.3: Position of seismic nodes of dense array A3

APPENDIX B

Appendix chapter 4

First section

This first part of the appendix constitutes the appendix to the article Le Bris et al. (2025) published in *Journal of Geophysical Research*.

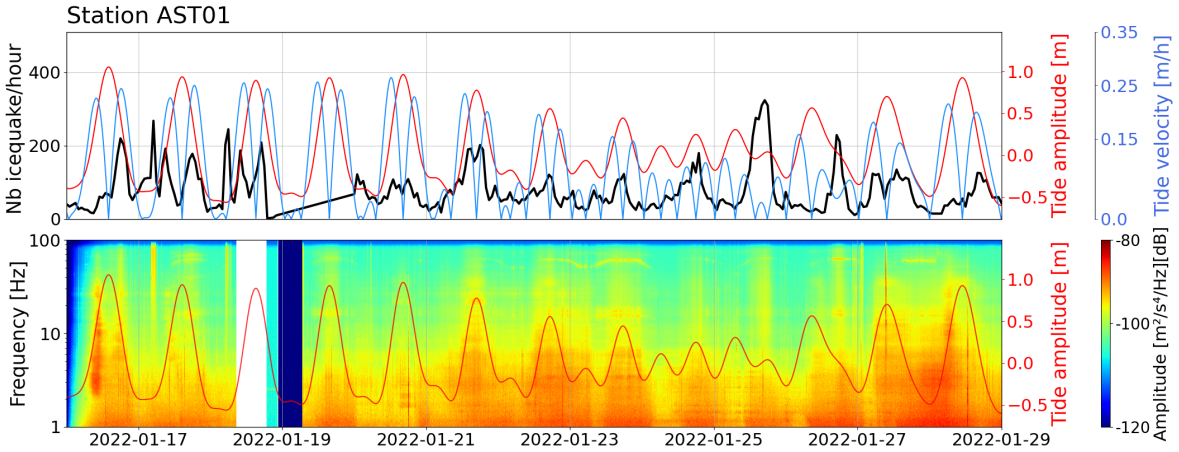

Figure B.1: Tide amplitude, tide velocity, icequake rate and spectral energy at AST01 for the period January 16 to 29, 2022. Top plot: Number of detected seismic events (black curve) per hour compared with tide amplitude (red curve) and tide vertical velocity (blue curve). Bottom plot: Spectrogram of seismic energy alongside tide amplitude (red curve). Spectrogram is generated using the Logarithmic Power Spectral Density (LPSD) method on the vertical (Z) component of the data, with 10-minute windows covering the 1-100 Hz frequency range. Welch's method is applied on 10-second segments within each window, and the mean power is computed and converted to decibels (dB). The instrumental response is removed.

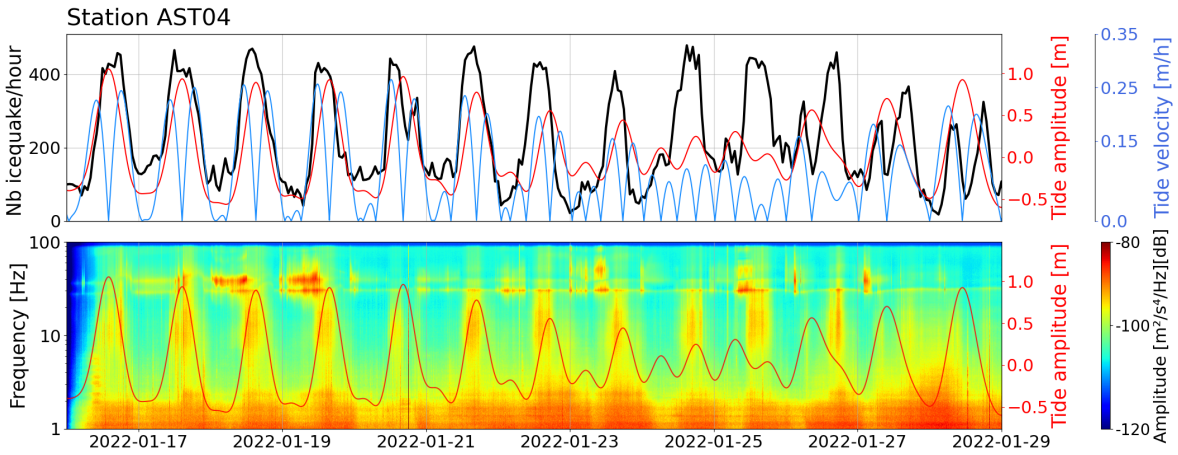

Figure B.2: Tide amplitude, tide velocity, icequake rate and spectral energy at AST04 for the period January 16 to 29, 2022. Top plot: Number of detected seismic events (black curve) per hour compared with tide amplitude (red curve) and tide vertical velocity (blue curve). Bottom plot: Spectrogram of seismic energy alongside tide amplitude (red curve). Spectrogram is generated using the Logarithmic Power Spectral Density (LPSD) method on the vertical (Z) component of the data, with 10-minute windows covering the 1-100 Hz frequency range. Welch's method is applied on 10-second segments within each window, and the mean power is computed and converted to decibels (dB). The instrumental response is removed.

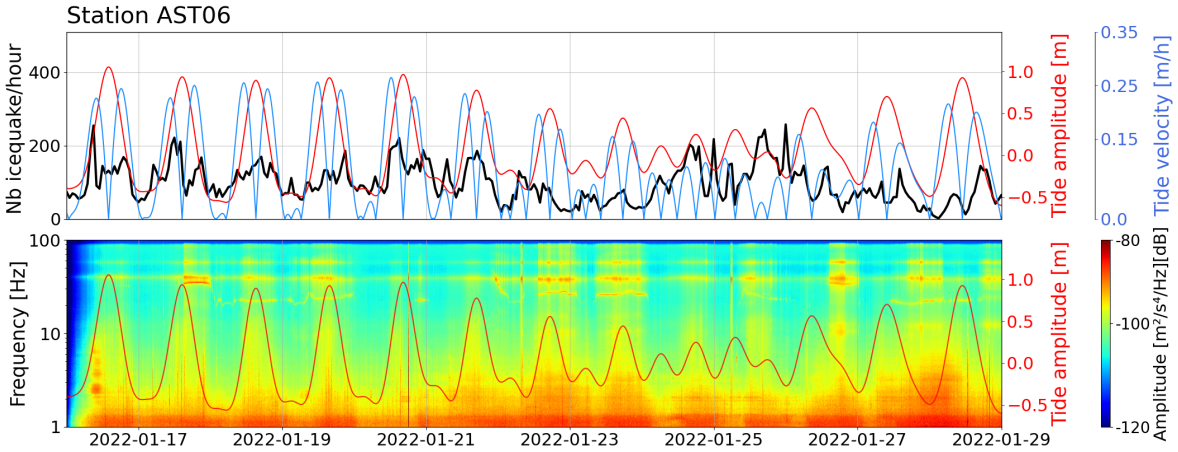

Figure B.3: Tide amplitude, tide velocity, icequake rate and spectral energy at AST06 for the period January 16 to 29, 2022. Top plot: Number of detected seismic events (black curve) per hour compared with tide amplitude (red curve) and tide vertical velocity (blue curve). Bottom plot: Spectrogram of seismic energy alongside tide amplitude (red curve). Spectrogram is generated using the Logarithmic Power Spectral Density (LPSD) method on the vertical (Z) component of the data, with 10-minute windows covering the 1-100 Hz frequency range. Welch's method is applied on 10-second segments within each window, and the mean power is computed and converted to decibels (dB). The instrumental response is removed.

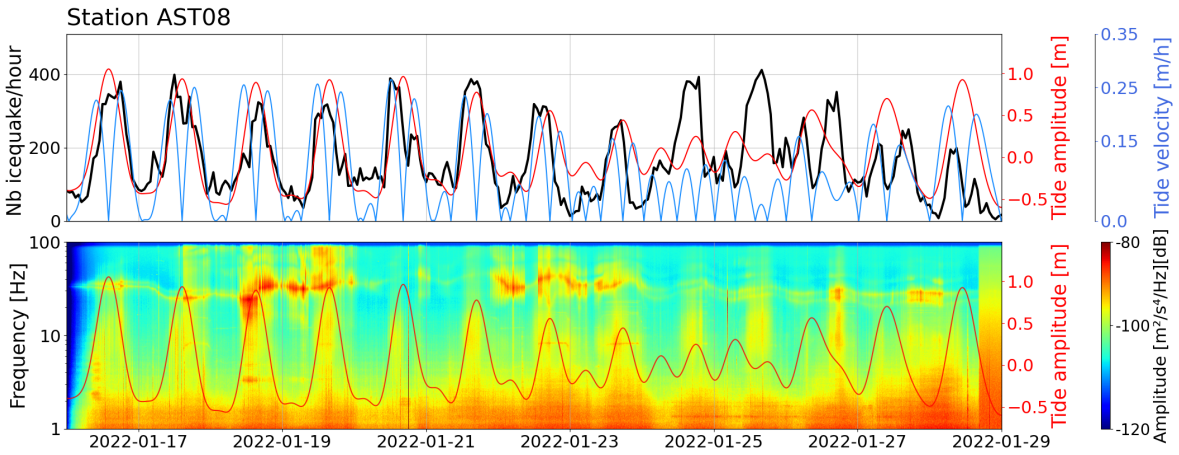

Figure B.4: Tide amplitude, tide velocity, icequake rate and spectral energy at AST08 for the period January 16 to 29, 2022. Top plot: Number of detected seismic events (black curve) per hour compared with tide amplitude (red curve) and tide vertical velocity (blue curve). Bottom plot: Spectrogram of seismic energy alongside tide amplitude (red curve). Spectrogram is generated using the Logarithmic Power Spectral Density (LPSD) method on the vertical (Z) component of the data, with 10-minute windows covering the 1-100 Hz frequency range. Welch's method is applied on 10-second segments within each window, and the mean power is computed and converted to decibels (dB). The instrumental response is removed.

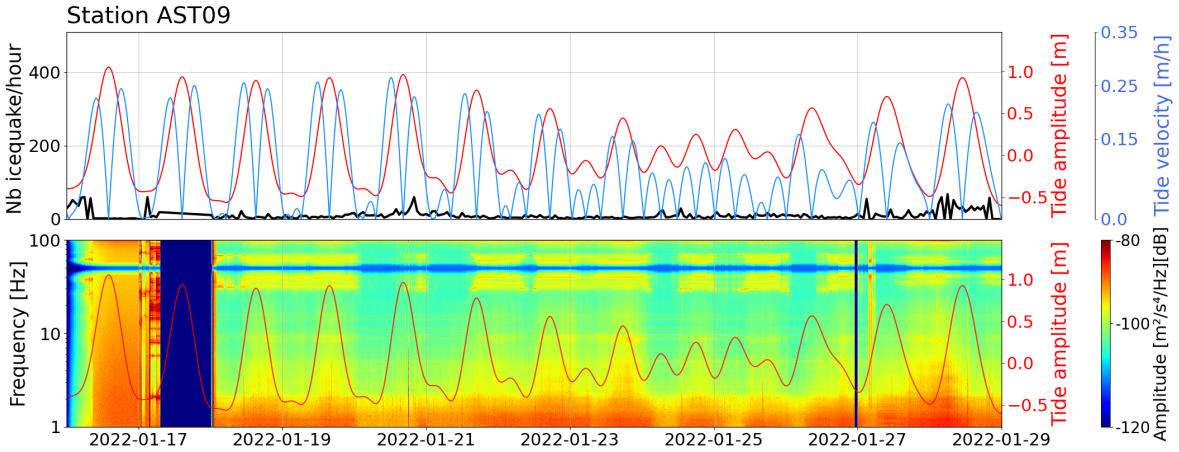

Figure B.5: Tide amplitude, tide velocity, icequake rate and spectral energy at AST09 for the period January 16 to 29, 2022. Top plot: Number of detected seismic events (black curve) per hour compared with tide amplitude (red curve) and tide vertical velocity (blue curve). Bottom plot: Spectrogram of seismic energy alongside tide amplitude (red curve). Spectrogram is generated using the Logarithmic Power Spectral Density (LPSD) method on the vertical (Z) component of the data, with 10-minute windows covering the 1-100 Hz frequency range. Welch's method is applied on 10-second segments within each window, and the mean power is computed and converted to decibels (dB). The instrumental response is removed.

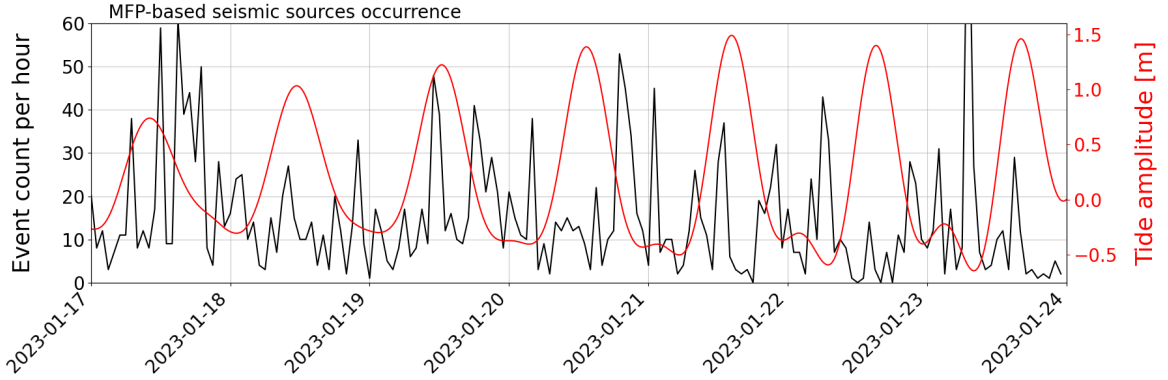

Figure B.6: Comparison between the hourly occurrence rate of MFP-located seismic events (black curve) and tidal amplitudes (red curve) over the period January 17–24, 2023. No clear correlation is observed between the timing of seismic activity and the tidal cycle.

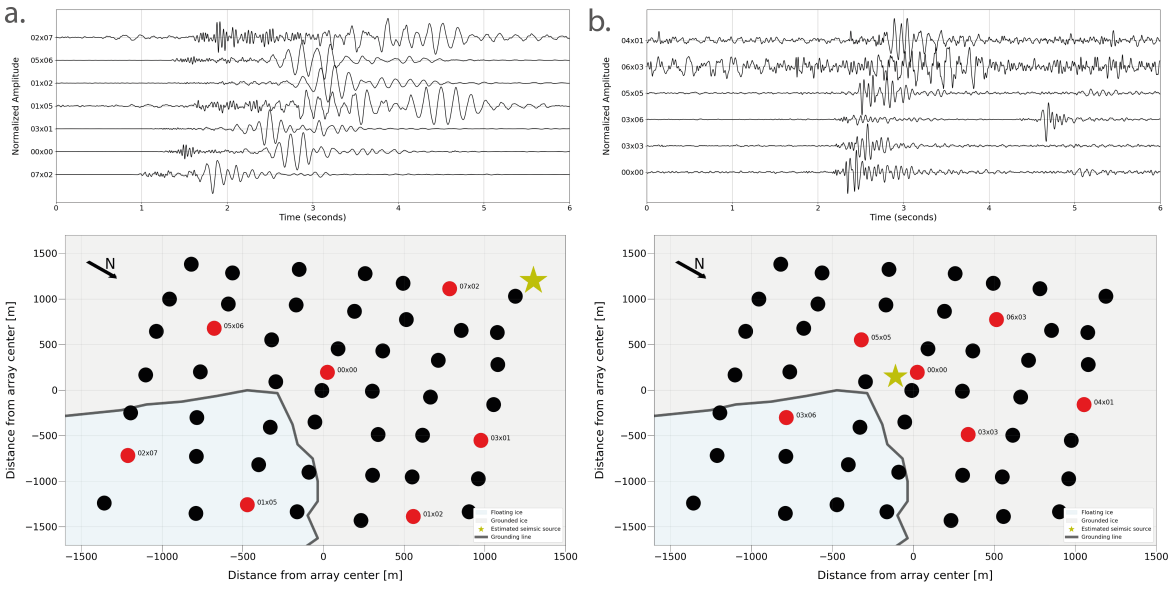

Figure B.7: Two examples of icequakes recorded across multiple seismic stations. (Top panels) Normalized waveforms observed at different stations. (Bottom panels) Map showing the locations of the stations used for the waveform examples (red dots) within the dense seismic array (black dots), along with the estimated seismic source location (yellow star). We observe a significant variability in waveforms, making it difficult to accurately pick P- and S-wave arrivals. This results in high location uncertainties, ultimately limiting the reliability of standard localization methods.

Second section

This second part of the appendix concerns section 4.3 of chapter 4.

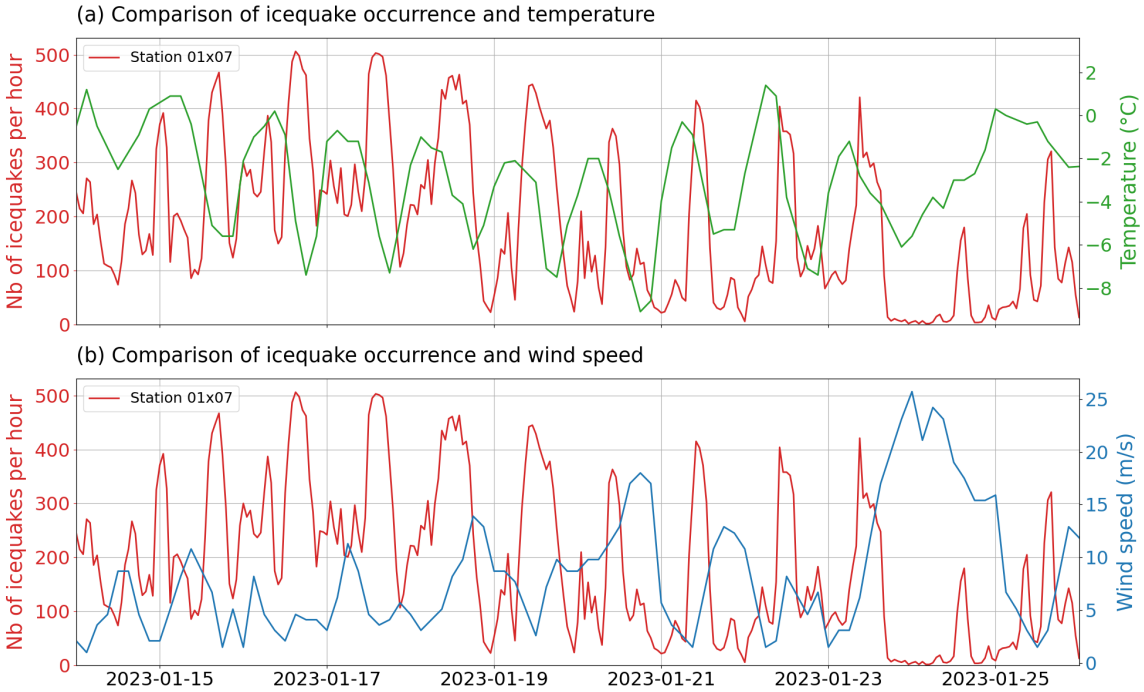

Figure B.8: Comparison between icequake activity rate (in count per hour) for station 01x07 (A1) and weather parameters: (a) Temperature and (b) Wind speed. Weather data are from MétéoFrance (donneespubliques.meteofrance.fr).

APPENDIX C

Appendix chapter 5

Text C.1 - Kriging methodology and parameters

Kriging method, as implemented in the Python function OrdinaryKriging() (Murphy et al., 2024). Input variables to the kriging-based interpolation include the (X, Y) coordinates of the seismic nodes and their respective icequake occurrence rates. We use a linear variogram model, with six distance bins to compute the experimental semivariogram, best fitting considering the station count (N=50). To ensure numerical stability, we solve the kriging system using a pseudo-inverted kriging matrix and average redundant points to avoid over-representation. Additionally, we apply a weighted semivariance approach, emphasizing smaller lag distances in the variogram fitting.

Cluster	Nb of initial detections	Nb of final detections	Long (°E)	Lat (°N)	Depth (m)
1	1493	285	139.93408	-66.75864	400
2	1488	1012	139.86294	-66.72408	-
3	1198	1191	139.89303	-66.72970	1500
4	3513	1985	139.93345	-66.74838	1000
5	1509	366	139.87546	-66.74256	350
6	5941	258	139.95032	-66.75220	1000
7	742	578	139.93745	-66.72967	850
8	4254	500	139.91466	-66.75169	650
9	7304	4850	139.88351	-66.72904	-
10	3418	782	139.92027	-66.75055	950
11	2681	1179	139.92179	-66.74973	900
12	4546	767	139.89923	-66.74636	850
13	11103	4010	139.86644	-66.73185	750
14	475	347	139.86819	-66.73430	850
15	60	49	139.92789	-66.72787	1450
16	402	300	139.92037	-66.72652	-
17	538	376	139.94768	-66.751857	950
18	556	285	139.91064	-66.74988	750
19	587	569	139.90397	-66.71565	800
20	244	243	139.88486	-66.72779	1500
21	770	719	139.88206	66.72823	1450
22	182	148	139.87930	-66.72693	1400
23	1065	963	139.86892	-66.73778	-
24	624	622	139.89286	-66.71886	-
25	885	40	139.86648	-66.73199	250
26	761	740	139.91231	-66.72389	-
27	448	393	139.87760	-66.72510	1150
28	422	415	139.90035	-66.73335	-
29	205	203	139.89502	-66.73182	1375

Table C.1: Stick-slip clusters detected and located beneath the Astrolabe Glacier grounding zone. For each cluster is shown the initial number of events detected, the final number of events detected after manual screening and the longitude, latitude and depth of the cluster.

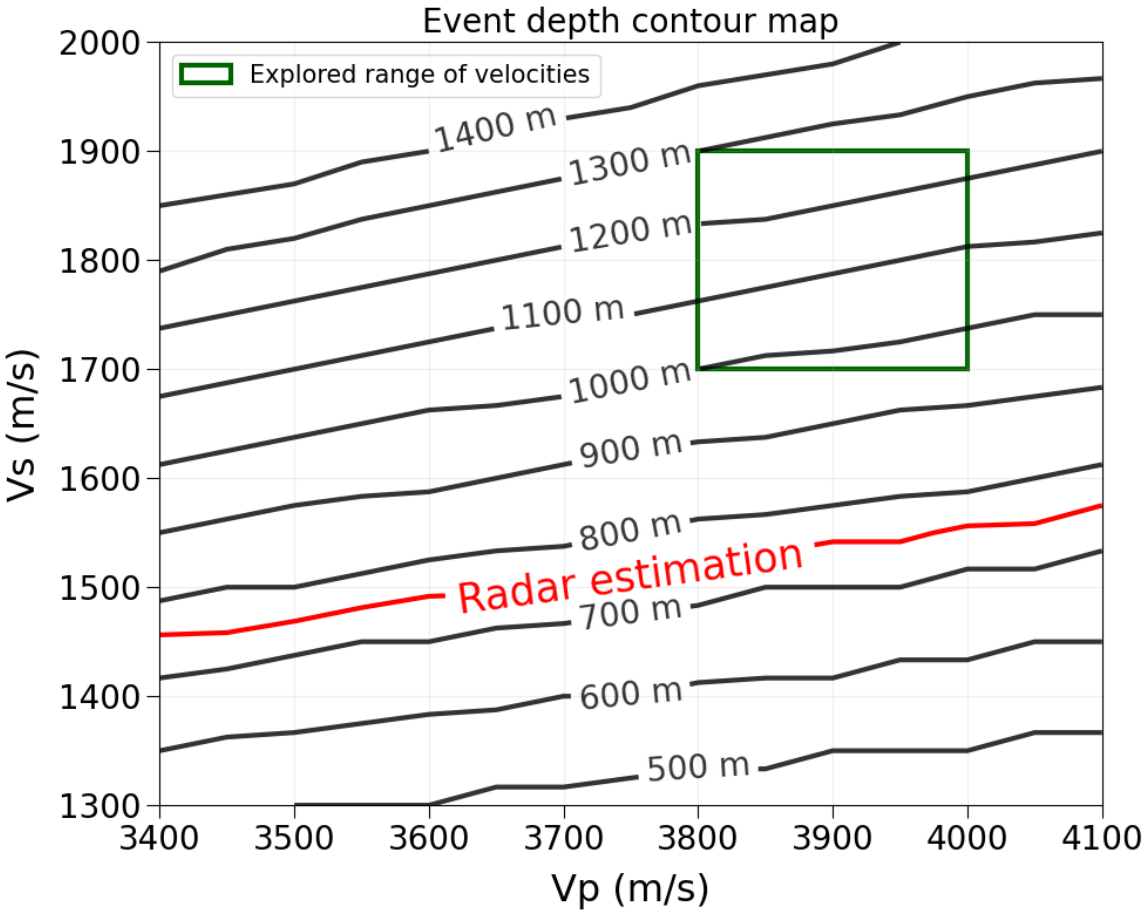

Figure C.1: Contour map of depth estimate as a function of P- wave velocity (Vp) and S- wave velocity (Vs) from grid search on cluster 4 (see Table A1, depth estimate: 1000 m) to explain the measured delay between the P- and S-phase arrival times. For each (Vp, Vs) couple, the depth is estimated based on the minimum RMSE value obtained. The black rectangle delineates the velocity domain explored in the present study. Red line indicates the bedrock depth estimate based on radar data, expected to be around 700 m (Le Meur et al., 2014). A clear trade-off is observed between seismic velocities and estimated depth. The diagram shows that the stick-slip depth estimate is more sensitive to variations in Vs than in Vp and that lower shear velocities may reconcile seismic and radar depth estimates. This highlights the importance of improving the seismic velocity structure of the Astrolabe Glacier to better constrain the absolute depth estimates of the stick-slips at the ice-bedrock interface.

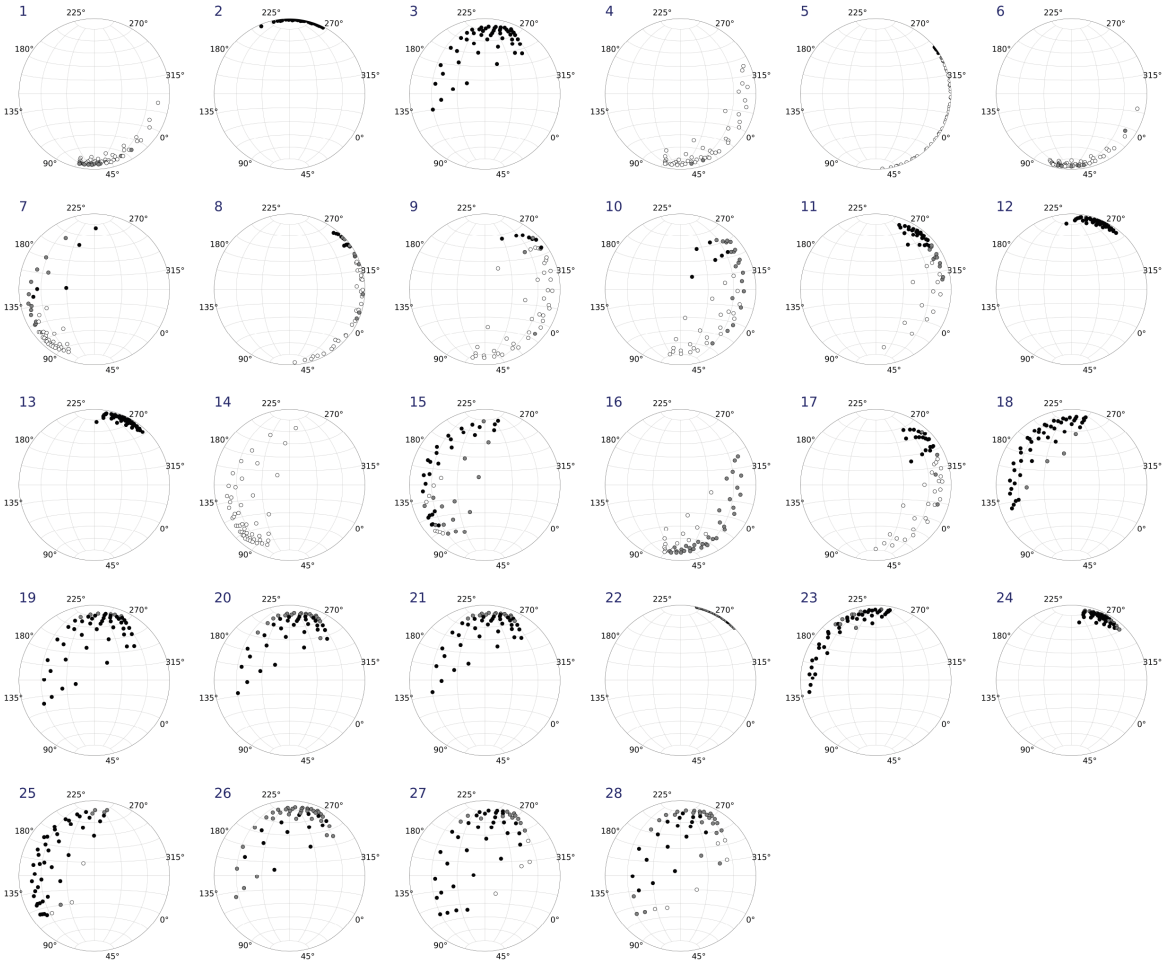

Figure C.2: Individual stereonets (lower hemisphere) representing the upward (black circles) and downward (white circles) first P-wave motion of each stick-slip cluster detected by the dense seismic node array A1, numbered as in Table C.1. Grey circles indicate unsure polarisation by at least one of the three analysts.

APPENDIX D

Appendix chapter 6

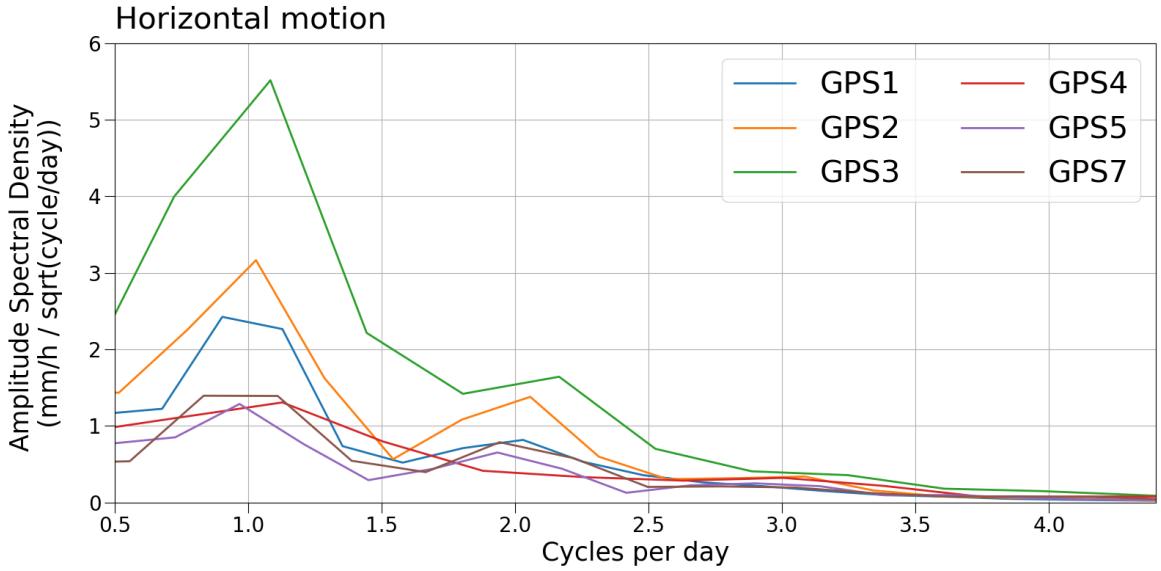

Figure D.1: Amplitude Spectral Density (ASD) of horizontal velocity timeseries at six GPS stations, computed using the Welch method. The x-axis shows frequency in cycles per day, and the y-axis shows ASD in mm/h per $\sqrt{}$cycle/day. Peaks near 1 cycle/day and 2 cycles/day indicate, respectively, diurnal and semidiurnal variability in horizontal motion.

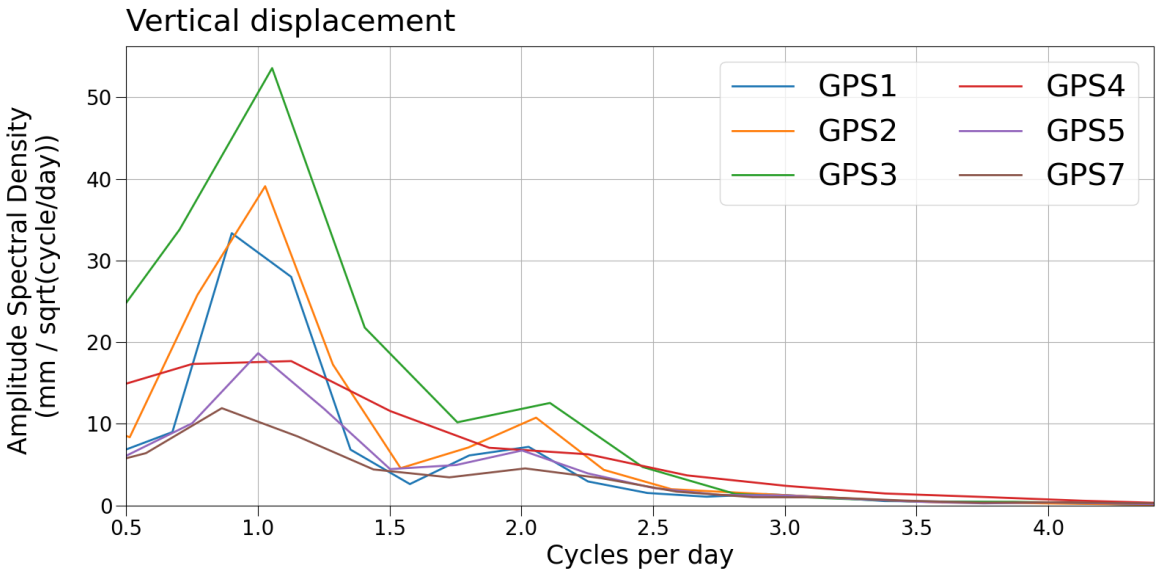

Figure D.2: Amplitude Spectral Density (ASD) of vertical displacement timeseries at six GPS stations, computed using the Welch method. The x-axis shows frequency in cycles per day, and the y-axis shows ASD in mm per $\sqrt{}$cycle/day. Peaks near 1 cycle/day and 2 cycles/day indicate, respectively, diurnal and semidiurnal variability in horizontal motion.

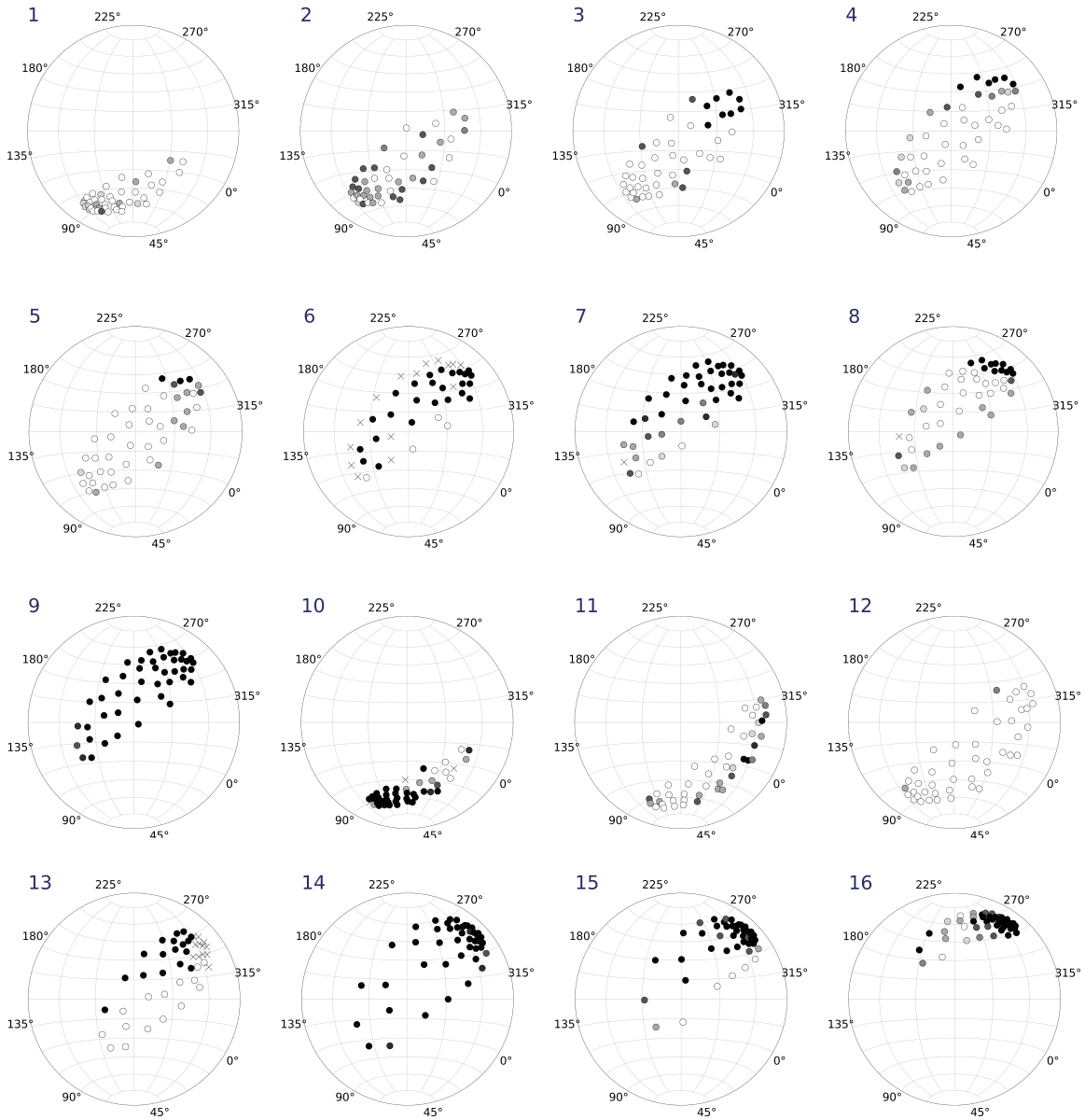

Figure D.3: Individual stereonets for stick-slip clusters detected with dense array A3 (2025) over the shear margin of the Astrolabe Glacier.

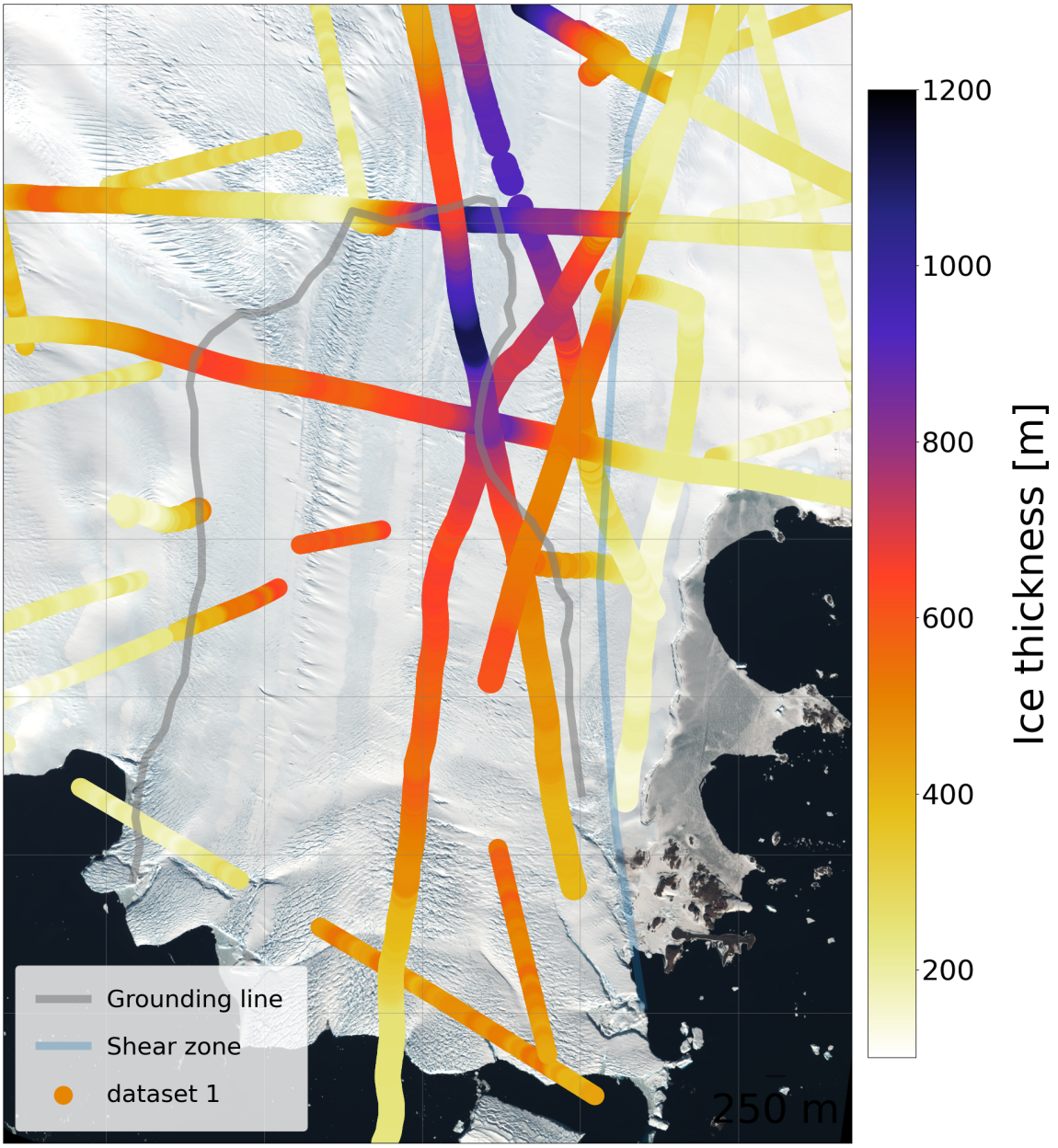

Figure D.4: Map of the ice thickness estimates inferred from radar data over the Astrolabe Glacier area. The radar dataset includes data from different campaigns. Airborne radar data were collected by NASA using the Warm Ice Sounding Explorer (WISE) during the 2008–09 season (Mouginot et al., 2014). Additional airborne measurements were acquired within the ICECAP project using the High Capability Radar Sounder (HiCARS) in 2008-09 and 2009-10 (Young et al., 2011). Ground-penetrating radar (GPR) profiles were collected during the 2007-08 field season (Le Meur et al., 2014). Each dataset was processed independently by the respective project teams.